



HAL
open science

Modeling of shaft precessional motions induced by unilateral and frictional blade/casing contacts in aircraft engines

Nicolas Salvat

► **To cite this version:**

Nicolas Salvat. Modeling of shaft precessional motions induced by unilateral and frictional blade/casing contacts in aircraft engines. Vibrations [physics.class-ph]. McGill University, 2015. English. NNT: . tel-01259136

HAL Id: tel-01259136

<https://theses.hal.science/tel-01259136>

Submitted on 19 Jan 2016

HAL is a multi-disciplinary open access archive for the deposit and dissemination of scientific research documents, whether they are published or not. The documents may come from teaching and research institutions in France or abroad, or from public or private research centers.

L'archive ouverte pluridisciplinaire **HAL**, est destinée au dépôt et à la diffusion de documents scientifiques de niveau recherche, publiés ou non, émanant des établissements d'enseignement et de recherche français ou étrangers, des laboratoires publics ou privés.



Distributed under a Creative Commons Attribution - NonCommercial - ShareAlike 4.0 International License

Department of Mechanical Engineering
McGill University
Montréal, Québec

DOCTORAL DISSERTATION

Modeling of shaft precessional motions induced by unilateral and frictional blade/casing contacts in aircraft engines

Nicolas Salvat

Structural Dynamics and Vibration Laboratory

November, 2015

A Thesis Submitted to McGill University in Partial Fulfillment of the
Requirements of the Degree of Doctor of Philosophy

©Nicolas Salvat, 2015



Dedication

I lovingly dedicate this dissertation to my mother, to offer her a small token of appreciation for her continuous guidance and support, for her love and affection, for her patience and understanding, and for being an amazing source of inspiration in my life.

Acknowledgements

Foremost, I would like to express my gratitude to my advisor Prof. Mathias LEGRAND, for his continuous guidance throughout these years, and whose patience and acute explanations have helped me finish this dissertation. To my fellow researchers and colleagues, specially Prof. Alain BATAILLY and Dr. Markus MEINGAST, for spending countless hours helping me in both coding and writing papers, and who always made themselves available in moments of doubt.

Thanks also go to SNECMA for its technical and financial support, as this work takes place in the framework of the MAIA mechanical research and technology program, sponsored by CNRS, ONERA and SAFRAN GROUP. In particular, to Dr. Antoine MILLECAMPS and Ing. François GARCIN, for providing all necessary documentation and industrial data as well as their guidance throughout this project. I would also like to express my gratitude to Dr. Marie-Océane PARENT and Prof. Fabrice THOUVEREZ for their insightful comments and questions during all the meetings held at SNECMA.

I am truly grateful to MCGILL UNIVERSITY for putting their trust in me and providing me with the MCGILL ENGINEERING DOCTORAL AWARD. Without their financial contribution and all the university resources that were at my disposal, not to mention the always friendly advice and help from the Department staff, this research project would never have been accomplished.

Last but not least, I would like to thank my family, specially my parents, my sister and of course *la tia favorita*, for their endless encouragement and support, and for always being present despite the distance. To my friends and particularly my roommates Jonathan and Roberto, for all the amazing moments we spent together discovering this great country and who have made my stay in Montréal better than I ever hoped for. And of course, I'll be forever grateful to my girlfriend Ruth Maria, whose warmth, love and trust have been without measure.

Abstract

In modern aircraft turbomachinery, undesirable unilateral and frictional contact occurrences between rotating and stationary components, favored by always tighter blade-tip clearances, are expected to arise during standard operating conditions. It has been shown that potentially harmful interactions may threaten the engine structural integrity. In particular, among various interaction mechanisms, shaft whirl motions may be a major ingredient in the blade-to-casing structural interactions at the fan stage. The present work targets the appropriate modeling of such shaft precessional motions and contact dynamics in order to enhance existing predictive numerical solution methods.

A qualitative study is first presented, employing a simplified two-dimensional in-plane finite element model representative of a bladed-disk/casing system, accounting for the shaft flexibility as well as the structural coupling provided by the fan frame and bearings. A previously established time-marching strategy is implemented to solve the equations of motion and unilateral contact constraints are enforced via Lagrange multiplier method, allowing to exactly satisfy non-penetration conditions. The interactions between these flexible structures are initiated via two distinct mechanisms: (1) a prescribed casing distortion and (2) a mass imbalance on the bladed-disk. The shaft dynamics proved to have a key role in producing potentially harmful regimes, in particular in the former scenario, which can lead to divergent modal interactions.

Further, a novel modal analysis of a fully coupled industrial bladed-disk/casing model is proposed in a three-dimensional cyclic-symmetric framework. This analysis considers the entire stage (rotating shaft+bladed-disk assembly+casing+frame+bearings) as a single global structural component. Parametric instabilities are revealed and critical rotational velocities emanate from the linear modal coincidence interaction speeds. As these fully coupled models exclude reasonable computational time in a nonlinear framework, the casing is then assumed rigid in a time-domain exploratory investigation of bladed-disk/abradable interactions.

Abradable coatings are disposed along the casing circumference in order to mitigate direct structural contacts between rotating blades and the surrounding stator while allowing for a self-tuning of operating blade-tip clearances. They should be sufficiently resilient to endure severe thermal conditions and hostile constraints but also adequately soft not to alter the structural integrity of the blades. However, divergent interactions are found within the engine operating speed range, characterized by high-amplitude backward whirling motions which could result in catastrophic structural failures. A time-stepping prediction-correction procedure is implemented part of which the wear of the abradable layer is accounted through a plastic constitutive law. A sensitivity analysis of the detected interactions to the shaft dynamics and associated gyroscopic terms shows that divergent backward whirling motions may emerge within the targeted speed range, generating high-stress levels on the bladed-disk/shaft assembly and significant material removal over the entire casing circumference. It is also shown that all the blades should be included in the modeling as simplified systems (single blade or contact handled on one sector) would lead to incorrect predictions.

An alternative method is developed based on the analogy between the abradable coating wear caused by the incursion of the blades and the material removal process in traditional machining operations. A set of Delay Differential Equations (DDE) is derived through an explicit yet simplified expression of the contact forces. The stability of the equilibrium solution of the DDE is then assessed through the semi-discretization method. An industrial compressor blade is employed to demonstrate the advantages of the proposed approach which features reduced computational costs and consistency with existing time-marching solution methods. Potentially dangerous interaction regimes are accurately predicted and instability lobes match both the flexural and torsional modal responses. A comparison of exploratory blade profiles illustrates how engine manufacturers may benefit from the presented methodology; in this last study, shaft motions should be ignored.

Résumé

Dans le domaine des turbomachines aéronautiques, les occurrences de contacts unilatéraux et de frottement entre composants en rotation et fixes, favorisés par des jeux fonctionnels en sommet d'aube constamment réduits, sont dorénavant considérées comme des événements prévisibles, bien qu'indésirables. Des études expérimentales et numériques ont démontré que des interactions potentiellement dangereuses peuvent surgir et menacer l'intégrité du moteur. En particulier, parmi plusieurs mécanismes d'interaction, les mouvements de tournoiement de l'arbre semblent jouer un rôle primordial dans les interactions structurales aube-carter au niveau de la soufflante. Le travail proposé concerne donc un modélisation appropriée de ces mouvements de précession de l'arbre et de la dynamique de contact associée, afin d'améliorer les outils numériques prédictifs existants.

Une étude qualitative est présentée en employant un modèle éléments finis planaire représentatif d'un système roue-aubagée/carter, où la flexibilité de l'arbre ainsi que le couplage fourni par les bras et les roulements de la soufflante sont pris en compte. Une stratégie d'intégration temporelle précédemment établie est mise en œuvre pour résoudre les équations de mouvement. Les inégalités de contact sont imposées par la méthode des multiplicateurs de Lagrange permettant de satisfaire les conditions de non-pénétration. Les interactions entre ces structures flexibles sont initiées par deux mécanismes distincts: (1) une distorsion initiale du carter et (2) un effort de balourd appliqué au centre du disque. La bonne représentation de la dynamique d'arbre est cruciale dans l'apparition de régimes potentiellement dangereux, en particulier dans le premier scénario qui peut conduire à des interactions modales divergentes.

Par ailleurs, une nouvelle méthode d'analyse modale d'un ensemble roue-aubagée/carter industriel est proposée dans un cadre tridimensionnel en symétrie cyclique. Cette analyse considère l'étage entier (arbre+roue aubagée en rotation+carter+bras+roulements) comme une unique structure globale. Des instabilités

paramétriques sont prédites et les vitesses critiques associées surgissent à partir des vitesses d'interaction modales. Ces modèles entièrement couplés excluent des temps de calcul raisonnables dans un cadre non-linéaire et par conséquent le carter est par la suite considéré comme rigide dans l'étude des interactions roue-aubagée/abradable. Les revêtements abradables sont disposés sur le carter afin d'atténuer les contacts directs entre parties tournantes et parties fixes, tout en permettant une optimisation des jeux fonctionnels en sommet d'aube. Ces matériaux doivent à la fois être résistants pour supporter des contraintes thermiques et mécaniques sévères mais également être souples pour ne pas altérer l'intégrité structurale des aubages en cas de contacts. Longtemps vus comme une solution robuste pour éviter l'apparition de hauts niveaux de vibration lors de contacts structuraux, ces matériaux n'empêchent toutefois pas certains phénomènes d'interaction de se produire. Un algorithme de prédiction-corréction est employé, en considérant un carter rigide et modélisant l'usure du revêtement d'abradable par le biais d'une loi elasto-plastique. Pour la plage de vitesses de rotation considérée, certains régimes d'interaction sont captés, caractérisés par des mouvements de tournoiement rétrogrades de fortes amplitudes qui pourraient éventuellement entraîner des défaillances structurales. L'étude se focalise sur la sensibilité de ces régimes à la dynamique d'arbre et aux termes gyroscopiques associés. Il est notamment montré que seul un modèle global incluant la gestion du contact en sommet d'aube sur l'ensemble des secteurs est pertinent. Cependant, les mouvements particuliers pouvant conduire à un tournoiement direct de l'arbre ne sont pas prédits par les modèles proposés.

Une méthode alternative est développée en se basant sur l'analogie entre l'usure du revêtement d'abradable par l'incursion des aubes et le processus d'enlèvement de matière dans les opérations d'usinage traditionnel comme le fraisage ou le tournage. Un ensemble d'équations différentielles à retard (EDR) est dérivé grâce à une expression explicite et simplifiée des efforts de contact. La stabilité de la solution d'équilibre de l'EDR est évaluée au moyen de la méthode de semi-discrétisation. Une aube de compresseur industriel est employée pour démontrer les avantages de l'approche proposée, qui permet notamment d'obtenir une réduction des temps de calcul et une cohérence avec les méthodes d'intégration temporelles existantes. Des régimes d'interaction potentiellement dangereux sont prédits correctement et les lobes d'instabilité obtenus coïncident avec les réponses modales en flexion et en torsion. Une comparaison de différents profils d'aube illustre comment les fabricants de moteurs peuvent bénéficier de la méthodologie afin de discriminer les géométries peu robustes au phénomène d'interaction. Dans cette étude les mouvements d'arbre sont ignorés.

Contents

Dedication	iii
Acknowledgements	v
Abstract	vii
Résumé	ix
1 Introduction	1
1.1 Project context: rotor/stator contact in turbomachines	1
1.1.1 Aircraft engine components and thermodynamic cycle	2
1.1.2 Operating clearance closure mechanisms	3
1.1.3 Rotor/stator interactions induced engine failures	7
1.2 Research objectives	8
1.3 Organization of the thesis	9
2 Literature review	11
2.1 General equations and basic concepts in rotor-dynamics	11
2.1.1 Spatial discretization: Finite Element Method	11
2.1.2 Brief review on phenomena and history	13
2.2 Dedicated numerical strategies	17
2.2.1 Time-marching techniques	17
2.2.2 Modal reduction techniques	18

2.2.3	Unilateral and frictional contact conditions	19
2.2.4	Frequency domain approaches	22
2.2.5	Abradable coatings and wear	22
2.3	Rotor/stator interactions	23
2.3.1	Modal coincidence	24
2.3.2	Rubbing	25
2.3.3	Whirling motions	28
3	Dynamics of an aircraft engine fan stage: industrial application	31
3.1	Modal properties of cyclically symmetric structures	31
3.1.1	Theoretical background	31
3.1.2	Analysis of shaft motions	34
3.2	Gyroscopic terms in the finite-element framework	37
3.2.1	Construction of the gyroscopic matrix	37
3.2.2	Illustrative example and validation	39
3.3	Modal features of the fan bladed-disk	41
3.3.1	Fundamental sector model	41
3.3.2	Modal analysis and mesh convergence	42
3.3.3	Shaft modal displacements	44
3.4	On bladed-disk/casing structural coupling	45
3.4.1	Bladed-disk at rest	46
3.4.2	Rotating bladed-disk	52
3.5	Summary	60
4	Two-dimensional modeling of bladed-disk/casing interactions	63
4.1	Structural models	63
4.1.1	Bladed-disk and casing models	63
4.1.2	Craig-Bampton model reduction	65
4.1.3	Bearings and frame coupling methodology	65
4.2	Modal analysis of the bladed-disk/casing system	66
4.2.1	Uncoupled structures	66
4.2.2	Coupled structures	69
4.3	Contact simulations	72

4.3.1	Solution algorithm	72
4.3.2	Space-time discretization convergence	74
4.3.3	Results and discussion	74
4.4	Summary	85
5	Three-dimensional contact and abradable wear investigation	87
5.1	Assumptions and simulation procedure	88
5.2	Industrial structural models	89
5.2.1	Single blade model	90
5.2.2	Full bladed-disk model	92
5.3	Space and time convergence analysis	93
5.4	Results and discussion	95
5.4.1	Reference simulations	95
5.4.2	Analysis at a critical speed	97
5.4.3	Sensitivity to gyroscopic terms	100
5.4.4	Investigation of exploratory scenarios of interaction	104
5.5	Summary	109
6	Modeling of abradable coating removal through delay differential equations	111
6.1	Delay differential equations	113
6.1.1	Theoretical background	113
6.1.2	Stability analysis	114
6.1.3	Semi-Discretization Method	116
6.2	Modeling strategy	117
6.2.1	Cutting law in milling	118
6.2.2	Abradable material removal strategy	119
6.3	Preliminary results	120
6.3.1	Validation and convergence analysis	120
6.3.2	Centrifugal stiffening	123
6.4	Results	124
6.4.1	Comparison with time domain simulations	124
6.4.2	Analysis of frictional forces	128
6.4.3	Application to improved compressor blade designs	129

6.4.4	Extension to fan blades	131
6.5	Summary	132
7	Summary and conclusions	133
7.1	Main findings	133
7.2	Current limitations and perspectives for future research	135
7.3	List of publications and contributions	136
A	Space and time Fourier transform	139
A.1	General notations	139
A.2	Examples	140
A.2.1	Example 1: single harmonic excitation	140
A.2.2	Example 2: dual harmonic excitation	142
B	DDE MATLAB source code	145
C	Blade/abradable separation in DDE	149
	Nomenclature	153
	Bibliography	157

List of Tables

4.1	Simulation parameters - scenario A	75
5.1	COROS simulation parameters	96
6.1	Relative frequency variations in %	130
A.1	Physical and cyclic coordinates	139
A.2	Example 1 - signal parameters	141
A.3	Example 2 - signal parameters	143

List of Figures

1.1	Turbofan engine components	2
1.2	Brayton cycle	3
1.3	Blade-tip clearance	3
1.4	HPT clearance variations during flight	4
1.5	Resulting casing distortion	5
1.6	Types of whirling motion and contact configurations	6
1.7	Engine fan stage after failure	8
2.1	Campbell diagram example	15
2.2	Types of systems subject to rotor/stator interactions	16
2.3	One-dimensional example of contact conditions	19
2.4	Approximation of Kuhn-Tucker conditions	21
2.5	Modal coincidence between $n_d = 3$ nodal diameter waves	24
2.6	Schematic of compressor blade after rubbing test	26
2.7	Experimental set-up for steel-on-steel rubbing	27
2.8	Mode shapes and contact configurations	29
3.1	Example of cyclically symmetric structures: $N = 6$	31
3.2	Illustrative example FE-model	39
3.3	Illustrative example Campbell diagram	40
3.4	Industrial fan stage components	41
3.5	Bladed-disk model: shaft/disk/blade fundamental sector	42

3.6	Mesh convergence study of the bladed-disk model	43
3.7	Modal analysis of bladed-disk model	43
3.8	Mode shapes of bladed-disk	44
3.9	Campbell diagram of bladed-disk with gyroscopic terms	44
3.10	Shaft modal displacements and associated mode shapes	45
3.11	Coupled bladed-disk/casing model with blocked rotation	46
3.12	Mass imbalance scenario: loading conditions and corresponding displacements	47
3.13	Intake-flow scenario: loading conditions and corresponding displacements	48
3.14	Mode shapes of bladed-disk/casing coupled model	49
3.15	Modal displacements of shaft and casing	50
3.16	Mode shapes of bladed-disk/casing coupled model: harmonic $n_d = 1$	51
3.17	Veering diagram and strain energy distribution along components	52
3.18	Coupled bladed-disk casing model with flexible bearings	52
3.19	Free vibration mode-shapes of bladed-disk and casing/frame components	54
3.20	Equivalent reduced-order coupled model under 1-nodal diameter distortion	55
3.21	Stability analysis	58
3.22	Eigenvalues for $\kappa = 3000$ N/m	59
3.23	Divergent mode characteristics: $\Omega = 3.8$ and $\kappa = 3000$ N/m	60
4.1	Simplified fan stage model: flexible bladed-disk and casing connected by array of springs	64
4.2	First family of bladed-disk free vibration modes	67
4.3	Veering diagram with clamped and free center node	67
4.4	Relative frame Campbell diagram	68
4.5	Regular contact configuration for 1-nodal diameter modes	68
4.6	Inverted contact configuration for 1-nodal diameter modes	69
4.7	Stability analysis of equilibrium solution	70
4.8	Evolution of eigenvalues of coupled structures for $\kappa = 500$ N/m	71
4.9	Deformed 1-nodal diameter mode shape in time	71
4.10	Center node motion characteristics: $\Omega = 1.17$ and $\kappa = 500$ N/m	72
4.11	Frequency response of center node for casing distortion excitation	76
4.12	Center node orbit: $\Omega = 1.05$ and $\kappa = 0$ N/m	76
4.13	Results for initial casing distortion at $\Omega = 1.05$ and $\kappa = 0$ N/m	77

4.14	Results for initial casing distortion at $\Omega = 1.39$ and $\kappa = 0 \text{ N/m}$	77
4.15	Frequency response of center node for mass imbalance excitation	79
4.16	Results for mass imbalance load at $\Omega = 1.05$ and $\kappa = 0 \text{ N/m}$	80
4.17	Contact characteristics: $\Omega = 1.05$ and $\kappa = 0 \text{ N/m}$	81
4.18	Strain energy at $\Omega = 1.6$ and $\kappa = 0 \text{ N/m}$	81
4.19	Results for casing distortion excitation at $\Omega = 1.05$ and $\kappa = 0 \text{ N/m}$	83
4.20	Maximal shaft displacements near Ω_1^{cr}	83
4.21	Results for mass imbalance excitation at $\Omega = 1.05$	84
4.22	Strain energy for $\kappa = 0 \text{ N/m}$ at $\Omega = 1.65$	85
5.1	Blade/abradable layer interaction	88
5.2	Abradable elasto-plastic constitutive law	89
5.3	Fan blade model	90
5.4	Modal analysis of the blade model	91
5.5	Blade-tip displacements under centrifugal loads	91
5.6	Comparison of 1-nodal diameter modes	92
5.7	Bladed-disk with additional boundary conditions	92
5.8	Blade-tip displacements under centrifugal loads	93
5.9	Modal basis convergence	94
5.10	Wear maps: multi-sector model without gyroscopic terms	96
5.11	Fourier transform of LE displacements	97
5.12	Results for $\Omega = 1.02$	98
5.13	Frequency analysis for $\Omega = 1.02$	99
5.14	Displacements modulus for $\Omega = 1.02$ recast in Finite-Element space	99
5.15	Normalized Von Mises stresses for $\Omega = 1.02$	100
5.16	Wear maps: multi-sector model with gyroscopic terms	101
5.17	Fourier transform of LE displacements	101
5.18	Results for Ω_2	102
5.19	Frequency response for Ω_2	102
5.20	Results for $\Omega = 1.44$	103
5.21	Results recast in Finite-Element space for $\Omega = 1.44$ at $N_{\text{rev}} = 45$	104
5.22	Wear maps: multi-sector model with contact on a single blade	105

5.23	Fourier transform of LE displacements	105
5.24	Results for Ω_2 - contact on single blade hypothesis	106
5.25	Spectrograms for Ω_2 - contact on single blade hypothesis	106
5.26	Wear maps: single blade model	107
5.27	Results for Ω_2 - rigid shaft hypothesis	108
5.28	Frequency response for Ω_2 - rigid shaft hypothesis	108
6.1	Analogy between abradable removal and milling	112
6.2	Different bifurcation mechanisms	115
6.3	Blade of interest	117
6.4	Schematic of milling with chatter	118
6.5	Schematic of abradable material removal	119
6.6	Test points in stability map	121
6.7	Tip radial displacement	121
6.8	Time convergence	122
6.9	Modal convergence	123
6.10	Instability lobes versus centrifugal effects	123
6.11	Instability lobes versus blade-tip contact location	125
6.12	Abradable wear map: contact at blade trailing edge	125
6.13	Abradable wear map: contact at blade leading edge	126
6.14	Instability lobes versus mode type	127
6.15	Spectrum of time-domain response	128
6.16	Instability lobes versus friction coefficient	129
6.17	Modified blade geometries compared to reference model	130
6.18	Comparison of stability maps	130
6.19	Fan blade instability lobes	131
A.1	Example of a cyclic structure	140
A.2	Time response of all sectors	141
A.3	Analysis of first sector response	142
A.4	2D-FFT of time response	142
A.5	Analysis of first sector response	143
A.6	Time response of all sectors	143

A.7	2D-FFT of time response	144
C.1	Hypothetical penetration and separation phases	150
C.2	Instability lobes: sensitivity to loss of contact	151

Introduction

The work presented in this dissertation was carried out at the STRUCTURAL DYNAMICS AND VIBRATION LABORATORY, within the Department of Mechanical Engineering of MCGILL UNIVERSITY. The main research focus of the laboratory, directed by Dr. Mathias LEGRAND, is the numerical modeling of nonlinear/non-smooth dynamical systems, in particular for the analysis of rotating machinery vibratory responses.

This research project was conducted in collaboration with SNECMA from SAFRAN GROUP, which is a worldwide leader engine manufacturer for civil and military aircrafts, launch vehicles and satellites. Among other projects, SNECMA designs, develops, markets and produces turbofan engines.

1.1. Project context: rotor/stator contact in turbomachines

In the aeronautical and space industry, reliability and efficiency stand as major concerns for both economical and environmental purposes. Among other challenges, gaining fuel consumption while increasing power, lowering noise and gas emissions, increasing the components lifespan while decreasing weight, have attracted considerable interest and effort. Various strategies have been adopted in distinct fields of this multidisciplinary industry, such as the use ultralight-weight materials (*e.g.* titanium alloys and composite materials) for the fuselage and wings of the aircrafts [WS03], the development of multidisciplinary optimization algorithms able to handle both structural and fluid constraints [SH97] as well as planning cost-efficient flight trajectories [FBB14], to name a few. In the particular field of propulsion, efficiency enhancement of aircraft engines [MHP02] is achieved through flow-path and geometry optimization, or the increase of compression ratios and combustion temperatures, among other strategies.

1.1.1. Aircraft engine components and thermodynamic cycle

Depending on the aircraft requirements, either *gas turbines* or *piston engines* are used to generate the thrust which propels the aircraft. In this work, the engine of interest is a so-called two-spool turbofan. As illustrated in Fig. 1.1, the Fan and Low Pressure (LP) compressor are connected to the LP turbine through one shaft while the High Pressure (HP) compressor and the HP turbine are linked through another independent shaft. This technology is most commonly adopted in turbofans, so that the LP stages may spin at much lower velocities than the HP ones in order to increase the *bypass ratio*. It is defined as the ratio between the mass

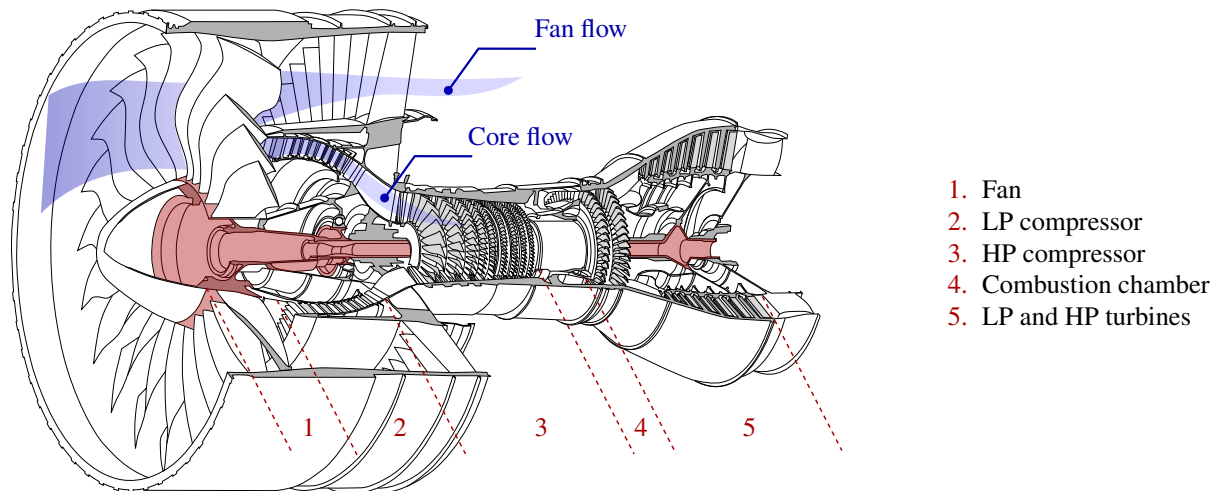


Figure 1.1: Turbofan engine components

flow of air going through the fan and the mass flow passing through the engine core. The flow going into the engine is divided in two separate paths: the *core flow* goes through all the above mentioned components and allows the engine to run, whereas the *fan flow* only travels through the fan stage and produces about 80 % of the total thrust. The bypass ratio for the mid-size engines is generally about 5:1 and newest technologies can achieve ratios up to 15:1 or more, thus significantly increasing the engine efficiency and lowering its noise emissions as the exhaust speeds are significantly lower.

Like most gas turbines, the basic operation of a turbofan is described through a Brayton cycle [Lie06], represented in the Pressure-Volume diagram 1.2, where the objective is to convert the intake air into a high pressure and high temperature fluid by compressing it, mixing it to fuel and igniting the mixture. The intake air at atmospheric pressure is compressed through the fan and compressor stages. It then goes into the combustion chamber where it is mixed with fuel and ignited, thus leading to a sharp increase in temperature. Finally, it reaches the turbine stages for the expansion phase, where the work is extracted from the fluid in order to drive the fan and compressor stages. Part of the remaining energy is transformed into thrust at the

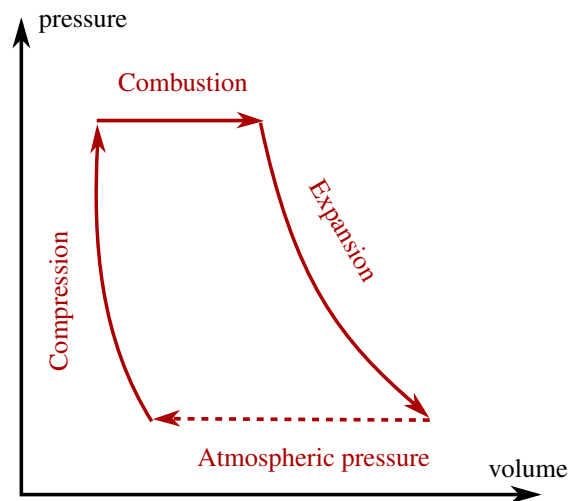


Figure 1.2: Brayton cycle

nozzle (not pictured in Fig. 1.1) due to the difference in velocity from intake to exhaust. It becomes clear that achieving the highest compression ratios and combustion temperatures are major factors driving the cycle efficiency.

1.1.2. Operating clearance closure mechanisms

From a structural standpoint, one of the most sensitive parameters to be tuned in compressor and fan stages is the *blade-tip clearance*. It is defined as the effective distance between the rotating airfoil tips and the surrounding stationary casing at nominal operating conditions and is illustrated in Fig. 1.3. In fact, this

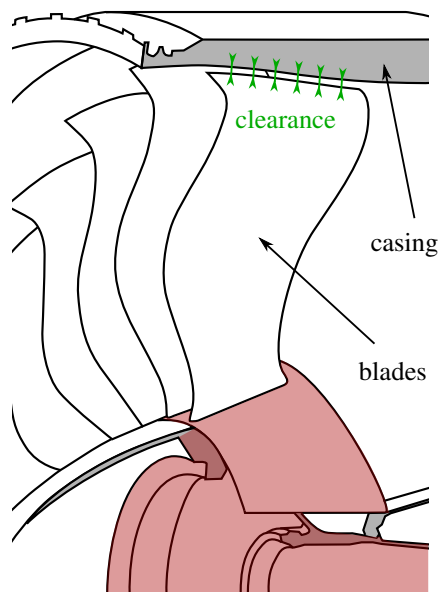


Figure 1.3: Blade-tip clearance

distance must be as small as possible to ensure high compression ratios and engine performance as detailed in [HP14]. Further, according to [KB00], “*in compressors, an increase of the rotor tip clearance from 1 % of blade chord to 3.5 % of blade chord reduces the pressure ratio of the stage by up to 15 %*”.

As explained in [LS04] and pictured in Fig. 1.4, different loads act on both rotating and stationary components while the engine is in service and produce significant fluctuations in the radial position of the airfoil tips with respect to their surrounding casing. Therefore, keeping the operating clearances to a minimum throughout the entire flight induces difficulties, both from manufacturing and design perspectives, mainly because these loads are often transient and non-deterministic, thus rendering an accurate prediction of the turbomachine structural behavior a very difficult task.

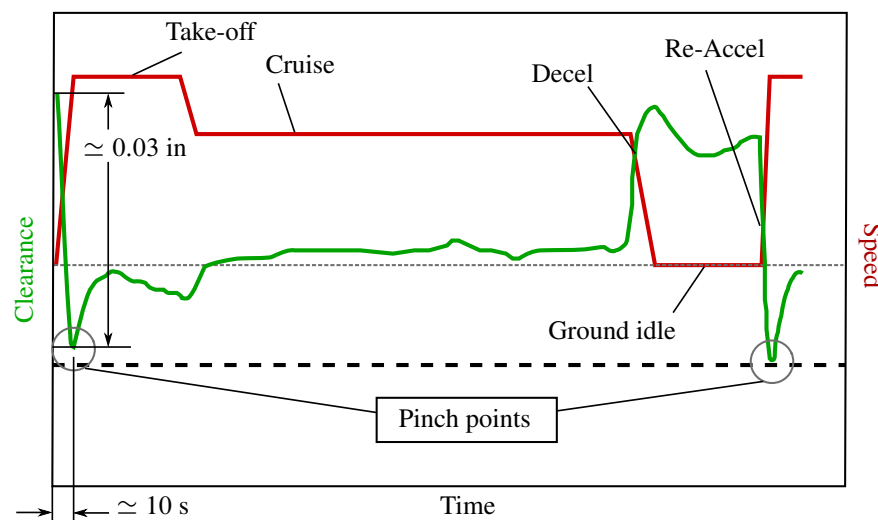


Figure 1.4: HPT clearance variations during flight [LS04]

In general, clearance changes are classified into two distinct categories: axisymmetric and asymmetric clearance changes.

Axisymmetric clearance changes Axisymmetric clearance changes are due to uniform loads on both casing and rotor, which translate into a uniform radial relative displacement between the two structures. The main sources for this kind of excitation are known to be the centrifugal loads, which are produced by the rotation of the rotor and generate an expansion of the blades, and the thermal loads, which induce thermal expansion/contraction of both stationary and rotating components.

These loads are predominant during acceleration and deceleration phases of the engine shown in Fig. 1.4. When a cold engine is started, the original clearance at rest starts to shrink as the rotor speed increases due to the centrifugal loads, followed by an expansion of the casing due to thermal loads thus opening the clearances again. Finally, the thermal expansion of the rotor (occurring at a lower rate than for the casing) produces a

gradual drop in the gap. The opposite phenomenon is observed during deceleration phases where clearances tend to open.

Asymmetric clearance changes Asymmetric clearance changes are due to nonuniform loads, usually on the stationary structures, and produce nonuniform radial relative displacements between rotor and stator. For instance, a nonuniform cooling/heating of the components may lead to local distortions and in particular to a phenomenon known as *casing ovalization*. Other mechanisms come from maneuver and aerodynamic loads (e.g. intake flow, thrust). As depicted in Fig. 1.4, the largest clearance variations occur during take-off and re-acceleration phases of the flight, giving rise to the so-called *pinch points*. During these phases, “*the thrust loads create a downward pitch moment causing clearances to open toward the top of the engine while closing at the bottom*”.

Further, as reported in [OM82] from experimental measurements of the PRATT & WHITNEY JT9D engine, the inflow loads during take-off “*cause the front flange of the fan case to deflect upward more than the front section of the low-speed rotor*”. A phenomenon referred to as *backbone bending*, in which case, unilateral contact is prone to occur at the fan section in a direction opposite to the shaft displacements. This scenario was also studied numerically in [FIO83] from a static viewpoint, as pictured in Fig. 1.5, where the deflection of the casing of an entire engine was explored via a high-fidelity three-dimensional finite element model.

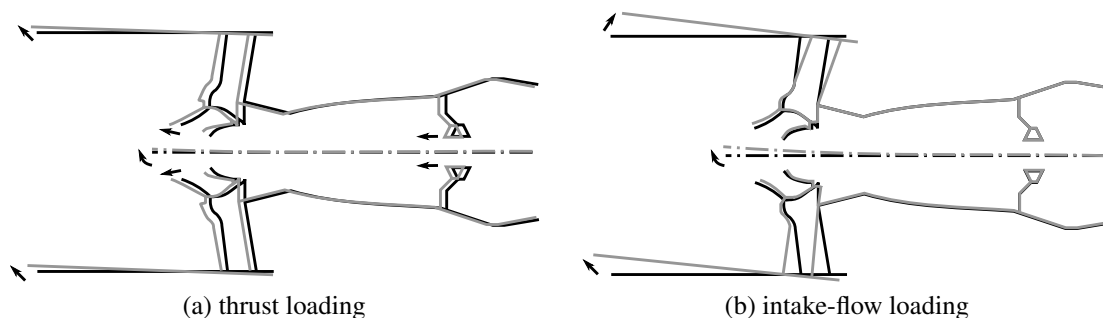


Figure 1.5: Resulting casing distortion from [FIO83]

It then seems clear that contact events between rotating airfoil tips and surrounding casing are favored with increasingly tight operating clearances. As will be further detailed in chapter 2, these are referred to as *rotor/stator interactions* and potentially lead to destructive vibratory behaviors that may put the engine structural integrity at risk [Leg+09]. In order to tackle this difficulty, the strategy adopted by SNECMA along other engine manufactures, is the implementation of abradable materials [Yi+99] on casings so that operating tip clearances are optimally reduced while direct unilateral contact occurrences between rotating and stationary

components are efficiently mitigated. These coatings must be sufficiently resilient to endure severe thermal gradients, elevated temperatures and hostile constraints due to particle ingestions and high pressure levels, but also be adequately soft not to alter the structural integrity of potentially incurring blades. Although considered as a robust technological solution to avoid high-amplitude blade vibrations, recent experimental [Mil+09] and numerical [Bat+12] investigations have shown that potentially harmful interactions may arise, thus jeopardizing safety and efficiency.

Therefore, there is a growing need for predictive numerical strategies that would accurately model the turbomachine vibratory behavior subjected to unilateral contact constraints in order to aid aircraft engine manufactures in the structural design process. Most existing works regarding bladed-disk/casing interactions neglect the dynamic contribution of the shaft and solely focus on the distortion of the blades [Leg+09]. However, the shaft dynamic contribution is of particular importance at the fan stage of the engine due to the overhung (or cantilevered) configuration which is commonly adopted, *i.e.* the bladed-disk is mounted on the free end of the LP shaft. In fact, important shaft vibration amplitudes were observed during several test campaigns held at SNECMA, where direct blade/casing contacts at the fan stage of an engine supposedly induced whirling motions and resulted in damage on that particular module. Whirl is generally defined as a precessional motion of the shaft where the entire rotor spins in a bent configuration [Gen05]. These motions were presumably excited through the tangential forces f_T stemming from the blade-tips frictional contacts and the subsequently generated torque at the center of the bladed-disk.

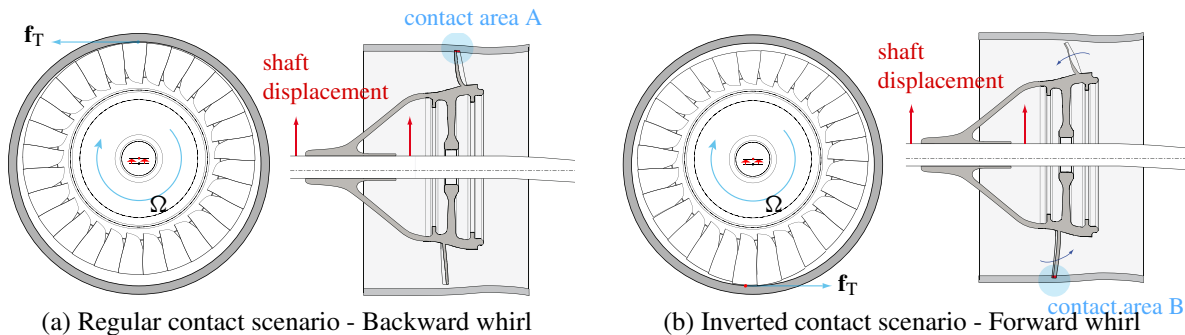


Figure 1.6: Types of whirling motion and contact configurations

Two contact scenarios are encountered and may lead to various types of whirling motions depending on the direction of the shaft precessional motion with respect to its intrinsic rotation [PTC14]:

Backward whirl Backward whirl emerges when the shaft orbits in the direction opposite to the rotational speed. It supposedly arises when contact takes place in the direction of the shaft displacement. As shown in Fig. 1.6a, the shaft moves upward and contact takes place at location A. The resulting frictional torque at the center of the bladed-disk would be in the direction opposite to the rotational

speed (considered in clock-wise direction in Fig. 1.6), thus potentially exciting backward or reverse whirling motions.

Forward whirl Forward whirl appears when the shaft orbits in the direction of the rotational speed. As shown in Fig. 1.6b, the shaft displacements remain in the upward direction while contact arises at the bottom of the engine in area B. The resulting frictional torque at the center of the bladed-disk would be in the direction of the rotational speed, thus potentially leading to a direct or forward whirling motion.

1.1.3. Rotor/stator interactions induced engine failures

Current industry standards regarding rotor/stator interactions limit to a linear prediction of critical speeds based on a modal analysis of the rotating and stationary components. As detailed in section 2.3.1, these critical velocities are defined based on the coincidence of the wave speeds of bladed-disk and casing modes of matching geometrical shape within the rotational speed range of the engine [Sch97]. If a coincidence is detected, small structural modifications may be applied to either structure in order to shift these critical velocities out of the operating speed range of the engine. Yet, as explained in [Mei14], this criterion is not sufficient and often misleading as not all the predicted interactions result in actual high amplitude vibrations. Moreover, sub and super-harmonic responses that may initiate the interactions are not accounted for. Therefore, it seems crucial to carry out further analyses in order to accurately predict potentially harmful interactions at early design stages of the engine.

The lack of knowledge on this nonlinear phenomenon has been responsible of several engine failures during the past decades, for instance, a particularly dramatic accident occurred in 1973 as reported by the National Transportation Safety Board (NTSB) [Nat73]: the probable cause of this accident was the disintegration of the engine fan assembly as a result of an interaction between the fan blade tips and the fan case. The remaining parts of the engine are pictured in Fig. 1.7, highlighting the violence of the interaction. It is said that the pilot and flight engineer were experimenting with the relationship between the fan speed signals and the automatic flight control systems that led to an over-speed of the engine, but according to the NTSB, “*the precise reason or reasons for the acceleration and the onset of the destructive vibration could not be determined conclusively*”. Although there is no mention of whirling motions in the report, given the state of what was left of the fan stage, high-amplitude shaft vibration were very likely part of the bladed-disk vibratory response. This incident is particularly remembered because a fragment of the engine impacted one of the cabin windows leading to a crack and a loss of pressure that forced one passenger through the opening.

More recent engine failures associated to heavy rubs in the fan and compressor stages have been reported, for example the GE90 powering the Boeing 777, where the engine automatically recovered from a surge at

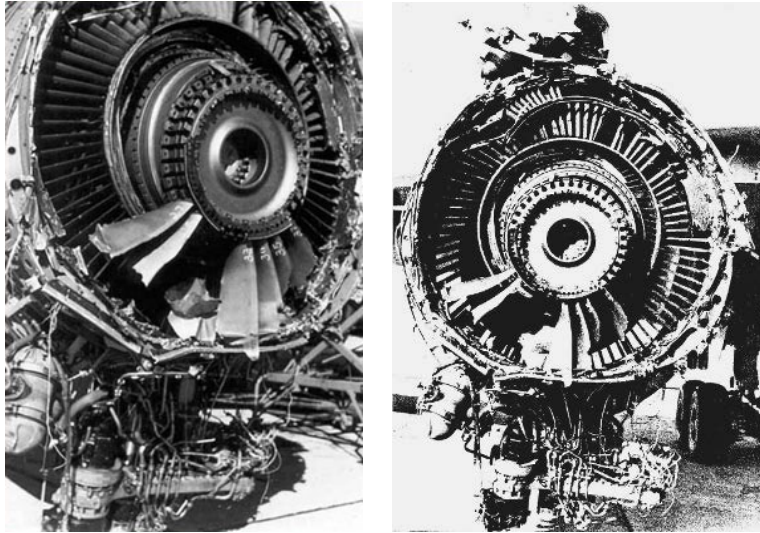


Figure 1.7: Engine fan stage after failure [Nat73]

early take-off and according to Boeing, “*the resulting damage to the fan-rub strip and fan blades themselves was worse than expected*” [Nor95]. A similar incident was reported by the Australian Transport Safety Bureau (ATBS) in 2010, where a Rolls-Royce RB211-524G engine failed after one blade of the HPC was liberated at blade-root and “*resulted in severe damage to all stages of the HPC*” [Yeo11]. To address the problem, the ATBS said that “*a revised geometry was designed to be more tolerant to stresses induced by blade-tip rub*”, but there is no mention of the design criteria that were implemented.

In 2012, after an aborted take-off caused by liberation of small pieces from the HPC, the GE90-110B1 and GE90-115B engines were issued an *Airworthiness Directive (AD)* by the Federal Aviation Agency to “*detect cracks in the HPC stages 1-2 seal teeth due to heavy rubs that could result in failure of the seal of the HPC stages 2-5 spool, uncontained engine failure and damage to the airplane*” [Nor12].

1.2. Research objectives

Current knowledge about the causes of whirling motions in aircraft engines is rather limited and quite intuitive, among others, the phenomenon can be initiated as a result of a maneuvering load, an acceleration or mass imbalance (icing, blade-off events), casing distortion due to thermal loads or shaft misalignment. Similar conclusions can be drawn for the parameters that influence the stability of the bladed-disk equilibrium position and that could lead to divergent vibratory behaviors, such as the magnitude of the contact forces (radial and tangential), operating blade-tip clearances, mechanical properties of the abradable lining, nature of the excited modes (*e.g.* bending or torsion) as well as the dynamics of the supporting bearings.

The need to predict whirl instabilities initiated by direct blade/casing contacts in early design phases of the engine is essential both for safety and enhanced components lifetime. Accordingly, assessing the role of the shaft dynamic in this nonlinear phenomenon is the prime concern of this investigation, focusing on the dynamics of the fan stage of a commercial aircraft engine from a purely structural perspective as no fluid dynamics will be incorporated. This main objective is to be achieved by means of the following methodology:

- Asses the role of the shaft dynamics in the modal properties of a bladed-disk in order to establish which types of modes are susceptible to exhibit an important whirling component.
- Consider a simplified model representative of a bladed-disk/casing system accounting for a flexible shaft and carry out a preliminary analysis of the interactions emerging from unilateral and frictional contacts. The developed numerical strategy is to bring a qualitative understanding on how potentially high-amplitude whirling motions may arise.
- Construct a three-dimensional model of an industrial fan bladed-disk and shaft assembly which is to be implemented in an advanced and efficient numerical strategy, capable of predicting the bladed-disk/abradable interactions. Evaluate the shaft contribution during high-amplitude vibratory regimes.
- Propose an alternative approach for a simplified qualitative analysis of blade/abradable interactions that could be incorporated to early design phases of the engine.

1.3. Organization of the thesis

In chapter 2, a literature survey is presented, going from historical and phenomenological findings in the rotordynamics field to rotor/stator interaction problems. The main numerical methods employed to solve such problems are exposed, highlighting the associated difficulties.

Chapter 3 regards the main dynamical features of the fan stage of a commercial aircraft engine. The focus is made on the shaft dynamics and the derivation of the corresponding gyroscopic terms as well as on the modeling of the structural connection between shaft and casing provided by the fan frame and bearings. The fan model described in this chapter, developed in a three-dimensional cyclic-symmetric framework, is employed in chapter 5 in order to explore bladed-disk/abradable coating interactions by means of a previously developed time-marching method.

A qualitative study is presented in chapter 4, employing a simplified finite element model representative of a bladed-disk/casing system while accounting for the shaft flexibility. The nonlinear interactions between these flexible structures are investigated with a similar time-stepping strategy and are initiated via two distinct mechanisms: (1) a prescribed casing distortion and (2) a mass imbalance on the bladed-disk.

Finally, in chapter 6, an alternative method for the modeling of blade/abradable interactions is derived. The proposed approach is based on an explicit formulation of the contact forces and results in a set of Delay Differential Equations (DDE). An industrial compressor blade is employed and its interactions with the abradable lining are characterized through a stability analysis of the DDE equilibrium solution.

Literature review

A review of the rotor-dynamics field is presented with special attention to the analysis of rotor/casing interactions, going through the phenomena, its potential consequences, the current trends regarding its numerical modeling and the respective experimental set-ups. All fluid excitations, either arising from oil bearings or from the external flow, are ignored in the present study.

2.1. General equations and basic concepts in rotor-dynamics

Rotor-dynamics is a branch of structural dynamics that focuses on the analysis of rotating structures, commonly named *rotors*. In a general manner, the rotor of a turbomachine as the one depicted in Fig. 1.1, is composed of a shaft or driving component, on which operating components, such as bladed-disks or gears, are mounted. It is typically supported by fluid or roller bearings and all non-rotating parts are called the *stator*. When operating, the energy of the engine stems from both rotational and vibrational terms, and the vibrational energy should be minimized for all operating conditions.

2.1.1. Spatial discretization: Finite Element Method

The solution to the local governing equation is generally separated in time and space independent variables, transforming a Partial Differential Equation (PDE) in time and space into a discrete system of Ordinary Differential Equations (ODE) in time. The Finite Element Method (FEM) is one of the most popular spatial discretization techniques nowadays and its necessity for conducting thorough dynamical investigations in turbomachinery is advocated by many researchers [Hug87]. The basic concept behind the FEM is to approximate a continuous quantity—typically displacements—by a set of interpolating functions \mathbf{N} (*e.g.* piece-wise linear or polynomials called *shape-functions*) defined over a finite number of sub-domains referred

to as *elements*. The so-called *equations of motion* are obtained in the form of a set of coupled second order ODE in time and may be written in its most general form as:

$$\mathbf{M}\ddot{\mathbf{x}}(t) + (\mathbf{D} + \mathbf{G}(\boldsymbol{\Omega}))\dot{\mathbf{x}}(t) + (\mathbf{K}(\mathbf{x}(t)) + \mathbf{P}(\dot{\boldsymbol{\Omega}}) + \mathbf{K}_S(\boldsymbol{\Omega}))\mathbf{x}(t) = \mathbf{f}_{\text{lin}}(t) + \mathbf{f}_{\text{nl}}(\mathbf{x}, t) \quad (2.1)$$

where \mathbf{x} corresponds to the nodal displacement, the operator $[\dot{\bullet}]$ represents the time-derivative and the external forcing term is generally decomposed into a linear term \mathbf{f}_{lin} (*e.g.* sinusoidal forcing, centrifugal loads and accelerations) and a nonlinear one \mathbf{f}_{nl} (*e.g.* contact forces) which is dependent on the state of the system.

The size n of the system of second-order ODE (2.1) depends on the number of elements chosen in the discretization and is referred to as the number of *degrees of freedom* (DoF). The associated structural matrices in their integral form defined over a volume \mathbb{V} (*e.g.* casing, shaft, blades, bladed-disk assemblies), correspond to the mass matrix \mathbf{M} which acts on the acceleration term and is established as:

$$\mathbf{M} = \int_{\mathbb{V}} \rho \mathbf{N}^T \mathbf{N} dV \quad (2.2)$$

The damping \mathbf{D} and gyroscopic $\mathbf{G}(\boldsymbol{\Omega})$ matrices arise on the velocity term, the former having several possible definitions and generally being symmetric, while the latter is $\boldsymbol{\Omega}$ -dependent, skew-symmetric and is defined as:

$$\mathbf{G} = \int_{\mathbb{V}} 2\rho \mathbf{N}^T \boldsymbol{\Omega} \mathbf{N} dV \quad (2.3)$$

The matrices acting on the displacements correspond to the stiffness $\mathbf{K}(\mathbf{x})$, itself depending on \mathbf{x} , the angular acceleration stiffening $\mathbf{P}(\dot{\boldsymbol{\Omega}})$ and the spin softening $\mathbf{K}_S(\boldsymbol{\Omega})$, which are determined from the expressions:

$$\mathbf{K}(\mathbf{x}) = \int_{\mathbb{V}} \boldsymbol{\epsilon}(\mathbf{x})^T \mathbf{C} \boldsymbol{\epsilon}(\mathbf{x}) dV, \quad \mathbf{P} = \int_{\mathbb{V}} \rho \mathbf{N}^T \dot{\boldsymbol{\Omega}} \mathbf{N} dV \quad \text{and} \quad \mathbf{K}_S = \int_{\mathbb{V}} \rho \mathbf{N}^T \boldsymbol{\Omega}^2 \mathbf{N} dV \quad (2.4)$$

where $\boldsymbol{\epsilon}$ corresponds to the strain tensor and \mathbf{C} is generally the linear elasticity tensor.

The rotational speed matrix $\boldsymbol{\Omega}$ has three components (rotation around each axis of the reference frame attached to the body) and takes the general form:

$$\boldsymbol{\Omega} = \begin{bmatrix} 0 & -\Omega_3(t) & \Omega_2(t) \\ \Omega_3(t) & 0 & \Omega_1(t) \\ -\Omega_2(t) & -\Omega_1(t) & 0 \end{bmatrix} \quad (2.5)$$

but for most applications, the rotor normally spins around a single fixed axis. For instance, $\Omega_3(t)$ can be the only non-null term in Eq. (2.5), $\Omega_1(t)$ and $\Omega_2(t)$ being neglected. Also, a constant rotational speed is commonly assumed, hence the angular stiffening term defined in Eq. (2.4) vanishes. In the conventions

adopted in the following chapters, $\Omega_3(t) = \Omega$ is solely considered and will remain constant.

As explained in [Hug87], the FEM is capable of approximating highly elaborate geometries, handling a wide variety of loading scenarios and implementing heterogeneous or nonlinear material properties over specific sub-domains, to name a few. As will be detailed in the following, Eq. (2.1) may be solved either in the time domain using time-stepping techniques, or in the frequency domain, through a decomposition of the solution into Fourier series, for instance. Prior to visiting these numerical strategies, a brief historical review is presented in the following on how the different terms composing Eq. (2.1) have been accommodated in the literature as well as their physical meaning.

2.1.2. Brief review on phenomena and history

Rankine [Ran69] modeled the dynamics of a rotating shaft as a rotating concentrated mass supported by a linear elastic spring. By deriving the potential and strain energies, Eq. (2.1) was reduced to a single degree of freedom linear oscillator:

$$m\ddot{x}(t) + (k - m\Omega^2)x(t) = 0 \quad (2.6)$$

where $x(t)$ represents the displacements in the rotating frame, m the concentrated mass and k the linear stiffness. Equation (2.6) is commonly written as:

$$\ddot{x}(t) + (\omega^2 - \Omega^2)x(t) = 0 \quad \text{with} \quad \omega = \sqrt{\frac{k}{m}} \quad (2.7)$$

where ω is the *natural frequency* and Ω the rotational velocity. He defined the concept of *whirling speed* as a speed beyond which the shaft would be considerably bent and would spin around this bent form. Since damping terms were neglected in the formulation, the whirling speed would reflect in his model at $\Omega = \omega$, for which the rotating mass would attain infinite vibrational amplitudes. The term arising in Eq. (2.6) as $(-m\Omega^2)$ corresponds to the previously introduced spin softening $\mathbf{K}_S(\Omega)$ in Eq. (2.1), however, in most turbomachinery applications, the stiffness k is much larger than this term and is often neglected.

A slightly more sophisticated model was proposed in [Jef19], composed of two uncoupled oscillators. Jeffcott aimed to model a rotating shaft/disk system by considering a mass-less flexible shaft supported by rigid bearings at its ends with a rigid imbalanced disk at its center. The imbalance load induced by the disk on the shaft coupled the two DoF and was represented as a linear external forcing:

$$\mathbf{f}_{\text{In}}(t) = m_{\text{imb}}\epsilon_{\text{imb}}\Omega^2 \begin{pmatrix} \cos(\Omega t) \\ \sin(\Omega t) \end{pmatrix} \quad (2.8)$$

where the analysis of the rotor response as a function of the geometrical imbalance parameter ϵ_{imb} and rotational speed Ω is commonly named *imbalance response*. The notion of critical speed was again introduced as a rotational velocity where the vibrational amplitude reaches its maximum. By adding the external viscous damping terms that were missing in [Ran69], it was demonstrated that a rotor could work beyond its first critical frequency in a stable manner. This type of rotor is known as the *Jeffcott rotor*¹ and is still widely used in the field. It is shown in [Jef19] that the critical speed coincides with the rotor natural frequency and that the amount of damping included in the formulation only affects the corresponding vibrational amplitudes.

In vibration analysis, the notion of natural frequencies (or eigenfrequencies) is often encountered as the above-mentioned critical speeds generally emerge when the rotational velocity is close to a natural frequency [Mei80]. Indeed, Eq. (2.1) may be recast into its state-space form, thus transforming it in a first order ODE as:

$$\begin{bmatrix} \mathbf{M} & \mathbf{0} \\ \mathbf{0} & \mathbf{M} \end{bmatrix} \begin{pmatrix} \dot{\mathbf{x}} \\ \ddot{\mathbf{x}} \end{pmatrix} + \begin{bmatrix} \mathbf{0} & -\mathbf{M} \\ \mathbf{K}(\mathbf{x}) + \mathbf{P}(\dot{\Omega}) + \mathbf{N}(\Omega) & \mathbf{D} + \mathbf{G}(\Omega) \end{bmatrix} \begin{pmatrix} \mathbf{x} \\ \dot{\mathbf{x}} \end{pmatrix} = \begin{pmatrix} \mathbf{0} \\ \mathbf{0} \end{pmatrix} \quad (2.9)$$

where external forces are neglected. By assuming an *ansatz* solution of the type $\mathbf{z}(t) = \mathbf{Z} \exp(\lambda t)$, the associated set of (\mathbf{Z}, λ) satisfying Eq. (2.9) are the so-called eigenmodes (or eigenvectors) and eigenvalues. These come in complex conjugate pairs, where the imaginary part of the eigenvalue $\Im \lambda$ corresponds to the frequency ω of the mode while the real part $\Re \lambda$ drives the stability of the equilibrium solution $\mathbf{z} = \mathbf{0}$.

The diagram showing the evolution of these natural frequencies as a function of the rotational speed, depicted as an example in Fig. 2.1, is known as the *Campbell diagram*. In 1924, Wilfred Campbell superimposed these curves to the synchronous response line (also called first or main Engine Order), in order to determine potential critical rotational frequencies Ω^{cf} where a rotor would exhibit high forced vibratory amplitudes. These speeds actually correspond to a coincidence of vibration sources with the Ω -dependent natural resonances. The Campbell diagram is still used on a daily basis for a quick visualization of potential vibratory problems that may arise within the operating speed range of a turbomachine.

A model of a steam turbine was proposed in [Sto27] where the rotational inertia of a rigid disk placed at the tip of a flexible shaft was established. A rigid bearing at its other end was assumed to be representative of the overhung or cantilevered configuration commonly adopted in this type of system. It was later used by Green [Gre48], who added the gyroscopic effects. The inclusion of the skew-symmetric gyroscopic matrix $\mathbf{G}(\Omega)$ was shown to induce a frequency split in backward and forward rotating modes at high rotational speeds, thus respectively shifting downward and upward the critical speeds obtained in the Campbell diagram.

¹It is also called *Föppl rotor*, since Föppl worked on a similar problem a few years before [Föp95]. In Europe, it is also frequently called *Laval rotor*, in honor to the Swedish engineer Gustav Laval.

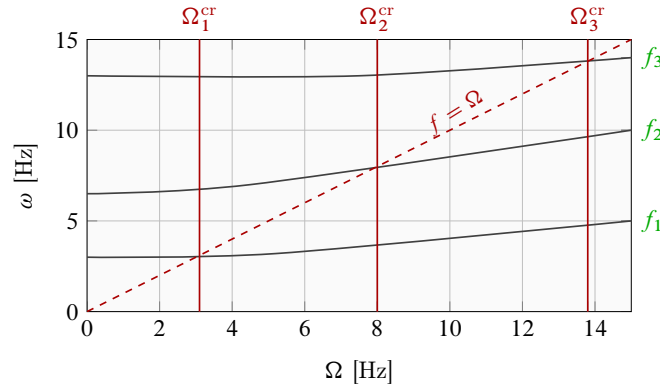


Figure 2.1: Campbell diagram example: frequencies [—] and synchronous excitation [- - -]

This model, known as *Stodola-Green rotor*, is still used to study the dynamic effects of overhung disks or turbine wheels [IJR99].

Important concern in the rotor-dynamics field regards the effect of bearings and damping [Chi93], whose dynamic contribution generally arises in the stiffness and damping matrices in Eq. (2.1). In [Lun87], a damped eigenvalue problem as Eq. (2.9) is solved, while neglecting gyroscopic terms as well as spin softening and angular stiffening terms. Lund obtained the associated set of complex eigenvalues, showing that internal hysteretic shaft damping and external damping in bearings can be critical to the system stability. The notion of the *stability margin* of the rotor system was established as “*the logarithmic decrement of the eigenvalue closest to the threshold of instability.*”

As the models used in the analysis of Eq. (2.1) get more advanced, the size of the associated FE-matrices increases and with it, the associated computational costs. The dynamical features that current 3D high-fidelity models can capture has also changed dramatically. A recent review regarding vibratory issues in rotating machinery is given in [Nel07], going through various basic concepts as natural whirling frequencies, lateral and torsional critical speeds, as well as stability analysis. All these concepts are treated in a more formal mathematical framework in [Gen05]. The notion of *controlled rotors* was introduced, also dealing with the modeling of anisotropy of rotors and supports, torsional and axial dynamics as well as the dynamics of rotating disks, rings and blades (modeled as an array of spherical pendulums). Dynamics of bladed rotors were also discussed in [San+04] comparing experimental data from four-bladed rotor in a test rig to a numerical model, where blades are represented by Euler-Bernoulli beams with concentrated masses at the tips, and the deformation are modeled by three different approaches of growing complexity.

Lalanne and Ferraris [LF98] focused on the modeling and analysis of rotors, going from monorotors to mult rotor systems, towards the analysis of industrial applications, *e.g.* turbochargers, centrifugal compressors

and steam turbines. The Rayleigh-Ritz and Finite Element Methods were also detailed. In [Chi93] the targeted systems are much more specific to turbomachinery, dealing with the phenomena and modeling behind industrial turbomachines, such as turbines and pump impellers, focusing mainly in the influence of the bearings (*e.g.* hydrodynamic bearings, liquid annular seals and gas seals). It is shown that under certain vibratory circumstances, the interactions arising when contact occurs between rotating and static components may significantly influence the system behavior.

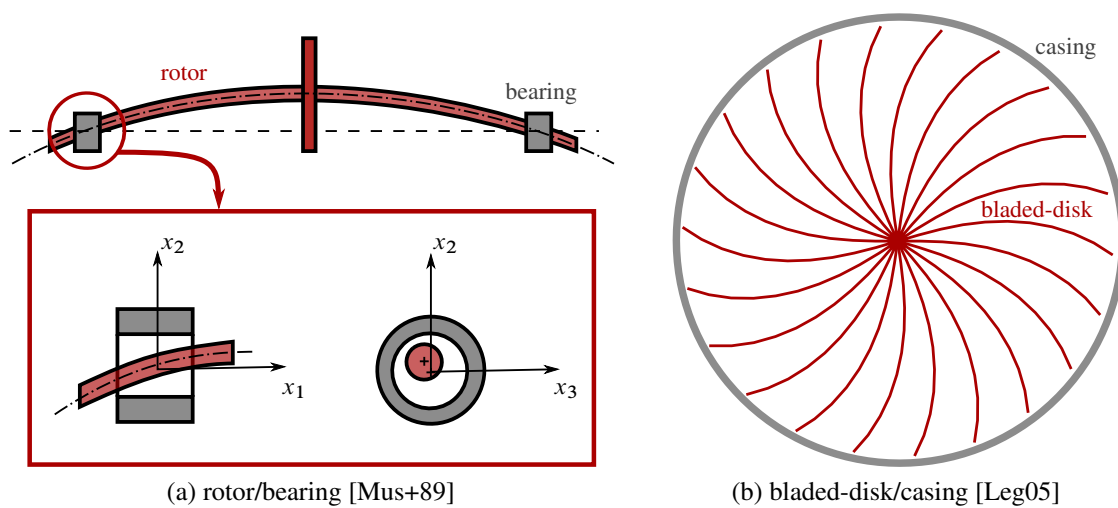


Figure 2.2: Types of systems subject to rotor/stator interactions

As mentioned in the introduction, these contact events are commonly named *structural rotor/stator interactions* where no fluid dynamics are accounted for. In the literature, this denomination is used for two types of systems which must be distinguished: *rotor/bearing systems*—illustrated in Fig. 2.2a—generally modeled by a flexible shaft with a rigid cross-section and supported by bearings, and *bladed-disk/casing systems*—depicted in Fig. 2.2b—where the deformation of the blades are the main concern and a rigid shaft is generally considered. In this class of dynamical problems, the contact reactions arise in the forcing term \mathbf{f}_{nl} in Eq. (2.1) and are generally decomposed into *unilateral* \mathbf{f}_N and *frictional* \mathbf{f}_T forces. Since contact induces a discontinuity in the velocity field $\dot{\mathbf{x}}$ at the time of impact, these non-smooth forces pose great challenges in terms of modeling. Closed form solutions are in general not available, hence dedicated numerical methods have been developed as reviewed in the following section.

2.2. Dedicated numerical strategies

The studies where the vibrational behavior of a mechanical system (flexible or rigid) is subject to contact constraints for which non-penetration conditions must be satisfied, fall into the branch of mechanics known as *unilateral contact dynamics*. Once the difficulty associated to the spatial discretization is tackled, by means of the above mentioned FEM for instance, Eq. (2.1) is obtained and for a given set of initial conditions—generally imposed in velocities, displacements and forces—two other problems must be addressed to solve it: (1) integration in time and (2) enforcement of contact constraints.

2.2.1. Time-marching techniques

Time-domain algorithms utilized to solve Eq. (2.1) are often referred to as *time-marching* or *time-stepping* techniques. The basic idea behind these methods is to calculate the state of the system at a future time t_{i+1} as a function of previous states, which are separated by a time-step Δt , moving in a stepwise fashion through time. Hence, the simplified discrete version of Eq. (2.1) that will be kept in the following may be written as:

$$\mathbf{M}\ddot{\mathbf{x}}(t_i) + (\mathbf{D} + \mathbf{G}(\boldsymbol{\Omega}))\dot{\mathbf{x}}(t_i) + \mathbf{K}\mathbf{x}(t_i) = \mathbf{f}_{\text{ln}}(t_i) + \mathbf{f}_{\text{nl}}(\mathbf{x}, t_i) \quad (2.10)$$

where the size of the discrete map is driven by Δt . Small strains and small displacements are assumed, thus the stiffness matrix becomes linear.

The equations of motion (2.10), are then solved by means of a numerical approximation of time-derivative terms, often in the form of a Taylor expansion to a given order [AB08]. The main advantage is that these techniques are able to capture various solutions (periodic, quasi-periodic or chaotic) and are rather simple to implement. However, the associated computational times can be very large, as an important number of iterations is often required to attain steady-state regimes. Two families of methods can be distinguished:

Explicit schemes In explicit schemes, the new solution $\mathbf{x}_{i+1} \simeq \mathbf{x}(t_{i+1})$ is solely dependent on known states of the system, *e.g.* \mathbf{x}_i and \mathbf{x}_{i-1} in a finite difference scheme. Hence, the calculation of the new state is straightforward. The main algorithms that fall into this category correspond to Euler's method, finite differences and Runge-Kutta methods. The main drawback of this type of technique is the conditional stability with respect to the time-step size, which renders the use of extremely small Δt values almost mandatory [HL78].

Implicit schemes In implicit schemes, the new solution \mathbf{x}_{i+1} is dependent on unknown velocities $\dot{\mathbf{x}}_{i+1}$ and accelerations $\ddot{\mathbf{x}}_{i+1}$ that must be calculated simultaneously, in which case a prediction-correction type of

algorithm must be implemented (*e.g.* Newton-Raphson procedure when nonlinear terms arise). The main benefit gained from using implicit schemes such as the Newmark- β or the generalized HHT- α families—which are a parametrically controlled methods—is the linear unconditional stability for certain parameter combinations [HL78]. Although this unconditional stability is destroyed when nonlinearities such as contact are introduced, which poses difficulties in terms of convergence, the restrictions for the time-step size are far less strict than for explicit techniques, allowing for one or two orders of magnitudes larger time-steps and generally improving the computational times.

Chosen solution method In the next chapters, the strategy proposed in [Leg+09] is implemented, where the equations of motions (2.10) are solved by means of an explicit central finite difference scheme, since this method is particularly adapted for solving dynamical systems subjected to unilateral contact constraints [DEP11]. With this integration scheme, time-derivative terms are approximated as:

$$\dot{\mathbf{x}}(t_i) \simeq \dot{\mathbf{x}}_i = \frac{1}{2\Delta t} (\mathbf{x}_{i+1} - \mathbf{x}_{i-1}) \quad (2.11a)$$

$$\ddot{\mathbf{x}}(t_i) \simeq \ddot{\mathbf{x}}_i = \frac{1}{\Delta t^2} (\mathbf{x}_{i+1} - 2\mathbf{x}_i + \mathbf{x}_{i-1}) \quad (2.11b)$$

which by substituting Eq. (2.11) into Eq. (2.10) and re-arranging the terms by time-step, yield the following discrete equations of motion solely dependent on displacements:

$$\mathbf{x}_{i+1} = \left[\frac{\mathbf{M}}{\Delta t^2} + \frac{(\mathbf{D} + \mathbf{G}(\boldsymbol{\Omega}))}{2\Delta t} \right]^{-1} \left[\left[\frac{2\mathbf{M}}{\Delta t^2} - \mathbf{K} \right] \mathbf{x}_i + \left[\frac{(\mathbf{D} + \mathbf{G}(\boldsymbol{\Omega}))}{2\Delta t} - \frac{\mathbf{M}}{\Delta t^2} \right] \mathbf{x}_{i-1} + \mathbf{f}_{\text{In}_i} + \mathbf{f}_{\text{nl}_i}(\mathbf{x}_i) \right] \quad (2.12)$$

that may be solved for each iteration in a single step.

Several methods permit to account for the unilateral and frictional contact forces stored in $\mathbf{f}_{\text{nl}_i}(\mathbf{x}_i)$, the most popular ones being described in section 2.2.3.

2.2.2. Modal reduction techniques

It should be noted that the computational times are not only driven by the number of iterations associated to the size of Δt , but are also related to the size n of the system (2.10). In this sense, the use of modal reduction techniques becomes particularly appropriate [Bat+10]. Accordingly, the FE-models employed in this investigation are reduced using a component mode synthesis method derived from the Craig-Bampton component mode synthesis [CB68] that accounts for the linear contribution of centrifugal stiffening [SB06], hence the stiffness matrix becomes dependent on the rotational speed $\mathbf{K} = \mathbf{K}(\boldsymbol{\Omega})$. The equations of motion

are projected onto the reduced-order space by means of the following transformation matrix:

$$\mathbf{x} = \begin{pmatrix} \mathbf{x}_b \\ \mathbf{x}_i \end{pmatrix} = \begin{bmatrix} \mathbf{I} & \mathbf{0} \\ \Psi_s & \Psi_c \end{bmatrix} \begin{pmatrix} \mathbf{x}_b \\ \mathbf{q}_{cb} \end{pmatrix} \quad (2.13)$$

where the physical DoF \mathbf{x} are partitioned into internal \mathbf{x}_i and boundary \mathbf{x}_b DoF.

The main advantage of such reduction technique is that the boundary displacement vector \mathbf{x}_b is defined so that the targeted contact forces can directly be handled in the reduced space. The internal displacement vector \mathbf{x}_i is reduced to η modal participations \mathbf{q}_{cb} of static and constraint modes computed at different rotational speeds (stored in matrices Ψ_s and Ψ_c respectively) in order to account for centrifugal stiffening. The number η of modal participations controls the accuracy of the reduction basis. More details may be found in [SB06] on how to build the reduction matrix and in [Bat+10] on how unilateral contact constraints are efficiently enforced in the reduced space.

2.2.3. Unilateral and frictional contact conditions

One of the most challenging aspects of unilateral contact dynamic problems is the modeling of the contact term, as it represents a non-smoothness in velocities, *i.e.* the non-smooth displacement field is continuous but at the time of impact a discontinuity arises in terms of velocity. In a purely mathematical framework, these constraints may be defined as a set of complementarity conditions:

$$\forall t > 0, \quad \mathbf{f}_N(t) \leq \mathbf{0}, \quad \mathbf{g}(\mathbf{x}(t)) \geq \mathbf{0} \quad \text{and} \quad \mathbf{g}(\mathbf{x}(t))\mathbf{f}_N(t) = \mathbf{0} \quad (2.14)$$

where $\mathbf{g}(\mathbf{x})$ is the so-called *gap* function representing the non-negative distance between the contacting surfaces, \mathbf{f}_N are the normal contact forces (chosen to be negative by convention), and as translated by the last expression of Eq. (2.14), both quantities may not vanish simultaneously. This concept is illustrated as

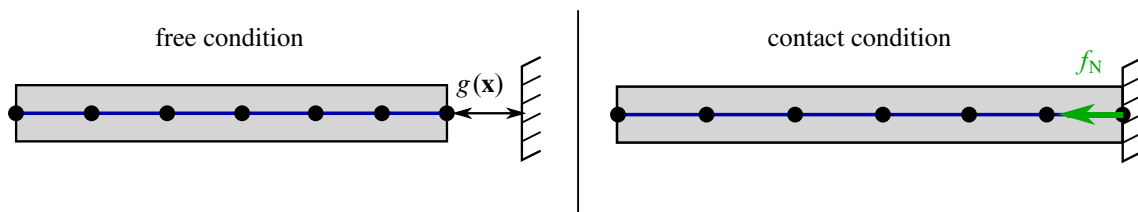


Figure 2.3: One-dimensional example of contact conditions

a one-dimensional problem in Fig. 2.3, where it can be seen how the system oscillates between free and clamped boundary conditions at the node where unilateral contact constraints are enforced. This change in boundary conditions gives rise to a phenomenon known as *contact stiffening*, in which the resonant frequency

of the system appears at higher levels than its linear counterpart [CL07].

Further, frictional contact is still an open problem in the field of tribology as reviewed in [OM85], where the phenomenon is described as highly nonlinear and dependent on the scale of observation, the roughness of the contact surfaces and the impact speed, to name a few. The most basic dry-friction model available in the literature is the Coulomb law, which was proposed around 1785 and may be written in the form:

$$\|\mathbf{f}_T\| \leq \mu \|\mathbf{f}_N\| \quad (2.15)$$

where μ is the friction coefficient.

In the turbomachinery field, the Coulomb law is largely adopted. Since permanent sliding can be assumed during contact phases due to the large blade-tip velocities and the rather small normal forces involved in the interactions, more complex phenomena such as stick-slipping or directionality of frictional behavior as studied in [MZ78] may be ignored. Hence, Eq. (2.15) simply becomes:

$$\|\mathbf{f}_T\| = \mu \|\mathbf{f}_N\| \quad (2.16)$$

which may be integrated into the forcing term of Eq. (2.12) once the normal contact forces are calculated. The determination of these unilateral contact forces \mathbf{f}_N goes through enforcement of the set of complementary conditions given in Eq. (2.14), which are generally referred to as *Kuhn-Tucker* [KT50] or *Signorini conditions* [JAM01]. Since a closed form solution is generally not available, dedicated numerical techniques have been developed to account for these constraints as detailed in [AB08]. The most popular methods can be classified into two distinct families:

Regularized techniques Regularized or penalty methods aim at an approximation of the contact force/gap distance relation by an explicit expression [KS80], which generally takes the form of a piece-wise linear or an exponential function. This approximation makes its numerical implementation straightforward, but introduces residual penetrations and/or "non-physical" contact forces.

Indeed, for a contact force f_N on a single DoF associated to the gap distance $g(\mathbf{x})$, a graphical representation of Kuhn-Tucker conditions is depicted in Fig. 2.4 corresponding to the signs convention adopted in Eq. (2.14). Two penalty-like approximations are also displayed and it may be seen how the exponential form introduces a contact force even if no actual contact exists while the piece-wise linear one violates non-penetration conditions.

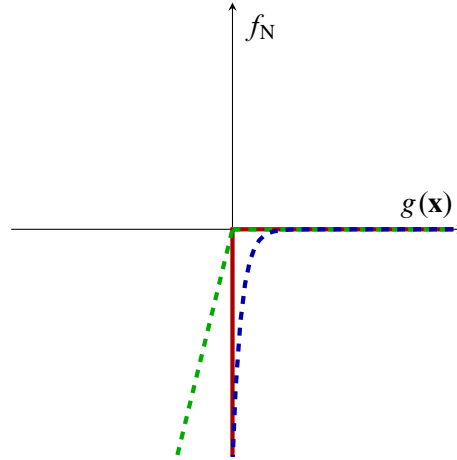


Figure 2.4: Kuhn-Tucker cond. [—], $f_N = \min(k_e g(\mathbf{x}), 0)$ [---] and $f_N = -\exp(-k_e g(\mathbf{x}))$ [---]

Non-regularized techniques Non-regularized techniques aim to fully satisfy non-penetration conditions of Eq. (2.14) through an implicit calculation of the contact forcing term. Therefore, these involves a more costly numerical procedure that often takes the form of a prediction-correction algorithm as in the Lagrange Multipliers approach, which is valid for very small time-steps [CTK91]. A prediction is made in displacements allowing to compute the gap distance, if a penetration is detected, the contact forces are calculated so that no residual penetrations remain when the displacements are corrected.

Among other strategies, the non-smooth methods are often used in rigid-body dynamics and treat contact occurrences with an impact law [JAM01]. For a one-dimensional continuous system, the impact law generally takes the form of $\dot{x}(t_{\text{imp}}^+) = -e\dot{x}(t_{\text{imp}}^-)$, where the discontinuity in the velocity field at the time of impact t_{imp} is imposed via the so-called coefficient of restitution $e \in [0; 1]$. The augmented Lagrangian or the Uzawa technique are also frequently encountered in the literature [WL06].

Chosen solution method In the following chapters, unilateral contact forces are calculated via Lagrange multiplier method [CTK91], thus exactly satisfying non-penetration conditions. The nonlinear forcing term in Eq. (2.12) storing these contact loads is generally written as:

$$\mathbf{f}_{\text{nl}_i}(\mathbf{x}_i) = \mathbf{B}\mathbf{f}_{\text{cn}_i}(\mathbf{x}_i) \quad (2.17)$$

where \mathbf{f}_{cn_i} are the Lagrange multipliers calculated at the i -th time-step and the rectangular matrix \mathbf{B} stores both unilateral and frictional contact constraints, the frictional forces being simply determined with Eq. (2.16).

2.2.4. Frequency domain approaches

A viable alternative to time-domain simulations correspond to the frequency domain approaches, where instead of fully satisfying the equations of motion (2.1), the solution is generally approximated as a truncated Fourier series in time up to a certain number of harmonics and is particularly adapted for enforcing periodicity conditions.

The most popular method is known as the Harmonic Balance Method (HBM), where periodic solution of nonlinear systems subject to a periodic excitation are obtained. For instance, in [GE01], the evolution of the obtained solution—often referred to as *solution branch*—is followed through the variation of system parameters (*e.g.* the rotational speed) via arclength continuation. This method catches in particular the occurrence of multiple solutions for a given set of parameters as well as states on their stability. This main feature is of great interest when compared to time-integration, since in time-stepping simulations unstable solutions cannot be predicted and amplitude jumps between solutions are challenging to capture as they often depend on the initial conditions.

However, as detailed in [Her+14], the enforcement of Kuhn-Tucker conditions (2.14) is particularly difficult to achieve directly in the frequency space, as the Fourier basis is not well-suited for the approximation of non-smooth functions and gives rise to the well known *Gibbs phenomenon*, where residual oscillation in the response emanate during contact phases regardless of the number of harmonics considered in the truncation. Hence, it is generally proposed to treat the contact conditions in the time-domain by means of Alternating Frequency-Time (AFT) methods [CG89]. The basic concept behind AFT is to decompose the solution in a HBM sense, treat the nonlinear part of the equation in the time-domain and recast the obtained solution into the frequency domain. Even if AFT gives a better approximation of the contact forces, the resulting solution decomposition into Fourier series is still subject to residual oscillations.

An extension to this method was proposed in [Nac+03], where the nonlinearity is treated directly in the harmonic space and the displacements are then corrected in the time domain via a penalty-like function, thereby providing a more accurate approximation of contact and frictional forces. This method was shown to have better robustness and convergence than the classical AFT.

2.2.5. Abradable coatings and wear

As mentioned in the previous sections, the implementation of abradable coatings has been widely adopted in the turbomachinery field in order to mitigate direct structural contacts between rotating blades and its surrounding casing while permitting a self-tuning of operating blade-tip clearances [HJW09]. However, as

shown in [Bat+12], the cyclic pattern in the material removal caused by the vibrations of incurring blades may play a non-negligible role as to why certain blade modes interact and potentially result in structural failures. Therefore, there is an increasing need for a better understanding of the physical phenomena involved in this type of interactions, where the blade/abradable interacting force is particularly difficult to access and constitutes a key feature to develop accurate numerical models [Man+15].

Although there are several types of wear mechanisms involved in the interactions, in particular depending on the scale of observation and vibratory energy levels as reported in experimental observations [Bor+89; Yi+99], from a macroscopic perspective two models have been proposed in the literature: (1) an analytical model studied in [Wil11], where the wear is approximated by an explicit nonlinear formulation dependent on the blade incursion and the associated normal force, and (2) an elasto-plastic constitutive law developed in [LBP12], where the abradable coating wear is captured by a permanent deformation of rod elements located throughout the casing circumference. Besides, a very recent phenomenological study [Ber+15] explored four key wear mechanisms involved in the abradable coating removal, namely: adhesive, abrasive, micro-rupture and machining wear mechanisms. For each type of wear, analytical formulations were proposed relating the blade penetration levels and edge velocity to the exerted contact reactions and amount of material removal. The numerical results were compared with respect to existing models and available experimental data.

2.3. Rotor/stator interactions

In this section, three distinct phenomena arising from rotor/stator interactions are discussed:

Modal coincidence Modal coincidence is only regarded in bladed-disk/casing systems. It may be described as a geometric matching between the vibration modes of the casing and the rotor, both exhibiting nodal diameters, where the associated eigenfrequencies concord in the frame of reference [Sch97].

Rubbing In rotor-bearing systems, rubbing refers to direct contact between the shaft and supporting bearings due to high amplitude lateral vibrations [Mus+89], while in bladed-disk/casing systems, it refers to contact occurrences between blade-tips and surrounding casing, often leading to significant wear at the contact interface [Eme+83].

Whirling motions Whirling motions are mostly studied for rotor/bearing systems and are generally caused by a mass imbalance or instabilities induced by nonlinear bearing forces, it refers to precessional orbits of the shaft leading to unstable behaviors [CB07].

2.3.1. Modal coincidence

Modal coincidence between a bladed disk and a surrounding casing, also called *traveling wave speed coincidence*, has proven to be a source of instability. According to [Sch97], “*the rotational kinetic energy of the rotor feeds the vibration of the rotor-stator system, which responds with growing vibration amplitudes*”. Schmiechen was the first to consider modal coincidence between these two flexible structures, modeling the interaction phenomenon as a unilateral impact and considering a penalty method to account for frictional forces. In this way, critical operational speeds $\Omega_{n_d}^{cr}$ were defined as:

$$\omega_{n_d}^c = n_d \Omega_{n_d}^{cr} - \omega_{n_d}^{bd} \quad (2.18)$$

where $\omega_{n_d}^c$ and $\omega_{n_d}^{bd}$ are respectively the eigenfrequencies of the casing and the bladed-disk of matching n_d nodal diameters. Further details on the dynamical properties of this class of structure are provided in the next chapter.

In [Leg+09], a 2D FE-model of a flexible bladed-disk mounted on a rigid shaft and a flexible casing were considered, targeting the case where the vibrations of both structure take the form of a 3-nodal diameter traveling waves. In sliding conditions, the frictional forces stemming from the contact reactions induce the waves to travel forward on the casing and backward on the rotor. As depicted in Fig. 2.5 in the static frame,

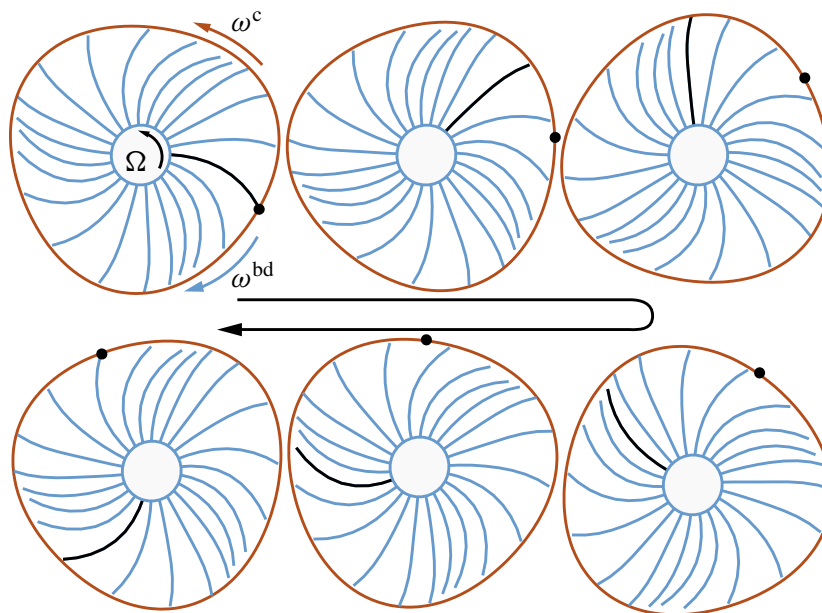


Figure 2.5: Modal coincidence between $n_d = 3$ nodal diameter waves [Leg+09]

while the bladed-disk rotates in counter-clockwise direction a 3-nodal diameter wave propagates in the same direction on the casing. It is illustrated by the motion of the black point which remains at the same vibratory

amplitude and travels forward. A wave of matching nodal diameter propagates backward on the bladed-disk and due to the rotation, as described by the motion of the reference blade in black, the vibratory frequencies of both structures coincides [Leg+09]. The equations of motion were solved with an explicit time marching algorithm and unilateral contact constraints were enforced via Lagrange multipliers method. Three types of behaviors were found depending on the rotational speed Ω : (1) *damped*, (2) *sustained* and (3) *divergent* motions.

A similar model was studied by [Bat08], while focusing on different modal reduction techniques, namely, *Craig-Bampton* and *Craig-Chang-Martinez* component mode synthesis. Comparable behaviors were observed and the influence of kinematic constraints imposed by each reduction technique was analyzed. In addition, another type of operating regime was observed, noted as *blocked*, where one or several blades remain in permanent contact with the casing. This type of regime only appeared when the number of nodal diameters on the casing was a common divisor of the number of blades. Finally, high rotational speeds and high friction coefficients seemed to give rise to divergent motions.

2.3.2. Rubbing

Rotor/bearing systems In [Mus+89], a comparison between results from a mathematical model of a rotor/bearing/seal system and experimental data was presented, in which two test rigs were used: one simulating a turbopump and the other representing a two-mode rotor. In this type of studies, the rotational speed is often considered as constant, which may lead to an increase of external torque when friction is accounted for. It was only in 2002, that Dai et al. [DJZ02] studied the transient response of the rotor considering the rotational velocity as an unknown function of time.

Rubbing was also shown to have significant influence in whirling motions of the shaft in [Yu+02]. A Jeffcott rotor was explored under a mass imbalance excitation and several operating conditions for which a shift from a synchronous response to reverse rub was observed. Contact forces were incorporated by means of a penalty method.

Analytical models have also been treated in order to predict stability conditions of rotor/bearing systems [JU03]. The most challenging aspect of this type of method is obtaining closed-form solutions with accurate contact modeling.

Bladed-disk/casing systems The first study dealing with bladed-disk/casing interactions was published in 1987 [PC87], where the transient response of a bladed Jeffcott rotor was studied. Using a Newmark integration algorithm, with a self-adaptive time step size and a nonlinear contact force dependent on the

blade distortion, three contact configurations were observed: (1) no contact, (2) single blade contact and (3) multiple blades contact. The influence of the friction coefficient and the mass imbalance were investigated, and backward whirling motions were observed, maximizing blade displacements and stresses. Multi-blade rub events appeared to lead to a saturation of the maximum stresses and potential low/high cycle fatigue problems were revealed.

In [Sin04], an analytical model was considered, where rotor blades were represented by beams and their lateral displacements were studied, taking into account lateral forces due to friction and pulse buckling. A rigid casing was assumed. The effect of the internal damping of the shaft and the magnitude of the contact load on the stability of the system was analyzed. The same rotor model was used in [LST07] while considering a flexible casing modeled by an elastic ring. Centrifugal stiffening, spin softening and gyroscopic effects were taken into account in the computation of the system eigenvalues. A stability analysis was then conducted and divergence instabilities were put forward, while exhibiting mode-couplings between rotor and casing in Campbell diagrams.

Another approach was proposed in [LBP12] with a rigid shaft and a flexible rotating blade targeting the blade-tip/abradable layer interactions. A 3D finite element model of the blade reduced with the Craig-Bampton method, a piecewise-linear plastic law to model the abradable coating wear and an explicit time marching technique were implemented. At critical speeds, “*slow and continuous opening of the operating clearance between the blade-tip and the casing synchronizes with the nonlinear resonance of the blade and then concedes growing vibratory amplitudes*”. These interactions, studied experimentally at SNECMA in [Mil+09],

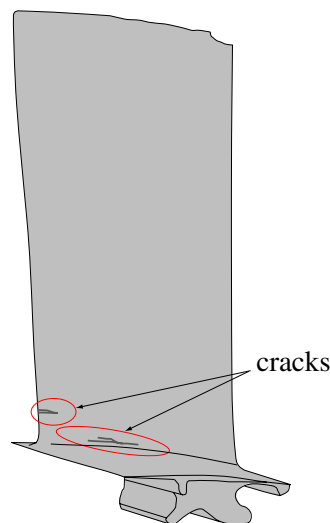


Figure 2.6: Schematic of compressor blade after rubbing test [Mil+09]

appeared to potentially lead to the blade failures pictured in Fig. 2.6 and were the focus of a numerical-

experimental comparison [Bat+12], concentrating on the critical stress levels in the blade and the final wear profiles in the abradable layer for different blade designs. It was applied for the re-design of a HP compressor blade [Bat+14], drastically enhancing the blade vibratory behavior under rubbing conditions. This method was recently extended to a full cyclic-symmetric model of an impeller, handling contact in all blades [BML15; Mei14]. The detection of potentially critical nonlinear interactions triggered by harmonic excitations and aliasing effects was the main concern. Independently, these interaction scenarios were explored experimentally in [Alm+14] for the same centrifugal compressor at low rotational speeds, assessing the role of local thermal constraints induced by the contact events. Highly localized casing distortions were revealed.

Experimental work was also reported for an Inconel compressor blade rubbing a steel casing in [Pad+07]. For a range of rotational speeds similar to in-flight conditions and different incursion levels, the evolution of the stress and contact forces was discussed, showing that potential failure may occur at the trailing edge of the blade. The variation trends between metal-to-metal and metal-to-abradable rub events were also scrutinized in [Pad+11], yielding conclusions similar to their first study. As illustrated in Fig. , tests were performed for

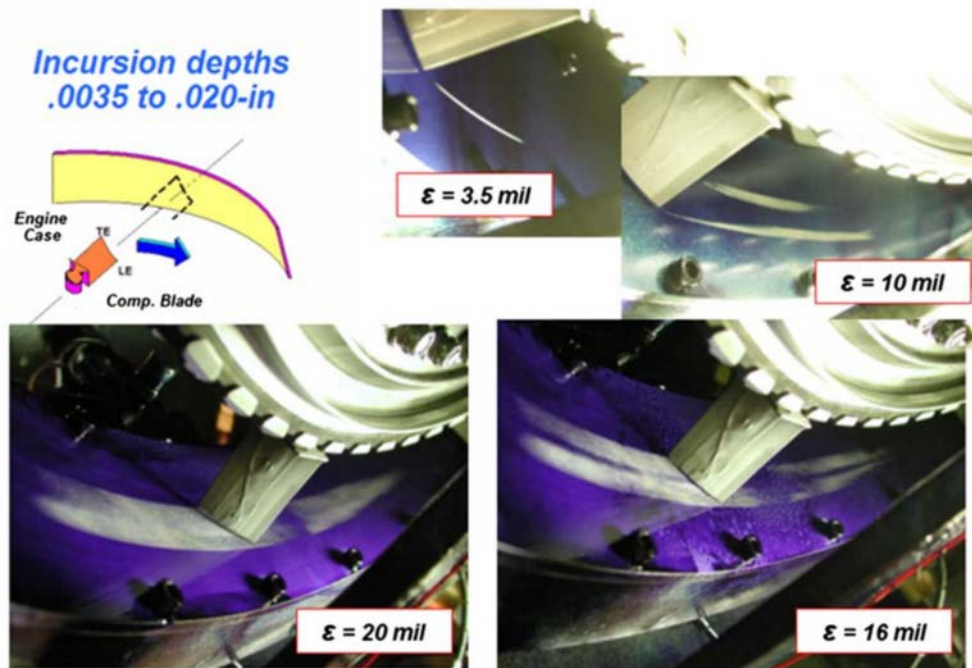


Figure 2.7: Experimental set-up for steel-on-steel rubbing [Pad+11]

different incursion levels and a strongly nonlinear phenomenon in the rub event was noted: an increase in penetration depths led to a much more important increase in circumferential loads than in axial ones.

2.3.3. Whirling motions

Rotor/bearing systems When the amplitude of the whirling motion is larger than the initial rotor/bearing clearance, contact occurs and may lead to *dry-friction whirl* [Bar00]. By comparing numerical results of a flexible rotor and casing models with experimental data from a test rig built to represent a small turbo-compressor, Bartha showed that this type of contact can only produce backward motions. He described the phenomenon as “*rare but potentially fatal malfunction of turbomachines*”.

The vibratory behavior of a three-bladed aircraft propeller was analyzed in [CD81], using a six DoF rigid body model for the engine and six vibration DoF for the blades. Multi-blade coordinates were introduced and a linear eigenvalue problem describing the whirling motions was derived, proving that whirling motions were excited by harmonics of the transverse forces on the engine. Later on, Muszynska [Mus86] made a substantial contribution to the understanding of rotor/bearing instability problems, considering a symmetric rotor reduced to its first bending mode, supported by one rigid and one fluid lubricated bearings, and analyzing the phenomena known as *oil whirl* and *oil whip*. Using a waterfall plot of the rotor response frequency content, the progression from whirl to whip was shown as a subsynchronous motion at about one-half of the running speed and a subsynchronous motion at the natural frequency, respectively.

Early work made by Black [Bla67] proved that this type of motion may lead to important changes in the behavior of the shaft at high speeds, *i.e.* once the first critical speed is passed. He considered a multi-degree of freedom rotor and stator with damping, and dry-friction interaction at the clearance. Using polar receptances in order to analyze the stability of the system, as well as experimental data from a test rig, a good agreement between the two was shown. In [CB07], a multi-mode extension of Black’s model was used in order to study the whirl-whip transition taking into account the dependence of the friction force sign on the relative sliding velocity. Good agreement was obtained between the prediction of precession frequencies and experimental values. The importance of the contact location was put forward and potentially destructive dry-friction whip was observed in the test rig. A recent extension of Black’s model was also developed in [Ma+15], proposing a novel explicit formulation of the normal rubbing forces dependent on the system parameters such as the rotational speed, the blade cross-section and disk diameter, which was validated with experimental data from a test rig.

Bladed-disk/casing systems A first approach to deal with contact in bladed flexible rotors and analyze its consequences in whirling motions, was recently developed by [Mas11] at SNECMA, based on the work of [LST07; Gru+11], where a one-dimensional model of a two-spool turbofan was built. An imbalance in the shaft was added to initiate the interactions, the blades of the fan stage were modeled as Euler-Bernoulli

beams and a perfectly rigid circular casing was assumed. The contact forces were produced by artificial linear springs, *i.e.* penalty method, and wear was ignored. The study focused on the influence of the rotor/stator interaction on the system eigenfrequencies, in order to determine critical rotational speeds.

A similar strategy was adopted by [PTC14], who built up on [Mas11] and included the flexibility of the casing in the formulation. The mass imbalance load responsible of initiating the interactions was included as an external forcing term at the LPT. An improved three-dimensional kinematic calculation of blade-to-casing

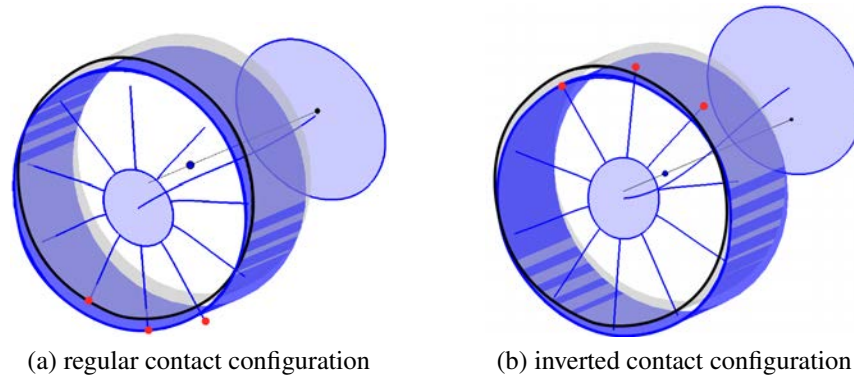


Figure 2.8: Mode shapes and contact configurations: minimum gap [•] [PTC14]

distances was incorporated into the penalty-like contact treatment. The focal point was the influence of the whole engine dynamics on the detection of *regular* and *inverted* contact scenarios at the fan stage, which appeared to lead to backward and forward whirling motions respectively. Two critical modes were identified and are depicted in Fig. 2.8, where it can be witnessed that in the regular configuration (Fig. 2.8a) most of the strain energy is localized in the fan stage and contact emerges in the same direction as the shaft displacement, while in the inverted case (Fig. 2.8b) contact occurs in the direction opposite to the shaft deflection and an important participation of the turbine disk is present.

Dynamics of an aircraft engine fan stage: industrial application

3.1. Modal properties of cyclically symmetric structures

3.1.1. Theoretical background

A cyclically symmetric structure¹ is one composed of a repetition of N identical entities called *sectors*, as those illustrated in Fig. 3.1. The main idea behind the cyclic-symmetry approach is to take advantage of this geometrical feature and recover the behavior of the global system by modeling a single sector only. The shaft/disk rotor pictured in Fig. 3.2b and the bladed-disk displayed in Fig. 3.5a are examples of such

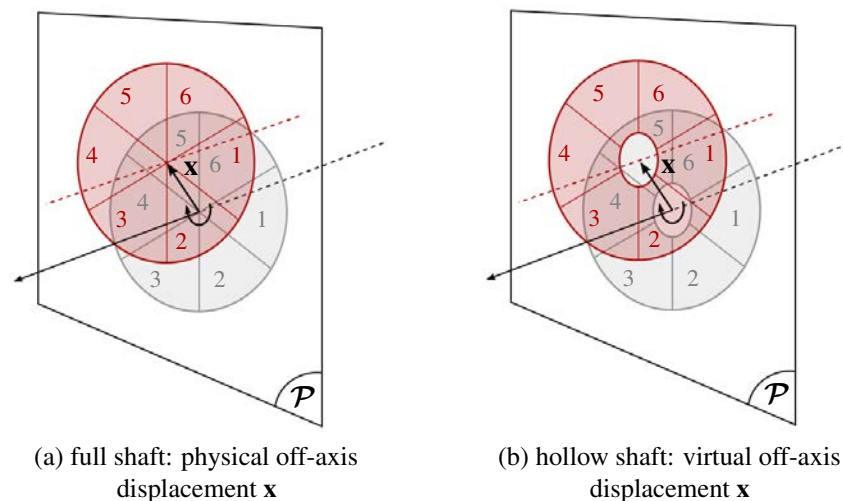


Figure 3.1: Example of cyclically symmetric structures: $N = 6$

¹Commonly named rotationally periodic structures [Tho79].

system, where appropriate boundary conditions must be enforced on the cyclic surfaces in order to ensure displacement compatibilities between neighboring sectors. In the following, some basic notions and specific notations related to cyclic-symmetry are briefly recalled, mainly based on the developments of [Bla01].

It is well known that cyclic structures exhibit very particular modal characteristics [Tho79], for instance, its modes may be regrouped by modal families and nodal diameters n_d —also called spatial harmonics—depending on their frequency and geometrical shape. By definition, the number of nodal diameters n_d of a given mode corresponds to the number of traveling waves along the structure circumference, and these waves may be of two kinds:

Single harmonics: seen as standing waves in the rotating frame, $n_d = 0$ where all sectors vibrate in phase and $n_d = N/2$ (for N even) where all sectors vibrate out of phase;

Double harmonics: composed of pairs of orthogonal eigenmodes sharing the same frequency which can be combined into a unique backward or forward rotating mode. The nodal diameters range from:

$$n_d \in [1; K] \quad \text{with} \quad K = \begin{cases} \frac{N-1}{2} & \text{if } N \text{ is odd} \\ \frac{N-2}{2} & \text{if } N \text{ is even.} \end{cases}$$

for which the phase shift in the displacements between neighboring sectors, often referred to as *inter-sector phase angle*, is equal to $\phi_{n_d} = n_d \alpha$, and $\alpha = 2\pi/N$ corresponds to the angular length of the *fundamental sector* that is called the *fundamental inter-blade phase shift*.

Since only adjacent sectors are structurally coupled, within the finite element framework, the associated mass and stiffness matrices of the full system given in Eq. (2.1) are symmetric and block-circulant [Bla01; Ols+14], and may thus be written in a general form²:

$$\mathbf{Y} = \mathbf{Bcirc}(\mathbf{Y}_0, \mathbf{Y}_1, \mathbf{Y}_1^T) = \begin{bmatrix} \mathbf{Y}_0 & \mathbf{Y}_1 & \mathbf{0} & \cdots & \mathbf{Y}_1^T \\ \mathbf{Y}_1^T & \mathbf{Y}_0 & \mathbf{Y}_1 & & \vdots \\ \vdots & \ddots & \ddots & \ddots & \mathbf{0} \\ \mathbf{0} & \cdots & \mathbf{Y}_1^T & \mathbf{Y}_0 & \mathbf{Y}_1 \\ \mathbf{Y}_1 & \cdots & \mathbf{0} & \mathbf{Y}_1^T & \mathbf{Y}_0 \end{bmatrix} \quad (3.1)$$

where matrices \mathbf{Y}_0 and \mathbf{Y}_1 are of size $n_s \times n_s$, n_s being the number of DoF of the fundamental sector, and the matrices \mathbf{Y} of the full structure are of size $n_s N \times n_s N$.

The mathematical properties of this class of matrix, as detailed in [Bla01; Ols+14], are such that a change

²It should be noted that this general form is solely valid when the matrices are expressed in an appropriate basis (*e.g.* polar coordinates or local Cartesian coordinates) so that the matrices of each sector are identical. The developments presented in the following are based on this assumption.

of space in order to relate some quantity in the physical coordinates $\mathbf{x}_{\mathcal{R}_j}$ (generally displacements) expressed in the local frame (\mathcal{R}_j) of the j -th sector to the corresponding quantity in the cyclic space using a spatial Fourier transform $\hat{\mathcal{F}}$ is available:

$$\mathbf{x}_{\mathcal{R}_j} = \frac{1}{\sqrt{N}} \hat{\mathbf{u}}^0 + \sqrt{\frac{2}{N}} \sum_{j=1}^N \left[\hat{\mathbf{u}}_c^{n_d} \cos((j-1)n_d\alpha) + \hat{\mathbf{u}}_s^{n_d} \sin((j-1)n_d\alpha) \right] + \frac{(-1)^{j-1}}{\sqrt{N}} \hat{\mathbf{u}}^{\frac{N}{2}} \quad (3.2)$$

which can be recast as follows:

$$\left(\mathbf{x}_{\mathcal{R}_1}^T \quad \mathbf{x}_{\mathcal{R}_2}^T \quad \dots \quad \mathbf{x}_{\mathcal{R}_N}^T \right)^T = \hat{\mathcal{F}} \left(\hat{\mathbf{u}}^{0,T} \quad \hat{\mathbf{u}}_c^{1,T} \quad \hat{\mathbf{u}}_s^{1,T} \quad \dots \quad \hat{\mathbf{u}}^{[N/2],T} \right)^T \quad (3.3)$$

and the construction of the real-valued Fourier matrix $\hat{\mathcal{F}}$ is briefly presented in appendix A.

Developing the backward transformation, which maps the physical displacements to the associated harmonic quantities $\hat{\mathbf{u}} = \hat{\mathcal{F}}^{-1} \mathbf{x}$, leads to the following set of expressions:

$$\hat{\mathbf{u}}^0 = \frac{1}{\sqrt{N}} \sum_{j=1}^N \mathbf{x}_{\mathcal{R}_j} \quad (3.4a)$$

$$\hat{\mathbf{u}}^{\frac{N}{2}} = \frac{1}{\sqrt{N}} \sum_{j=1}^N (-1)^{j-1} \mathbf{x}_{\mathcal{R}_j} \quad (3.4b)$$

for single harmonics, and:

$$\hat{\mathbf{u}}_c^{n_d} = \sqrt{\frac{2}{N}} \sum_{j=1}^N \mathbf{x}_{\mathcal{R}_j} \cos((j-1)n_d\alpha) \quad (3.5a)$$

$$\hat{\mathbf{u}}_s^{n_d} = \sqrt{\frac{2}{N}} \sum_{j=1}^N \mathbf{x}_{\mathcal{R}_j} \sin((j-1)n_d\alpha) \quad (3.5b)$$

for double ones.

As mentioned previously, in order to recover the behavior of the full structure from the fundamental sector model, an appropriate set of boundary conditions must be enforced on the cyclic surfaces, relating the cyclic coordinates associated to the displacements on the left l boundary to those of the right r boundary (visible in Fig. 3.5a). These can be shown to be:

$$\hat{\mathbf{u}}_c^{n_d,l} = \hat{\mathbf{u}}_c^{n_d,r} \cos n_d\alpha + \hat{\mathbf{u}}_s^{n_d,r} \sin n_d\alpha \quad (3.6a)$$

$$\hat{\mathbf{u}}_s^{n_d,l} = -\hat{\mathbf{u}}_c^{n_d,r} \sin n_d\alpha + \hat{\mathbf{u}}_s^{n_d,r} \cos n_d\alpha \quad (3.6b)$$

As proved in [Ols+14], the structural matrices (3.1) become symmetric and block-diagonal matrices in

the cyclic space and may be organized by spatial harmonics³:

$$\hat{\mathbf{Y}} = \hat{\mathcal{F}}^T \mathbf{Y} \hat{\mathcal{F}} = \mathbf{B} \text{diag}(\hat{\mathbf{Y}}_0, \hat{\mathbf{Y}}_1, \dots, \hat{\mathbf{Y}}_{\lfloor N/2 \rfloor}) = \begin{bmatrix} \hat{\mathbf{Y}}_0 & \mathbf{0} & \cdots & \mathbf{0} \\ \mathbf{0} & \hat{\mathbf{Y}}_1 & \mathbf{0} & \vdots \\ \vdots & & \ddots & \mathbf{0} \\ \mathbf{0} & \cdots & \mathbf{0} & \hat{\mathbf{Y}}_{\lfloor N/2 \rfloor} \end{bmatrix} \quad (3.7)$$

Hence, considering the wave propagation conditions presented in Eq. (3.2) and the associated boundary conditions in Eq. (3.6), each block of simple harmonics in Eq. (3.7) may be expressed as:

$$\hat{\mathbf{Y}}_0 = \mathbf{Y}_0 + \mathbf{Y}_1 + \mathbf{Y}_1^T \quad (3.8a)$$

$$\hat{\mathbf{Y}}_{N/2} = \mathbf{Y}_0 - \mathbf{Y}_1 - \mathbf{Y}_1^T \quad \text{for } N \text{ even,} \quad (3.8b)$$

while for double harmonics these blocks become:

$$\hat{\mathbf{Y}}_{n_d} = \begin{bmatrix} \mathbf{Y}_0 + (\mathbf{Y}_1 + \mathbf{Y}_1^T) \cos n_d \alpha & (\mathbf{Y}_1 - \mathbf{Y}_1^T) \sin n_d \alpha \\ (\mathbf{Y}_1 - \mathbf{Y}_1^T) \sin n_d \alpha & \mathbf{Y}_0 + (\mathbf{Y}_1 + \mathbf{Y}_1^T) \cos n_d \alpha \end{bmatrix} \quad (3.9)$$

In summary, the mass and stiffness matrices of the fundamental sector are sufficient to compute the full structural matrices in the cyclic space by means of Eqs. (3.8) and (3.9). This coordinate change produces $\lfloor N/2 \rfloor + 1$ uncoupled problems of size $n_s \times n_s$ for simple harmonics and $2n_s \times 2n_s$ for double ones, which are considerably smaller than the original problem of size $n_s N \times n_s N$.

3.1.2. Analysis of shaft motions

In the literature, it is generally known that the modes of the shaft can be present solely in $n_d = 0$ and $n_d = 1$ modes, with torsional and longitudinal modes in the former and bending ones in the latter [CDM86; LK84]. In bladed-disk/shaft assemblies, this is explained by the fact that “*the disk modes with 0-nodal diameter, which are characterized by a resultant axial force, interact with the longitudinal shaft deformations. The modes with 1-nodal diameter, which exert a net pitching moment and shear force, interact with the shaft bending modes*” [IJR99]. This phenomenon is also known to occur in circular plates [KCB12], where the in-plane motions of the plate center are only admissible for 1-nodal diameter modes while longitudinal displacements can only occur in 0-nodal diameter ones.

However, to the author’s knowledge, there is lack of a formal proof regarding the phenomena described in [LK84] and [IJR99]. Within the previously introduced finite element framework, it is here proposed to

³The number of nodal diameters n_d goes from 0 to $\lfloor N/2 \rfloor$, where the operator $\lfloor A \rfloor$ extracts the largest previous integer of A . Hence, for N even the last harmonic is simple, while for N odd it is double [Bla01].

determine which spatial harmonics are affected by an off-axis motion⁴ of a node belonging to the axis of rotation of a cyclically symmetric structure. The displacements \mathbf{x} , which can be regarded as physical or virtual displacements depending if the shaft is full or hollow respectively, limited to the components associated to such node as illustrated in Fig. 3.1, are translated into the Fourier space $\hat{\mathbf{u}}$ by means of the change of variable proposed in [Bla01]. In the local frame (\mathcal{R}_j) of the j -th sector, this displacement is:

$$\mathbf{x}_{\mathcal{R}_j} = \begin{pmatrix} a \cos(j\alpha) \\ -a \sin(j\alpha) \end{pmatrix} \quad \text{with } j = [1; \dots; N] \quad (3.10)$$

where a is the displacement amplitude and $\alpha = 2\pi/N$ corresponds to the fundamental inter-blade phase shift previously defined.

3.1.2.1. Single harmonics: $n_d = 0$ and $n_d = N/2$

For the zeroth-nodal diameter, inserting \mathbf{x}_j from Eq. (3.10) into Eq. (3.4a) and using a complex exponential notation ($i^2 = -1$), Eq. (3.4a) becomes:

$$\hat{\mathbf{u}}^0 = \frac{1}{\sqrt{N}} \sum_{j=1}^N \begin{pmatrix} a \cos(j\alpha) \\ -a \sin(j\alpha) \end{pmatrix} = \frac{1}{\sqrt{N}} \sum_{j=1}^N \begin{pmatrix} a \operatorname{Re}(\exp(ij\alpha)) \\ -a \operatorname{Im}(\exp(ij\alpha)) \end{pmatrix} \quad (3.11)$$

this sum of exponentials is a geometric sequence of reason $\exp(i\alpha)$ and may thus be written as:

$$\sum_{j=1}^N a \exp(ij\alpha) = a \exp(i\alpha) \frac{1 - \exp(i\alpha)^N}{1 - \exp(i\alpha)}, \quad (3.12)$$

since

$$\exp(i\alpha)^N = \exp\left(i \frac{2\pi}{N}\right)^N = \exp(i2\pi) = 1, \quad (3.13)$$

then

$$\sum_{j=1}^N a \exp(ij\alpha) = 0 + i0 \quad \Rightarrow \quad \hat{\mathbf{u}}^0 = \mathbf{0} \quad (3.14)$$

and therefore, the zeroth harmonic does not participate in the off-axis displacement of the central node.

The same mathematical framework employed for the zeroth harmonic is now considered for $n_d = N/2$, but this harmonic only emerges when N is even. By exploiting the exponential formulation (3.11),

⁴Only displacements perpendicular to the axis of rotation are considered.

expression (3.4b) becomes:

$$\hat{\mathbf{u}}^{\frac{N}{2}} = \frac{1}{\sqrt{N}} \begin{pmatrix} \sum_{j=1}^N (-1)^{j-1} a \cos(j\alpha) \\ \sum_{j=1}^N -(-1)^{j-1} a \sin(j\alpha) \end{pmatrix} = \frac{1}{\sqrt{N}} \begin{pmatrix} \sum_{j=1}^N -a \operatorname{Re}((-1)^j \exp(ij\alpha)) \\ \sum_{j=1}^N a \operatorname{Im}((-1)^j \exp(ij\alpha)) \end{pmatrix} \quad (3.15)$$

By following the line of thought leading to Eq. (3.12), the sum of exponentials is translated into a geometric sequence of reason $-\exp(i\alpha)$:

$$\sum_{j=1}^N (-1)^j a \exp(-ij\alpha) = -a \exp(i\alpha) \frac{1 - (-\exp(i\alpha))^N}{1 - (-\exp(i\alpha))} \quad (3.16)$$

since

$$(-\exp(i\alpha))^N = \left(-\exp\left(i \frac{2\pi}{N}\right) \right)^N = \exp(i2\pi) = 1 \quad \text{as } N \text{ is even,} \quad (3.17)$$

then

$$\sum_{j=1}^N (-1)^j a \exp(-ij\alpha) = 0 + i0 \quad \Rightarrow \quad \hat{\mathbf{u}}^{\frac{N}{2}} = \mathbf{0} \quad (3.18)$$

and consequently, the projection of the off-axis shaft displacement in the cyclic space results into a null participation of the nodal diameter $n_d = N/2$.

3.1.2.2. Double harmonics: $n_d = [1, \dots, K]$

For double harmonics, by manipulating the sums of sines and cosines in the associated change of variable given in Eqs. (3.5a) and (3.5b), it can be proven that:

$$n_d \in]1; K], \quad \hat{\mathbf{u}}_c^{n_d} = \hat{\mathbf{u}}_s^{n_d} = \mathbf{0} \quad (3.19a)$$

$$n_d = 1, \quad \hat{\mathbf{u}}_c^{n_d} = \hat{\mathbf{u}}_s^{n_d} = a\sqrt{2N} \cos(\alpha) \quad (3.19b)$$

where the only non-zero contribution corresponds to the first spatial harmonic.

It is then evident that a point lying on the rotational axis of a cyclically symmetric structure displays off-axis displacements on 1-nodal diameter modes only. Accordingly, any precessional motion of the shaft is completely described through a combination of 1-nodal diameter modes. Similar conclusions hold for circular plates [KCB12].

3.2. Gyroscopic terms in the finite-element framework

For rotating bodies, gyroscopic effects or Coriolis forces stem from the conservation of the angular momentum, *i.e.* the tendency that such body has to resist any change of direction. In the finite-element framework, it corresponds to a skew-symmetric matrix which is linearly dependent on the rotational speed Ω [Gen05]. These effects are generally ignored when investigating the dynamical properties of bladed-disks in the turbomachinery field, yet, according to [IJR99], “*when dealing with bladed-disk/shaft assemblies, gyroscopic effects can no longer be neglected and the variations of frequencies with respect to the rotation speed are relatively large*”.

There is little information in the literature on how to build this matrix in the FE-space, particularly for cyclic structures, nor on how its effects are accurately captured in reduced spaces (*e.g.* Craig-Bampton) [JFR96]. It is proposed in the following to detail this procedure, starting from the integral definition of the elementary matrix \mathbf{G} (2.3), which has a very similar expression than the mass elementary matrix \mathbf{M} (2.2). As suggested in [Gen05], when the rotational speed is constant over the volume and that the formulation contains solely orthogonal displacements, as in a Cartesian formulation for instance, the matrix $\mathbf{\Omega}$ may be extracted from the integral and Eq. (2.3) becomes:

$$\mathbf{G} = 2\mathbf{\Omega}_{\hat{n}}\mathbf{M} \quad \text{with} \quad \mathbf{\Omega}_{\hat{n}} = \mathbf{\Omega} \otimes \mathbf{I}_{\hat{n}} \quad (3.20)$$

where \otimes represents the Kronecker product and \hat{n} corresponds to the number of nodes of the full system. Therefore, it is the matrix $\mathbf{\Omega}$ which confers its skew-symmetric property to \mathbf{G} and knowing that \mathbf{M} is generally sparse, the resultant gyroscopic matrix is sparse as well.

3.2.1. Construction of the gyroscopic matrix

As mentioned in Eq. (3.1), for a cyclically symmetric structure composed of N identical sectors, the mass matrix is symmetric and block-circulant [Bla01]. By considering expression (3.20), it can be deduced that the gyroscopic matrix is skew-symmetric and block-circulant, and takes the form:

$$\mathbf{G} = 2\mathbf{\Omega}_{\hat{n}}\mathbf{M} = \mathbf{Bcirc}(\mathbf{G}_0, \mathbf{G}_1, \mathbf{G}_2) = \begin{bmatrix} \mathbf{G}_0 & \mathbf{G}_1 & \mathbf{0} & \cdots & \mathbf{0} & \mathbf{G}_2 \\ \mathbf{G}_2 & \mathbf{G}_0 & \mathbf{G}_1 & \mathbf{0} & \cdots & \mathbf{0} \\ \mathbf{0} & \mathbf{G}_2 & \mathbf{G}_0 & \mathbf{G}_1 & \mathbf{0} & \vdots \\ \vdots & & \ddots & \ddots & \ddots & \mathbf{0} \\ \mathbf{0} & \cdots & \mathbf{0} & \mathbf{G}_2 & \mathbf{G}_0 & \mathbf{G}_1 \\ \mathbf{G}_1 & \mathbf{0} & \cdots & \mathbf{0} & \mathbf{G}_2 & \mathbf{G}_0 \end{bmatrix} \quad (3.21)$$

with

$$\mathbf{G}_0 = 2\Omega_{\hat{n}_s} \mathbf{M}_0, \quad (3.22a)$$

$$\mathbf{G}_1 = 2\Omega_{\hat{n}_s} \mathbf{M}_1, \quad (3.22b)$$

$$\mathbf{G}_2 = 2\Omega_{\hat{n}_s} \mathbf{M}_1^T \quad (3.22c)$$

and $\Omega_{\hat{n}_s} = \Omega \otimes \mathbf{I}_{\hat{n}_s}$, where \hat{n}_s represents the number of nodes of the fundamental sector in \mathbf{M}_0 .

The change of variable going from physical to cyclic coordinates in Eq. (3.3) may be used, which leads to a symmetric block diagonal mass matrix as in Eq. (3.7), whereas for the gyroscopic matrix (3.21) it results in a matrix $\hat{\mathbf{G}}$ skew-symmetric and block-diagonal:

$$\hat{\mathbf{G}} = \mathbf{Bdiag}(\hat{\mathbf{G}}_0, \hat{\mathbf{G}}_1, \dots, \hat{\mathbf{G}}_{\lfloor N/2 \rfloor}) \quad (3.23)$$

As the dimension of the blocks in (3.7) and (3.23) remains too large to be used directly in a time-marching strategy, the Craig-Bampton component mode synthesis is employed for every harmonic n_d , by computing a multi-speed reduction basis [Mei+13; SB06]. As explained in [JFR96], the presence of gyroscopic terms generate frequency splits between forward and backward rotating modes, but do not alter significantly the associated modeshapes of the structure. Thus the computation of the reduction matrices Φ_{n_d} solely involves the mass and stiffness matrices of the non-rotating system. Once these are built for each harmonic n_d , the mass, stiffness and gyroscopic matrices may be reduced as usual:

$$\hat{\mathbf{M}}_{r,n_d} = \Phi_{n_d}^T \hat{\mathbf{M}}_{n_d} \Phi_{n_d}, \quad \hat{\mathbf{K}}_{r,n_d} = \Phi_{n_d}^T \hat{\mathbf{K}}_{n_d} \Phi_{n_d}, \quad \text{and} \quad \hat{\mathbf{G}}_{r,n_d} = \Phi_{n_d}^T \hat{\mathbf{G}}_{n_d} \Phi_{n_d} \quad (3.24)$$

with, $n_d = 0, 1 \dots \lfloor N/2 \rfloor$.

In order to avoid repeating the reduction procedure (3.24) for every rotational speed, $\Omega = 1$ can be considered for the construction of the gyroscopic matrix blocks (3.22). Thus, the resultant gyroscopic matrix should be multiplied by the rotational speed ($\mathbf{G}(\Omega) = \Omega \mathbf{G}(1)$) in the equations of motion when implementing the time-marching algorithms and modal analyses detailed in the following. As described in [Mei14], these reduced matrices (3.24) are added in order to obtain the final multi-sector model, which enables to handle unilateral contact conditions on each blade independently.

The numerical procedure implemented for the construction of the gyroscopic matrix may thus be summarized as follows:

1. Extraction of the mass matrix blocks \mathbf{M}_0 and \mathbf{M}_1 in Eq. (3.1) from the sector mesh.
2. Construction of gyroscopic matrix blocks \mathbf{G}_0 , \mathbf{G}_1 and \mathbf{G}_2 in Eq. (3.22).

3. Calculation of each block of the gyroscopic matrix (3.23) in the harmonic space, using cyclic-symmetry expressions (3.11), (3.15) and (3.19).
4. Reduction of each harmonic block by means of Eq. (3.24), where the Craig-Bampton reduction matrix is built using the modes of the non-rotating system as suggested in [JFR96].
5. Recomposition of the reduced model as in [BML15].

3.2.2. Illustrative example and validation

In order to validate the gyroscopic matrix construction procedure presented above, part of the results presented in [IJR99] were reproduced. In [IJR99], the modal properties of an overhung rotating disk—mesh represented in 3.2a—are studied both numerically and experimentally, putting particular emphasis on the mode splits induced by the gyroscopic terms. However, as in [JFR96], the numerical method incorporating the gyroscopic terms is not clearly presented nor detailed.

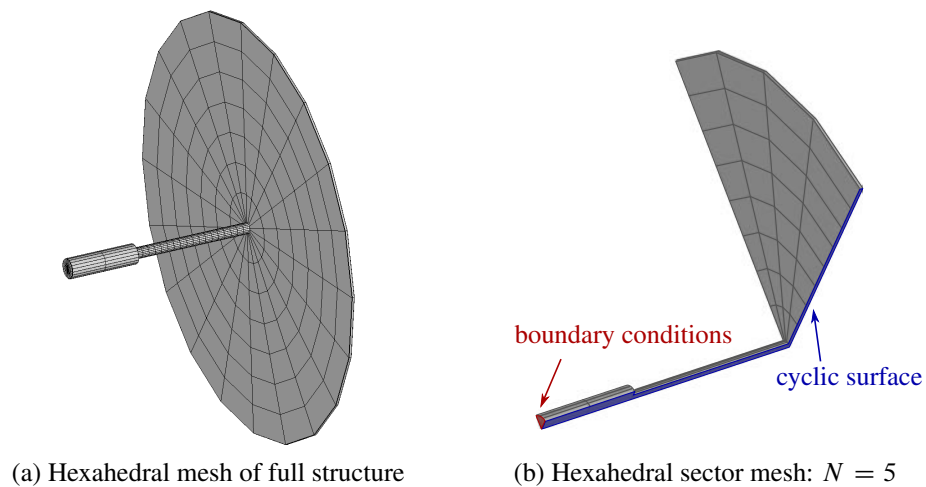


Figure 3.2: FE-models built from [IJR99]

Two models were built using CALCULIX FE software: (1) full 3D FE-model, depicted in Fig. 3.2a, and (2) a full cyclic-symmetric model, where only a fifth of the rotor was meshed and illustrated in Fig. 3.2b. From these, the mass and stiffness matrices were extracted and the above mentioned procedure was followed to build the gyroscopic matrix for each model (Eqs. (3.20) and (3.23) respectively). A third model was then constructed as a reduced version of the cyclic-symmetric model, using Craig-Bampton component mode synthesis [Mei14; SB06] by means of Eq. (3.24), in order to verify that the influence of the gyroscopic terms on the system eigenfrequencies is accurately captured in the reduced space. To perform a modal analysis of

these models, the state-space form of the equations of motion is considered:

$$\begin{bmatrix} \mathbf{M} & \mathbf{0} \\ \mathbf{0} & \mathbf{M} \end{bmatrix} \begin{pmatrix} \dot{\mathbf{x}}(t) \\ \ddot{\mathbf{x}}(t) \end{pmatrix} + \begin{bmatrix} \mathbf{0} & -\mathbf{M} \\ \mathbf{K}(\Omega) & \mathbf{G}(\Omega) \end{bmatrix} \begin{pmatrix} \mathbf{x}(t) \\ \dot{\mathbf{x}}(t) \end{pmatrix} = \begin{pmatrix} \mathbf{0} \\ \mathbf{0} \end{pmatrix} \quad (3.25)$$

which is a simplified version of Eq. (2.9) since $\mathbf{K}(\Omega)$ is linear and contains centrifugal terms, spin softening is neglected and Ω is constant, thus acceleration stiffening terms vanish.

As mentioned in section 2.1.2, the associated eigenmodes of the system are complex conjugate pairs, coupling speed and displacements, and gyroscopic terms tend to stiffen forward modes and soften backward ones, hence inducing a frequency split between forward and backward traveling waves [JFR96].

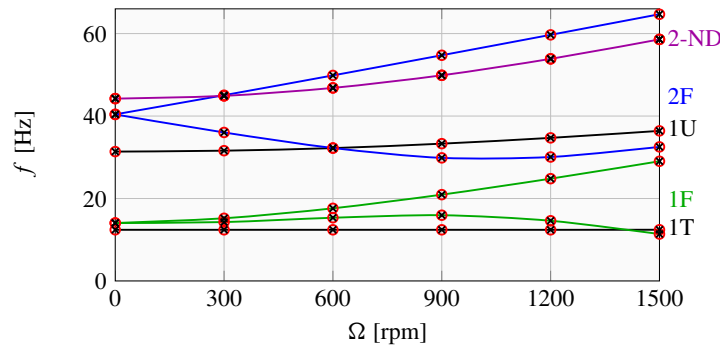


Figure 3.3: Campbell diagram from [IJR99]: full 3D model [—], full cyclic model [○] and reduced model [✕]

It can be seen in Fig. 3.3 that the Campbell diagram of the overhung rotor shows excellent agreement between the calculated eigenfrequencies with the full 3D finite element model, the global cyclic-symmetric model as well as the reduced cyclic-symmetric model. As explained in [IJR99], the important split observed in flexural modes (1F and 2F), which are 1-nodal diameter modes, is produced by the gyroscopic terms and the important disk/shaft coupling. On the contrary, there is a negligible split in the torsional and umbrella modes (1T and 1U), which are 0-nodal diameter modes, as well as on the 2-nodal diameter mode for which the shaft has no off-axis displacements.

Since the results presented in Fig. 3.3 are consistent with those provided in the paper [IJR99], it is understood from this illustrative example that the numerical procedure implemented for building the gyroscopic matrix, both for full 3D models as well as for cyclic-symmetric models is validated. Furthermore, it also demonstrated that the Craig-Bampton modal reduction basis composed of static and constrained modes of the non-rotating system is perfectly capable of capturing the frequency splits between forward and backward waves induced by the gyroscopic terms.

3.3. Modal features of the fan bladed-disk

The stage of the engine which is the most susceptible to undergo whirling motions is the fan stage. This is due to overhung configuration commonly adopted in high bypass ratio aircraft engines and the couplings arising between the shaft bending modes and the bladed-disk dynamics [CDM86].

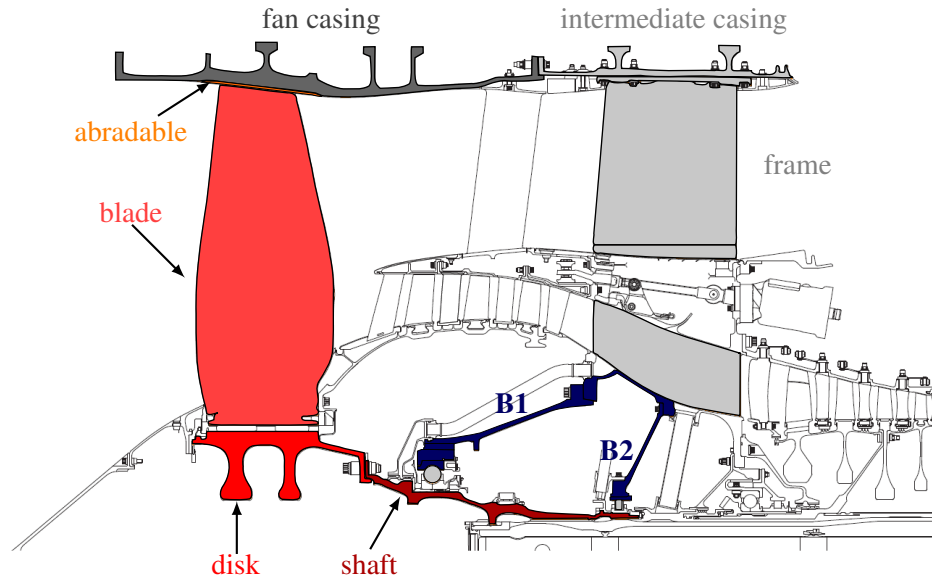


Figure 3.4: Industrial fan stage components: blades, disk and shaft assembly linked to fan casing through bearings B1 and B2, frame and intermediate casing

In the case of the engine illustrated in Fig. 3.4, the shaft is supported by two bearings—denoted B1 and B2—which are connected to the casing through the frame. The fan bladed-disk is mounted on the shaft free end and is composed of 24 blades and a disk. The surrounding casing is decomposed into the fan casing and the intermediate casing, the latter supporting the frame and being attached to the wing of the aircraft.

High-fidelity finite element models of the blade, disk, shaft and casing systems were constructed using commercial softwares (ANSYS and SAMCEF) based on mesh and geometry data provided by SNECMA. In the following, some basic modal features of the bladed-disk are presented, mainly focusing on how the dynamics of the shaft is coupled to the bladed-disk and how gyroscopic terms affect the modal properties of the assembly. These key features are essential to the analyses presented in the chapter 5.

3.3.1. Fundamental sector model

The model built in this investigation corresponds to a perfectly tuned bladed-disk, composed of *shaft*, *disk* and *blades*, which are assumed to be merged together in order to exploit cyclic-symmetry. In this particular case, the bladed-disk is composed of $N = 24$ sectors, the final geometry is illustrated in Fig. 3.5a and the

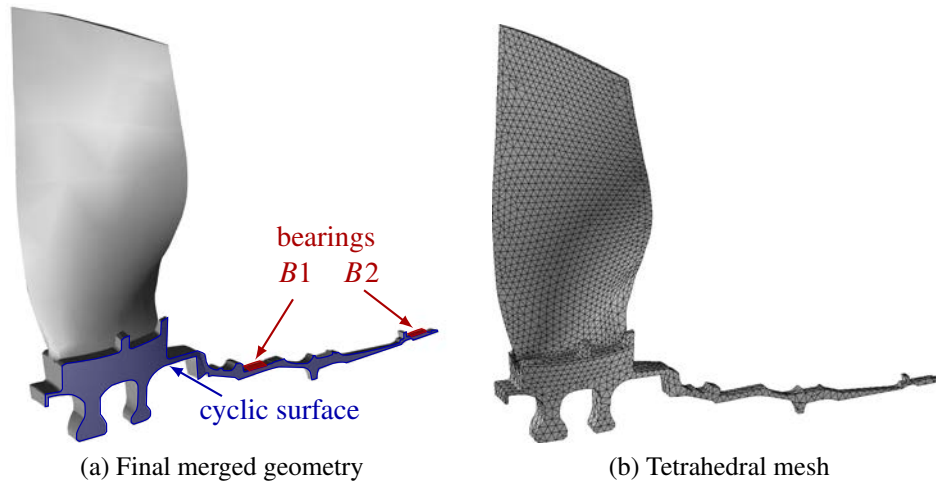


Figure 3.5: Bladed-disk model: shaft/disk/blade fundamental sector

associated mesh composed of tetrahedral elements is displayed in Fig. 3.5b. The position of the supporting bearings is highlighted in Fig. 3.5a. As a first approximation, these are assumed to be perfectly rigid, thus resulting into clamped boundary conditions.

It should be noted that in a real engine, due to manufacturing tolerances or material imperfections for instance, sectors are not perfectly identical. This is commonly referred to as *mistuning*. It requires the use of probabilistic or stochastic equations of motion and has been a topic of prime interest in the field over the last decades [CP06]. These small imperfections from one sector to the next are generally known to magnify the blades response at resonance, since they translate into a disruption of nodal diameter modes and produce highly localized vibrations [WP88]. This phenomenon however, is beyond the scope of this dissertation and will not be considered in the following.

3.3.2. Modal analysis and mesh convergence

The influence of the mesh density on the bladed-disk modal properties was assessed in order to ensure convergence of the first 20 modes per spatial harmonic. The reference sector has about 120000 nodes and four coarser meshes were built for the comparison. This convergence analysis was carried out without accounting for centrifugal or gyroscopic terms, *i.e.* the eigenfrequencies were calculated at rest. As depicted in Fig. 3.6, the convergence of both 0 and 1 spatial harmonics is achieved and similar results were obtained for the remaining harmonics. The chosen sector model has about 25000 nodes and properly approximates the considered modes below a 3% error with respect to the finest mesh.

The frequencies at rest of the first six modal families are presented in the veering diagram 3.7a as a function of n_d . In this figure, the modes associated to the $n_d = 1$ harmonic are highlighted, which are the

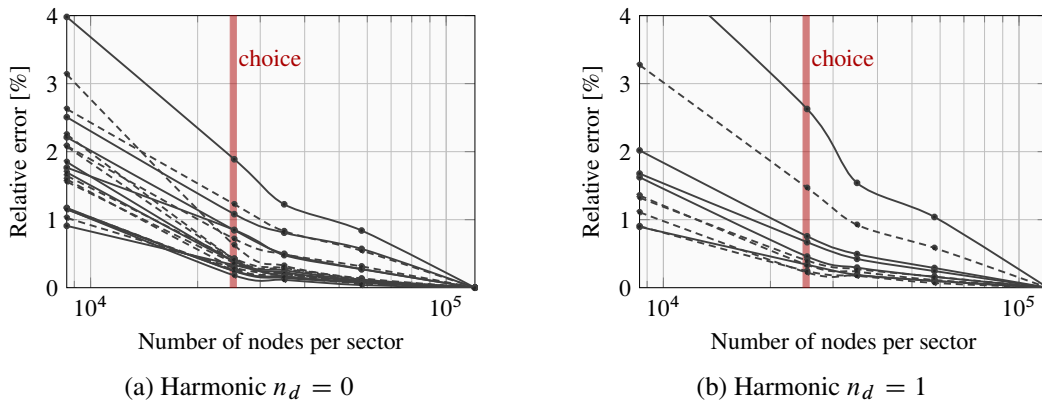


Figure 3.6: Mesh convergence study of the bladed-disk model: chosen mesh [■]

only modes affected by the off-axis dynamics of the shaft [IJR99; SBL14]. As will be detailed later on, some of these modes involve a substantial coupling with the shaft dynamics, which produces a significant drop in the associated eigenfrequencies when compared to other harmonics of the same modal family.

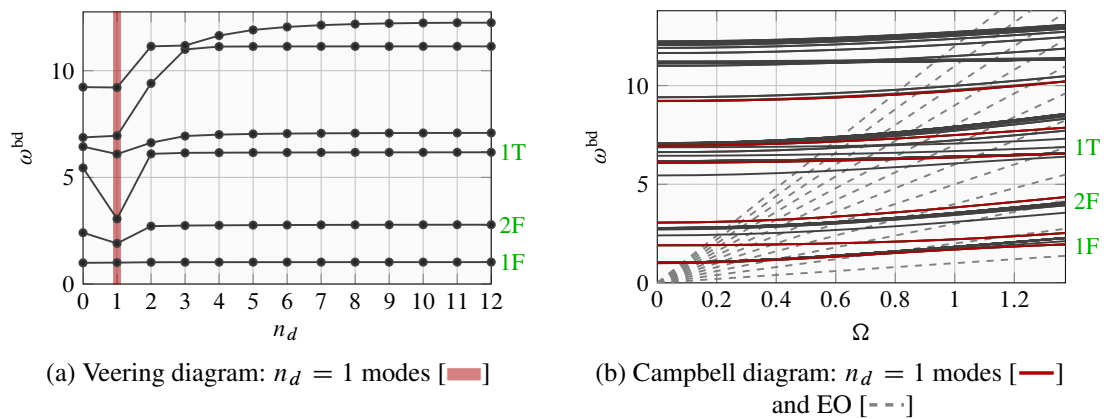


Figure 3.7: Modal analysis of bladed-disk model

Further, the evolution of the first six modal families as a function of the rotational speed is depicted in the Campbell diagram 3.7b while neglecting gyroscopic terms, and some of the 1F mode shapes are illustrated in Fig. 3.8. The 1-nodal diameter modes are highlighted and the Engine Order (EO) excitations are also displayed. It may be noted how the 1-EO never crosses a modal line throughout the rotational speed range, thus indicating that no major vibration amplitudes are expected to be induced by synchronous excitations (*e.g.* mass imbalance). However, as unilateral contact is known to potentially excite sub and super harmonics, a critical speed is expected to occur at $\Omega^{cr} \simeq 0.9$, with the crossing of the 2-EO and 4-EO with the 1F and 2F modal families respectively. Although, as shown in [SBL14], this type of symmetric excitation should not involve large displacements of the shaft.

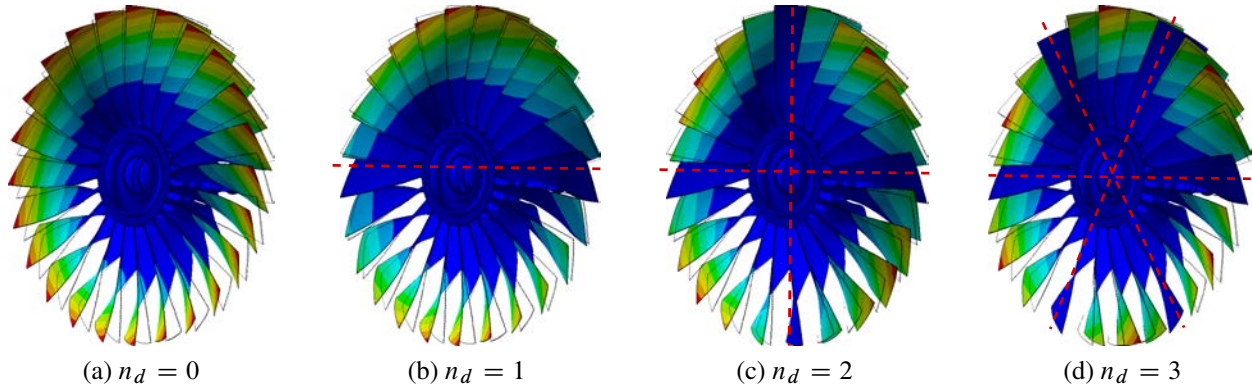


Figure 3.8: Mode shapes of the bladed-disk: first bending (1F) modal family and nodal lines [---]

In order to assess the influence of the gyroscopic matrix $\mathbf{G}(\Omega)$ on the modal properties of the bladed-disk, the procedure presented in section 3.2 was used to build $\mathbf{G}(\Omega)$, and a complex modal analysis was performed considering the free vibration equations of motion in its state-space form (3.25). The results are depicted in

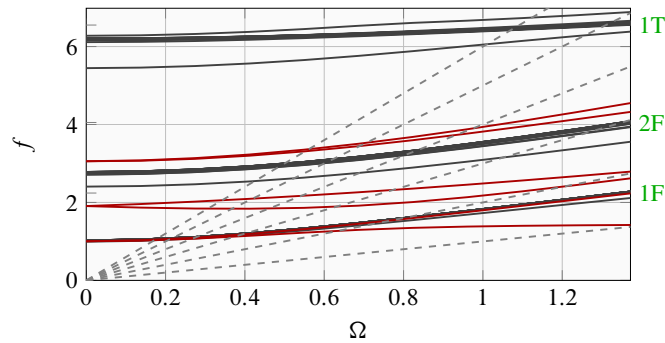


Figure 3.9: Campbell diagram of bladed-disk with gyroscopic terms: $n_d = 1$ modes [—]

Fig. 3.9. An important split may be observed for $n_d = 1$ modes, in particular for the bending modal families, whereas all other harmonics seem barely affected by the gyroscopic terms (similar results than in Fig. 3.7b). Furthermore, it should be noted how the 1-EO almost crosses the backward $n_d = 1$ mode of the first bending family at the maximal operating speed, a crossing that could result in potentially harmful interactions and that cannot be predicted without taking gyroscopic terms into consideration.

3.3.3. Shaft modal displacements

Not all 1-nodal diameter modes involve important shaft displacements [IJR99], for instance, the shaft appears to have a negligible participation on the 1F mode pictured in Fig. 3.8b. In order to quantify the participation of the shaft on each family of modes, the modal displacements of the shaft are represented in diagram 3.10a for the first 10 $n_d = 1$ modes. These are extracted from the nodes located on free end of the disk and are

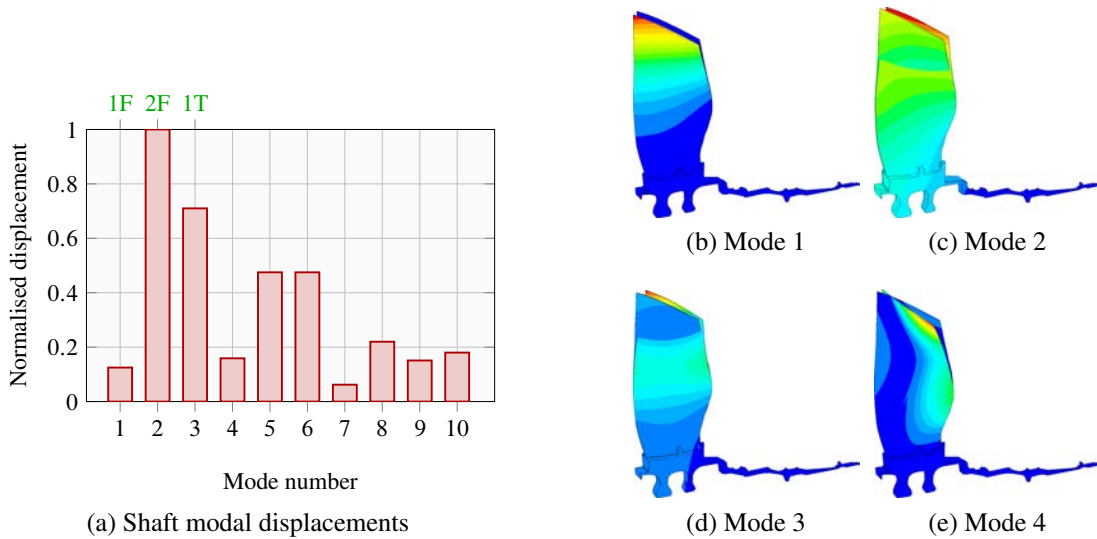


Figure 3.10: Shaft modal displacements and associated mode shapes

normalized with respect to the highest modal amplitude. The first four mode shapes are also presented in Fig. 3.10 to illustrate this phenomenon.

It can be clearly distinguished in Figs. 3.10c and 3.10d that modes 2F and 1T involve non-negligible shaft/bladed-disk coupling, whereas the 1F mode displayed in Fig. 3.10b does not. Therefore, high amplitude whirling motions are expected to occur when 1-nodal diameter modes of 2F and 1T modal families are excited, as opposed to the study [SBL14], where the main response involved the first bending modal family only. The 5-th and 6-th modal families could also be expected to exhibit important whirling orbits, even if for previous studies [Bat+12; Mil10], only lower modes seem to be excited during blade/abradable interactions.

The exposed results on the industrial bladed-disk are consistent with the illustrative example presented in section 3.2.2 and emphasize the importance of accounting for gyroscopic terms in the formulation as well as the bladed-disk/shaft coupling, as these significantly modify 1-nodal diameter modes of the system.

3.4. On bladed-disk/casing structural coupling

The frame and supporting bearings illustrated in Fig. 3.4 represent a structural connection between the rotating shaft and its surrounding casing, which leads to bladed-disk/casing coupled modes that may bring new contact scenarios into consideration. Therefore, it is proposed in this section to evaluate the influence of such a coupling from static and modal perspectives. In section 3.4.1, a non-rotating shaft is considered and it is simply merged to the bearings, thus the entire stage is considered as a single component at rest. The

rotation is then accounted for in section 3.4.2, where the stiffness of the rolling elements in the bearings is modeled through a density of linear springs yielding equations of motion with time-periodic coefficients.

3.4.1. Bladed-disk at rest

3.4.1.1. Geometry and mesh properties

The industrial model of the fan stage depicted in Fig. 3.4 is considered, resulting in the geometry depicted in Fig. 3.11a. The casing is connected to the frame and bearings, denoted B1 and B2, which are attached to shaft, *i.e.* the bladed-disk is at rest. The geometry of the frame was not provided by SNECMA but instead was

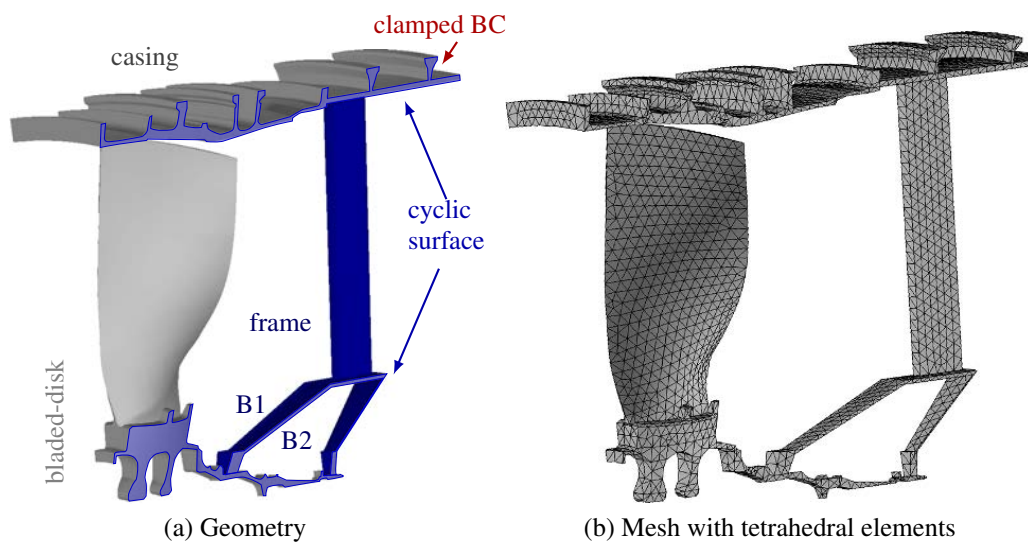


Figure 3.11: Coupled bladed-disk/casing model with blocked rotation

drawn from picture 3.4 considering the same number of supports than sectors of the bladed-disk ($N = 24$), while in the actual engine the frame is composed of 12 non-identical sectors. Similarly, the exact geometry of the bearings was only approximated from drawing 3.4 as full axi-symmetric structures. These approximations do not affect the qualitative analysis presented in the following.

The corresponding sector mesh was built using the same tetrahedral elements employed for the bladed-disk and is shown in Fig. 3.11b, where the cyclic surface and the boundary conditions applied to the casing are put forward. This first approximation enables to treat the entire engine stage as a single cyclically symmetric structure and visualize its mode shapes at rest. The modes of particular interest are those exhibiting coupled casing and bladed-disk dynamics which could bring new interaction scenarios into play. Further, two clearance closure mechanisms are investigated from a static viewpoint, in order to properly characterize how potential bladed-disk/casing interactions would be initiated.

3.4.1.2. Static analysis and clearance closure

As a preliminary study, two static loading conditions representative of clearance closure mechanisms evoked in section 1.1.2. Attention is paid to the preferred contact location with respect to the shaft displacements.

Mass imbalance load The mass imbalance is a common source of synchronous vibrations in turbomachinery. It is often modeled through a force acting on the disk (constant direction when expressed in the rotating frame) and its magnitude is proportional to the square of the rotational speed, as evoked in Eq. (2.8).

As depicted in Fig. 3.12a, the casing is clamped at the rear while a force representing the mass imbalance acts on one of the sectors of the disk. The associated displacements (in modulus) are displayed in Fig. 3.12b,

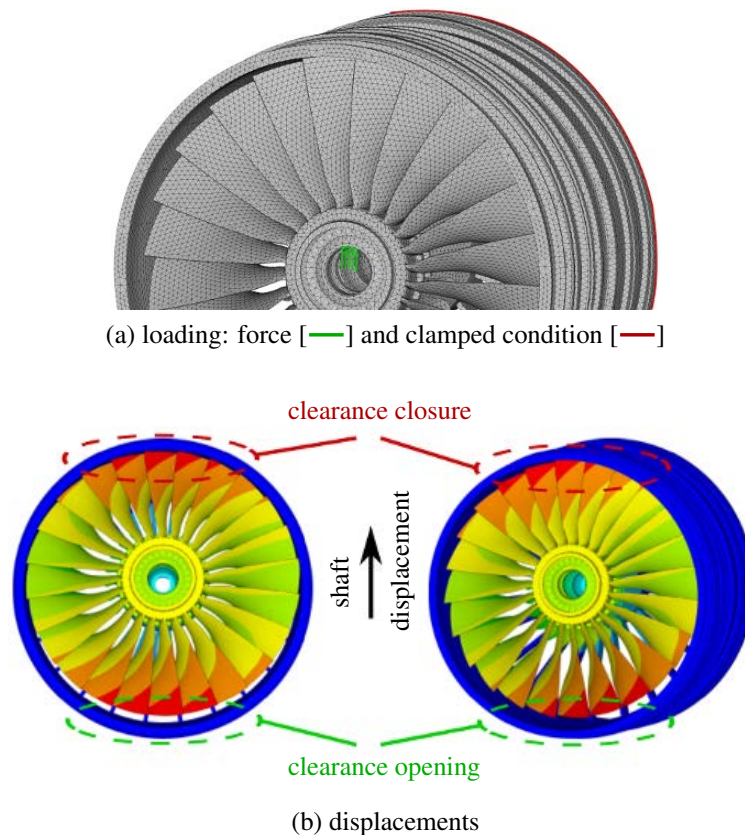


Figure 3.12: Mass imbalance scenario: loading conditions and corresponding displacements

where it can clearly be distinguished how the clearance closes on the direction of the shaft displacements, hence leading to the *standard* contact scenario. Additionally, it appears that for the current stage model the casing is barely affected by this kind of loading conditions.

However, as mentioned in the literature section 2.3.3, it is shown in [PTC14] that a mass imbalance load located at the LP-turbine stage is prone to initiate contact in both *standard* and *inverted* configurations, thus

suggesting that the stage model considered throughout this thesis is not sufficient to account for all possible interaction scenarios and that entire engine models are required.

Intake-flow load The loads arising from the intake-flow during take-off act both on rotating and stationary components as displayed in Fig. 3.13a. These are here modeled by a pressure field on the upper half of the casing as well as on a small portion of the disk. As mentioned in the introduction section 1.1.2, this loading scenario is known to give rise to a pinch point during actual engine operations [LS04].

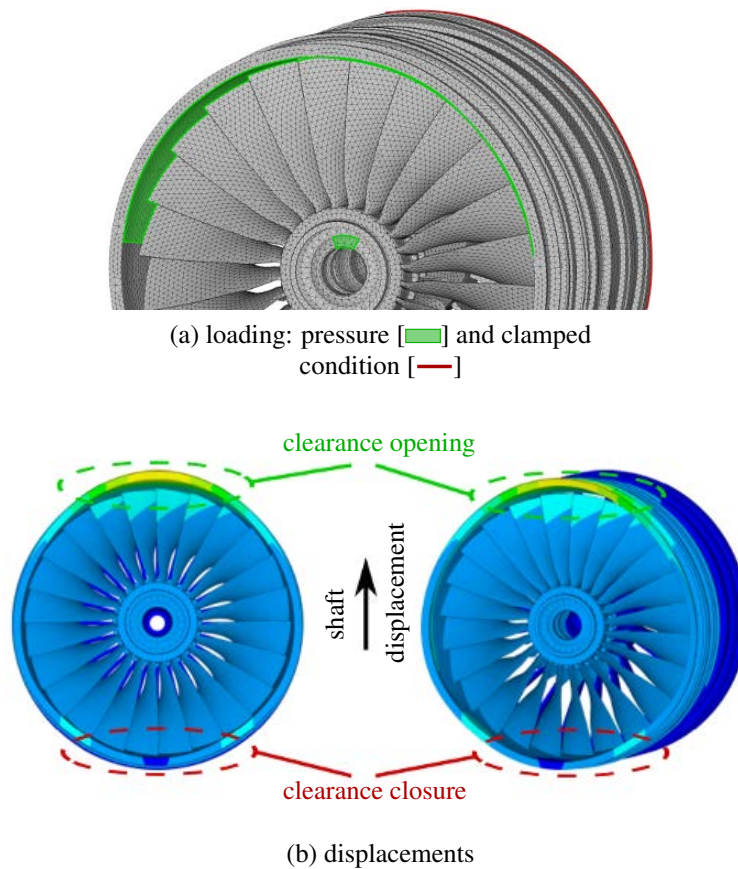


Figure 3.13: Intake-flow scenario: loading conditions and corresponding displacements

It can be seen in the associated displacement field of Fig. 3.13b how the clearance closure occurs at the bottom of the engine while it opens at the top, and that the shaft moves upwards. This observation is in good agreement with the experimental findings made in [OM82] as well as the numerical results reported in [FIO83]. Consequently, it may be concluded that during this operating phase, the entire stage is subject to a one nodal diameter deformation prone to initiate contact in the *inverted* configuration which would potentially excite forward whirling motions of the shaft.

3.4.1.3. Linear modal analysis

Different types of modes are identified by means of a modal analysis of the fan stage, namely: (1) bladed-disk, (2) casing, (3) frame and (4) coupled modes, depending on the modal energy distribution along each component. Some of these are displayed in Fig. 3.14 as an illustrative example.

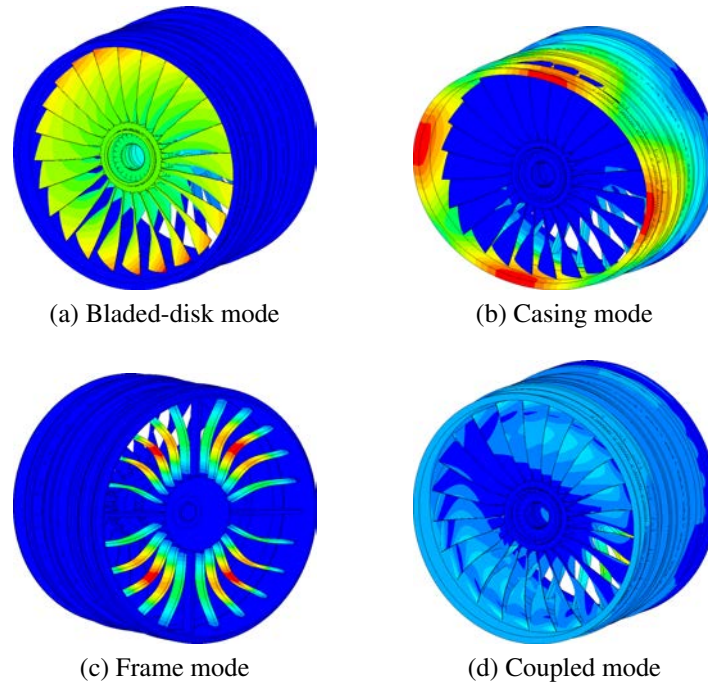


Figure 3.14: Mode shapes of bladed-disk/casing coupled model

In order to properly characterize how the frame affects the overall system behavior, two studies are carried out in the following: (1) a sensitivity analysis of the shaft and casing modal displacements to the frame stiffness and (2) the calculation of the strain energy distribution along each component.

Sensitivity to frame stiffness Three modal analyses are carried out in order to assess the influence of the frame stiffness on the modal properties of the structure, focusing solely on 1-nodal diameter modes. A different Young's modulus is used in each case, allowing to compare a stiffer and softer frame to the reference model: $E = \zeta E_0$ with $\zeta = [0.1, 1, 10]$, where E_0 corresponds to the nominal value considered for the bladed-disk in the previous section.

For the first ten 1-nodal diameter modes, the normalized modal displacements of the shaft and the casing free ends are compared in Fig. 3.15. For the reference value $\zeta = 1$, the most important shaft displacements are observed for the first mode, which couples the shaft bending to the 1F bladed-disk mode as illustrated in Fig. 3.16a. This kind of mode is the one responsible for the divergent motions obtained in [SBL14], leading

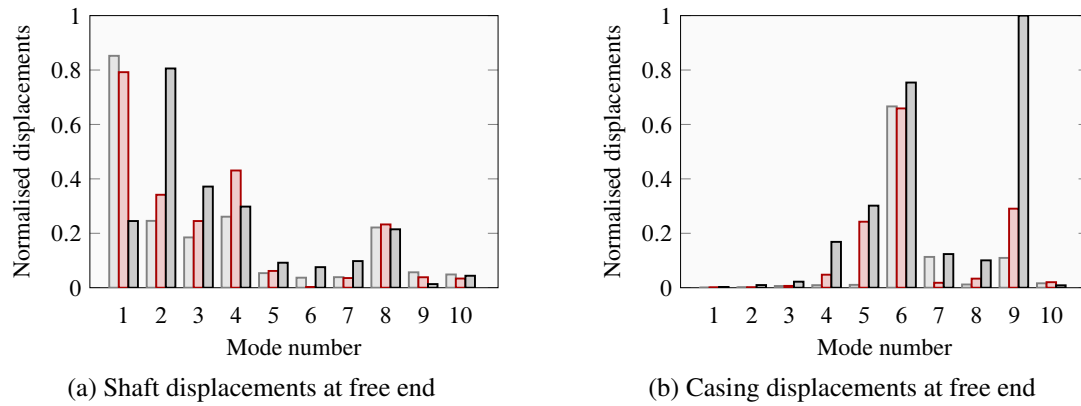


Figure 3.15: Modal displacements of shaft and casing ($n_d = 1$), sensitivity to frame stiffness : $\zeta = 0.1$ [■], $\zeta = 1$ [■] and $\zeta = 10$ [■]

to contact in the same direction as the shaft displacements and thus resulting in backward whirling motions.

High amplitude shaft motions are also observed for modes 2, 3 and 4, the first two mode shapes being depicted in Figs. 3.16b and 3.16c, which do not involve any casing participation. A similar trend is observed for $\zeta = 0.1$ and $\zeta = 1$, whereas for a stiffer frame ($\zeta = 10$) the bending of the shaft is rather coupled to the second modal family. This observation is consistent with the results presented in Fig. 3.10a, where the bladed-disk was modeled with perfectly rigid bearings and the highest shaft displacements were obtained for modes 2F and 1T. For all other modes, the shaft displacements seems less sensitive to ζ as modal displacements are almost identical.

The frame stiffness also strongly affects the casing displacements as shown in Fig. 3.15b. A stiffer frame generally increases the casing displacements, in particular for mode 9. As opposed to the shaft, it can be seen that important casing displacements appear solely for higher modes, the sixth one being pictured in Fig. 3.16e and corresponding to a coupled frame/casing mode.

Accordingly, out of the ten chosen modes, mode 5 exhibits the highest bladed-disk/casing coupling. It is illustrated in Fig. 3.16d and corresponds to the first family of frame modes, which for $n_d = 1$ couples 1-nodal diameter modes of both bladed-disk and casing. This mode is of particular interest since the two structures vibrate in phase and may potentially lead to the *inverted* contact scenario described above.

Modal strain energy distribution Similar to the analysis carried out in [Mei14], where the mode shapes of the centrifugal compressor of a helicopter engine are decomposed into the contribution of its components, namely: disk, main blade and splitter blade, it is here proposed to evaluate the strain energy distribution along

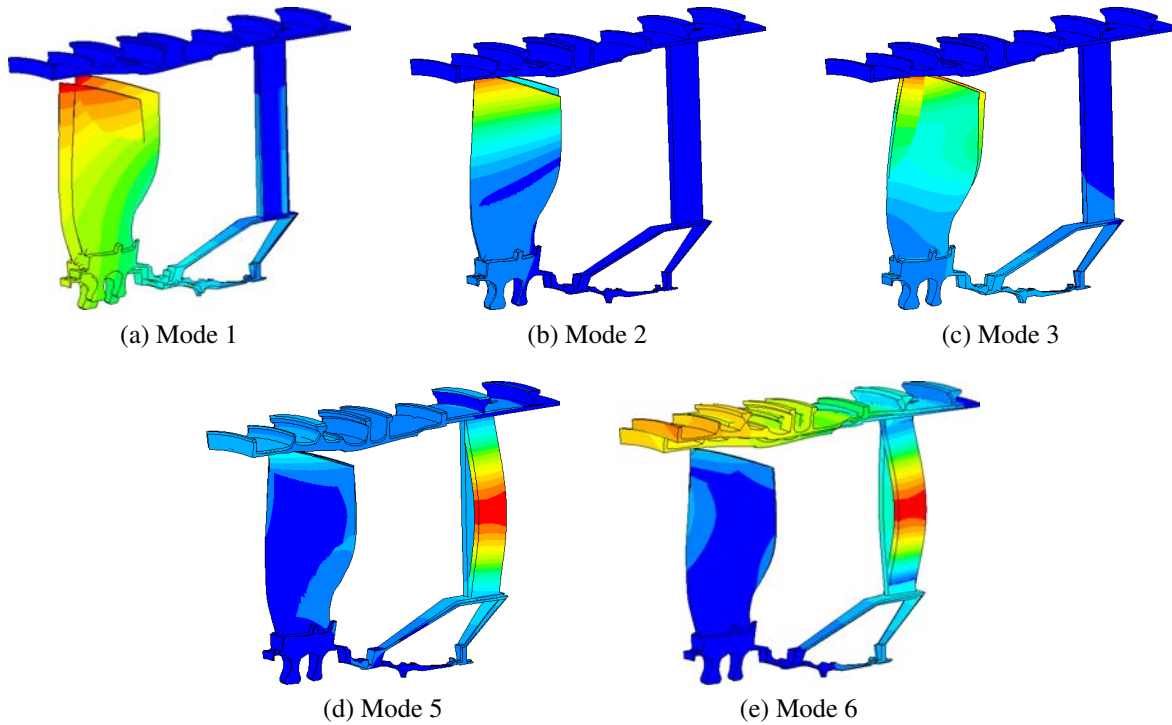


Figure 3.16: Mode shapes of bladed-disk/casing coupled model: harmonic $n_d = 1$

each subcomponent⁵ of the fan stage depicted in Fig. 3.11. For the j -th mode, the modal strain energy can be decomposed as $SE^{\text{tot}} = SE^{\text{bd}} + SE^{\text{c}} + SE^{\text{f}}$, hence, the following relation is obtained:

$$\begin{pmatrix} \mathbf{u}_j^{\text{bd}} \\ \mathbf{u}_j^{\text{c}} \\ \mathbf{u}_j^{\text{f}} \end{pmatrix}^{\text{T}} \Lambda \begin{pmatrix} \mathbf{u}_j^{\text{bd}} \\ \mathbf{u}_j^{\text{c}} \\ \mathbf{u}_j^{\text{f}} \end{pmatrix} = \begin{pmatrix} \mathbf{u}_j^{\text{bd}} \\ \mathbf{0} \\ \mathbf{0} \end{pmatrix}^{\text{T}} \Lambda \begin{pmatrix} \mathbf{u}_j^{\text{bd}} \\ \mathbf{0} \\ \mathbf{0} \end{pmatrix} + \begin{pmatrix} \mathbf{0} \\ \mathbf{u}_j^{\text{c}} \\ \mathbf{0} \end{pmatrix}^{\text{T}} \Lambda \begin{pmatrix} \mathbf{0} \\ \mathbf{u}_j^{\text{c}} \\ \mathbf{0} \end{pmatrix} + \begin{pmatrix} \mathbf{0} \\ \mathbf{0} \\ \mathbf{u}_j^{\text{f}} \end{pmatrix}^{\text{T}} \Lambda \begin{pmatrix} \mathbf{0} \\ \mathbf{0} \\ \mathbf{u}_j^{\text{f}} \end{pmatrix} \quad (3.26)$$

where Λ is a diagonal matrix containing the system eigenvalues and \mathbf{u}_j are the modal displacements associated to the j -th mode.

The results are plotted in the veering diagram 3.17, where the color of each bullet is proportional to its energy content. The first four modal families of the veering diagram 3.7a corresponding to the bladed-disk alone are included for comparison purposes.

For $n_d > 1$, it can be seen in this figure how bladed-disk modes—represented in red—are unchanged by the presence of the frame and casing, but for $n_d = 0$ and $n_d = 1$ a drop in frequency is generally produced by the change in the shaft boundary conditions, *i.e.* the flexibility of the supports compared to the clamped boundary conditions imposed in section 3.3 tends to decrease the $n_d = 1$ frequencies. The shaft bending

⁵Superscripts ^{bd,c} and ^f denote the bladed-disk, casing and frame respectively.

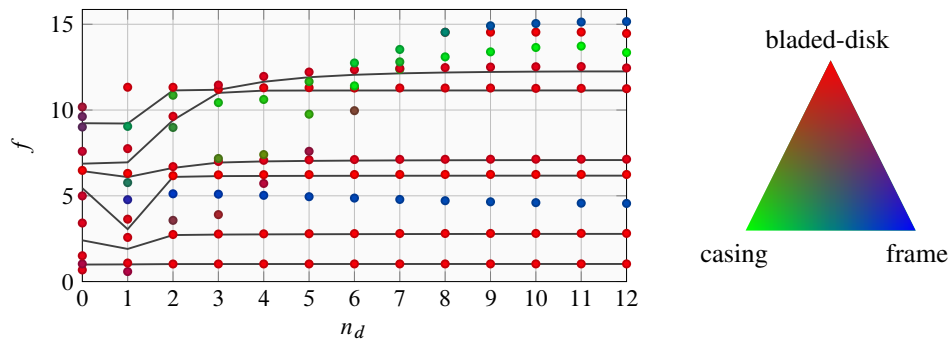


Figure 3.17: Veering diagram and strain energy distribution along components

modes are coupled to $n_d = 1$ bladed-disk modes, while for $n_d = 0$, the shaft longitudinal displacements may be coupled to bladed-disk modes. For instance, the $n_d = 1$ of the 1F family is now highly coupled with the frame and exhibits an important whirling component (c.f. Fig. 3.16a).

With the current frame structural characteristics, the first family of frame modes lies between the 2F and 1T modal families of the bladed-disk. Also, casing modes appear at higher frequencies, are generally uncoupled from the bladed-disk but are coupled to the frame.

3.4.2. Rotating bladed-disk

In order to account for the bladed-disk rotation, the casing/frame system is separated from the bladed-disk depicted in Fig. 3.11a and includes the flexibility of the bearings coupling through an array of linear springs. In this sense, the two independent sub-components are represented in Fig. 3.18, where the coupling at the

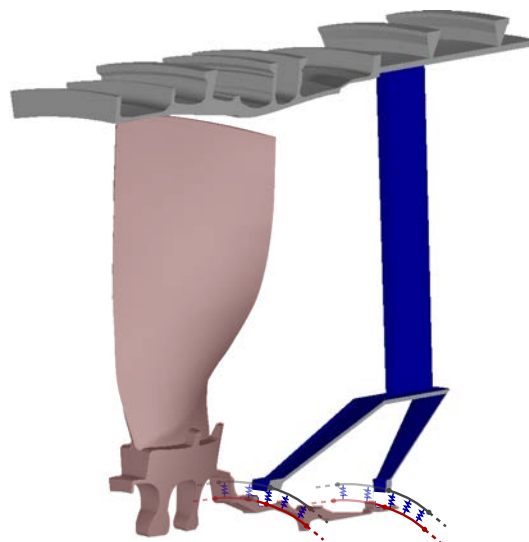


Figure 3.18: Coupled bladed-disk casing model with flexible bearings

shaft/bearings interface is highlighted.

Accordingly, mass and stiffness matrices are extracted for both sub-structures, which are reduced using Craig-Bampton component mode synthesis, as detailed in a cyclic-symmetric framework in [Mei+13] and briefly described in section 2.2.2. Three nodes are kept in the reduced space for each system elementary sector, carefully positioned at the shaft/bearings interface as well as at the blade-tip LE and corresponding casing location. As detailed in the following, these physical displacements will serve for the calculation of the shaft whirling orbits at each bearing and the correspondent blade-to-casing distances, for a proper characterization of the potential contact scenarios associated to the investigated coupled modes while accounting for the bladed-disk rotation.

Hence, the governing equations of motions of the free and conservative system are written in the reduced-order basis as:

$$\begin{bmatrix} \mathbf{M}^c & \mathbf{0} \\ \mathbf{0} & \mathbf{M}^{bd} \end{bmatrix} \begin{pmatrix} \ddot{\mathbf{x}}^c \\ \ddot{\mathbf{x}}^{bd} \end{pmatrix} + \left[\begin{bmatrix} \mathbf{K}^c & \mathbf{0} \\ \mathbf{0} & \mathbf{K}^{bd} \end{bmatrix} + \mathbf{K}^* \right] \begin{pmatrix} \mathbf{x}^c \\ \mathbf{x}^{bd} \end{pmatrix} = \begin{pmatrix} \mathbf{0} \\ \mathbf{0} \end{pmatrix} \quad (3.27)$$

where \mathbf{x} and $\ddot{\mathbf{x}}$ are the displacement and acceleration vectors respectively, \mathbf{M} stores the mass matrices and the stiffness matrix \mathbf{K} stores uncoupled blocks \mathbf{K}^{bd} and \mathbf{K}^c corresponding to each structure⁶, and a coupling term \mathbf{K}^* reflecting the stiffness of the bearings whose derivation is the focus of the next section.

3.4.2.1. Flexible bearings model

The flexibility of the bearing rolling elements is incorporated in the model through an array of linear springs, which are illustrated in Fig. 3.18. This differs from the approach in [PTC14] where they are represented by a pair of simple isotropic springs. As detailed in the following, the added complexity in the bearings model introduces time-dependent periodic terms in the stiffness matrix due to the rotation.

As detailed in previous sections, 1-nodal diameter bladed-disk modes are the only modes potentially exhibiting off-axis shaft motions and participating in the coupling with the casing through the bearings. Hence, it is proposed to explicitly derive the coupling matrix \mathbf{K}^* of Eq. (3.27) in a reduced-order modal space, limiting the bladed-disk distortions to a specific set of modes: the rigid-body off-axis translations and the first 1-nodal diameter flexural mode (1F) pictured in Fig. 3.19a, which feature non-negligible shaft motions. For the casing/frame sub-components, all nodal diameters actually participate in the coupling and should be retained to obtain a general version of matrix \mathbf{K}^* . However, as a first approximation, it is proposed to solely consider its first 1-nodal diameter mode, which exhibits major distortions at the shaft/bearing interface as displayed in Fig. 3.19b.

⁶It should be noted that the block \mathbf{K}^{bd} is dependent on the rotational speed if centrifugal effects are accounted for.

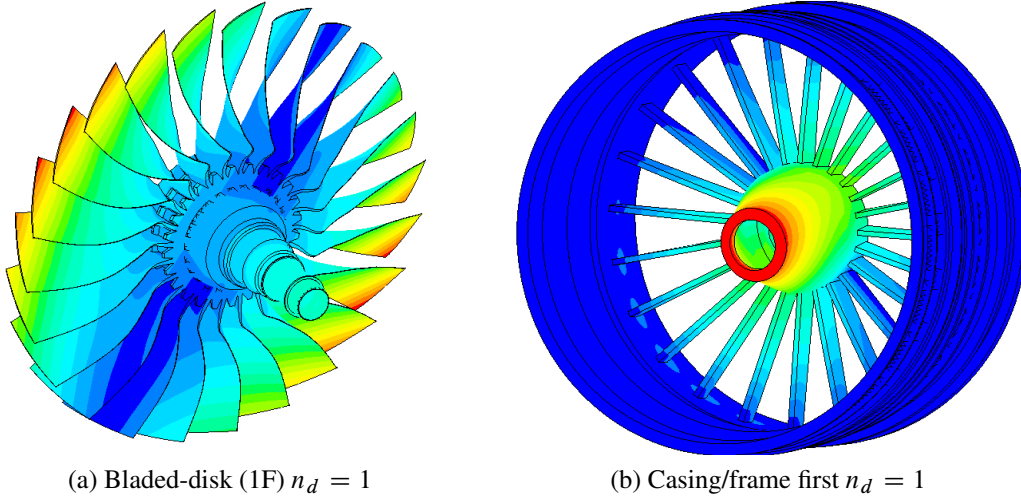


Figure 3.19: Free vibration mode-shapes of bladed-disk and casing/frame components

In this way, the projection of the physical displacements into the reduced-order modal basis is achieved through the change of variable:

$$\mathbf{x} = \tilde{\mathbf{V}}\tilde{\mathbf{u}} \quad \text{with} \quad \tilde{\mathbf{u}}^T = (v_c, v_s, u_c, u_s, u_{c_0}, u_{s_0}) \quad \text{and} \quad \tilde{\mathbf{V}} = \begin{bmatrix} \tilde{\mathbf{V}}^c & \mathbf{0} \\ \mathbf{0} & \tilde{\mathbf{V}}^{\text{bd}} \end{bmatrix} \quad (3.28)$$

where the truncated set of modes correspond to: the translational rigid body modes of the bladed-disk (u_{c_0}, u_{s_0}), the first flexural 1-nodal diameter modes of the bladed-disk (u_c, u_s) and the first 1-nodal diameter modes of the casing/frame (v_c, v_s).

Therefore, as adopted in [LST07], the resulting reduced-order model can be represented by the two coupled elastic rings pictured in Fig. 3.20 and leads to the following assumed displacement fields:

$$u^{\text{bd}}(\alpha, t) = (u_c(t) + u_{c_0}(t)) \cos \alpha + (u_s(t) + u_{s_0}(t)) \sin \alpha \quad (3.29a)$$

$$v^c(\theta, t) = v_c(t) \cos \theta + v_s(t) \sin \theta \quad (3.29b)$$

where the displacements $u^{\text{bd}}(\alpha, t)$ and $v^c(\theta, t)$ correspond to the bladed-disk and the casing respectively, with $\theta \in [0; 2\pi]$ and $\alpha = \theta - \Omega t$. The gap between the two structures $g(\theta, t)$ is expressed as:

$$g(\theta, t) = \delta + v_c(t) \cos \theta + v_s(t) \sin \theta - (u_c(t) + u_{c_0}(t)) \cos(\theta - \Omega t) - (u_s(t) + u_{s_0}(t)) \sin(\theta - \Omega t) \quad (3.30)$$

where δ is the initial operating clearance. The rotational speed Ω of the bladed-disk is assumed to be constant in counter-clockwise direction and the springs coupling stiffness is denoted κ .

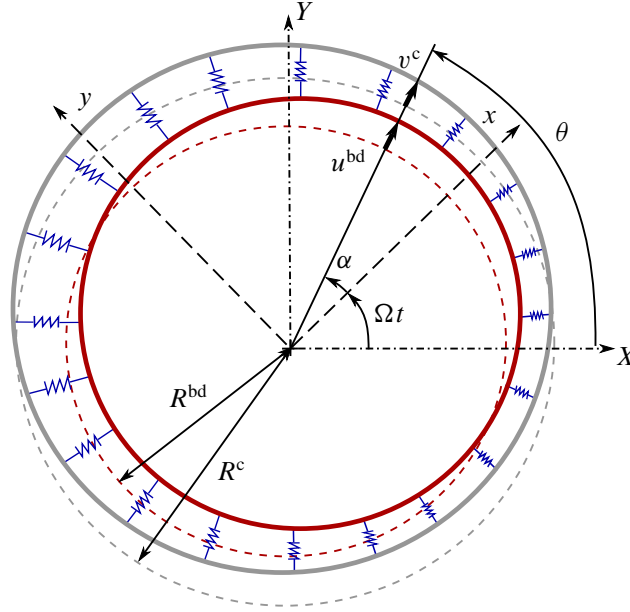


Figure 3.20: Equivalent reduced-order model of coupled bladed-disk [—] and casing/frame [---] under 1-nodal diameter distortion

From the assumed displacement forms in Eq. (3.29), Hamilton's principle is adopted to derive the associated equations of motion. The kinetic energy of the two elastic rings is:

$$T^{\text{bd}}(t) = \frac{1}{2}m_u(\dot{u}_c(t)^2 + \dot{u}_s(t)^2) + \frac{1}{2}m_o(\dot{u}_{c_o}(t)^2 + \dot{u}_{s_o}(t)^2) \quad (3.31a)$$

$$T^c(t) = \frac{1}{2}m_v(\dot{v}_c(t)^2 + \dot{v}_s(t)^2) \quad (3.31b)$$

and the corresponding strain energy is:

$$K^{\text{bd}}(t) = \frac{1}{2}k_u(u_c(t)^2 + u_s(t)^2) + \frac{1}{2}k_o(u_{c_o}(t)^2 + u_{s_o}(t)^2) \quad (3.32a)$$

$$K^c(t) = \frac{1}{2}k_v(v_c(t)^2 + v_s(t)^2) \quad (3.32b)$$

where (m_u, m_o, k_u, k_o) and (m_v, k_v) are the modal masses and stiffnesses of the bladed-disk and the casing respectively.

Also, the strain energy of the coupling stiffnesses κ arises as:

$$K^\kappa(t) = \frac{1}{2}\kappa \int_0^{2\pi} [v_c(t) \cos \theta + v_s(t) \sin \theta - (u_c(t) + u_{c_o}(t)) \cos(\theta - \Omega t) - (u_s(t) + u_{s_o}(t)) \sin(\theta - \Omega t)]^2 d\theta \quad (3.33)$$

Accordingly, the following stiffness matrix is obtained in the modal coordinates:

$$\begin{aligned}
\tilde{\mathbf{K}}(\Omega, t) &= \tilde{\mathbf{K}} + \tilde{\mathbf{K}}^*(\Omega, t) \\
&= \tilde{\mathbf{V}}^T \mathbf{K} \tilde{\mathbf{V}} + \tilde{\mathbf{K}}^*(\Omega, t) \\
&= \begin{bmatrix} \omega_v^2 + \epsilon_v & 0 & -\epsilon_u c\beta & \epsilon_u s\beta & -\epsilon_u c\beta & \epsilon_u s\beta \\ 0 & \omega_v^2 + \epsilon_v & -\epsilon_u s\beta & -\epsilon_u c\beta & -\epsilon_u s\beta & -\epsilon_u c\beta \\ -\epsilon_v c\beta & -\epsilon_v s\beta & \omega_u^2 + \epsilon_u & 0 & 0 & 0 \\ \epsilon_v s\beta & -\epsilon_v c\beta & 0 & \omega_u^2 + \epsilon_u & 0 & 0 \\ -\epsilon_v c\beta & -\epsilon_v s\beta & 0 & 0 & \omega_o^2 + \epsilon_u & 0 \\ \epsilon_v s\beta & -\epsilon_v c\beta & 0 & 0 & 0 & \omega_o^2 + \epsilon_u \end{bmatrix} \quad (3.34)
\end{aligned}$$

with $c\beta = \cos \Omega t$ and $s\beta = \sin \Omega t$, $\omega_u^2 = k_u/m_u$, $\omega_o^2 = k_o/m_o$ and $\omega_v^2 = k_v/m_v$. The normalized coupling terms⁷ become $\epsilon_u = \kappa/m_u = \kappa/m_o$ and $\epsilon_v = \kappa/m_v$, and the resulting stiffness matrix—symmetric only under the condition that $m_v = m_u = m_o$ —has time-periodic coefficients. This matrix is the sum of the uncoupled stiffness matrices projected onto the reduced-order modal basis and the bearings coupling matrix, which contains the time-dependent terms. It should be noted that the modal stiffness of the rigid body modes ω_o vanishes but is kept in the formulation for the sake of generality. Hence, the equations of motion (3.27) of the free and conservative system are written in the reduced-order modal basis as:

$$\ddot{\tilde{\mathbf{u}}} + \tilde{\mathbf{K}}(\Omega, t)\tilde{\mathbf{u}} = \mathbf{0} \quad (3.35)$$

In order to explore the modal properties of the coupled structures described by Eq. (3.35), which is a type of Mathieu equation, the time-periodic coefficients of the stiffness matrix defined in Eq. (3.34) can be advantageously transformed into time-independent terms through the change of variable suggested in [Sha01]:

$$\begin{pmatrix} v_c \\ v_s \\ u_c \\ u_s \\ u_{c_o} \\ u_{s_o} \end{pmatrix} = \begin{bmatrix} 0 & 0 & 0 & 0 & s\beta' & c\beta' \\ 0 & 0 & 0 & 0 & -c\beta' & s\beta' \\ 0 & 0 & s\beta' & -c\beta' & 0 & 0 \\ 0 & 0 & c\beta' & s\beta' & 0 & 0 \\ s\beta' & -c\beta' & 0 & 0 & 0 & 0 \\ c\beta' & s\beta' & 0 & 0 & 0 & 0 \end{bmatrix} \begin{pmatrix} q_1 \\ q_2 \\ q_3 \\ q_4 \\ q_5 \\ q_6 \end{pmatrix} \quad (3.36)$$

with $c\beta' = \cos \frac{\Omega t}{2}$ and $s\beta' = \sin \frac{\Omega t}{2}$, corresponding to a change of frame at a rotation of half the rotational speed. Therefore, this change of variable—which is not available for most Mathieu equations [Sha01]—

⁷In the projection onto the modal space, the eigenvectors are generally normalized with respect to the mass matrix, hence the corresponding modal masses are unitary and the coupling terms would simply become $\epsilon_u = \epsilon_v = \kappa$.

implies:

$$\tilde{\mathbf{u}}(t) = \mathbf{P}(t)\mathbf{q}(t) \quad (3.37a)$$

$$\dot{\tilde{\mathbf{u}}}(t) = \dot{\mathbf{P}}(t)\mathbf{q}(t) + \mathbf{P}(t)\dot{\mathbf{q}}(t) \quad (3.37b)$$

$$\ddot{\tilde{\mathbf{u}}}(t) = \ddot{\mathbf{P}}(t)\mathbf{q}(t) + 2\dot{\mathbf{P}}(t)\dot{\mathbf{q}}(t) + \mathbf{P}(t)\ddot{\mathbf{q}}(t) \quad (3.37c)$$

and leads to the following transformed equation of motion with constant coefficients:

$$\begin{pmatrix} \ddot{q}_1 \\ \ddot{q}_2 \\ \ddot{q}_3 \\ \ddot{q}_4 \\ \ddot{q}_5 \\ \ddot{q}_6 \end{pmatrix} + \begin{bmatrix} 0 & \Omega & 0 & 0 & 0 & 0 \\ -\Omega & 0 & 0 & 0 & 0 & 0 \\ 0 & 0 & 0 & \Omega & 0 & 0 \\ 0 & 0 & -\Omega & 0 & 0 & 0 \\ 0 & 0 & 0 & 0 & 0 & \Omega \\ 0 & 0 & 0 & 0 & -\Omega & 0 \end{bmatrix} \begin{pmatrix} \dot{q}_1 \\ \dot{q}_2 \\ \dot{q}_3 \\ \dot{q}_4 \\ \dot{q}_5 \\ \dot{q}_6 \end{pmatrix} + \begin{bmatrix} \Delta_o & 0 & \epsilon & 0 & \epsilon & 0 \\ 0 & \Delta_o & 0 & \epsilon & 0 & \epsilon \\ \epsilon & 0 & \Delta_u & 0 & \epsilon & 0 \\ 0 & \epsilon & 0 & \Delta_u & 0 & \epsilon \\ \epsilon & 0 & \epsilon & 0 & \Delta_v & 0 \\ 0 & \epsilon & 0 & \epsilon & 0 & \Delta_v \end{bmatrix} \begin{pmatrix} q_1 \\ q_2 \\ q_3 \\ q_4 \\ q_5 \\ q_6 \end{pmatrix} = \begin{pmatrix} 0 \\ 0 \\ 0 \\ 0 \\ 0 \\ 0 \end{pmatrix} \quad (3.38)$$

with, $\Delta_o = \omega_o^2 + \epsilon - \frac{\Omega^2}{4}$, $\Delta_u = \omega_u^2 + \epsilon - \frac{\Omega^2}{4}$, $\Delta_v = \omega_v^2 + \epsilon - \frac{\Omega^2}{4}$, and $\epsilon = \epsilon_u = \epsilon_v$ is the normalized coupling stiffness considering that $m_u = m_v = m_o$.

Thus, Eq. (3.38) is written in a compact form as:

$$\ddot{\mathbf{q}}(t) + \mathbf{G}(\Omega)\dot{\mathbf{q}}(t) + \mathbf{K}(\Omega)\mathbf{q}(t) = \mathbf{0} \quad (3.39)$$

corresponding to a set of second-order linear ODE with constant coefficients with:

$$\mathbf{P}^{-1}\mathbf{P} = \mathbf{I}_6, \quad \mathbf{G}(\Omega) = 2\mathbf{P}^{-1}\dot{\mathbf{P}} \quad \text{and} \quad \mathbf{K}(\Omega) = \mathbf{P}^{-1}\ddot{\mathbf{P}} + \mathbf{P}^{-1}\tilde{\mathbf{K}}(\Omega, t)\mathbf{P} \quad (3.40)$$

and for which a stability analysis of the equilibrium solution $\mathbf{q} = \mathbf{0}$ becomes straightforward [Mei80].

3.4.2.2. Stability analysis and mode types

First, Eq. (3.39) is expressed in its state-space form:

$$\dot{\mathbf{z}}(t) + \mathbf{A}(\Omega)\mathbf{z} = \mathbf{0} \quad \text{with} \quad \mathbf{z} = \begin{pmatrix} \mathbf{q} \\ \dot{\mathbf{q}} \end{pmatrix} \quad \text{and} \quad \mathbf{A}(\Omega) = \begin{bmatrix} \mathbf{0} & -\mathbf{I}_6 \\ \mathbf{K}(\Omega) & \mathbf{G}(\Omega) \end{bmatrix} \quad (3.41)$$

The stability of the fixed-point is then addressed through Floquet theory [Mei80] by calculating the eigenvalues of the transformation matrix $\mathbf{A}(\Omega)$ in Eq. (3.41). For a pair (Ω, κ) , the equilibrium position becomes unstable when one of the eigenvalues show a strictly positive real part.

The stability chart of Fig. 3.21 is computed with respect to κ and Ω , as the modal properties of the bladed-disk and casing are not considered as variables: unstable responses are represented in red, the color

being proportional to the magnitude of the associated eigenvalue real part. Two unstable zones, denoted A and B, are distinguished in this figure. These emanate from the linearly predicted modal coincidence speeds

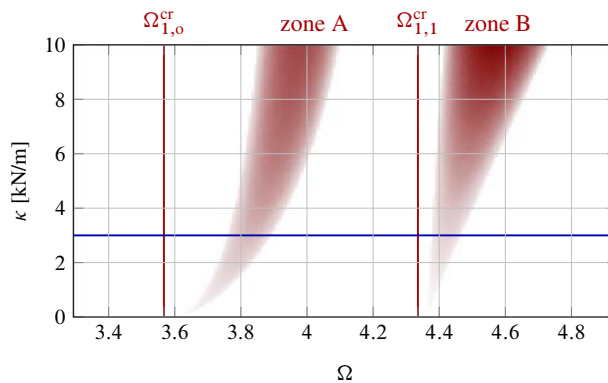


Figure 3.21: Stability analysis: [■] unstable configurations

obtained via Eq. (2.18), that correspond to the coupling of the casing modes with the rigid body modes ($\Omega_{1,0}^{cr} = \omega_v + \omega_o = \omega_v$) and the 1-nodal diameter modes ($\Omega_{1,1}^{cr} = \omega_v + \omega_u$) of the bladed-disk respectively.

As detailed in [Sha01], this instability is a parametric resonance which depends on Ω and κ as well as the eigenvalues of both bladed-disk and casing. It is worth noticing that co-rotating modes do not yield unstable configurations and that the range of the associated unstable rotational speeds appears to increase with κ , with a shift in the first unstable configuration due to the added stiffness. It appears that the casing/frame first eigenfrequency ω_v is the main parameter controlling the position of the attained critical speeds $\Omega_{1,0}^{cr}$ and $\Omega_{1,1}^{cr}$, thus suggesting that structural changes can be applied to the casing in order to increase its modal stiffness and shift the detected unstable configurations out of the engine operating speed range. This is indeed the case for the considered industrial models, as detected instabilities arise well beyond the maximal operating speed of the engine, which is about $\Omega = 1.55$.

For the chosen coupling stiffness $\kappa = 3000$ N/m represented in Fig. 3.21, the evolution of the eigenvalues real and imaginary parts with respect to the rotational speed is represented in Fig. 3.22, accounting or not for centrifugal stiffening⁸. It is shown in this figures that for velocities yielding unstable regimes three types of modes actually coexist: damped ($\Re(\lambda) < 0$), oscillatory ($\Re(\lambda) = 0$) and divergent ($\Re(\lambda) > 0$). Also, as expected from the stability analysis, there is a visible shift between the linearly predicted interaction speeds and the actual unstable configurations. Interestingly, the centrifugal effects appear to increase the 1F frequency so drastically that it avoids the 1F backward mode to reach a forward motion. Hence, in the sense of Eq. (2.18) [Sch97], the waves speeds of the bladed-disk and the casing no longer coincide and the resulting coupled modes remain oscillatory throughout the entire speed range. Further, as mentioned

⁸When centrifugal loads are accounted for, the bladed-disk eigenfrequencies ω_u become Ω -dependent.

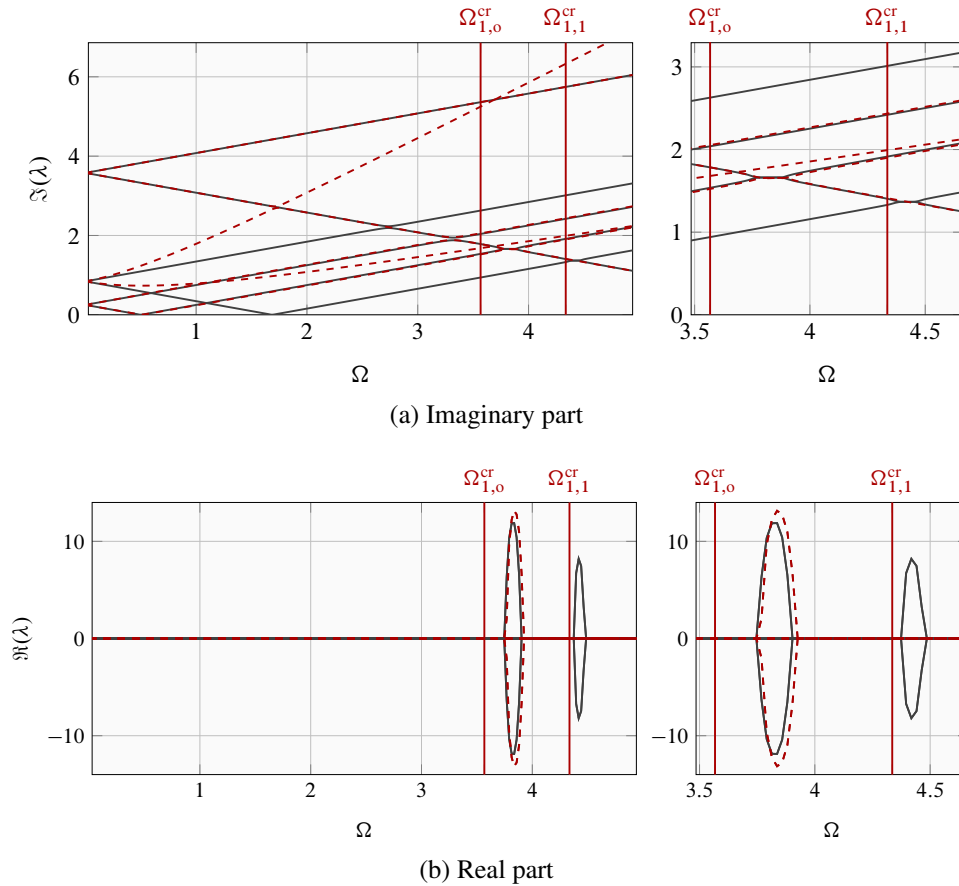


Figure 3.22: Eigenvalues for $\kappa = 3000$ N/m: with [---] and without [—] centrifugal stiffening

above, the crossings of co-rotating modes, which appear at lower rotational speeds, do not yield unstable configurations.

3.4.2.3. Coupled modes visualization and contact initiation

To obtain a visual representation of the bladed-disk/casing system coupled modes, the resulting modal displacements in the time-invariant modal space must be recast into the original physical space. In this sense, for a given pair of (κ, Ω) , a complex modal analysis of the transformation matrix \mathbf{A} in Eq. (3.41) is carried out. For the k -th mode, the obtained modal displacements may thus be expressed as:

$$\mathbf{q}(t) = Q_0 \exp(\alpha_k t) [\Re(\mathbf{v}_k) \cos(\omega_k t) - \Im(\mathbf{v}_k) \sin(\omega_k t)] \quad (3.42)$$

where $\omega_k = \Im(\lambda_k)$ and $\alpha_k = \Re(\lambda_k)$ correspond to the complex eigenvector \mathbf{v}_k .

The modal solution (3.42) is projected into its associated $\tilde{\mathbf{u}}$ coordinates by means of Eq. (3.36). These are finally recast into the initial physical space \mathbf{x} through the modeshapes of the uncoupled structures $\tilde{\mathbf{V}}$

in Eq. (3.28), in order to obtain the corresponding bladed-disk and casing modal displacements. This is of particular interest for the appropriate characterization of the contact initiation: direction of contact with respect to the shaft displacement and types of waves traveling along the casing and the bladed-disk.

For the divergent mode associated to the pair of parameters $\Omega = 3.8$ and $\kappa = 3000$ N/m, the procedure described above allows to obtain the divergent whirling orbits depicted in Figs. 3.23a and 3.23b. These correspond to the shaft displacements at bearing B1 and are represented in the rotating and static frames respectively, the blue arrow indicating the whirling direction. Since the direction of the rotational speed is

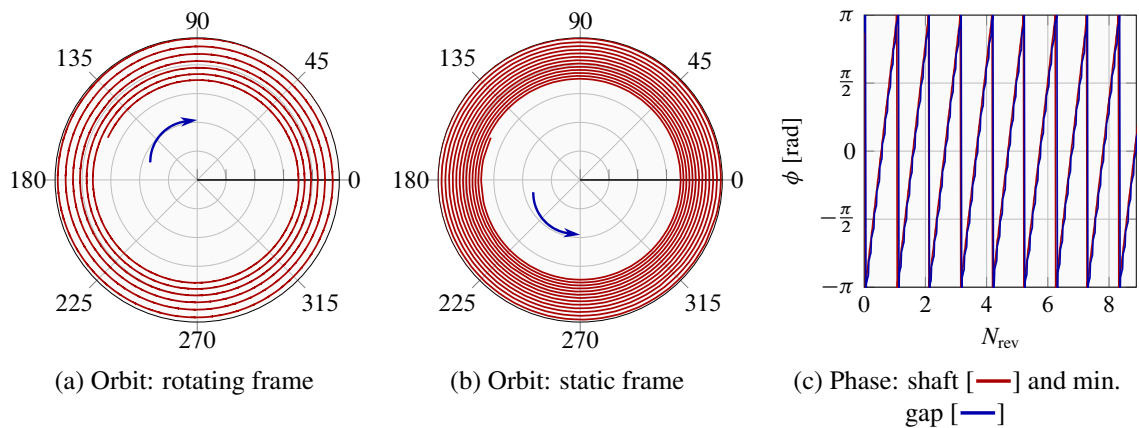


Figure 3.23: Divergent mode characteristics: $\Omega = 3.8$ and $\kappa = 3000$ N/m

counter-clockwise, the divergent mode is characterized by a backward whirling motion in the rotating frame, which translates into a forward rotating one in the static frame. The obtained displacements at bearing B2 are in perfect phase with those at B1, but are an order of magnitude smaller.

In terms of the potential contact locations, it is shown in Fig. 3.23c how the shaft displacements and the minimum blade-to-casing distances are in perfect phase. Hence, the attained divergent coupled mode is characterized by cylindrical shaft displacements of growing amplitudes which would tend to initiate contact in the same direction, thus potentially leading to backward whirling motions. A very similar behavior is observed for the other unstable configuration at $\Omega \simeq 4.4$, therefore suggesting that the parametric instabilities stemming from the bladed-disk/casing coupling could be responsible of initiating divergent modal interactions in the sense of [Sch97] and [Leg+09].

3.5. Summary

A thorough analysis of the modal features of an engine fan stage is presented, showing that the shaft can participate only in 1-nodal diameter modeshapes. A methodology to build the gyroscopic matrix is developed

within a cyclic-symmetric finite element framework: it is first validated and shows how these effects are accurately captured in the reduced-order Craig-Bampton space. It is demonstrated that a non-negligible frequency split in 1-nodal diameter modes occurs when gyroscopic terms are accounted for, in particular for the 1F modal family as the backward branch becomes parallel to the main engine order in the Campbell diagram, thus potentially leading to critical speeds that cannot be predicted without gyroscopic terms.

Further, special attention is paid to the shaft/bladed-disk/casing structural couplings, involving the fan frame and the bearings. A static analysis revealed how a mass imbalance load is prone to induce contact in the same direction as the shaft displacements, while the in-take flow loads during take-off induce a clearance closure in the direction opposite to the shaft deflection. A flexible bearings model through an array of linear springs is proposed, yielding a set of coupled ordinary differential equations with time-periodic coefficients when the rotation of the bladed-disk is incorporated. A change of frame allows to transform these equations into a time-invariant modal space, in which a linear modal analysis of the three-dimensional coupled structures exposed divergent parametric instabilities emanating from the linearly predicted modal coincidence speeds. A coupling stiffness increase not only shifts the first unstable configuration but also widens the range of critical speeds. This novel perspective enables to handle the entire fan stage as a single structure where the rotation of the bladed-disk is incorporated. It provides access to important modal features without the need of costly time-stepping solution methods.

The size of the industrial models considered in this chapter excludes reasonable computational times in the time-marching strategies implemented in the following chapters. Therefore, a simplified 2D model of the fan stage is employed in chapter 4, in order to further investigate the role of the bladed-disk/casing structural coupling in a nonlinear framework. Further, as mentioned in section 2.2.5, abrasion coatings are sprayed on casings in order to mitigate direct contact occurrences. Hence, the industrial bladed-disk presented in section 3.3 is utilized in chapter 5, where its interactions with the surrounding abrasion lining are explored.

Two-dimensional modeling of bladed-disk/casing interactions

In this chapter, a representative 2D in-plane FE-model of the fan stage is considered, accounting for both the flexibility of the shaft and the structural coupling provided by the frame and bearings. A qualitative analysis is carried out with respect to two contact initiation mechanisms: (1) an initially prescribed casing distortion and (2) a mass imbalance on the bladed-disk. As will be detailed in the following, the interactions between these two flexible structures are studied by means of a time-marching strategy similar to [Leg+09] and was published in [SBL14; SBL16].

First, the structural 2D in-plane models of the engine stage are presented. In a second section, similar than for the industrial models presented in chapter 3, the modal properties of the bladed-disk/casing system are explored, highlighting the influence of the shaft flexibility and the role of the frame/bearings coupling on the overall dynamics of the system. Lastly, the simulation procedure is introduced along with a brief analysis of convergence issues related to the implemented numerical strategy. These are followed by the results and discussion of emerging trends, mainly focusing on the types of operating regimes detected and the localization of the strain energy of the dominant modes involved in the interactions.

4.1. Structural models

4.1.1. Bladed-disk and casing models

The fan stage model in this investigation corresponds to a two-dimensional simplified version of the industrial model considered in chapter 3. It extends the one introduced in [Leg+09] and incorporates the flexibility of the shaft through two linear springs connected to the center node of the disk driving the so-called *suspension*

modes. This modeling innovation targets potential whirl motions as the blade dynamics and the in-plane motions of the shaft are now coupled.

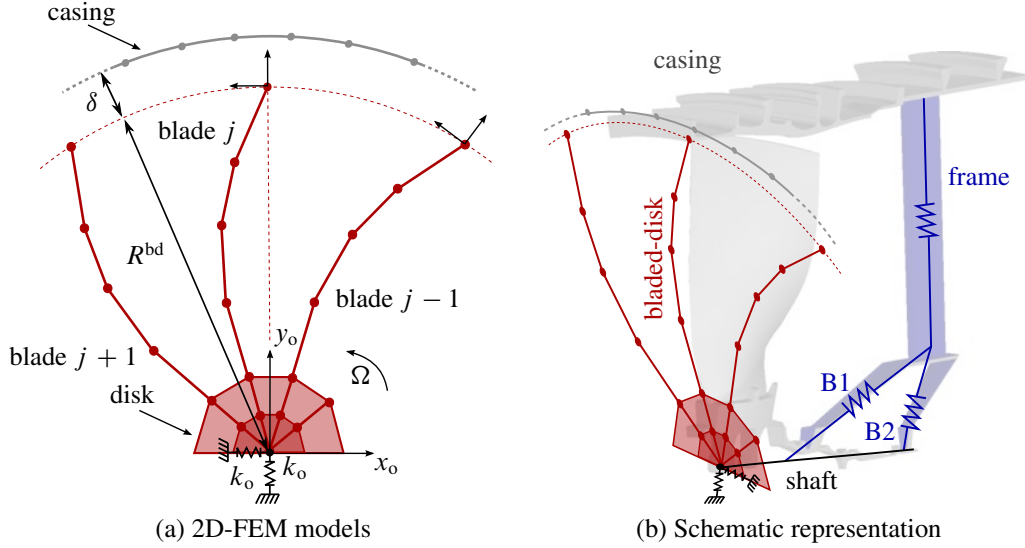


Figure 4.1: Simplified fan stage model: flexible bladed-disk and casing connected by array of springs

The bladed-disk, illustrated in Fig. 4.1a, is composed of an assembly of straight beams. Each element has two nodes with three degrees of freedom (DoF) per node and is a combination of simple Bernoulli beams (flexural displacements) and rod elements (longitudinal displacements), allowing to account for both radial and tangential displacements. As in [Leg+09], the model consists of 22 blades, with radius of $R^{\text{bd}} = 0.5$ m and ten elements per blade, as well as a dedicated set of beams representing the disk and allowing the structural coupling between neighboring blades. The stiffness of the center node linear springs is arbitrarily chosen to $k_o = 3.4 \times 10^7$ N/m, which corresponds to about 500 times the tangential stiffness of a blade and is representative of the industrial fan introduced in section 3.3.

The casing, also depicted in Fig. 4.1a, is built using a set of curved beams (40 elements). These elements have two nodes and four DoF per node, leading to a total of 160 DoF. Its radius is defined by the radius of the bladed-disk plus an initial clearance δ arbitrarily prescribed: $R^c = R^{\text{bd}} + \delta$.

The considered material is steel for both structures and the equations of motion governing the dynamics of the system, similar to Eq. (3.27), are:

$$\begin{bmatrix} \mathbf{M}^c & \mathbf{0} \\ \mathbf{0} & \mathbf{M}^{\text{bd}} \end{bmatrix} \begin{pmatrix} \ddot{\mathbf{x}}^c \\ \ddot{\mathbf{x}}^{\text{bd}} \end{pmatrix} + \begin{bmatrix} \mathbf{D}^c & \mathbf{0} \\ \mathbf{0} & \mathbf{D}^{\text{bd}} \end{bmatrix} \begin{pmatrix} \dot{\mathbf{x}}^c \\ \dot{\mathbf{x}}^{\text{bd}} \end{pmatrix} + \left[\begin{bmatrix} \mathbf{K}^c & \mathbf{0} \\ \mathbf{0} & \mathbf{K}^{\text{bd}} \end{bmatrix} + \mathbf{K}^* \right] \begin{pmatrix} \mathbf{x}^c \\ \mathbf{x}^{\text{bd}} \end{pmatrix} = \begin{pmatrix} \mathbf{f}_{\text{ext}}^c \\ \mathbf{f}_{\text{ext}}^{\text{bd}} \end{pmatrix} + \begin{bmatrix} \mathbf{B}^c \\ \mathbf{B}^{\text{bd}} \end{bmatrix} \mathbf{f}_{\text{cn}} \quad (4.1)$$

that is, in a compact form:

$$\mathbf{M}\ddot{\mathbf{x}} + \mathbf{D}\dot{\mathbf{x}} + \mathbf{K}\mathbf{x} = \mathbf{f}_{\text{ext}} + \mathbf{B}\mathbf{f}_{\text{cn}} \quad (4.2)$$

where \mathbf{x} is the n -dimensional displacement vector, \mathbf{M} is the mass matrix as defined in Eq. (2.2) and \mathbf{D} is the damping matrix, here computed from the modal domain. As detailed in section 3.4.2.1, the stiffness matrix \mathbf{K} stores uncoupled blocks corresponding to each structure and a coupling term \mathbf{K}^* reflecting the stiffness of the bearings, denoted B1 and B2, and the fan frame depicted in Fig. 4.1b. Finally, \mathbf{f}_{ext} stores the prescribed external loads and \mathbf{f}_{cn} stores the contact forces which couple the two underlying linear systems through the unilateral and frictional contact constraints matrices \mathbf{B} .

4.1.2. Craig-Bampton model reduction

In order to gain computational efficiency while capturing the essential dynamic response, the bladed-disk dynamics is reduced through the Craig-Bampton component mode synthesis method [CB68] briefly described in section 2.2.2. Both radial and tangential DoF of every blade-tip are kept in the reduced model for the enforcement of unilateral and frictional constraints, as well as the two DoF from the center node in order to have direct access to the shaft displacements. The remaining DoF are reduced to η modal participations \mathbf{q}_{cb} controlling the accuracy of the reduction basis¹. As for the casing, it is not reduced in this investigation and all 40 nodes are considered for contact treatment.

4.1.3. Bearings and frame coupling methodology

Contrary to the assumptions made in [SBL14], where the bladed-disk and the casing are considered to be independent structures solely coupled by the unilateral and frictional contact constraints, as displayed in Fig. 4.1b, the structural couplings provided by the fan frame and bearings are accounted for in the present study. These two components are incorporated in the model through an array of linear springs. As detailed in section 3.4.2.1, the coupling matrix \mathbf{K}^* of Eq. (4.1) is constructed in a reduced order modal basis, limited to the bladed-disk and casing modes exhibiting important distortions at the shaft bearing interface. For the two-dimensional models here considered, the modes retained in the projection correspond to: the suspension modes $(u_{\text{co}}, u_{\text{so}})$, the first flexural (1F) 1-nodal diameter modes of the bladed-disk $(u_{\text{c}}, u_{\text{s}})$ and the first 1-nodal diameter modes of the casing $(v_{\text{c}}, v_{\text{s}})$, as these modes were shown to be dominant in the interactions [SBL14].

Accordingly, the dynamics of both structures is limited to this 6-dimensional reduced-order basis in which the coupling matrix \mathbf{K}^* was explicitly derived, leading to its expression (3.34). The physical displacements are thus projected onto the modal basis through the change of variable $\mathbf{x} = \tilde{\mathbf{V}}\tilde{\mathbf{u}}$, where $\tilde{\mathbf{V}}$ contains the uncoupled eigenvectors \mathbf{V}^{bd} and \mathbf{V}^{c} , and $\tilde{\mathbf{u}}$ are the corresponding modal coordinates as established in Eq. (3.28). Thus,

¹Without any explicit notice, the structural matrices of the bladed-disk of Eq. (4.1) are the reduced version of the finite element ones in this chapter.

the equations of motions (4.2) are projected onto the reduced-order modal basis and result in the following reduced equations:

$$\ddot{\tilde{\mathbf{u}}} + \tilde{\mathbf{D}}\dot{\tilde{\mathbf{u}}} + \tilde{\mathbf{K}}(\Omega, t)\tilde{\mathbf{u}} = \tilde{\mathbf{V}}^T(\mathbf{f}_{\text{ext}} + \mathbf{B}\mathbf{f}_{\text{cn}}) \quad (4.3)$$

where the forcing terms are kept in the physical space for readability: this is where the blade-to-casing clearances and contact forces can be determined precisely. The reduced modal damping matrix $\tilde{\mathbf{D}} = \tilde{\mathbf{V}}^T\mathbf{D}\tilde{\mathbf{V}}$ is diagonal and the time-dependent stiffness matrix (3.34) must be computed at each time-step of the time-marching strategy implemented in the following.

4.2. Modal analysis of the bladed-disk/casing system

This section explores the modal properties of the introduced bladed-disk/casing system. First, a linear modal analysis of the uncoupled structures is carried out and modal coincidence critical speeds are predicted, based on the criterion (2.18). Then, similar to section 3.4.2.2, the dynamics of the coupled structures is analyzed from a modal perspective in order to understand how the frame/bearings coupling affects the overall dynamics.

4.2.1. Uncoupled structures

The modal properties of the bladed-disk and casing are now studied independently. The prediction of modal coincidence in the sense of [Sch97] and the corresponding whirling motions involved in the interactions are discussed. For the sake of confidentiality, all frequencies are normalized with respect to the bladed-disk lowest eigenfrequency.

4.2.1.1. Bladed-disk

The sensitivity of the structure mode shapes and eigenfrequencies to the flexibility of the shaft is now assessed. In agreement with the developments presented in chapter 3, Figs. 4.2 display a center node displacement for $n_d = 1$ only. Additionally, the two DoF of the center node drive the suspension modes through the linear springs connected to it. These modes arise between the first two modal families with a frequency $f_o \simeq 2.5$, as displayed in Fig. 4.3b, and have a shape similar to Fig. 4.2b thus exhibiting a major whirling component. The veering diagrams in Fig. 4.3 show a comparison of the eigenfrequencies with a free and clamped center node. Clearly, such conditions only affect the 1-nodal diameter modes of each modal family.

In summary, accounting for the flexibility of the shaft has two main consequences: it generates a shift in 1-nodal diameter eigenfrequencies as these modes can now reveal a whirling component, and it engenders the

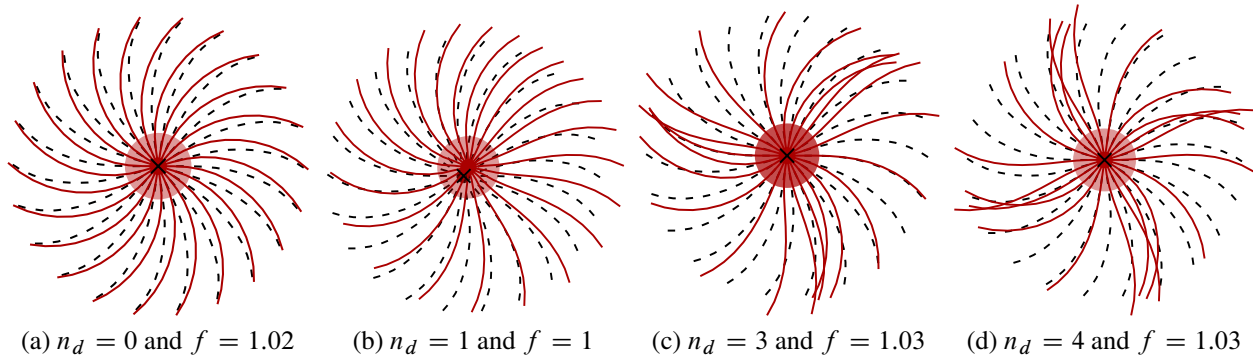


Figure 4.2: First family of free vibration modes: center node displaced [●] and rest [×] position

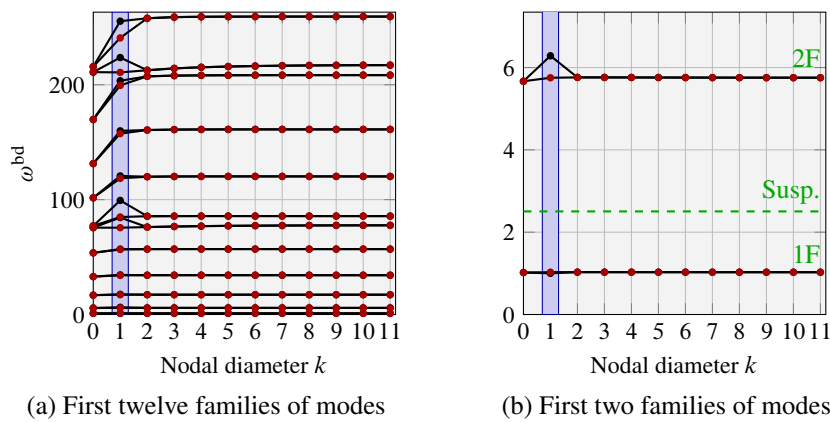


Figure 4.3: Veering diagram with clamped [●] and free [●] center node

suspension modes, similar in shape to the $n_d = 1$ (1F) mode but featuring a weaker distortion of the blades.

4.2.1.2. Modal coincidence and whirling motions

As discussed in section 2.3.1, modal coincidence occurs when traveling waves of matching nodal diameters exhibit the same propagation speed [Sch97]. The high linear blade-tip velocities make it possible to assume that sliding only occurs during contact phases. Accordingly, the waves stemming from the interactions are always counter-rotating on the rotor and co-rotating on the stator. Therefore, the linear modal coincidence criterion given in Eq. (2.18) and utilized in [BML15], allow for the prediction of critical speeds $\Omega_{n_d}^{cr}$, which are represented by the crossing of modal lines in the Campbell diagram 4.4. For the models considered in this investigation, in Fig. 4.4 several crossings occur in the rotational speed range $\Omega \in [0.7; 1.3]$ for the first family of modes, while for the second family, these crossings are spread over a larger frequency range and occur at higher rotational speeds. With regard to interactions between 1-nodal diameter modes that potentially lead to high-amplitude whirling motions, as established in [SBL14], the first flexural (1F) modal family

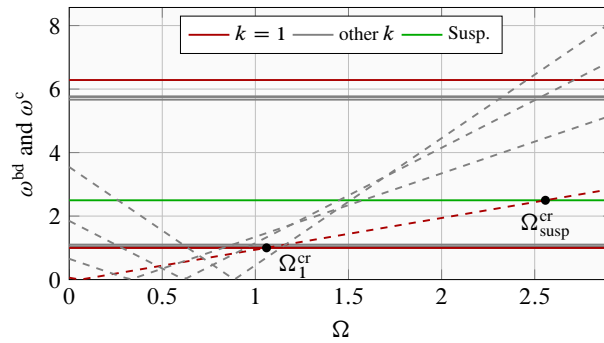


Figure 4.4: Relative frame Campbell diagram: bladed-disk [—] and casing [---]

crossing appears at $\Omega_1^{cr} \simeq 1.05$, while for the suspension modes it occurs at $\Omega_{susp}^{cr} \simeq 2.6$, which lies well beyond the operating speed range corresponding to $\Omega \in [0.6; 2]$.

According to [PTC14] and introduced in section 1.1.2, depending on the contact location with respect to the shaft displacements, either forward or backward whirling motions are likely to be excited because of the torque that frictional forces generate at the center of the bladed-disk. In this sense, by a qualitative analysis of the considered stage model two scenarios are identified:

Standard scenario Contact occurs in the direction of the shaft displacements as illustrated in Fig. 4.5a where the blue arrow indicates the shaft displacement and the blue zone, the preferred contact location. The casing distortion is of smaller magnitude than that of the bladed-disk and the frictional forces (green arrows) create a torque on the shaft which is in a direction opposite to the rotational speed, thus potentially leading to backward whirling.

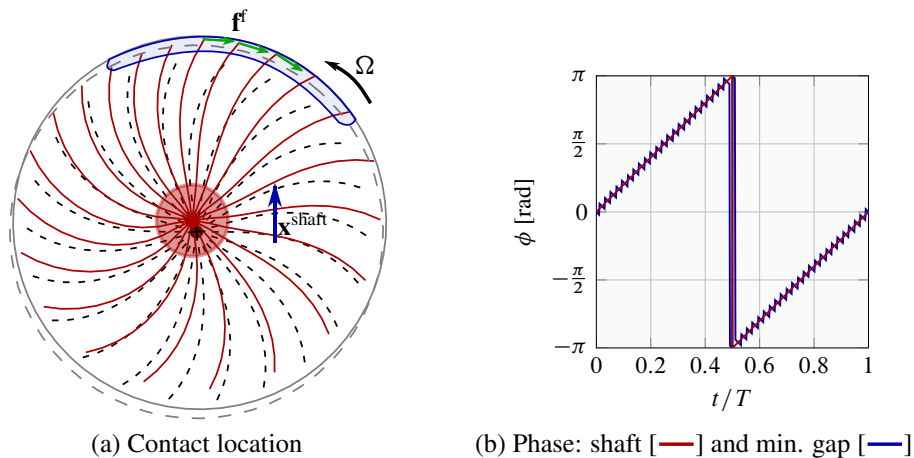


Figure 4.5: Regular contact configuration for 1-nodal diameter modes

Inverted scenario In this configuration illustrated in Fig. 4.6a, the distortion of the casing is larger than that of the bladed-disk, absorbing the blade-tip clearance in the opposite side of the shaft displacements. This potentially yields forward whirling motions since the frictional torque generated by the contact reactions is now in the direction of the rotational speed.

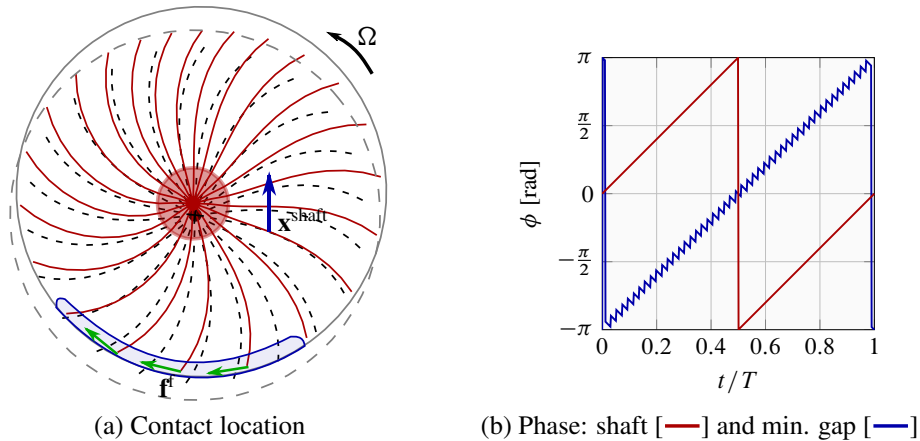


Figure 4.6: Inverted contact configuration for 1-nodal diameter modes

The particularity of the inverted scenario is that two traveling waves of opposite direction would be propagating simultaneously on the bladed-disk. Indeed, a co-rotating wave would be generated on the shaft while the frictional contact forces also produce a counter-rotating one on the blade-tips according to the permanent sliding assumption. This suggests that there exists a node of vibration along the radius of the bladed-disk for the change of sign in the traveling waves to occur, hence it is necessary that several 1-nodal diameter modes participate in the response.

For both contact configurations, the kinematic phase angle of the shaft and the shortest blade-to-casing clearance are plotted in Figs. 4.5b and 4.6b over one period of rotation. In the standard scenario, the minimum gap is always in phase with the shaft displacement, while for the inverted scenario, they are also in phase but shifted by an angle $\Delta\phi = \pi$.

4.2.2. Coupled structures

The modal properties of the coupled structures—through the bearings and frame—described in the modal subspace by Eq. (4.3) are now assessed, thereby neglecting the forcing and damping terms. Hence, the free and conservative system is of the same form as Eq. (3.35), which are exploited in the time-invariant modal space as detailed in section 3.4.2.2. In this way, the associated state-space form is written as Eq. (3.41) and the stability of the zero solution is assessed via Floquet theory [Mei80].

The stability chart in Fig. 4.7 is computed with respect to κ and Ω , as the modal properties of the bladed-disk and casing are not considered as variables: unstable responses are represented in red, the color being proportional to the magnitude of the associated eigenvalue real part. In agreement with the observations made for the industrial model in section 3.4.2.2, two unstable zones denoted A and B correspond to the coupling of the casing modes with the 1-nodal diameter bladed-disk and suspension modes respectively, where the range of the associated unstable rotational speeds increases with κ . As detailed in [Sha01] and

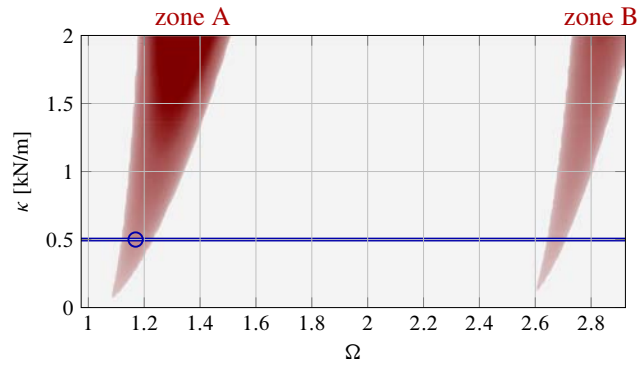


Figure 4.7: Stability analysis: [■] unstable configurations and [○] example point

mentioned in section 3.4.2.2, this instability is a parametric resonance which depends on the Ω and κ parameters considered, as well as the eigenvalues of both bladed-disk and casing. Similar to the observations made for the 3D models, it is worth noticing that co-rotating modes do not yield unstable configurations, as both unstable zones emanate from the linear modal coincidence condition (2.18) calculated in the previous section ($\Omega_1^{cr} \simeq 1.05$ and $\Omega_{susp}^{cr} \simeq 2.6$).

The stability diagram 4.7 suggests that structural changes either on the bladed-disk or on the casing can shift Ω_1^{cr} out of the operating range in order to avoid instabilities. The stiffness of the frame and bearings between the two structures not only appears to modify the band width of the predicted unstable speeds but it also introduces a shift in the first unstable configuration. The imaginary and real parts of the eigenvalues corresponding to a fixed $\kappa = 500$ N/m and a variable rotational speed are depicted in Fig. 4.8. As shown in Fig. 4.8b and consistently with the results of section 3.4.2.2, for a given pair (κ, Ω) leading to unstable motions, three types of modes actually coexist: oscillatory, damped and divergent modes.

As described in section 3.4.2.3, to obtain a visual representation of the bladed-disk/casing system coupled modes, the resulting modal displacements in the time-invariant modal space must be recast into the original physical space. This is of particular interest for the appropriate characterization of the contact initiation: direction of contact with respect to the shaft displacement and types of waves traveling along the casing and the bladed-disk.

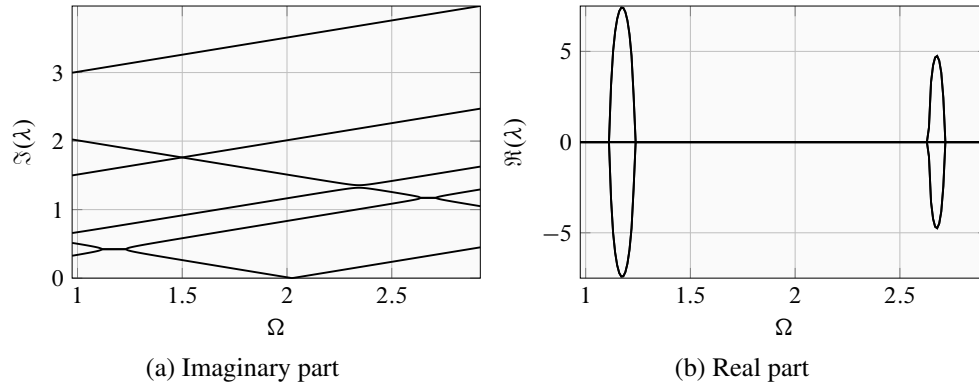


Figure 4.8: Evolution of eigenvalues of coupled structures for $\kappa = 500 \text{ N/m}$

Similar than for the industrial models, the mode considered in the projection is the divergent one, arising from the (κ, Ω) parameters represented by the circle in Fig. 4.7 that render the equilibrium solution unstable. As expected from the stability analysis and from the results in section 3.4.2.3, this divergent mode is characterized by a backward traveling wave on the bladed-disk and a forward rotating one on the casing, whose deformed shapes are displayed in Fig. 4.9 as a function of time and are similar to those of the uncoupled system illustrated in Fig. 4.5a.

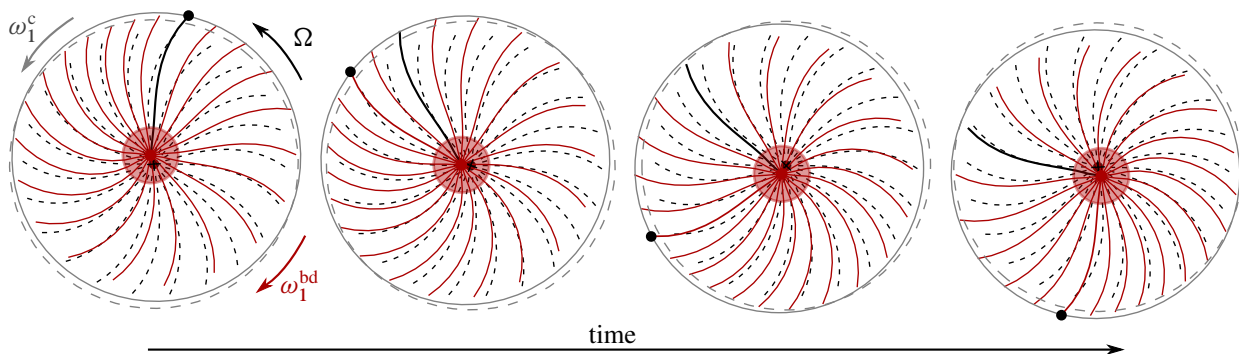


Figure 4.9: Deformed 1-nodal diameter mode shape in time

Indeed, the comparison between the shaft phase and the smallest operating clearance phase provided in Fig. 4.10c shows how the two structures vibrate in phase and how contact takes place in the same side of the shaft displacement. This contact configuration is in agreement with the kinematic predictions of linear modal coincidence given in Figs. 4.5b for the standard contact scenario. The corresponding divergent whirling orbits are depicted in Figs. 4.10a and 4.10b where the blue arrow indicates the whirling direction. It is shown how a (growing) backward traveling wave in the rotating frame translates into a (growing) forward traveling wave in the static frame because of the bladed-disk rotation. Therefore, instabilities induced by the frame/bearing flexibility might initiate interactions between the casing and bladed-disk, which potentially develop into

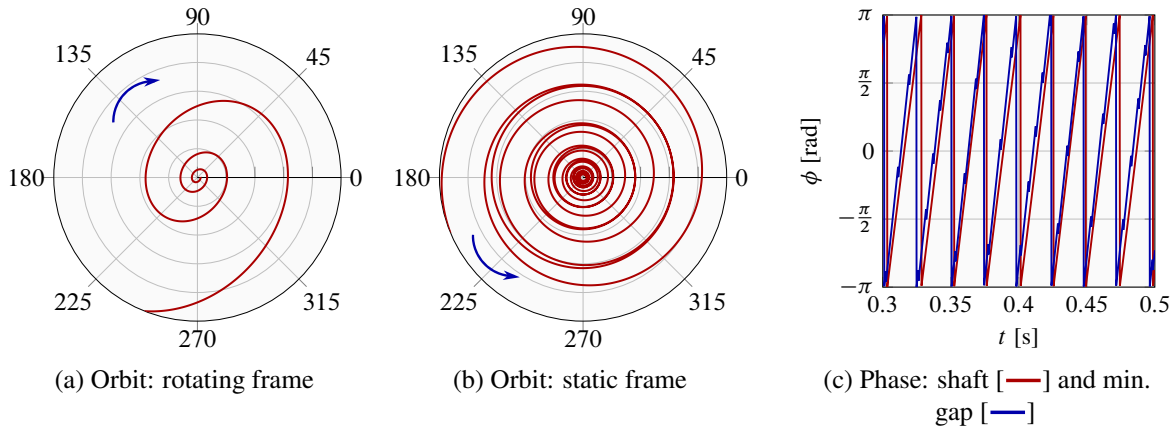


Figure 4.10: Center node motion characteristics: $\Omega = 1.17$ and $\kappa = 500$ N/m

modal interactions in the sense of [Leg+09; Sch97].

4.3. Contact simulations

As discussed in section 1.1.2, various mechanisms affect the blade-to-casing clearances while the engine is in service [LS04]. These are classified into *axisymmetric* and *asymmetric* clearance changes, the former being caused by uniform loads on both casing and rotor (*e.g.* centrifugal loads) and the latter by non-uniform loads generally acting on the stationary components (*e.g.* casing ovalization due to thermal gradients, in-take flow aerodynamic loads). In this context, two contact configurations, both leading to asymmetric clearance changes and potentially producing harmful interactions are now investigated: (1) initial casing distortion, where an external static load is applied on the casing and (2) mass imbalance on the bladed-disk.

4.3.1. Solution algorithm

The numerical procedure implemented in this investigation can be described by the following steps:

1. A perturbation is applied to the system to absorb the initial blade-tip clearance δ and initiate contact, two mechanisms are considered independently as suggested by the results of the static analysis of section 3.4.1.2:
 - The casing is statically distorted along a 1-nodal diameter shape during a short time interval; the two structures are then left free to interact.
 - A mass imbalance force is applied to the bladed-disk center.
2. Equations of motion are solved through the explicit time-marching scheme presented in section 2.2.1 and implemented in [Leg+09]. These can be treated in two bases:

- In the physical space through Eq. (4.1) as in [SBL14].
 - In the truncated modal space through Eq. (4.3), where the proposed formulation of frame/bearings coupling can be incorporated.
3. If the frame/bearings coupling is included in the formulation, the stiffness matrix given in Eq. (3.34) is calculated at each time-step.
 4. The blade-to-casing distances are calculated and when a penetration is detected, the associated contact forces \mathbf{f}_{cn} are computed using a Lagrange multipliers method in the physical space [CTK91].
 5. Friction is accounted for through a Coulomb law and sliding is assumed during contact phases.

Based on previous work [Leg+09], the solution algorithm 1 is used to compute the time response of the system.

Input:

- geometrical and mechanical properties of casing and bladed-disk
- reduction basis: η
- coupling stiffness: κ
- simulation parameters: speed range, time-step, simulation time T_{tot} ,
- perturbation for contact initiation, either:
 - casing distortion: n_d , amplitude, loading duration
 - mass imbalance: amplitude
- initial conditions

for $\Omega = \Omega_i : \Omega_f$ **do**

Initialization

for $t = 0 : T_{tot}$ **do**

if $\kappa \neq 0$ **– then**

 computation of coupling stiffness matrix;

end

 prediction of displacements (physical or modal);

 blade-tips to casing gap calculation;

if *penetration detected* **– then**

 contact forces (Lagrange multipliers);

 friction forces (Coulomb law);

if *modal truncation* **– then**

 forces projection to modal space

end

 displacements correction (physical or modal);

end

 time increment;

end

end

Output:

- bladed-disk and casing displacements (\mathbf{x}^{bd} , \mathbf{x}^c)
 - contact forces (\mathbf{f}_{cn})
-

Algorithm 1: Simulation procedure

4.3.2. Space-time discretization convergence

In order to ensure the accuracy of the results, a convergence study was carried out with regards to the spatial and temporal discretization for both contact initiation scenarios. In this sense, two parameters are of interest: the size of the reduced-order model, which is controlled by the number of static modes η kept in the reduction basis and the time-step size Δt , driving the number of iterations of the time integration procedure. The results of these convergence analyses are not presented for the sake of brevity, as these are analogous to those performed with the 3D models in section 5.3.

The nonlinearity of the contact force and the explicit nature of the time-stepping scheme make the algorithm strongly sensitive to the time-step size. Convergence is reached in displacements and contact forces for $\Delta t = 10^{-6}$ s which is preserved for all simulations performed in this chapter.

Similarly, convergence is verified for increasing η . As in [Bat+10], where the notion of *motion convergence* is introduced, asymptotic convergence is not perfectly achieved in displacements but is reached in the types of motion detected even for a small reduction basis, since the lower frequency modes have a major participation in the response. The value $\eta = 110$ is kept for the rest of the study, giving a good approximation in terms of the bladed-disk eigenfrequencies in the Craig-Bampton space when compared to those of the full FE-model, reaching a relative error lower than 0.75 % for the first five families of modes. Thus, the reduced bladed-disk model has 156 DoF.

4.3.3. Results and discussion

The nonlinear dynamics of the bladed-disk/casing system is first investigated by means of Eq. (4.2) in the full space with respect to the above-mentioned perturbation mechanisms and where the frame/bearings coupling is omitted as in [SBL14]. The system response is then considered in the reduced-order modal basis through Eq. (4.3), where the effects of the kinematic constraints imposed by the modal projection are discussed and the role of the frame/bearings coupling is addressed.

4.3.3.1. Scenario A: casing distortion excitation

The first scenario involves a casing statically distorted into a n_d -nodal diameter shape in order to absorb the initial blade-tip clearance. It is shown in [SBL14] that a casing ovalization ($n_d = 2$) generates a symmetric response on the rotor with two diametrically opposed blades exhibiting an identical response: this results into a zero displacement of the center node and is not further discussed. Instead, it is assumed that the casing distortion is along a 1-nodal diameter shape, which may be caused by aerodynamic loads at take-off [LS04]

and which seems to favor high-amplitude whirling motions as reported in [SBL14] where three motion types are predicted:

Divergent motion Vibration amplitudes increase in time, thus involving whirling orbits of growing amplitude: this is the most critical scenario from a structural standpoint.

Sustained motion Intermittent contacts lead to a shaft whirling orbit of almost constant amplitude with a radius of about the initial gap δ . This motion type is generally witnessed for rotational speeds close to critical regimes and the associated vibration amplitudes are sufficiently large to generate high-cycle fatigue issues.

Damped motion It is characterized by decreasing vibratory amplitudes in time subsequently producing a loss of contact. The interaction is limited to the transient part of the response.

Parameter	Value
simulation time	$T_{\text{tot}} = 3 \text{ s}$
coupling	$\kappa = 0 \text{ N/m}$
gap	$\delta = 1 \text{ mm}$
friction coefficient	$\mu = 0.1$
rotational speeds	$\Omega \in [0.95 ; 2] \text{ rad/s}$
casing distortion	$n_d = 1$
modal force	$F^c = 30 \text{ kN}$

Table 4.1: Simulation parameters - scenario A

The simulations are carried out considering the parameters listed in Tab. 4.1, where the structural coupling κ is set to zero. The resulting frequency response of the bladed-disk is depicted in Fig. 4.11, evaluating the center node displacements ($\mathcal{F}x_o$). The FFT is computed once the transient response is damped out. This figure features a first group of critical speeds around the linearly predicted one $\Omega_1^{\text{cf}} \simeq 1.05$ for which the highest amplitudes are reached. In general, it is shown that the dynamics is mainly driven by the first family of modes regardless of the rotational speed, with a minor contribution of the suspension modes and a negligible participation of all other modes. Other critical interactions are also detected—denoted $\Omega_{\text{nl}}^{\text{cf}}$ in Fig. 4.11—that cannot be predicted by the linear modal coincidence criterion.

The linear modal interaction at Ω_1^{cf} is further analyzed in Fig. 4.12 where the associated whirling orbits of the shaft are depicted. The interaction is characterized by a backward whirl in the rotating frame and the whirling direction is unchanged in the static frame. However, since the first eigenfrequency of the casing ω_1^c is very low and the resulting critical speed Ω_1^{cf} is very close to ω_1^{bd} , the precessional motion of the shaft is almost inexistent in the static frame as shown in Fig. 4.12b.

The spectrogram of the response is displayed in Fig. 4.13a along with the modal strain energy associated to the first family of modes, the suspension modes and the global response of the bladed-disk in Fig. 4.13b.

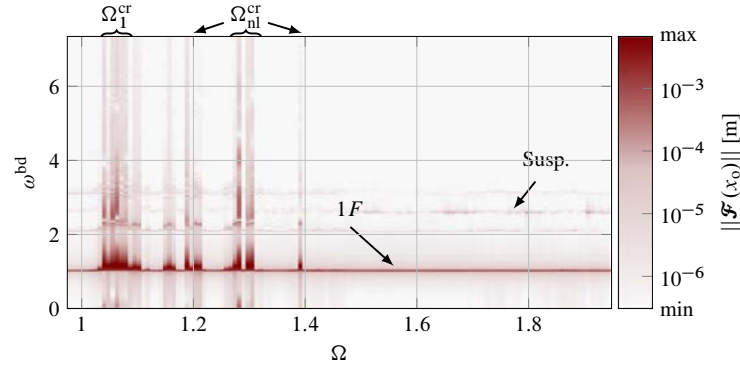


Figure 4.11: Frequency response of center node for casing distortion excitation

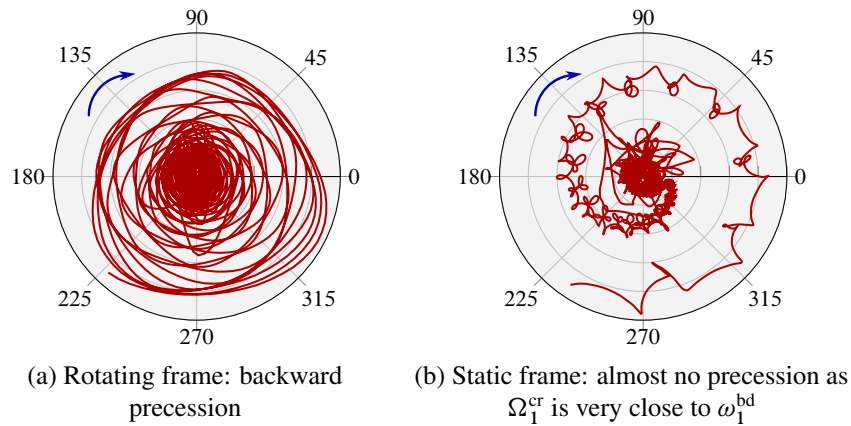


Figure 4.12: Center node orbit ($u_{r_o}^{\max} \simeq 3.6$ mm): $\Omega = 1.05$ and $\kappa = 0$ N/m. Blue arrows indicate whirling direction and the bladed-disk rotation is counter-clockwise

This energy is calculated as:

$$SE^{\text{bd}} = \frac{1}{2} \mathbf{x}^{\text{bdT}} \mathbf{K} \mathbf{x}^{\text{bd}} = \frac{1}{2} \mathbf{u}^{\text{bdT}} \mathbf{\Lambda} \mathbf{u}^{\text{bd}} \quad \text{with} \quad \mathbf{\Lambda} = \mathbf{V}^T \mathbf{K} \mathbf{V} \quad (4.4)$$

where \mathbf{u}^{bd} contains the modal contributions of specific modes² and $\mathbf{\Lambda}$ the eigenvalues associated to the eigenmodes \mathbf{V} of the system.

Spectrogram 4.13a shows how the suspension modes have a non-negligible contribution during the transient part of the response $t \in [0 \text{ s}; 0.5 \text{ s}]$ while the remaining of the response lies on the 1F modal family. This is consistent with the energy distributions in Fig. 4.13b where it is clear that the 1-nodal diameter mode is responsible for the divergence (as expected), with a very rapid growth in amplitude after $t = 1.8$ s. It is also shown that the $n_d = 0$ mode is present in the divergent part of the response along with the suspension modes, while all other nodal diameters do not seem to participate. However, during the transient part of the

²All modes are considered when calculating the global strain energy

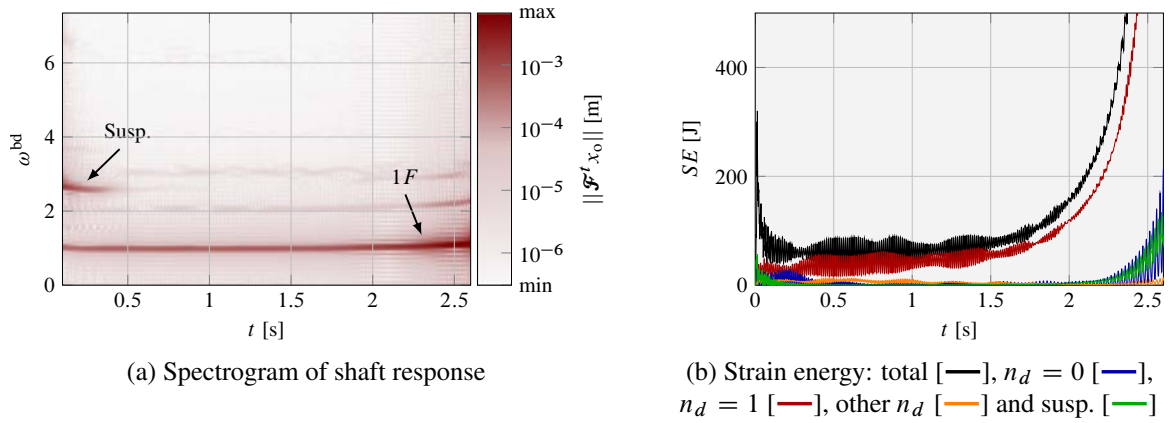


Figure 4.13: Results for initial casing distortion at $\Omega = 1.05$ and $\kappa = 0$ N/m

response higher order modes also participate in the response, as it may be seen that the 1F modal family and the suspension modes cannot account for the total strain energy.

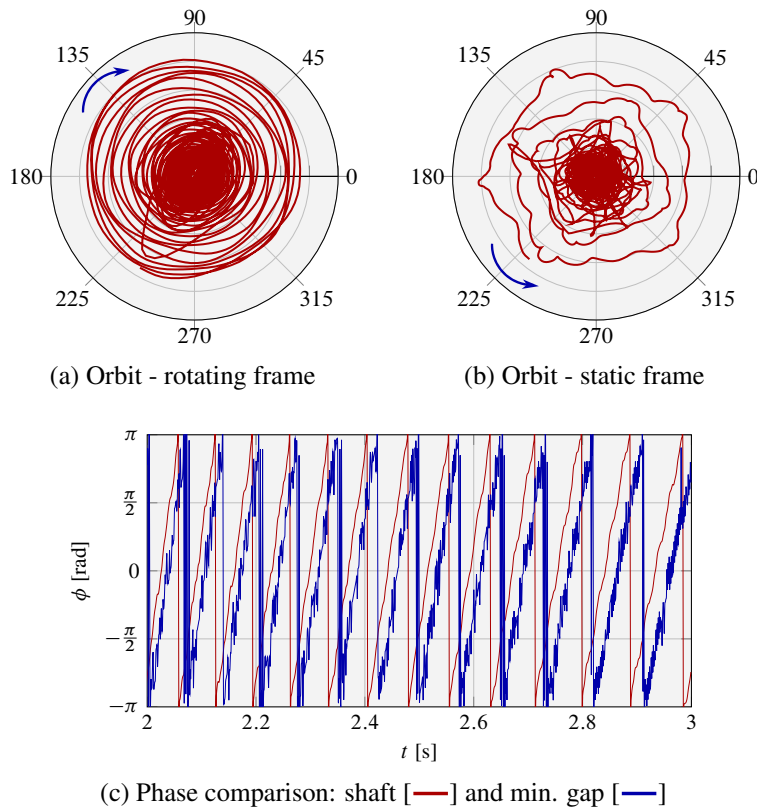


Figure 4.14: Results for initial casing distortion at $\Omega = 1.39$ and $\kappa = 0$ N/m

Further post-processing of the other critical interactions mentioned above result in a very similar behavior in terms of strain energies, vibration amplitudes and frequency content, not shown here for the sake of brevity.

However, as depicted in Figs. 4.14a and 4.14b for $\Omega_{nl}^{cr} = 1.39$, a backward whirling orbit is obtained in the rotating frame similar to the case of Ω_1^{cr} , which is translated into a forward traveling one in the static frame due to the higher rotational speed. In this particular case, the 1-nodal diameter of the 1F modal family of the bladed-disk interacts with the 5th-super-harmonic in time of the 1-nodal diameter mode of the casing ($\omega^c = 5\omega_1^c$). This type of interaction cannot be predicted by the linear modal coincidence criterion (2.18) but exhibits a similar order of magnitude in terms of displacements than those detected for Ω_1^{cr} , hence being just as critical from a structural integrity perspective.

In terms of contact location versus shaft displacement, it is shown in the phase comparison depicted in Fig. 4.14c that the system responds as in the *standard* contact scenario described in the previous section. Although in this case, for the mode responsible of the divergence whose modeshape is illustrated in Fig. 4.2b, the most elongated blade is not perfectly aligned with the shaft maximum radial displacement, thus introducing the phase shift between the two quantities visible in Fig. 4.14c. A decrease in the whirling frequency is also visible in this figure: there are three oscillations for $t \in [2 \text{ s}; 2.2 \text{ s}]$ while there are only two for $t \in [2.8 \text{ s}; 3 \text{ s}]$. This behavior can be explained by the frequency increase of the bladed-disk response in the relative frame during the divergent phase of the simulation, visible in spectrogram 4.13a for $\Omega = 1.05$, which translates into a frequency decrease in the fixed frame due to the wave propagation direction. A similar behavior was observed for all the other divergent interactions detected. Further, analogous conclusions than in [SBL14] can be drawn for other types of regimes, as sustained behaviors are observed near critical speeds and damped motions are attained elsewhere in the rotational speed range. It should also be noted that the shaft dynamics appeared to be crucial in the emergence of divergent regimes, as a clamped center node configuration led only to damped motions with the same simulation parameters listed in Tab. 4.1.

4.3.3.2. Scenario B: mass imbalance excitation

The mass imbalance is reflected via an external forcing term with a constant component in the rotating frame and proportional to the square of the rotational speed. Its magnitude is selected so that the initial blade-tip clearance is absorbed with the lowest Ω value considered in Tab. 4.1. The main difference with scenario A is that the zero solution of Eq. (4.2) no longer exists and therefore, the former damped regimes cannot be reached. This type of contact initiation mechanism is only meaningful when extending the scope of the interactions to whirl motions and hence could not be studied with a rigid shaft assumption considered in [Leg+09].

The same post-processing strategy as for scenario A is considered. The frequency response of the shaft is depicted in Fig. 4.15 over the entire rotational speed range without accounting for the frame/bearings

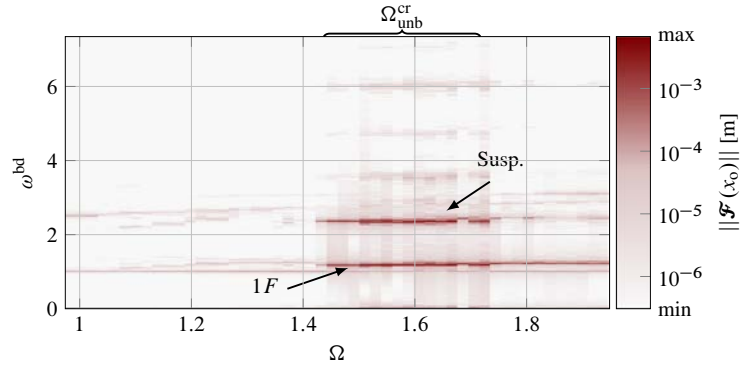


Figure 4.15: Frequency response of center node for mass imbalance excitation

coupling but with the input parameters listed in Tab. 4.1. In this figure, the same colormap as in Fig. 4.11 is used in order to highlight the change in vibration amplitudes, which are generally smaller than those obtained when a modal interaction arises. The shaft is shown to respond mainly on the suspension modes and the 1F modal family, and some interaction regimes are detected for $\Omega \in [1.42; 1.75]$ where the amplitudes become of the same order of magnitude as in the first configuration.

For the critical speed Ω_1^{cr} , the shaft displacement versus time is displayed in Fig. 4.16a along with the associated whirling orbit in the static frame in Fig. 4.16b. It can be seen that the solution reaches a stable limit cycle where the shaft whirls in an circular co-rotating orbit of about 1.1 mm radius with oscillations in the order of 0.1 mm. This behavior is highly different from the one observed in scenario A, where for the same rotational speed, the transient excitation develops into a modal interaction resulting into a continuous growth of vibration amplitudes.

Further, the strain energy distribution depicted in Fig. 4.16c shows how the mass imbalance load mainly excites the suspension modes while the remaining of the strain energy is localized on the 1-nodal diameter mode, all other modes having a negligible contribution to the overall dynamics. Indeed, it is expected for the mass imbalance to mainly excite the suspension modes in a linear framework, yet in the nonlinear framework introduced by the unilateral and frictional contact constraints, all modes of both structures tend to be excited by the contact loads. For the current models, at the predicted modal coincidence speed, the arising rotor/stator interactions do not seem to develop into divergent regimes and are well contained by the surrounding casing (vibration levels are in the order of $10 \mu\text{m}$ for the casing). It appears that the energy levels stabilize after $t \simeq 1.1$ s as steady-state is reached and are about ten times lower in comparison to Fig. 4.13b when a modal interaction arises.

The blade-to-casing distances are displayed in Figs. 4.17a and 4.17b where it is shown that: several blades remain in permanent contact; two blades exhibit intermittent contacts and the remaining ones vibrate freely,

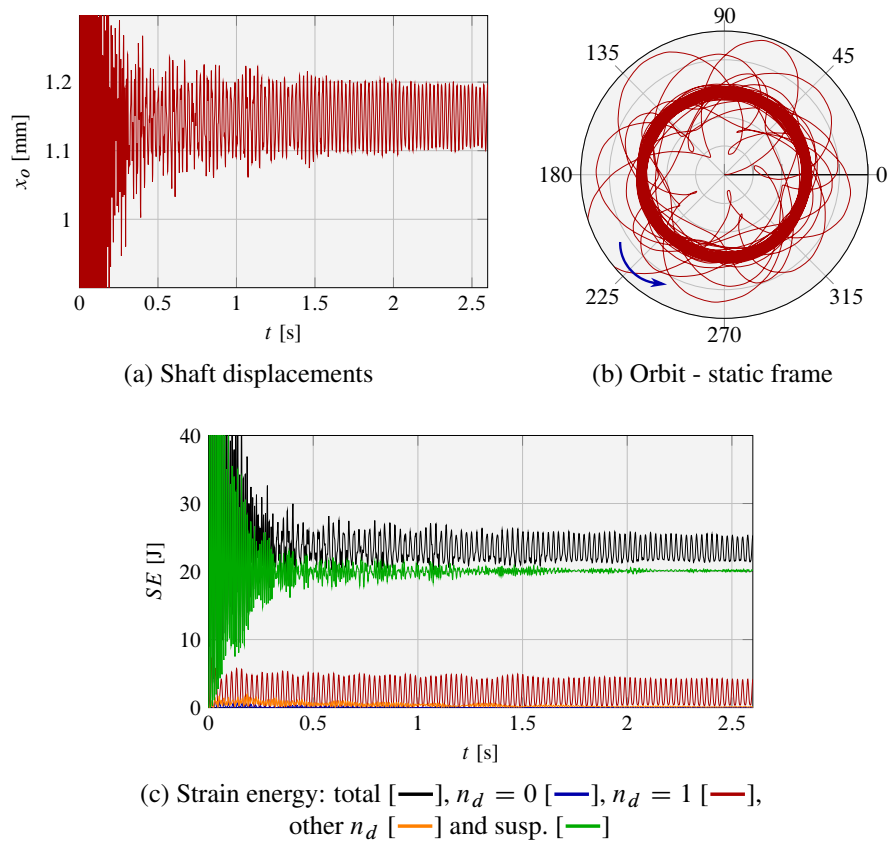


Figure 4.16: Results for mass imbalance load at $\Omega = 1.05$ and $\kappa = 0$ N/m

solely excited by the disk coupling with the neighboring blades. This behavior is consistent with the findings reported in [LST07; PTC14], where the resulting contact loads are almost constant on the bladed-disk and act as rotating loads on the casing. However, in [PTC14], these operating conditions appeared to induce a growth of vibration amplitudes on both structures at the modal coincidence speed, combining the whirling motion of the shaft with a 2-nodal diameter wave on the casing and the blades. This major difference with respect to the behavior observed in the current investigation might be explained by the rigid disk assumption and the clamped boundary conditions imposed at the blades foot in [PTC14], and as suggested in [Bat+10], by the strong kinematic constraints induced on the models in [PTC14] which tend to artificially favor the detection of modal interactions. Additionally, in the phase comparison depicted in Fig. 4.17c, it is shown how unilateral contact takes place in the same direction as the shaft displacement once a steady-state is reached. These observations are in agreement with the kinematic predictions given in the previous section in Fig. 4.5b and indicate that the imbalance is prone to initiate contact in the expected *standard* direction.

Nevertheless, some high-amplitude interaction regimes are indeed detected for $\Omega \in [1.42; 1.75]$. It is proposed in the following to further characterize the system response in this speed range and determine

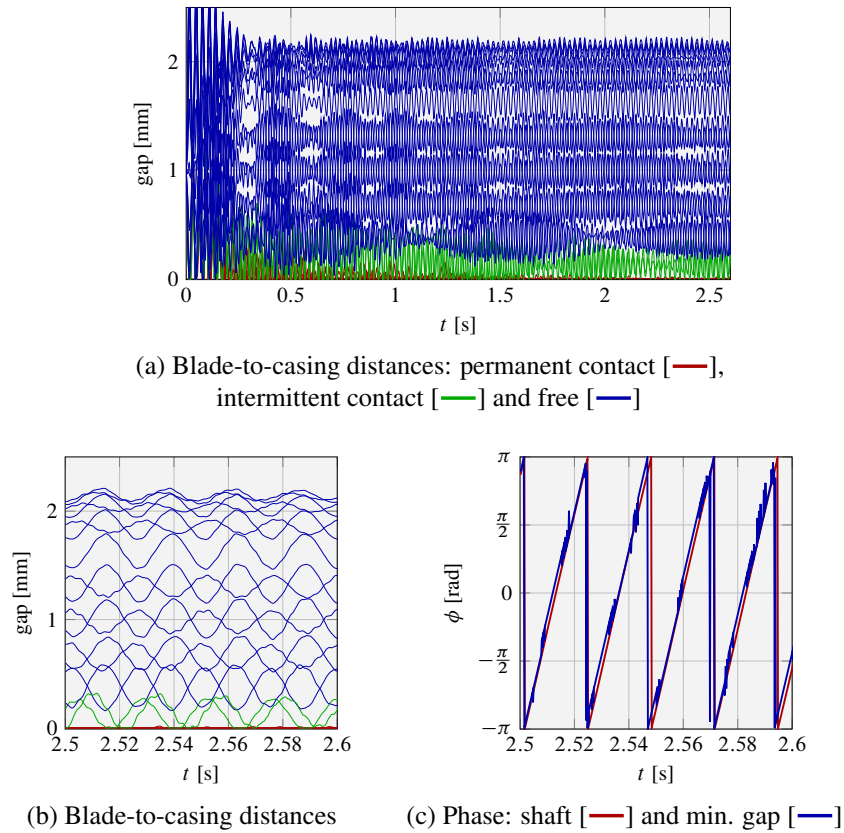


Figure 4.17: Contact characteristics: $\Omega = 1.05$ and $\kappa = 0 \text{ N/m}$

whether or not divergent regimes are observed. In the energy distribution for $\Omega = 1.6$ shown in Fig. 4.18, it is clearly visible how the energy levels are much higher than those depicted in Fig. 4.16c for $\Omega = 1.05$ and are in the same order of magnitude than when a modal interaction arises in Fig. 4.13b. The main difference between the two types of interactions is that the vibrations are contained by the casing when a mass imbalance is the source of excitation, while the vibrations grow exponentially when modal coincidence occurs. Indeed,

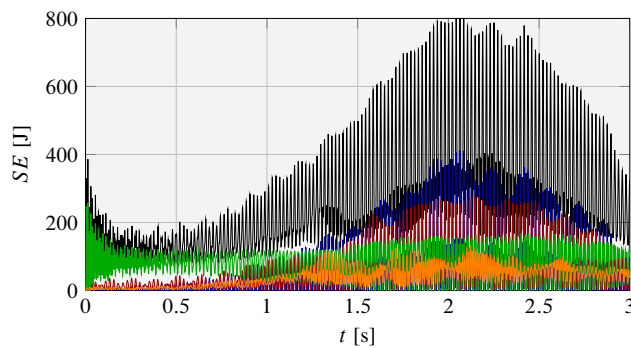


Figure 4.18: Strain energy at $\Omega = 1.6$ and $\kappa = 0 \text{ N/m}$: total [—], $n_d = 0$ [—], $n_d = 1$ [—], other n_d [—] and susp. [—]

as displayed in Fig. 4.18, a rapid growth in the strain energy is detected after $t = 0.5$ s, reaching a peak in amplitude of about 800 J over the time interval $t \in [1.8 ; 2.2]$ s and decaying to a minimum by the end of the simulation³. As for the modes participating this interaction, it is shown that: besides the contribution of the suspension modes which are dominant during the first 0.2 s of the response and exhibit rather constant energy levels throughout the rest of the simulation, a major influence of the $n_d = 0$ and $n_d = 1$ modes is noted during the transient growth in energy levels as well as a non-negligible participation of all other harmonics throughout the entire response.

4.3.3.3. Sensitivity to the frame/bearings coupling

Lastly, the nonlinear dynamics of the reduced-order bladed-disk/casing coupled model are investigated with respect to the loading scenarios discussed for the full uncoupled system, the objective is to characterize the influence of the frame/bearings stiffness κ on the interactions detected.

Casing distortion excitation The linear modal coincidence captured in the full space at Ω_1^{cf} depicted in Figs. 4.12 and 4.16, is also detected in the reduced space since the modes kept in the truncation are those having a major participation in the system response. This is shown in Fig. 4.19 for $\kappa = 0$ N/m where it may be seen how the 1-nodal diameter mode is the one responsible for the divergence, in agreement with prior observations. It is followed by a very rapid growth in amplitude of the suspension modes strain energy, which generate a far more aggressive response than with the full system. Indeed, as explained in [Bat+10], the kinematic restrictions imposed by the modal projection artificially favor the initiation of high-amplitude interactions.

The sensitivity of the bladed-disk response to the frame/bearings coupling stiffness κ is analyzed in Fig. 4.20, where the maximal displacement of the center node is displayed for rotational speeds near Ω_1^{cf} and three different values of $\kappa = [0 ; 500 ; 1000]$ N/m. It is shown in this figure how the structural coupling introduces a stiffening of the system and produces a shift in the modal interaction speed, as would be expected from the stability analysis carried out in section 4.2.2. The frequency content and energy distributions, as well as the contact direction with respect to the shaft displacements, are not affected by the coupling and again the 1-nodal diameter of the 1F family generates the divergences.

Mass imbalance excitation When considering a mass imbalance excitation, the coupling matrix appears to have a negligible influence on the system response. As depicted in Fig. 4.21a, very similar shaft displacements

³These simulations were conducted over larger simulation times and vibration levels stabilize at the same order of magnitude as for $\Omega = 1.05$. For this source of excitation, no divergent regimes were detected.

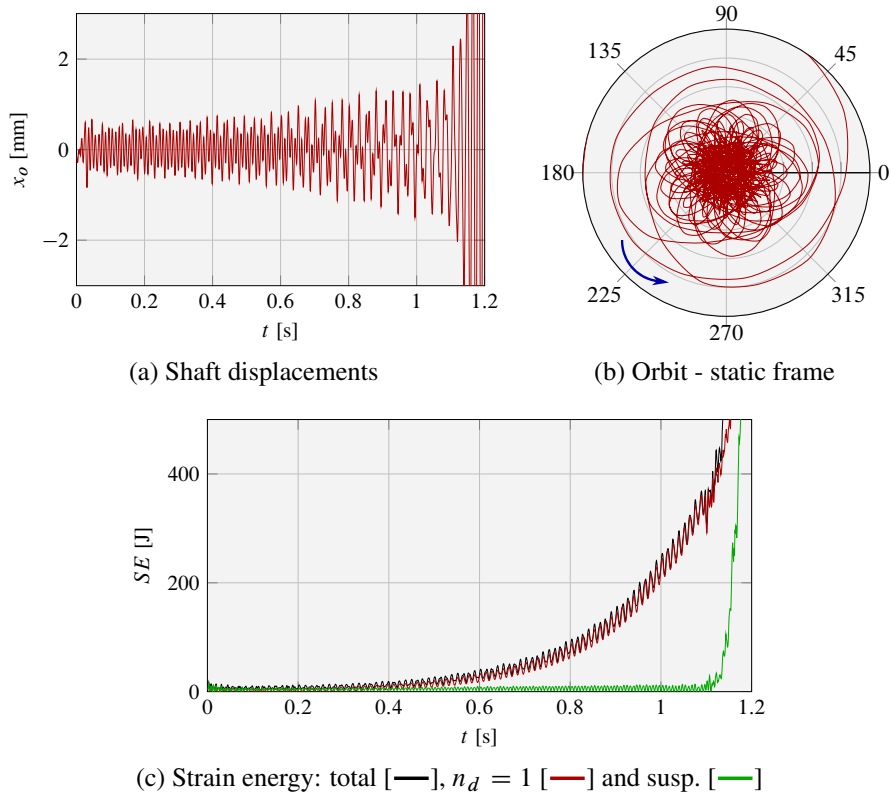


Figure 4.19: Results for casing distortion excitation at $\Omega = 1.05$ and $\kappa = 0$ N/m

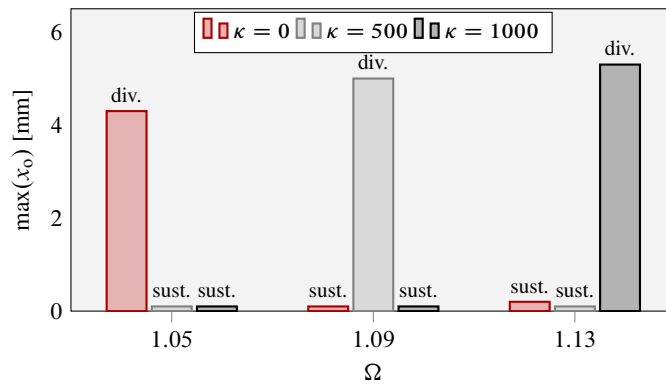
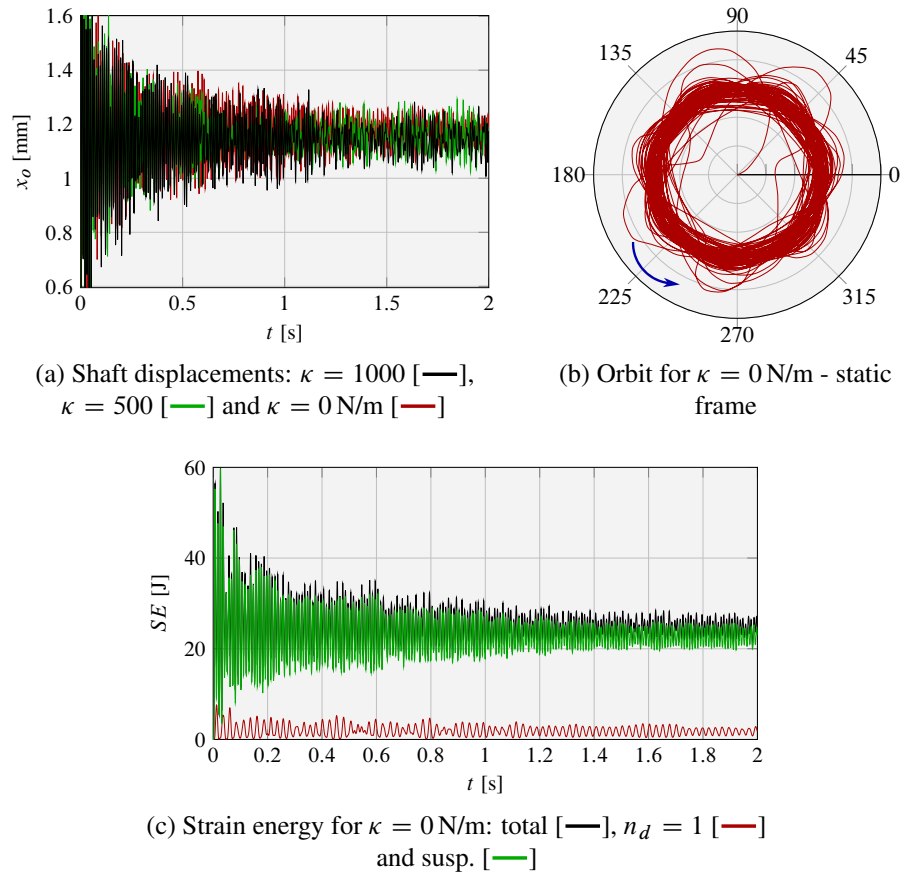


Figure 4.20: Maximal shaft displacements near Ω_1^{cr}

are obtained at Ω_1^{cr} for all values of $\kappa = [0 ; 500 ; 1000]$ N/m tested. Similar than for the full system, these displacements correspond to a forward whirling circular orbit in the static frame of about 1.2 mm radius with oscillations in the order of 0.1 mm. As for the modal deformations illustrated in Fig. 4.21c, these are also in agreement with prior observations in terms of energy levels and localization, since the suspension modes are largely dominant throughout the entire response.

Also, regarding the interactions encountered in the speed range $\Omega \in [1.42 ; 1.75]$ for scenario B, these

Figure 4.21: Results for mass imbalance excitation at $\Omega = 1.05$

could not be observed in the truncated modal space, since they were characterized by a transient growth of vibration amplitudes and a non-negligible participation of all the 1F harmonics, in particular the $k = 0$ and $k = 1$ as was shown in Fig. 4.18. Instead, divergent regimes were obtained for $\Omega > 1.52$ where, as illustrated in Fig. 4.22, the strain energy distribution and associated magnitudes become similar to those of modal interactions (c.f. figure 4.19c). This indicates that the truncation modal basis chosen in Eq. (3.28) is not sufficiently rich to capture the overall system behavior.

These observations suggest that the frame/bearings coupling between casing and bladed-disk plays a major role in the modal interaction regimes detected in scenario A and in the subsequent high-amplitude precessional motions of the shaft, while having a limited influence in the system behavior when a mass imbalance is the source of excitation. The modal truncation basis proved to be sufficient to capture the dominant dynamics of the system in the scenario A. However, even if this basis is appropriate in scenario B for small rotational speeds, for $\Omega > 1.52$ non-physical divergences were reached regardless of the coupling stiffness κ considered due to the strong kinematic constraints imposed by the modal projection.

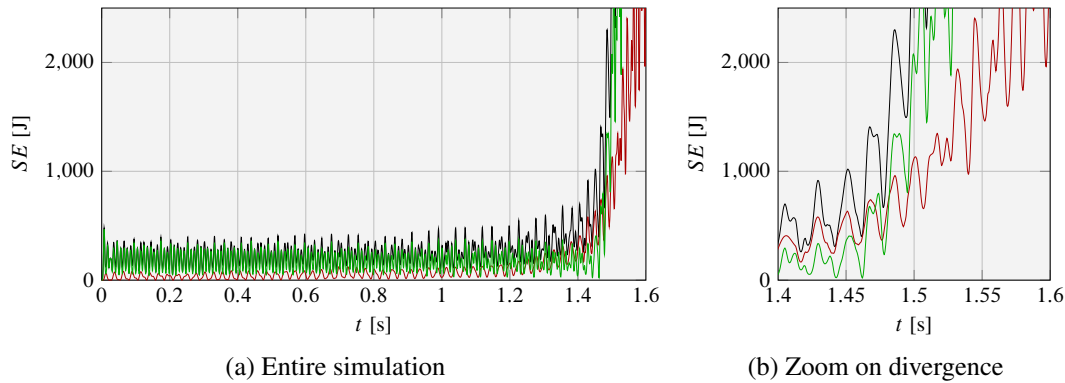


Figure 4.22: Strain energy for $\kappa = 0$ N/m at $\Omega = 1.65$: total [—], $k = 1$ [—] and susp. [—]

4.4. Summary

This chapter targets the occurrence of shaft precessional motions induced by unilateral blade/casing contacts in a two-spool commercial engine fan stage. A 2D in-plane FE-model representative of a bladed-disk/casing system is built, where the flexibility of the shaft is represented by a pair of linear springs linked to the center of the disk which drive the so-called *suspension modes*. Additionally, it is proposed to model the structural connection between bladed-disk and casing provided by the fan frame and the bearings through an array of linear springs. The associated methodology, based on the derivation of Hamilton's principle for the calculation of the corresponding coupling stiffness matrix, involves a truncated set of modes utilized for the projection of the equations of motion. This coupling stiffness matrix contains time-periodic coefficients which can be eliminated through a change of frame. A stability analysis of the zero solution in the time-invariant modal space revealed two unstable zones where damped, oscillatory and divergent modes coexist.

Within a time-marching solution method, the unilateral contact interactions between these flexible structures are initiated via two distinct mechanisms: (1) a prescribed casing distortion and (2) a mass imbalance on the bladed-disk. The shaft dynamics proved to have a major role in producing potentially harmful regimes, in particular in the former scenario which can lead to divergent modal interactions. For most of the interactions detected, the shaft precessional motion takes the form of a backward traveling wave in the rotating frame which is translated into a forward traveling one in the static frame. Through a projection from physical to cyclic coordinates and the calculation of the associated modal strain energy, it is shown how the 1-nodal diameter mode of the first modal family of the bladed-disk is dominant when a modal interaction occurs, while the suspension modes have major participation when a mass imbalance is the source of excitation.

In the truncated modal space, the nonlinear dynamics of the reduced-order coupled system are studied

considering both loading scenarios. The modal projection proved to be suitable for the detection of modal interactions initiated by the casing distortion, where the frame/bearings stiffness introduces a shift in the detected critical speeds in agreement with the linear stability predictions. However, when a mass imbalance is the source of excitation, the results are shown to be valid up to a certain rotational velocity beyond which only divergent regimes are observed. The strong kinematic constraints imposed by the modal projection do not capture the behavior of the full system where an important contribution of all harmonics is noted.

Three-dimensional contact and abradable wear investigation

Complementing the investigation of the previous chapter, which addresses the influence of the bladed-disk/casing coupling provided by the structural frame and bearings with a simplified 2D FE-model, it is here proposed to assess the participation of the abradable layer wear in the detected interactions and the potentially induced high-amplitude whirling motions. The 3D industrial fan bladed-disk model (see section 3.3) is employed within the framework of the numerical procedure [LBP12]. This methodology was adapted to an industrial environment at SNECMA where it is referred to as COROS [Mil+15] and was recently used for the redesign of a HP-compressor blade [Bat+15], improving its dynamical response in the event of contact occurrences.

As mentioned in section 2.2.5, abradable coatings are deposited along the casing circumference in order to mitigate direct structural contacts between rotating blades and the surrounding stator while permitting a self-tuning of operating blade-tip clearances. They must be sufficiently resilient to endure severe thermal gradients and elevated temperatures, resist particle ingestions and high pressure levels, but also be adequately soft not to alter the structural integrity of potentially incurring blades. Even though these coatings are considered as a robust technological solution to avoid high-amplitude vibrations of the blades, both numerical and experimental studies have shown that potentially harmful interactions may emerge from repeated blade/abradable lining contacts. As detailed in [Bat+15], existing studies focus on blade/abradable interactions in HP and LP axial compressor stages under the assumption that contact occurs solely on a single blade. In [BML15], a centrifugal compressor is analyzed, exploiting its cyclic-symmetric properties and enforcing unilateral contact constraints on all blades. The fan stage of an engine has never been studied within this framework and is the focal point of this chapter, paying close attention to the sensitivity of the interactions

with respect to the shaft dynamics and the associated gyroscopic terms. An analysis of the hypothetical contact on the longest blade scenario often assumed in compressor stages [Bat+15] is also presented.

5.1. Assumptions and simulation procedure

In the strategy [LBP12] a rigid casing is assumed, as illustrated in Fig. 5.1, thus the blades dynamics and the abradable wear are the main concern. Similar to the considerations of chapter 4, the casing is statically

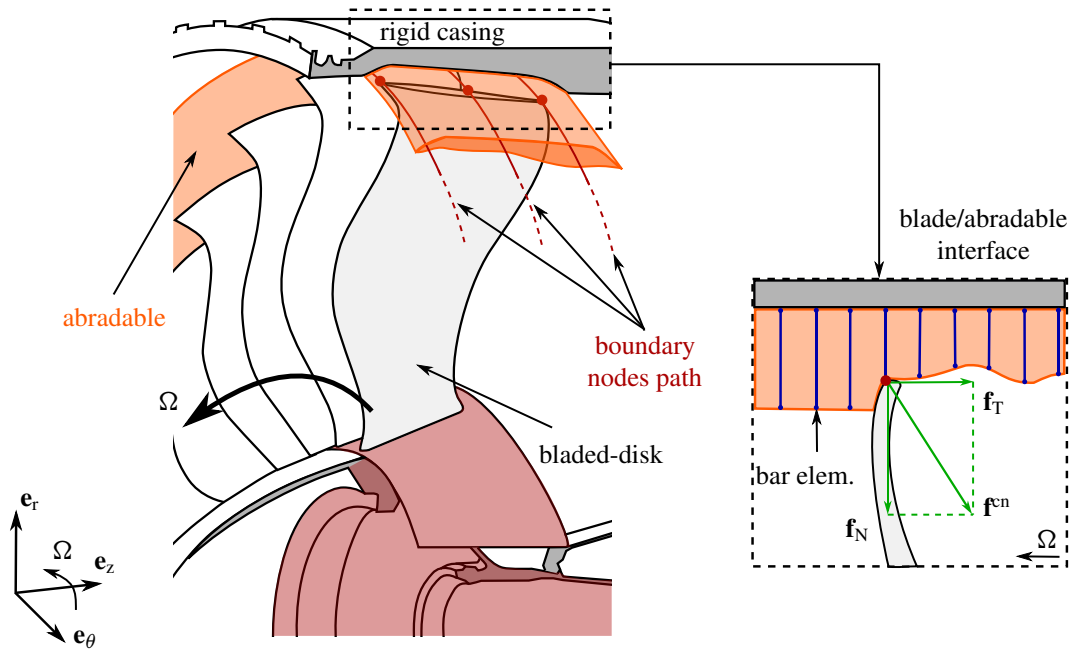


Figure 5.1: Blade/abradable layer interaction [LBP12]: abradable discretization into bar elements, retained boundary nodes on bladed-disk and associated contact forces

distorted onto a 1-nodal diameter shape in order to absorb the initial blade-tip clearance and initiate the interactions, hence potentially favoring high-amplitude off-axis motions of the shaft. As reported in the literature review in chapter 2, the method proposed in [LBP12] is based on an explicit time-marching strategy and unilateral contact constraints are enforced via the Lagrange multipliers technique. Thus, a procedure similar to algorithm 1 is implemented, where instead of considering the casing displacements, the abradable profile is tracked. As in chapter 4, the frictional contact constraints are accounted for by means of a Coulomb law in sliding conditions, where the friction coefficient $\mu = 0.1$ is retained [Sin04] for all the simulations.

In the macroscopic wear law proposed in [LBP12], the abradable coating is discretized into one-dimensional bar elements as highlighted in Fig. 5.1, which are subjected to a bilinear elasto-plastic constitutive law so that incurring blades “squash” the abradable coating and may yield a permanent deformation of the rod elements. The three parameters controlling the ductility of the coating, specified in Fig. 5.2, are its Young’s

modulus E_{ab} , plastic modulus K_{ab} and yield stress limit σ_{ab}^y .

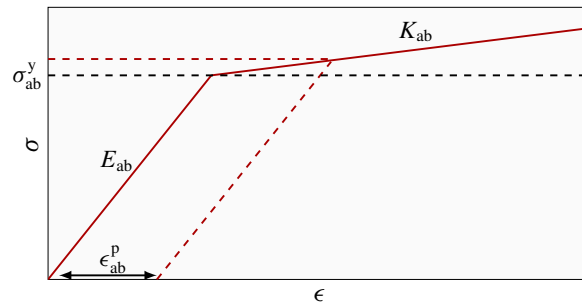


Figure 5.2: Abradable elasto-plastic constitutive law [LBP12]

In line with the prediction-correction algorithm implemented for the 2D-models in section 4.3.1, a detected penetration induces a correction of the bladed-disk displacements through the computation of unilateral and frictional contact forces, which is achieved by means of the Lagrange multipliers method exposed in section 2.2.3. The associated strains and stresses of the abradable rod elements are determined accordingly, using a linear Hooke's law. If the limit yield stress is exceeded, the strains are corrected with the plastic modulus and the permanent deformation of the rod elements ϵ_{ab}^p is stored, thus updating the abradable profile and setting new operating blade-tip clearances. The abradable profile is updated for each boundary node independently.

Three types of simulations are carried out:

- Full bladed-disk handling unilateral contact constraints on *all* sectors, including or not gyroscopic terms.
- Full bladed-disk handling unilateral contact constraints on a *single* sector.
- Single blade.

The last two simulations are undertaken for the hypothetical scenario evoked in [Bat+15], where contact solely occurs on the longest blade. The main objective of this comparison is to determine certain limits of this simplified approach as well as to emphasize the role of the shaft and disk flexibility in the detected interactions. The models employed are described in the next section.

5.2. Industrial structural models

Two industrial models are implemented in the following: (1) a single blade model and (2) the full bladed-disk model presented in section 3.3.

5.2.1. Single blade model

Rather than employing the entire bladed-disk, designers often optimize the geometry of a single blade, not only in terms of aerodynamic performances but also from a structural viewpoint. In this sense, *mono-sector* COROS simulations involve a single blade in contact with the abradable layer [Bat+15].

The blade geometry pictured in Fig. 5.3a belongs to the industrial fan stage depicted in Fig. 3.4. Clamped boundary conditions are imposed at the blade foot, hence assuming a perfectly rigid disk and shaft. Also

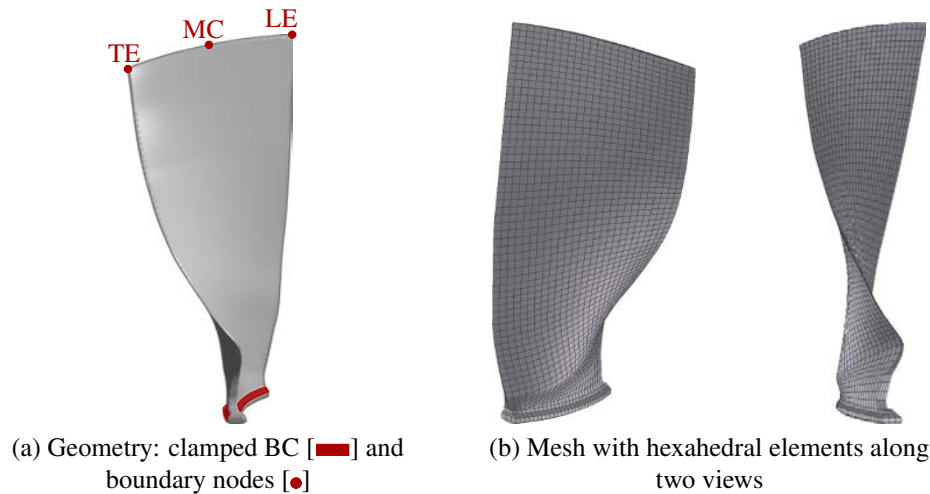


Figure 5.3: Fan blade model: geometry and associated mesh

in this figure, the red dots represent the three carefully selected boundary nodes kept in the reduced-order model, where unilateral and frictional contact constraints are enforced. The associated mesh was built in ANSYS using 20-node hexahedral elements and is displayed in Fig. 5.3b. This model is used for *mono-sector* COROS simulations which will be compared to the full cyclically symmetric strategy that is studied in the following.

In the Campbell diagram 5.4 the first three eigenfrequencies of the blade are represented with respect to the rotational speed along with the associated mode shapes, which correspond to the first two flexural modes (1F and 2F) and the first torsional one (1T) respectively. In agreement with the observations made for the full bladed-disk in section 3.3, the important influence of centrifugal effects is visible: the 1F mode doubles its frequency from rest to the maximal rotational speed considered and the 2F is also subject to important variations throughout the operating speed range. Additionally, Engine Order (EO) excitations are also displayed in Fig. 5.4. These lines correspond to synchronous and harmonic excitations potentially leading to vibratory resonances for speeds located at the crossing of modal lines [BML15], *e.g.* at $\Omega \simeq 0.82$ the 2-EO and the 4-EO cross the 1F and the 2F respectively, giving rise to the potential critical speed Ω^{ct} .

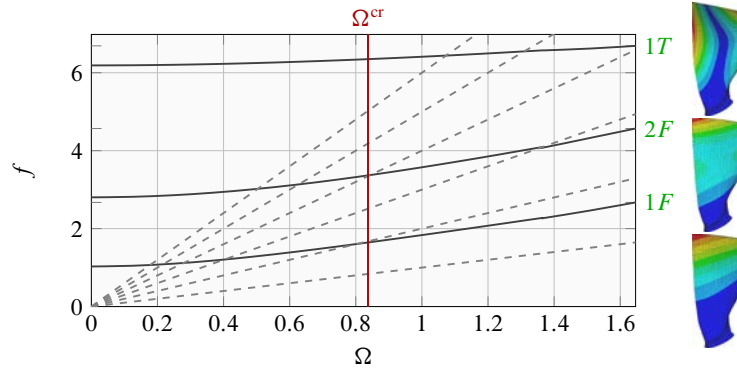


Figure 5.4: Modal analysis of the blade model: frequencies [—] and EO [- -]

Further, the boundary node displacements due to the centrifugal forces are displayed in Fig. 5.5, which result in significant variations of the initial blade-tip clearances depending on the rotational speed. The leading edge is barely affected for $\Omega \in [0; 0.9]$ and the clearance at this node tends to open for $\Omega > 0.9$ as it moves away from the casing (negative direction). At mid-cord and trailing edged the corresponding displacements tend to open the gap even for low rotational speeds. Additionally, the amplitude of the 1-nodal

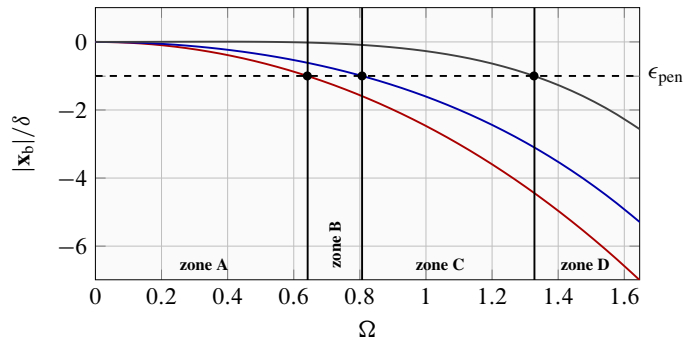


Figure 5.5: Blade-tip displacements under centrifugal loads: LE [—], MC [—] and TE [—]

diameter casing distortion—induced for instance by the aerodynamic loads at take-off—is represented by the black dashed line. In accordance to the experimental observations reported in [LS04], this distortion is set to $\epsilon_{\text{pen}} = 0.5$ mm, which is equal to the size of the selected initial blade-tip clearance δ and is constant throughout the entire speed range. For this set of parameters $(\delta, \epsilon_{\text{pen}})$, four zones are clearly distinguished in Fig. 5.5, characterized by different initial contact configurations: in **zone A** all nodes are in contact; in **zone B** contact is lost at the TE; in **zone C** only the leading edge remains in contact and in **zone D** no interactions are initiated. Within the operating rotational speed range of the engine, corresponding to $\Omega \in [0.7; 1.5]$, only zones B, C and D are present.

5.2.2. Full bladed-disk model

The industrial bladed-disk¹ was constructed by exploiting cyclic-symmetry (see chapter 3). The associated fundamental sector is illustrated in Fig. 3.5a with the corresponding mesh in Fig. 3.5b. It is recalled in Fig. 5.6

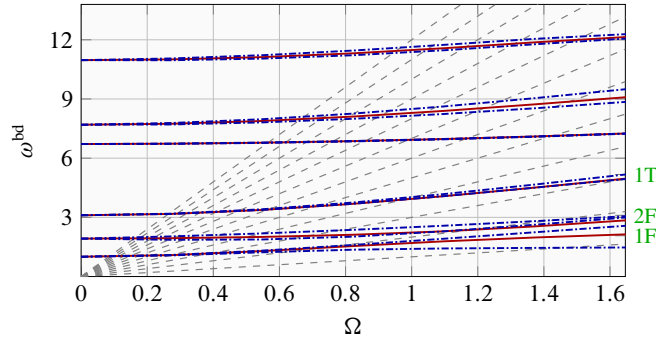


Figure 5.6: 1-nodal diameter modes: with [---] and without [—] gyroscopic terms

how these terms, often neglected in turbomachinery studies, induce a non-negligible frequency split of 1-nodal diameter modes which are strongly coupled with the shaft dynamics. The split is particularly visible in the 1F mode, where the backward branch crosses the 1-EO around $\Omega = 1.3$ and leads to a potentially critical speed that cannot be predicted if gyroscopic terms are omitted.

Additionally, a second multi-sector model was built with clamped boundary conditions imposed at the base of the disk in order to suppress any off-axis displacements of the shaft as illustrated in Fig. 5.7a. The

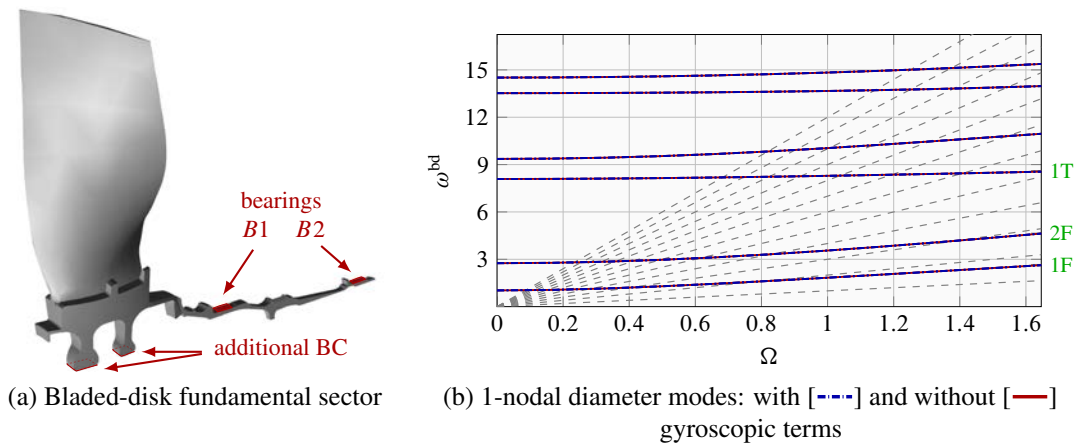


Figure 5.7: Bladed-disk with additional boundary conditions

associated set of 1-nodal diameter modes are represented in Fig. 5.7b, from which two main observations can be made: (1) the frequency difference between backward and forward traveling waves induced by

¹Its main modal characteristics are also presented in that chapter, where the corresponding veering diagram is depicted in Fig. 3.7a, the Campbell diagrams are shown in Figs. 3.9 and 3.7b, with and without accounting for gyroscopic terms respectively.

the gyroscopic terms becomes negligible (in the order of 0.01 Hz) and (2) all modes exhibit a much higher frequency, as the system is stiffened by the additional boundary conditions. The latter observation is consistent with the frequency drop of 1-nodal diameter modes with respect to other harmonics of the same modal family, which is induced by the flexibility of the shaft and is clearly visible in the veering diagram 3.7a.

With regards to the blade-tip clearance variations associated to the centrifugal effects, the displacements of the three nodes retained for contact management are displayed in Fig. 5.8. The main difference between the multi-sector and the single blade models resides in the displacements of the leading edge and mid-cord. Indeed, for the same initial casing distortion and initial clearance, only zones A, B and C are visible in Fig. 5.8 and a clearance closure is exhibited at the leading edge throughout the entire operating speed range. The maximum displacement of this node arises around $\Omega = 1.3$ and is almost equal to the clearance at rest. Therefore, even small vibration amplitudes are susceptible to engage all the blades in the interaction with the abradable lining. This tendency of the blades to close the operating clearance at the leading edge is not

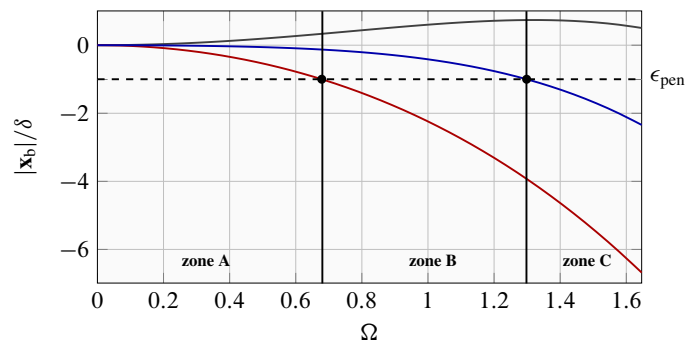


Figure 5.8: Blade-tip displacements under centrifugal loads: LE [—], MC [—] and TE [—]

captured with the single blade model and is essentially caused by the over-constraining clamped boundary conditions imposed on the mono-sector model, which fail to account for the deformation of the disk and shaft. Hence, significant differences in the nonlinear dynamics of each model are to be expected.

5.3. Space and time convergence analysis

Three convergence analyses are performed: (1) the modal reduction basis η , (2) spatial discretization of the abradable layer n_{ab} and (3) the time discretization in the time-marching scheme Δt . The convergence analyses are performed for rotational speeds arbitrarily set to $\Omega = 1.4$ and 1.45 , where no interactions are expected from the linear modal analysis. Simulations are carried out for 10 revolutions, with a 1-lobe deformation of the casing and a penetration equal to the initial gap set to 0.5 mm. Similar to the previous

chapter, convergence is met in terms of blade displacements, associated contact forces and final profile of the abradable layer.

Modal reduction basis Comparable to chapter 4, the number of η modes composing the reduction basis is the most critical parameter to ensure convergence [Bat+10]. Since this parameter controls the size of the recomposed reduced model, it plays a key role in the associated computational times and should be kept to a minimum. As displayed in Fig. 5.9, motion convergence is achieved for $\eta = 30$. Indeed, the blade-tip displacements in Fig. 5.9a and the associated final abradable profile, unfolded in Fig. 5.9b, are almost perfectly superimposed with those obtained using a larger reduction basis ($\eta = 100$).

For the converged results, the abradable wear displayed in Fig. 5.9b is solely localized around $\theta = \pi$, which corresponds to the location of maximum penetration induced by the prescribed casing distortion. The

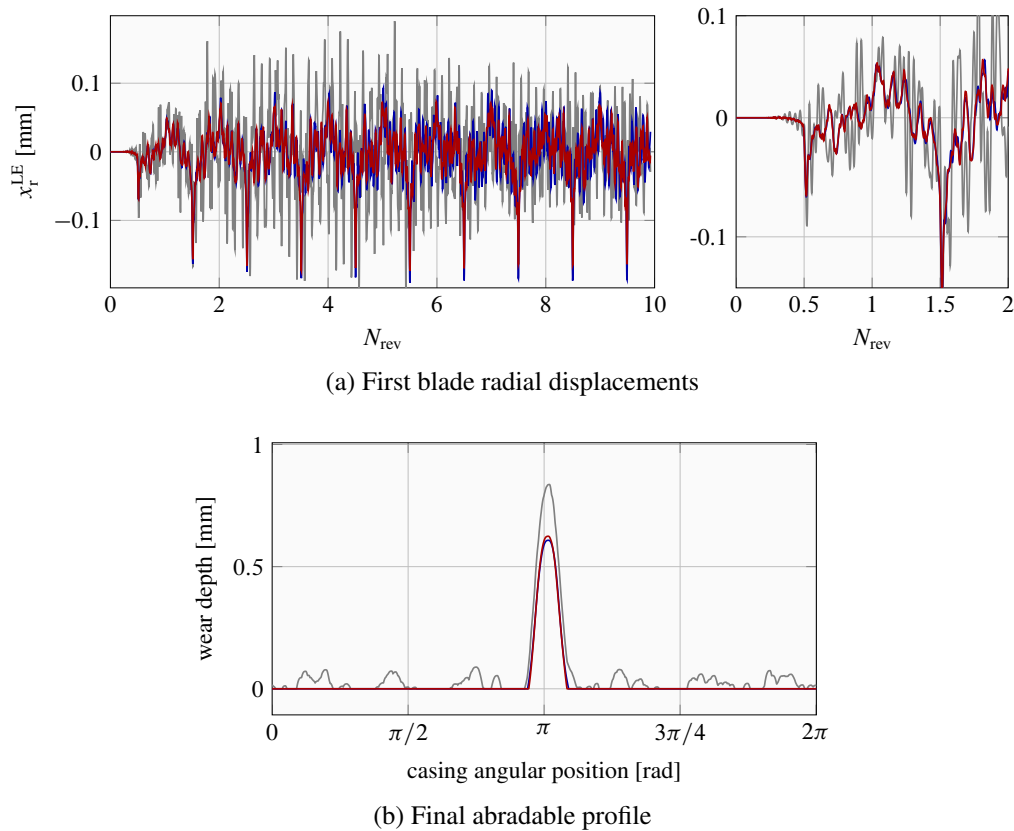


Figure 5.9: Modal basis convergence: $\eta = 15$ [—], $\eta = 30$ [—] and $\eta = 100$ [—]

poorest reduction basis exhibits generally overpredicted displacements as depicted in Fig. 5.9a, thus leading to a widely different behavior and significant abradable removal at various locations. The reduction parameter $\eta = 30$ is kept, leading to a 600 DoF reduced-order model.

Abradable discretization The abradable discretization is reflected by the number of elements n_{ab} used along the casing circumference. The displacements of the blades appeared to be far less sensitive to n_{ab} than to η , and for all the values, the time histories overlapped almost perfectly. The main difference between the lowest value and the converged one was in the contact forces, where a finer discretization of the abradable layer results in much smoother contact reactions. A small discrepancy was also observed in the final wear profiles, where for the smallest number of abradable elements a more significant wear was obtained. The value $n_{ab} = 2000$ is selected in the following.

Time-step size The last parameter of interest corresponds to the time step size Δt , which drives the conditional stability of the explicit time-marching algorithm used in COROS. Similarly to previous convergence studies, different Δt were examined to verify the accuracy of the obtained results. For the two rotational speeds tested, convergence was reached even with large time-step sizes, *e.g.* $\Delta t = 1 \cdot 10^{-6}$ s. Yet $\Delta t = 1 \cdot 10^{-7}$ s is retained for the simulations in order to ensure that high-frequency content of the bladed-disk response is captured, as it may be critical at running speeds where interactions are detected.

A similar analysis was performed while accounting for gyroscopic terms and leading to analogous conclusions. Thus, the same parameters regarding time-step size, number of abradable elements and number of modes retained in the reduction basis are employed in the corresponding simulations.

5.4. Results and discussion

The role of the shaft dynamics in the detected interactions of the multi-sector model is first assessed and two comparisons are provided: (1) sensitivity to gyroscopic terms and (2) sensitivity to the disk off-axis displacements. Secondly, moving closer to the scenario investigated in [Bat+12], it is assumed that contact may solely occur on a single blade employing both the multi-sector and the mono-sector models.

5.4.1. Reference simulations

Computations are run over 50 revolutions for every rotational speed with the simulation parameters listed in Tab. 5.1 and the multi-sector model described in section 5.2.2. The casing is statically distorted to a 1-nodal diameter shape in order to induce off-axis motions and contact is handled on all 24 sectors.

One of the parameters characterizing the interactions corresponds to the abradable profile observed at the end of each simulation, as it is directly related to the bladed-disk vibratory amplitudes [LBP12]. These profiles are unfolded and juxtaposed for every rotational speed in Fig. 5.10 creating a so-called *wear map*,

Parameter	Value
number of revolutions	50
clearance at rest	0.5 mm
friction coefficient	$\mu = 0.1$
rotational speed	$\Omega \in [0.95 ; 1.5]$
casing distortion	0.5 mm
abradable thickness	5 mm

Table 5.1: COROS simulation parameters

where the colorcode indicates the depth of the worn lobes caused by the incurring blades and ranges from 0 mm to 5 mm. These wear maps are displayed for the leading edge and mid-cord of the blades, and enable to

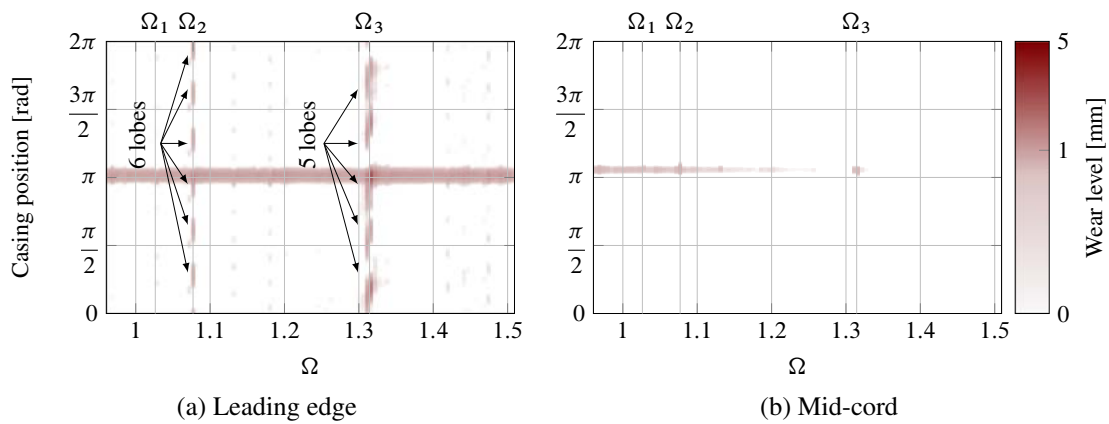


Figure 5.10: Wear maps: multi-sector model without gyroscopic terms

highlight the preferred contact locations for each rotational speed. In accordance with the clearance variations given in Fig. 5.8, it is clearly visible that most of the material removal occurs at the leading edge. The main worn lobe located around $\theta = \pi$ corresponds to the initial casing distorted profile and is visible throughout the entire rotational speed range. Further, two main interactions are identified at Ω_2 and Ω_3 , with 6 and 5 worn lobes at the leading edge respectively. Minor interactions are also visible such as Ω_1 , involving a higher number of lobes and potentially indicating that high EO are responsible of initiating the interactions.

When exploring the frequency content of the time response of the first blade, the FFT of the leading edge radial displacements are computed for the last 25 revolutions at each rotational speed. The results are displayed in Fig. 5.11, where it may be seen that the dynamic content of the fan bladed-disk response is much more elaborate than previous observations made for compressor blades [Bat+12], where only the first flexural and torsional modes were involved in the interactions. It also differs from the behavior of the 2D-model explored in chapter 4, where the response is highly localized on the first modal family. In Fig. 5.11, the different EO lines may be clearly distinguished, producing responses at crossings with modal lines similar to

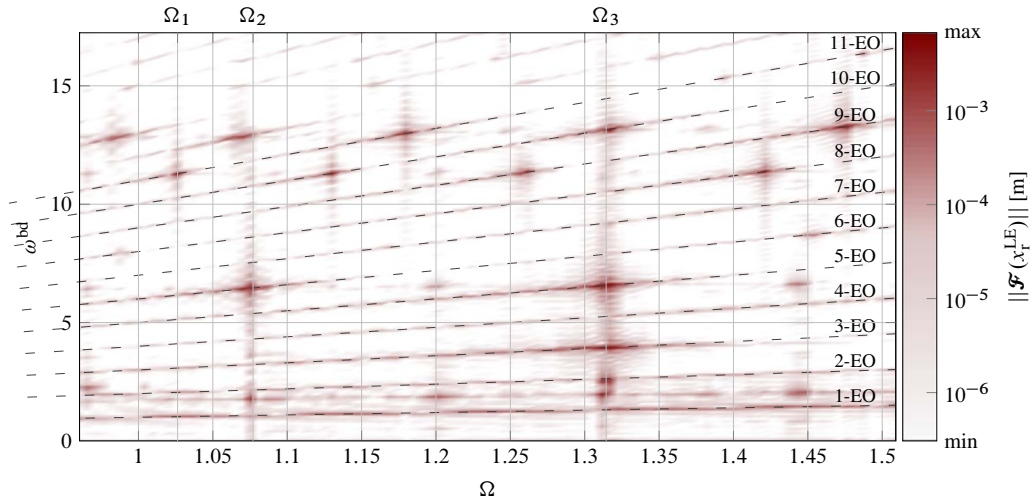


Figure 5.11: Fourier transform of LE displacements

those reported in [Mei14]. As expected, the 1-EO never crosses a modal line within the targeted rotational speed range, thus, all interactions are caused by its sub-harmonics. For instance, 6-EO at $\Omega = \Omega_2$ crosses the 1T modal family, while the 3-EO and 5-EO at $\Omega = \Omega_3$ cross the 2F and 1T respectively. Also visible in Fig. 5.11, is the response of the first flexural mode with $n_d = 1$, which lies between 1-EO and 2-EO as shown in the Campbell diagram 5.6. The response is visible for all the rotational speeds considered and in particular for the interaction speeds Ω_2 and Ω_3 . The presence of the 1-nodal diameter 1F mode indicates that potential non-negligible whirling motions are induced by the bladed-disk/abradable interactions.

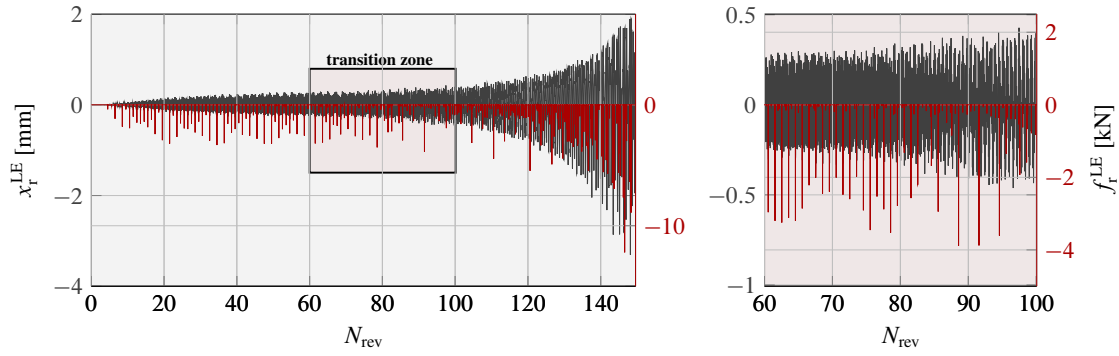
Further, in agreement with the abradable profile observations, higher modes also respond with higher EO lines resulting, for example, into 11 worn lobes at $\Omega_1 = 1.02$ with the crossing of 11-EO and the fifth modal family. More details are provided in the following.

5.4.2. Analysis at a critical speed

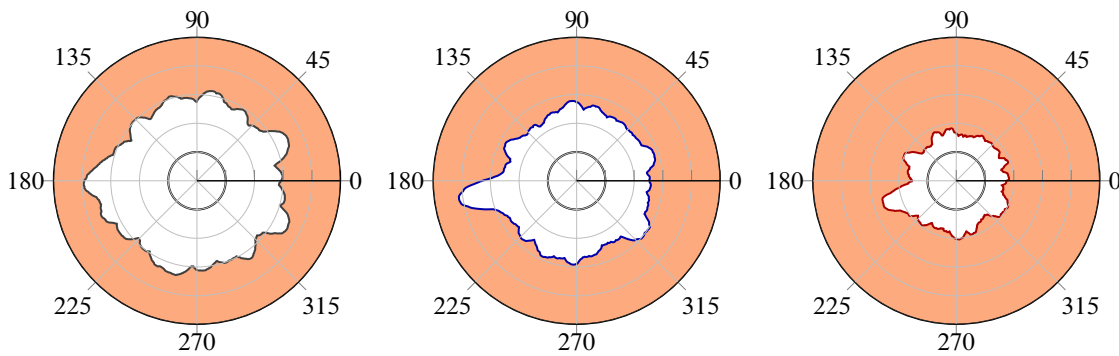
Simulations were run for 150 revolutions in the conditions of Tab. 5.1. The results presented in the following regard $\Omega_1 = 1.02$, but similar conclusions and observations hold for other interactions at Ω_2 and Ω_3 .

Figure 5.12 indicates how the blade responds with increasing vibration amplitudes and an important change in the contact patterns after about $N_{\text{rev}} \simeq 75$ revolutions is visible. In agreement with the frequency response analysis of the blades, presented in the 2-dimensional FFT 5.13a—obtained with the procedure of Appendix A—and the spectrogram 5.13b of the first blade leading edge radial displacements, the bladed-disk behavior can be described as follows:

- At the beginning of the simulation, the bladed-disk responds on a 11-nodal diameter mode at $\omega^{\text{bd}} \simeq$



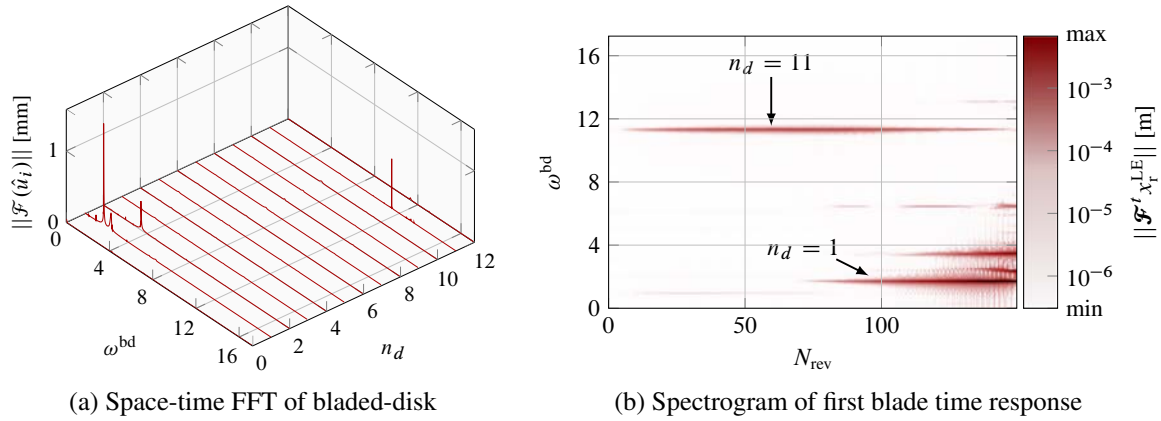
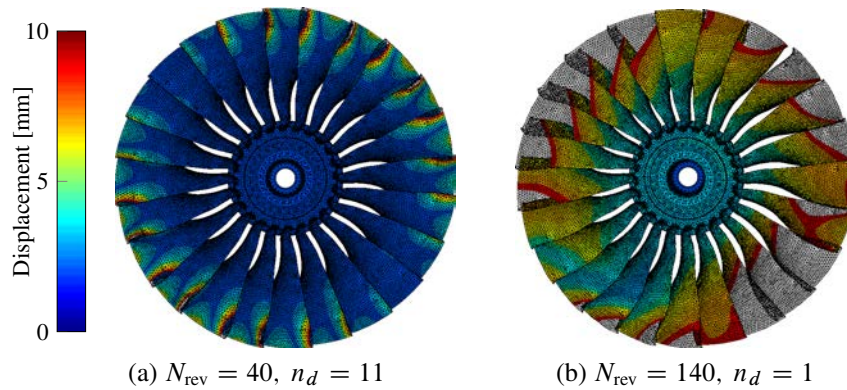
(a) First blade response: radial displacements and contact force

(b) Final abradable profiles ($\epsilon_{ab}^{max} = 2.4$ mm): LE [—], MC [—] and TE [—]Figure 5.12: Results for $\Omega = 1.02$

11.22 excited by the 11-EO. The blades contact only one time per revolution and start incising an 11-lobe wear pattern on the abradable layer at the leading edge.

- As the wear of the abradable layer increases along with the associated blade-tip clearances, the contribution of the 1F mode of $n_d = 1$ starts to appear after $N_{rev} \simeq 75$ rev with a normalized frequency $\omega^{bd} \simeq 2$. This mode exhibits an important coupling with the shaft bending and increases the wear of the abradable layer along the entire casing circumference. The corresponding wear pattern becomes apparent throughout the blade cord as shown in Fig. 5.12b.
- At the end of the simulation vibration levels increase exponentially and the bladed-disk mainly responds on the 1F ($n_d = 1$) mode through a divergent backward whirling motion in the rotating frame. This divergent behavior is very similar to the results obtained with the 2D-models in chapter 4. The presence of the 2F, with $n_d = 1$ and $n_d = 2$, is also noted in the divergent part of the response.

The sharp increase in bladed-disk displacements is graphically represented in Fig. 5.14, where the displacements of the reduced model are recast into the full FE-space at two different instants of the simulation. As expected, at $N_{rev} = 40$ rev the bladed-disk responds on an $n_d = 11$ nodal diameter mode, thus the

Figure 5.13: Frequency analysis for $\Omega = 1.02$ Figure 5.14: Displacements modulus for $\Omega = 1.02$ recast in Finite-Element space

vibrations are solely localized on the blades, whereas at $N_{rev} = 140$ rev the bladed-disk responds mainly on a 1-nodal diameter mode and clearly exhibits an important shaft deflection. Vibration levels reach about 15 mm at blade-tips while shaft displacements attain about 2.5 mm. The associated Von Mises stresses are depicted in Fig. 5.15 where a fourth of the bladed-disk is represented along two views. A high concentration of stresses is noted around the blade-tip contact locations, in particular at the leading edge, which are essentially caused by the reduced-order model in which contact forces are applied on points. Further, as shown in Fig. 5.15b, the shaft whirling motions and the associated increase in contact forces appear to induce extremely important stress levels at the blade-foot leading and trailing edges as well as on the shaft near the first bearing.

For other critical rotational speeds, for instance Ω_2 and Ω_3 in Fig. 5.11, even more rapid divergent behaviors are produced (important abradable wear and shaft whirling after 70 revolutions). The associated dynamic behavior of the bladed-disk is in fact very similar: the interaction is initiated by a high frequency mode due to a harmonic EO crossing and as the wear of the abradable layer increases, the system starts being driven by the $n_d = 1$ mode of the 1F family and exhibits a backward whirling orbit of growing amplitudes.

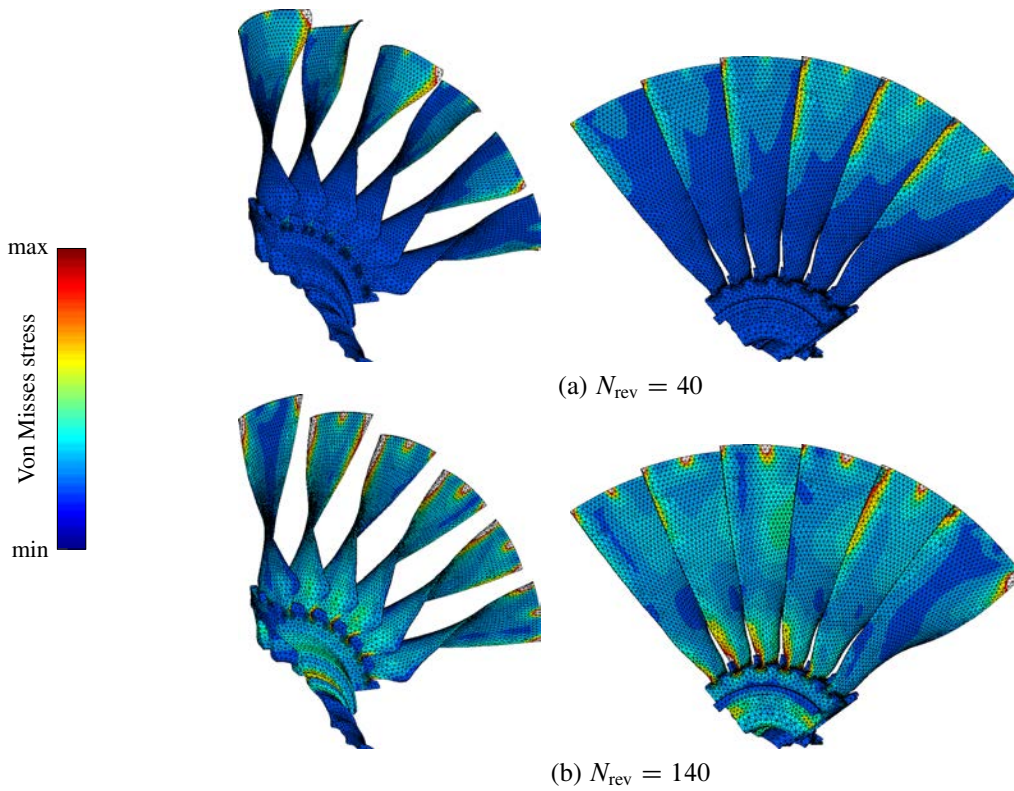


Figure 5.15: Normalized Von Mises stresses for $\Omega = 1.02$

This kind of divergent behavior has never been witnessed in previous studies conducted with COROS, since a rigid shaft was assumed.

5.4.3. Sensitivity to gyroscopic terms

Gyroscopic terms are included in the formulation with the parameters in Tab. 5.1. As detailed in the modal analysis of section 3.3 and recalled in the Campbell diagram 5.6, a non-negligible frequency split between forward and backward rotating waves appears on 1-nodal diameter modes. Hence, a change in the frequency of the 1F mode responsible of the observed divergent motions is to be expected. The corresponding wear maps are depicted in Fig. 5.16, where the same colorcode than in Fig. 5.10 is utilized. For $\Omega < \Omega_3$, similar wear patterns are observed (*e.g.* 6 worn lobes at Ω_2), but a new range of critical speeds is clearly visible for $\Omega \in [1.35; 1.52]$ where the whole abradable layer is removed over the entire casing circumference, both at leading edge and mid-cord, thus clearly indicating that important whirling motions are participating.

Indeed, in the frequency map pictured in Fig. 5.17 a similar frequency content than in Fig. 5.11 is obtained for $\Omega < \Omega_3$. Also, the $n_d = 1$ of the 1F backward mode responds throughout the rotational speed range between 1-EO and 2-EO, and crosses the main EO excitation around $\Omega = 1.3$, after which only divergent

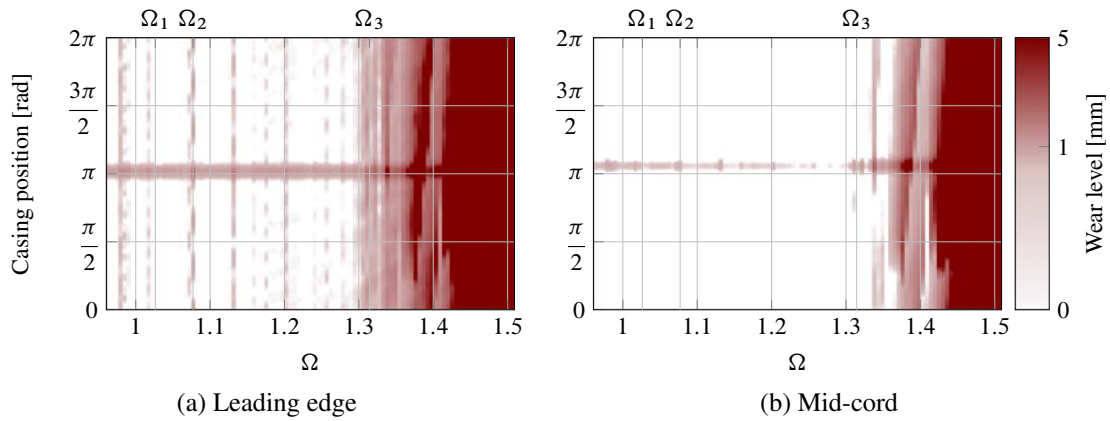


Figure 5.16: Wear maps: multi-sector model with gyroscopic terms

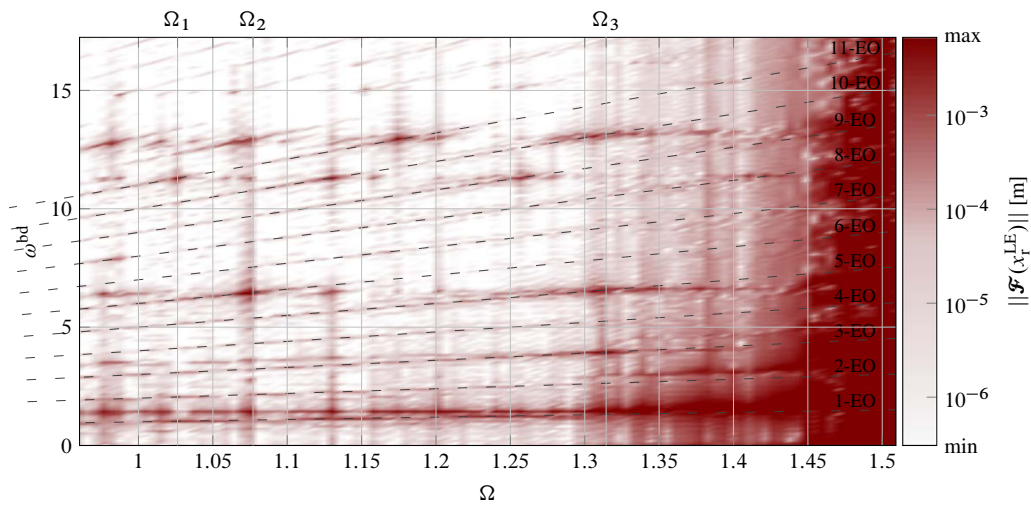


Figure 5.17: Fourier transform of LE displacements

regimes are attained.

Further, in Fig. 5.18, a comparison of the bladed-disk response is provided at Ω_2 with and without gyroscopic terms. The interaction leads to a divergent regime in both cases, with very similar blade radial displacements as well as final abraddable profiles. Although, during the last five revolutions, slightly higher vibration amplitudes are reached when accounting for gyroscopic terms. The 6-lobe wear pattern is present in both configurations, as the bladed-disk is excited by the 6-EO visible in Fig. 5.17 and responds with a normalized frequency of $\omega^{\text{bd}} \simeq 6.45$. The abraddable wear appears to be slightly larger when gyroscopic terms are included in the formulation, in particular in-between lobes, thus indicating that significant whirling motions take place.

The main difference between the two interactions lies in the frequency of the involved $n_d = 1$ divergent

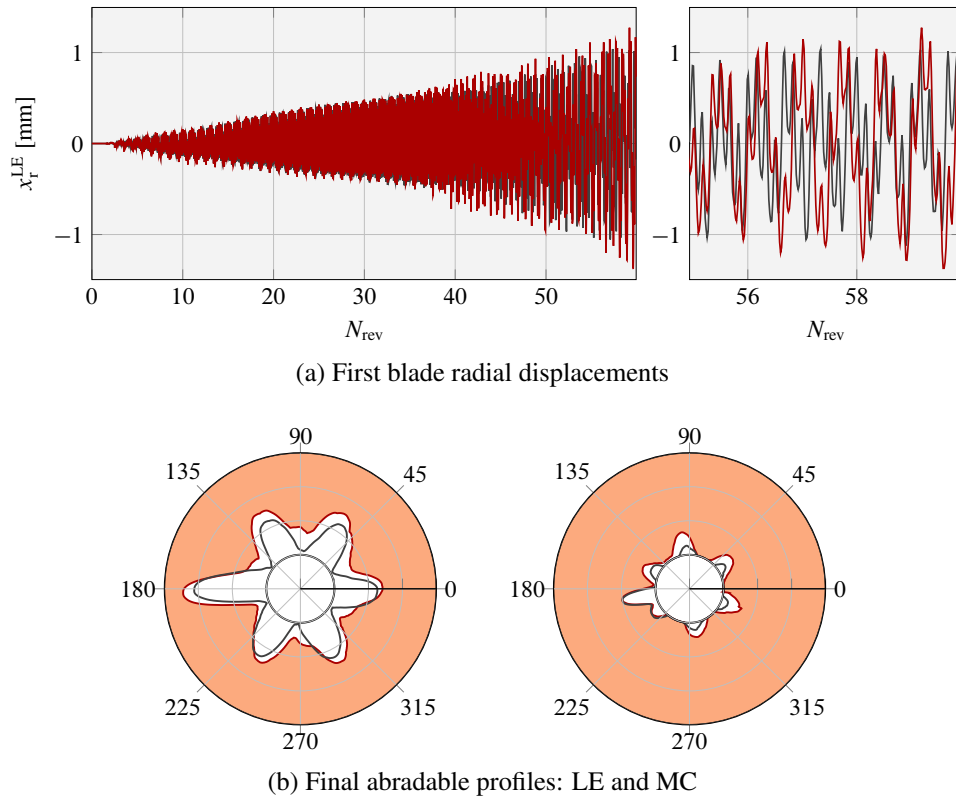
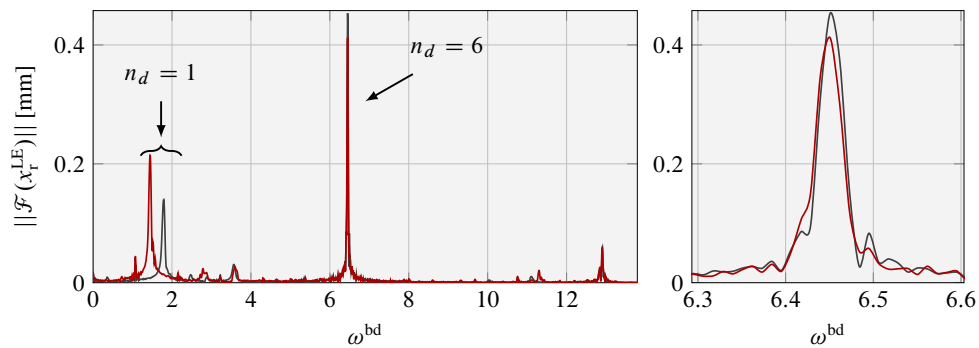


Figure 5.18: Results for Ω_2 : with [—] and without [—] gyroscopic terms

mode, which is in accordance to the modal predictions previously discussed. As shown in Fig. 5.19, the response peaks associated to the $n_d = 6$ mode are almost perfectly superimposed at $\omega^{bd} \simeq 6.45$ while there is a significant difference in the frequency of the $n_d = 1$ modes and their corresponding amplitudes. Indeed,



the frequency drop of the 1F ($n_d = 1$) backward mode induced by the presence of gyroscopic terms results in higher vibratory levels.

With regards to the new range of critical speeds $\Omega \in [1.35 ; 1.52]$ for which the entire abradable layer is removed, for $\Omega = 1.44$, the first blade radial displacements are displayed in Fig. 5.20a. This figure shows

how the bladed-disk responds with growing vibration amplitudes, reaching similar levels than for $\Omega = \Omega_1$ (c.f. Fig. 5.14) but in a much shorter time. As opposed to prior observations, where the interactions are

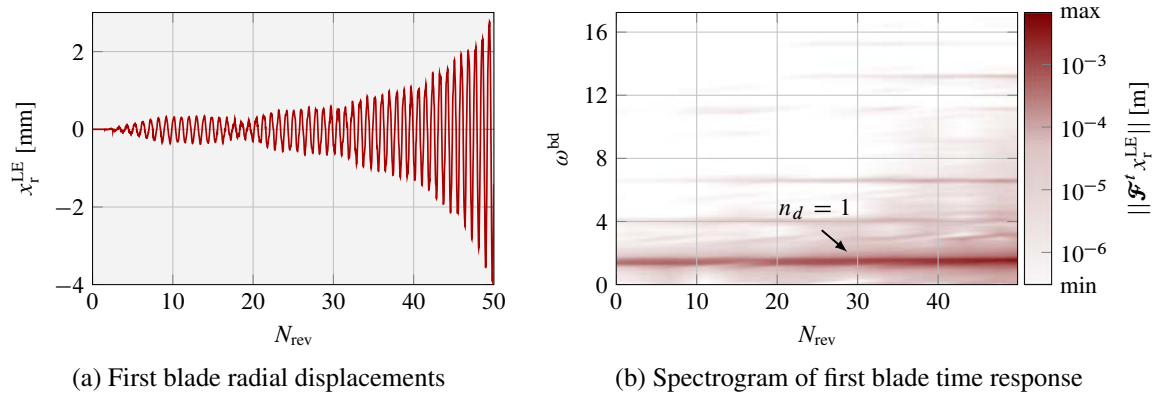


Figure 5.20: Results for $\Omega = 1.44$

initiated by a high frequency mode excited by high EO, it is shown in the spectrogram 5.20b that the $n_d = 1$ harmonic of the 1F modal family is dominant during the entire simulation as it is excited by the 1-EO. This behavior is similar to the interactions observed for the 2D-models (see chapter 4), where the bladed-disk is mainly excited along the 1F modal family.

The displacements are expanded in the full FE-space for 4 sectors in Fig. 5.21a, where it is clearly visible that important off-axis shaft motions take place. Vibration levels are similar in magnitude to those attained at the resonant speed Ω_1 (explored in section 5.4.2). Further, the corresponding Von Mises stresses are represented in Fig. 5.21b, where it can be seen how the bending motions of the shaft generate highly localized stresses near the first bearing and the rear portion of the disk. This is also in accordance with the observations made for the critical speed Ω_1 analyzed in Fig. 5.15 (same colormap). Important stress levels are also attained along the entire blade leading edge as well as at the blade-foot, and around the contact locations at the blade-tip due to the localization of the contact forces on single points.

The bladed-disk vibratory response for all the speeds within this critical range is analogous to the one described for $\Omega = 1.44$, exhibiting a backward whirling motion of growing amplitudes. Hence, these results clearly show that the frequency split on the 1F $n_d = 1$ mode induced by the gyroscopic terms is crucial for the detection of this group of extremely aggressive resonances.

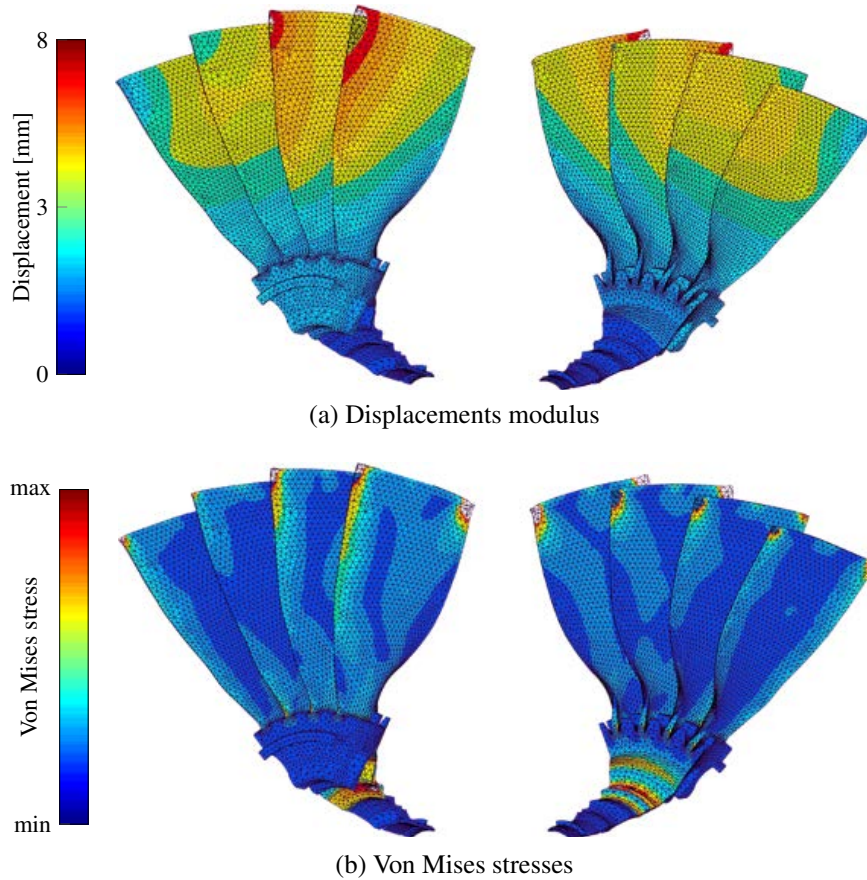


Figure 5.21: Results recast in Finite-Element space for $\Omega = 1.44$ at $N_{\text{rev}} = 45$

5.4.4. Investigation of exploratory scenarios of interaction

5.4.4.1. Contact on the longest blade scenario

Parameters as in Tab. 5.1 are considered, but unilateral and frictional contact constraints are enforced on a *single* sector. The objective is to move closer to the modeling scenario studied in axial compressors [Bat+12; SBL13b] while including the shaft dynamics. The equivalent mono-sector simulations are also presented.

Multi-sector model For the 50 revolutions of simulation time, Fig 5.22 and Fig. 5.10 feature almost identical wear maps. The two main interactions at Ω_2 and Ω_3 are indeed captured, with 6 and 5 worn lobes at the blade leading edge respectively. The main difference is that only pure blade modes are excited when contact is enforced on a single sector. This can be explained by the weak coupling provided by the disk, which is insufficient to transmit important vibratory energies to neighboring sectors. Further, in agreement with the clearance variations and previous results, the abradable wear at mid-cord is much lower than at the leading edge.

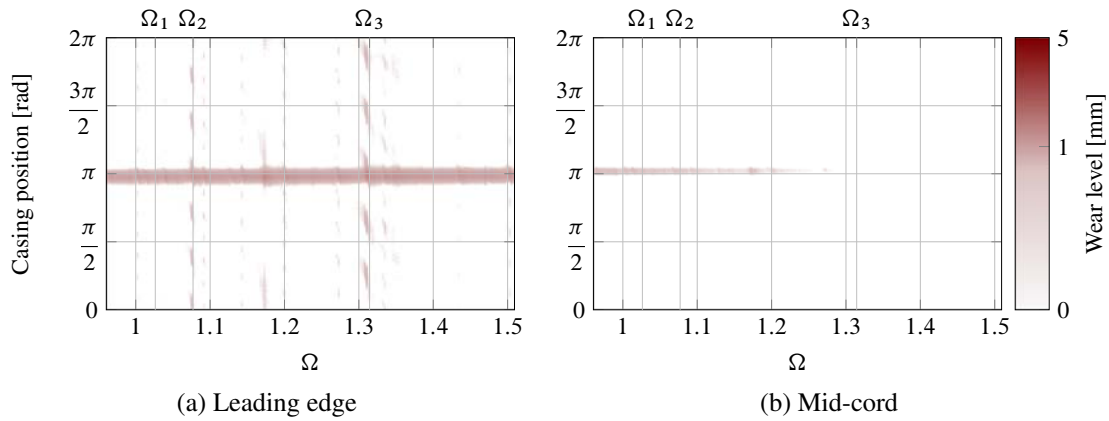


Figure 5.22: Wear maps: multi-sector model with contact on a single blade

In terms of the frequency content, for the blade where contact conditions are enforced, the FFT of leading edge radial displacements is presented in Fig. 5.23. As expected, the response is very similar to the reference simulations in Fig. 5.11. These results clearly indicate that the detected interactions are initiated by blade

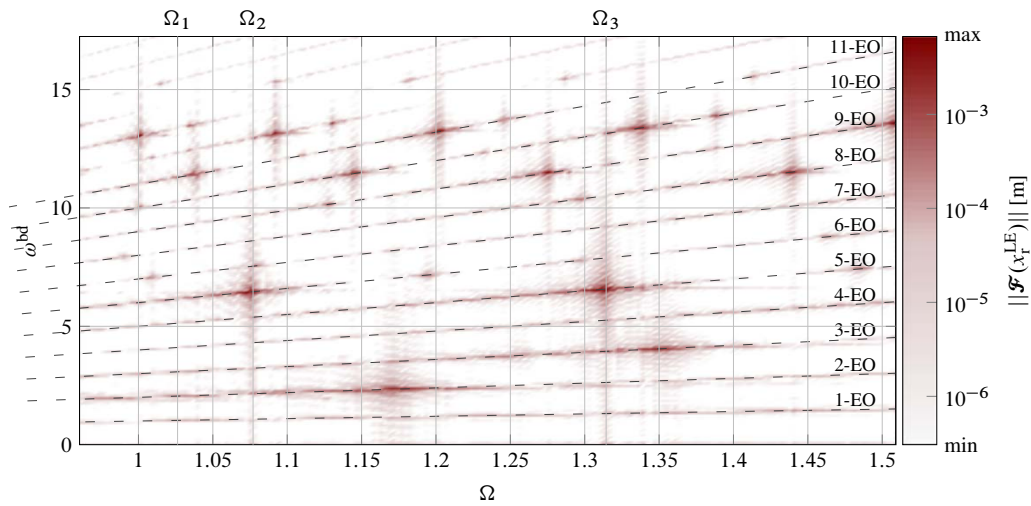
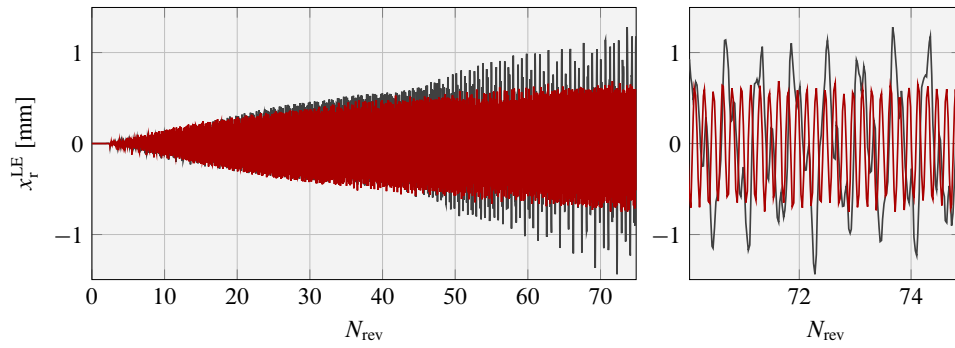


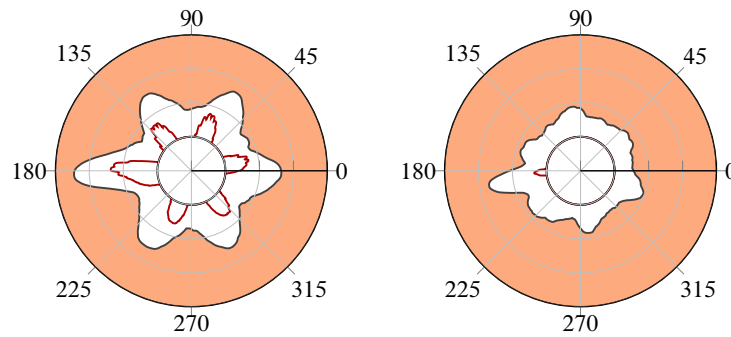
Figure 5.23: Fourier transform of LE displacements

modes, for which the shaft and the disk have a minor contribution.

However, as highlighted in the comparison for $\Omega = \Omega_2$ during 75 rev, major differences are observed both in displacements and wear profiles in Fig. 5.24. When contact solely occurs on one sector, the divergence appears to be contained and vibration levels stabilize with an amplitude of about 0.8 mm, incising the 6 lobe pattern at the leading edge and barely removing any material at mid-cord. While for the reference simulation, the abradable wear is more important and is present throughout the casing circumference, thus indicating a major whirling component. Indeed, the divergence caused by the $n_d = 1$ of the 1F mode—which is highly



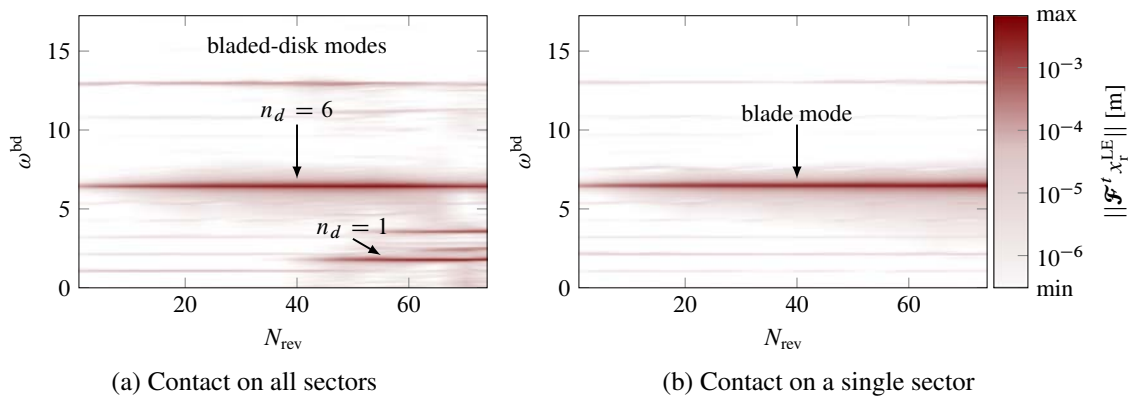
(a) First blade radial displacements



(b) Final abradable profiles: LE and MC

Figure 5.24: Results for Ω_2 : contact on a single [—] or on all [—] sectors

coupled to the shaft dynamics—is only visible in Fig. 5.25a. Whereas in Fig. 5.25b, the blade response is shown to remain on its higher mode with a frequency $\omega^{\text{bd}} \simeq 6.45$.



(a) Contact on all sectors

(b) Contact on a single sector

Figure 5.25: Spectrograms of first blade time response for Ω_2

In conclusion, contact on a single sector is unable to excite the bladed-disk 1-nodal diameter mode which is responsible of the divergence. Thus, for whirling motions to be induced by direct unilateral blade/casing contacts, all sectors are necessarily involved in the interaction.

Mono-sector model Mono-sector simulations are performed with the parameters in Tab. 5.1 and the blade model presented in section 5.2.1. The rotational speed range is extended to lower velocities: $\Omega \in [0.56; 1.5]$.

The resulting wear maps are pictured in Fig. 5.26 for the leading edge and mid-cord. It is clear that all the previously detected interactions cannot be captured with the blade model. Only a 5-lobe interaction is detected at $\Omega \simeq 0.63$. As explained with Fig. 5.5, the clearance variations due to centrifugal effects are

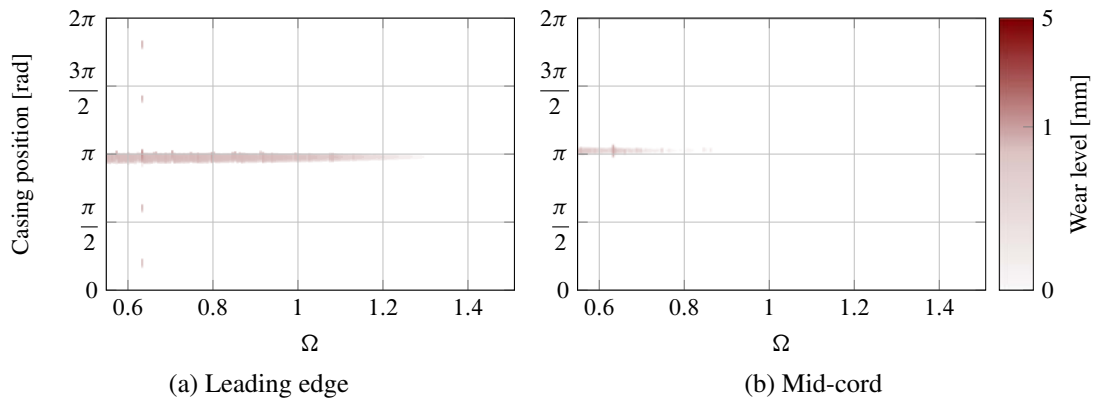


Figure 5.26: Wear maps: single blade model

altered by the over-constraining boundary conditions which fail to account for the deformation of the shaft and disk, and thus significantly modify the initial contact configuration. Also in agreement with Fig. 5.5, contact is lost for $\Omega > 1.3$, at which point no material removal takes place.

In conclusion, since the interactions are mainly initiated by pure blade modes, the optimization of a single blade profile to make it more robust to potential interactions seems essential in early design phases of the engine. Nonetheless, the results provided in this section clearly highlight the importance of considering multi-sector models and how critical it is to accurately predict the blade-tip clearance variations which drive the initial contact configuration.

5.4.4.2. Perfectly rigid shaft scenario

In order to assess the influence of the shaft off-axis motions in the detected interactions, the multi-sector model with additional boundary conditions described in section 5.2.2 is here considered. A comparison of the displacements and wear patterns in Fig. 5.27 at $\Omega = \Omega_2$ indicates that the divergence is suppressed for the over-constrained bladed-disk model. Also, in accordance to the modal analysis provided in Fig. 5.7b, gyroscopic terms scarcely affect the bladed-disk behavior and the associated displacements overlap almost perfectly in Fig. 5.27a. As expected, the resulting abradable profiles exhibit a 6-lobe pattern at the leading edge and almost no material removal at mid-cord.

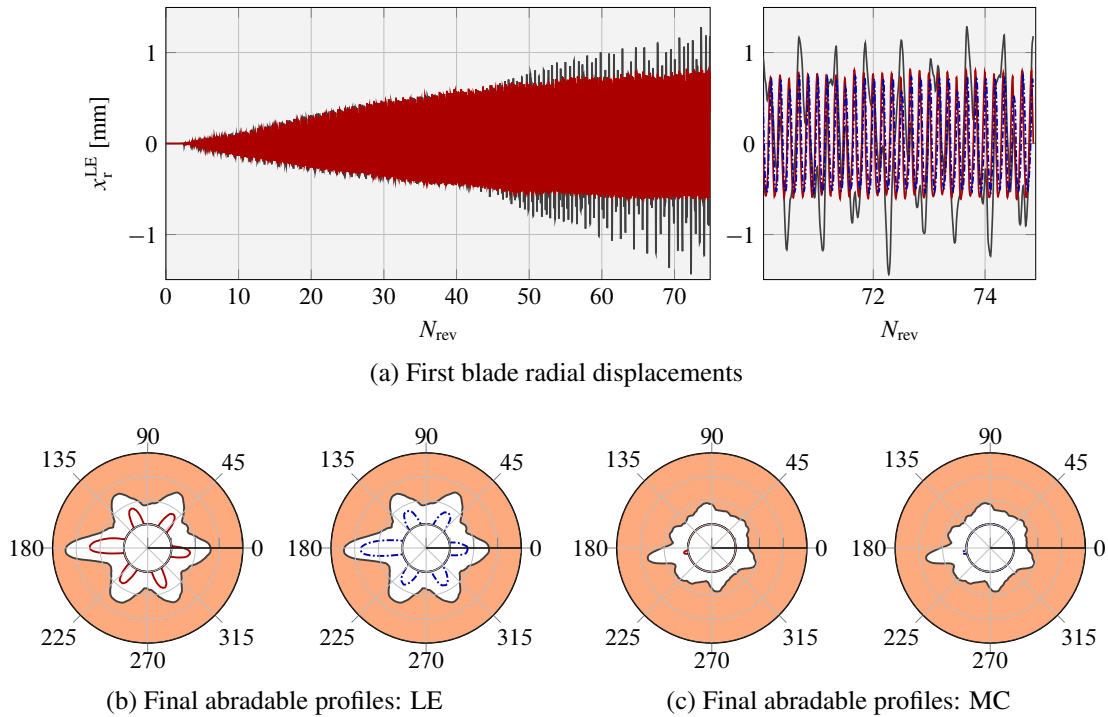


Figure 5.27: Results for Ω_2 : reference model [—]; rigid shaft model with [—] and without [---] gyroscopic terms

Figure 5.28 shows that the bladed-disk with a rigid shaft mainly responds at $\omega^{\text{bd}} \simeq 6.45$ along a 6-nodal diameter shape, which is dominant regardless of the gyroscopic terms. The suppression of potential whirling motions through the rigid shaft avoids the excitation of the 1-nodal diameter mode responsible of the divergence in the reference simulation. These results highlight that the shaft flexibility plays a key role

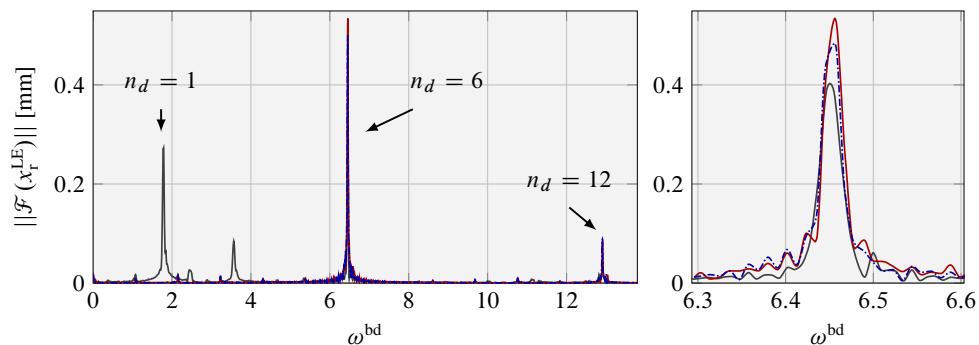


Figure 5.28: Frequency response for Ω_2 : reference model [—]; rigid shaft model with [—] and without [---] gyroscopic terms

in the appearance of divergent vibratory motions, in which high-amplitude backward whirling motions are induced.

5.5. Summary

This chapter deals with an exploratory investigation of bladed-disk/abradable interactions, employing an industrial bladed-disk of the engine fan stage. A previously established time-marching strategy [LBP12] is implemented, where the abradable wear is modeled through an elasto-plastic constitutive law and the casing is statically distorted onto a 1-nodal diameter form in order to absorb the initial blade-tip clearance. The dynamics of the casing is ignored and it solely acts as a mathematical profile dictating the initial shape of the abradable layer.

Several interactions are predicted within the targeted rotational speed range, leading to distinct worn abradable profiles and vibratory levels. These are essentially caused by sub-harmonics of the main EO excitation at crossings with modal lines. An analysis at a resonant speed highlights the central role of the shaft dynamics in producing potentially harmful regimes, as the vibratory energy of the initially excited high-frequency mode shifts towards the 1F mode of $n_d = 1$ and leads to a divergent backward whirling motion in the rotating frame.

Further, it is shown that the frequency split induced by the gyroscopic terms on 1-nodal diameter modes can greatly affect the bladed-disk behavior. As shown in the Campbell diagram, the backward 1-nodal diameter 1F mode becomes tangent with the main EO excitation at high speeds and results in a group of extremely aggressive resonances. During these regimes, high stress levels are mainly localized near the bladed-disk first bearing and the rear portion of the disk.

Two hypothetical scenarios are also explored:

- Unilateral contact on single blade, often evoked in axial compressors, is investigated for both the multi-sector and mono-sector models. For the bladed-disk model, only localized blade modes are excited and the divergence appeared to be suppressed, indicating that all sectors are necessarily involved in the interaction for whirling motions to occur. Also, the over-constraining boundary conditions at blade-foot for the single blade model did not allow to capture any of the interactions.
- The suppression of off-axis motions through additional boundary conditions on the disk avoids the excitation of the 1-nodal diameter mode responsible of the divergence. Hence, a stiffer shaft is less prone to exhibit high-amplitude whirls and limits the interactions solely to the blades.

Modeling of abradable coating removal through delay differential equations

This chapter is mainly composed of the work presented in [SBL13a; SBL13b; SBL13c], where a novel method for the modeling of abradable material removal is developed. The plastic constitutive law [LBP12] is replaced by a simplified formulation of the contact force, storing the abradable wear in a delay term, thus yielding a set of delay differential equations. The detailed MATLAB code is presented in appendix B. As will be explained in the following, this qualitative analysis of the blade/abradable interaction proves to be a viable alternative to the costly time-marching techniques—implemented in chapters 4 and 5—generally utilized for studying this nonlinear phenomenon. In this exploratory investigation, the dynamic contribution of the shaft targeted in previous chapters is neglected, thus employing a single blade model as a first approximation of the interaction events.

Delay differential equations (DDE) differ from ordinary differential equations (ODE) in that the system of interest involves lags [Ern09]. Retarded DDE, that only involve the delayed state of the system, are usually distinguished from advanced and neutral DDE, for which the equation involves both delayed states and delayed rates of change. Only retarded DDE with a single constant delay will be considered in this investigation:

$$\dot{\mathbf{z}}(t) = \mathbf{g}(t, \mathbf{z}(t), \mathbf{z}(t - \tau)) \quad (6.1)$$

where t is the time, τ is the so-called time delay and $\dot{\mathbf{z}}$ denotes the derivative of \mathbf{z} with respect to time. Accordingly, one of the major differences between DDE and ODE, is that initial conditions of a DDE are a function defined over the interval $[-\tau; 0]$, while for ODE a single vector at $t = 0$ is required.

DDE are used in widely different fields such as species dynamics [WC97], neural networks [CYL06] and

torque control within combustion engines [CP88] to name a few. In manufacturing, DDE have proved to be very suitable for the modeling of the cutter-workpiece interaction phenomena occurring in various machining processes such as milling [Sté+05] and turning [IST07]. In these research areas, it is highly desirable to avoid self-excited vibrations between the cutter and the workpiece, also known as chatter effect, in order to obtain smooth surfaces without major wear of the tool. The equations of motion, which are a simplified version of Eq. (2.1), are generally written as:

$$\mathbf{M}\ddot{\mathbf{x}}(t) + \mathbf{D}\dot{\mathbf{x}}(t) + \mathbf{K}\mathbf{x}(t) = \mathbf{f}(t, \mathbf{x}(t), \mathbf{x}(t - \tau)) \quad (6.2)$$

where the external forcing term is a function of the delayed state of the system.

As depicted in Fig. 6.1, milling shares similarities with the aircraft engine structural interaction events discussed in the previous chapters: blade-tips may slightly cut the surrounding abradable coating due to vibrations of the blades or the casing. Abradable coatings are implemented as a sacrificial material deposited

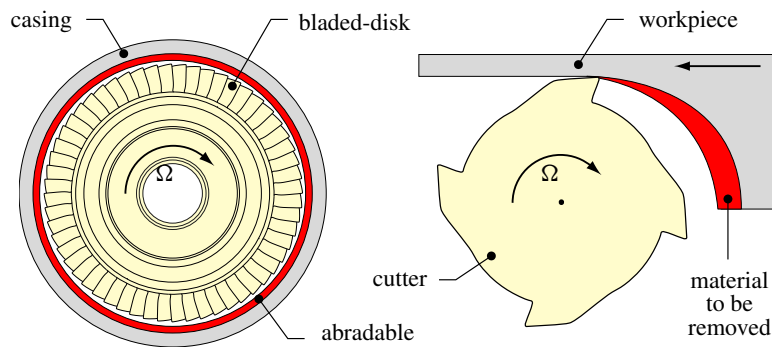


Figure 6.1: Analogy between abradable removal and milling

on the casing in order to minimize operating clearances while mitigating direct blade/casing structural contacts. However, as detailed in chapter 5, blade/abradable interactions may lead to blade structural failure thus jeopardizing safety. An accurate modeling of the abradable coating removal is of prime importance to better understand the initiation of the divergence. As discussed in section 2.2.5, two models are proposed in the literature [Bat+12; Wil11] and a good agreement with experimental data was found. However, the proposed solution methods involve costly time-stepping techniques that are not well adapted to fast sensitivity analyses.

An improved understanding of the interaction calls for a qualitative model to quickly identify critical rotational speeds or critical material parameters for instance. On that account, the present study aims at taking advantage of the DDE framework to explore the stability of the equilibrium position of the abradable-incurring blades system. A rod-like blade model is studied in [Sal11], using two stability analysis techniques:

Semi-Discretization Method (SDM) and Chebyshev Collocation. Different critical speeds are predicted and compared to a penalty time-stepping algorithm.

Similar to the assumptions considered in [Sal11], it is supposed that the axis of rotation of the shaft is perfectly rigid and contact initiation between the blade-tip and surrounding abradable coating originates from casing distortion or blade vibration only. Even if actual blade/abradable contacts are not permanent as shown in chapter 5, it is here assumed that the blade never separates from the abradable layer during the revolution considered for the stability analysis, which is in agreement with what is inferred in the modeling of the milling and turning processes¹.

First, the respective mathematical background is briefly recalled. The second section is devoted to the industrial model of the targeted compressor blade, also, main assumptions, limitations, and properties of the developed model of abradable coating removal through DDE are introduced. A convergence study is carried out in the third section in order to ensure the accuracy of the results. Finally, the results are compared with existing time-domain simulations, the sensitivity to frictional forces is addressed and a comparison of different blade profiles is presented.

6.1. Delay differential equations

6.1.1. Theoretical background

DDE are a mathematical tool commonly used to model the dynamical behavior of systems involving lags [GN03], *i.e.* the evolution of the system $\dot{\mathbf{z}}(t)$ not only depends on its current state $\mathbf{z}(t)$, but also on a past state $\mathbf{z}(t - \tau)$ as specified in Eq. (6.1). For more formal developments, such as proves of uniqueness and existence of solutions, as well as fundamental definitions and terminology of DDE, refer to [Die+95].

Generally, DDE are classified in the literature into five categories depending on the nature of the delay term in Eq. (6.4) [BKG09]:

- single constant delay: $\tau_i = \tau_1 = \tau$, which is the simplest and most frequently encountered case,
- multiple discrete delays: $\tau_i = [\tau_1 ; \tau_2 \dots \tau_n]$,
- distributed or continuous delays, where the delayed term takes a weighted integral form: $\dot{\mathbf{z}} = \mathbf{g}(t, \mathbf{z}(t), \int_0^\infty \alpha(\tau) \mathbf{z}(t - \tau) d\tau)$, as in viscoelasticity,
- time-dependent delays: $\tau = \tau(t)$,
- state-dependent delays: $\tau = \tau(\mathbf{z}(t))$.

¹The relative displacement between the tool and the workpiece usually makes it possible to consider that, at any time t , the cutter is in contact with the workpiece. Only a few studies consider cutter/workpiece detachment [Dom+11; Lon06].

Even if all these kind of DDE have several uses in the engineering field [KH10], in the particular case of mechanical systems, the delay is often constant and the forcing term \mathbf{f} in Eq. (6.2) is written as:

$$\mathbf{f}(t) = \mathbf{\Gamma}(t)(\mathbf{x}(t - \tau) - \mathbf{x}(t)) \quad (6.3)$$

where $\mathbf{\Gamma}(t)$ is a time-dependent external forcing matrix. By introducing state-space coordinates in order to obtain a first order DDE, Eqs. (6.2) and (6.3) yield:

$$\dot{\mathbf{z}}(t) = \mathbf{A}(t)\mathbf{z}(t) + \mathbf{B}(t)\mathbf{z}(t - \tau) \quad (6.4a)$$

$$\mathbf{z}(t) = \boldsymbol{\varphi}(t), \quad t \in [-\tau; 0] \quad (6.4b)$$

with

$$\mathbf{z}(t) = \begin{pmatrix} \mathbf{x}(t) \\ \dot{\mathbf{x}}(t) \end{pmatrix}, \quad \mathbf{A}(t) = \begin{bmatrix} \mathbf{0}_n & \mathbf{I}_n \\ -\mathbf{M}^{-1}(\mathbf{K} + \mathbf{\Gamma}(t)) & -\mathbf{M}^{-1}\mathbf{D} \end{bmatrix} \quad \text{and} \quad \mathbf{B}(t) = \begin{bmatrix} \mathbf{0}_n & \mathbf{0}_n \\ \mathbf{M}^{-1}\mathbf{\Gamma}(t) & \mathbf{0}_n \end{bmatrix} \quad (6.5)$$

where, $\mathbf{z}(t)$ is the $2n$ -dimensional state-space vector, $\mathbf{A}(t)$ and $\mathbf{B}(t)$ ² are $2n \times 2n$ matrices dependent on the system parameters and external forcing term, and $\boldsymbol{\varphi}$ is the initial condition function that is defined over the interval $[-\tau; 0]$.

Two cases are of particular interest:

1. *DDE with constant coefficients*: $\mathbf{A}(t) = \mathbf{A}$ and $\mathbf{B}(t) = \mathbf{B}$ are constant matrices. This kind of equations are often called Linear Time Invariant (LTI) delayed systems,
2. *DDE with time-periodic coefficients*: $\mathbf{A}(t + T) = \mathbf{A}(t)$ and $\mathbf{B}(t + T) = \mathbf{B}(t)$, where T is the period.

When the aforementioned conditions are satisfied, the first order system given in Eqs. (6.4) and (6.5) is propitious to a stability analysis of the $\mathbf{z} = \mathbf{0}$ solution, also referred to as equilibrium solution. In the present chapter, both cases are considered, limiting the theoretical developments to the case $T = \tau$.

6.1.2. Stability analysis

Different methods have been developed to study DDE throughout the years [GN03], and from the literature, these are often divided into two categories. A first class attempts to derive a nonlinear eigenvalue problem assuming an *ansatz* exponential solution to obtain the characteristic equation of Eq. (6.4) in the Laplace domain written as:

$$\det(s\mathbf{I} - \mathbf{A} - \mathbf{B} \exp(-\tau s)) \quad (6.6)$$

²Since the considered DDE is of retarded type, note that the last n columns of $\mathbf{B}(t)$ are zeros accordingly.

where s is the Laplace variable, \mathbf{A} and \mathbf{B} are necessarily constant matrices (Linear Time Invariant DDE) and the time delay $\tau > 0$.

The delay introduces an exponential term within the characteristic equation (6.6), thus, the derived delayed eigenvalue problem becomes infinite-dimensional [Jar08]. Dedicated solution methods generally consider a rational or polynomial approximation of the characteristic equation in order to solve it such as the Solution Operator Discretization (SOD) and the Infinitesimal Generator Discretization (IGD) methods.

A recent method called Cluster Treatment of Characteristic Roots (CTCR) was developed by [OS02], for which the exponential term in Eq. (6.6) is replaced by a polynomial expansion derived from [Rek80]. Since the stability of the zero solution is driven by $\Re(s)$, the CTCR aims at the exact computation of all purely imaginary characteristic roots by means of an explicit expression. It was very recently applied to the blade/casing rub problem [OZK14], considering a rod-like blade model similar to [Sal11] and including the dynamics of the casing through a modal decomposition. The stability results obtained via the CTCR are compared to the SDM, exhibiting an important gain in computational times as well as much higher accuracy at low rotational speeds. However, it seems unclear how the blade to casing relative displacement induced by the blade rotation is accounted for in the formulation.

A second family—capable of dealing with time-periodic coefficients and known as spectral methods—aims at building the monodromy matrix Φ which connects the state of the system at time t_i to its delayed counterpart at $t_i - \tau$, *i.e.* $\mathbf{z}(t_i) = \Phi \mathbf{z}(t_i - \tau)$. The monodromy matrix Φ is in fact a finite-dimensional approximation of the monodromy operator, which acts on the space of continuous functions and is infinite-dimensional. Different approaches have been developed, for example, the SDM [IS04], the full discretization method [Din+10], collocation techniques employing Chebyshev [BB11] or Legendre polynomials as well as temporal finite element analysis [KM11]. A recent method was developed by [DZD14] where the DDE is

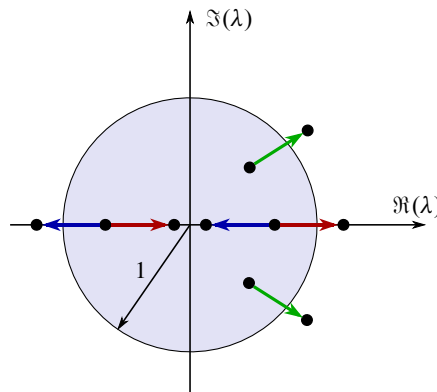


Figure 6.2: Bifurcation mechanisms: Hopf [—], period-doubling [—] and cyclic-fold [—]

discretized into a set of algebraic equations using Daubechies wavelets in order to obtain an approximation of Φ . From Floquet theory, the stability of the zero solution is addressed through the computation of the eigenvalues λ of Φ . Different bifurcation mechanisms may be predicted, such as Hopf, period-doubling or flip, and cyclic-fold bifurcations depending on the values of λ [BKG09], as illustrated in Fig. 6.2.

6.1.3. Semi-Discretization Method

The Semi-Discretization Method (SDM) is a recent development in the stability analysis of linear time-periodic DDE. It builds an approximation of the previously introduced monodromy operator and computes its eigenvalues. Floquet theory is then invoked for the stability analysis. SDM has been used for the analysis of a delayed Mathieu equation, as well as in turning and milling applications [IS11].

For a linear time-periodic $2n$ -dimensional DDE such as Eq. (6.4), the SDM is based on the discretization of the delayed term $\mathbf{z}(t - \tau)$ into a piece-wise constant function over one time period $\tau = M \Delta t$, while all the other time-dependent terms remain unchanged. For Δt sufficiently small (or M sufficiently large), the time-step interval is defined as $\Delta t = [t_i ; t_{i+1}]$, with $t_i \in [0 ; \tau]$ and $i = 0, 1 \dots (M - 1)$.

This way, $\forall t \in [t_i ; t_{i+1}]$, Eq. (6.4) may be approximated by:

$$\dot{\mathbf{z}}(t) = \mathbf{A}(t)\mathbf{z}(t) + \mathbf{B}(t)\mathbf{z}_{\tau,i} \quad (6.7)$$

where $\mathbf{z}_{\tau,i}$ is a weighted linear combination of the delayed vectors $\mathbf{z}(t_{i-M})$ and $\mathbf{z}(t_{i-M+1})$:

$$\mathbf{z}_{\tau,i} = \frac{1}{2}\mathbf{z}_{i-M+1} + \frac{1}{2}\mathbf{z}_{i-M} \simeq \mathbf{z}(t - \tau) \quad (6.8)$$

The delayed term is thus assumed to be constant over $[t_i ; t_{i+1}]$ yielding a finite-dimensional ODE approximation of (6.4) for which a general analytical solution is available in the form:

$$\mathbf{z}(t) = \exp(\mathbf{A}_i(t - t_i))(\mathbf{z}_i + \mathbf{A}_i^{-1}\mathbf{B}_i\mathbf{z}_{\tau,i}) - \mathbf{A}_i^{-1}\mathbf{B}_i\mathbf{z}_{\tau,i} \quad (6.9)$$

where $\mathbf{z}(t_i) = \mathbf{z}_i$ is a chosen initial condition, and the discrete linear coefficients are approximated by their mean value over the chosen interval as:

$$\mathbf{A}_i = \frac{1}{\Delta t} \int_{t_i}^{t_{i+1}} \mathbf{A}(t) dt \quad \text{and} \quad \mathbf{B}_i = \frac{1}{\Delta t} \int_{t_i}^{t_{i+1}} \mathbf{B}(t) dt \quad (6.10)$$

Merging Eqs. (6.8) and (6.9) at $t = t_{i+1}$ leads to:

$$\mathbf{z}_{i+1} = \mathbf{P}_i\mathbf{z}_i + \frac{1}{2}\mathbf{R}_i\mathbf{z}_{i-M+1} + \frac{1}{2}\mathbf{R}_i\mathbf{z}_{i-M} \quad (6.11)$$

with $\mathbf{P}_i = \exp(\mathbf{A}_i \Delta t)$ and $\mathbf{R}_i = (\exp(\mathbf{A}_i \Delta t) - \mathbf{I}_{2n})\mathbf{A}_i^{-1}\mathbf{B}_i$. Accordingly, a discrete map can be built which defines a $n(N + 1)$ column state vector \mathbf{y}_i as:

$$\mathbf{y}_i = [\mathbf{x}_i \dot{\mathbf{x}}_i \mathbf{x}_{i-1} \mathbf{x}_{i-2} \cdots \mathbf{x}_{i-N}]^T \quad \text{and} \quad \mathbf{y}_{i+1} = \mathbf{D}_i^{\text{SDM}} \mathbf{y}_i \quad (6.12)$$

with:

$$\mathbf{D}_i^{\text{SDM}} = \begin{bmatrix} \mathbf{P}_{i,1:n} & \mathbf{P}_{i,n+1:2n} & \mathbf{0}_n & \cdots & \mathbf{0}_n & \frac{1}{2}\mathbf{R}_{i,1:n} & \frac{1}{2}\mathbf{R}_{i,1:n} \\ \mathbf{I}_n & \mathbf{0}_n & \mathbf{0}_n & \cdots & & \mathbf{0}_n & \mathbf{0}_n \\ \mathbf{0}_n & \mathbf{0}_n & \mathbf{I}_n & & & \mathbf{0}_n & \mathbf{0}_n \\ \vdots & & & \ddots & & & \vdots \\ \mathbf{0}_n & \mathbf{0}_n & & & \mathbf{I}_n & \mathbf{0}_n & \mathbf{0}_n \\ \mathbf{0}_n & \mathbf{0}_n & \cdots & & \mathbf{0}_n & \mathbf{I}_n & \mathbf{0}_n \end{bmatrix} \quad (6.13)$$

where $\mathbf{P}_{i,1:n}$ denotes the 1 to n columns of the matrix \mathbf{P}_i . Because the delay applies on displacements, only the first n columns of matrix \mathbf{R}_i are accounted for and the delayed terms in speed are not included in the discrete map. An approximation of the monodromy operator Φ can then be built:

$$\mathbf{y}_M = \Phi \mathbf{y}_0 \quad \text{with} \quad \Phi = \mathbf{D}_{M-1}^{\text{SDM}} \mathbf{D}_{M-2}^{\text{SDM}} \cdots \mathbf{D}_1^{\text{SDM}} \mathbf{D}_0^{\text{SDM}} \quad (6.14)$$

where the number of multiplications required to build Φ solely depends on the time discretization M , whereas the size of the system is dependent on both time and spatial discretizations. Finally, the stability analysis tests whether the eigenvalues moduli of Φ are less than 1 or not.

6.2. Modeling strategy

In agreement with experimental and numerical investigations reported in [Mil+09] and [Bat+12], it is assumed that the interaction phenomenon of interest involves a single blade and the surrounding abradable coating. Hence, as a first approximation, the dynamic contribution of the shaft and its potential off-axis displacements are ignored. For this exploratory investigation the blade of interest, depicted in Fig. 6.3, was studied in [Bat+12] and belongs to the last stage of the low-pressure compressor of an aircraft engine similar to the one pictured in Fig. 1.1. The finite element mesh of the blade comprises over 11000 quadratic tetrahedron elements and 22500

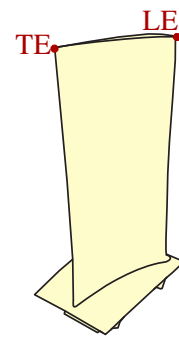


Figure 6.3: Blade of interest

connecting nodes. Similar to previous chapters, Craig-Bampton mode synthesis is employed to obtain a reduced-order model, in which contact between blade and abradable coating is treated on carefully selected boundary nodes on the blade tip. The number and location of these nodes (between the leading edge and the trailing edge) vary in this work depending on the contact configuration of interest.

6.2.1. Cutting law in milling

During the cutting process in milling, when vibrations between cutter and workpiece are negligible, the evolution of the nominal chip thickness h is periodic and depends on the cutting angle ϕ and the feed per tooth f_t . Since the cutting force F is often considered as proportional to the chip thickness, it is also time-periodic:

$$F(t) = K_e h(t) \quad \text{with} \quad h(t) = f_t \sin(\phi(t)) \quad (6.15)$$

where K_e is the so-called *specific force coefficient* and depends on the workpiece material and the depth of cut [Tlu00].

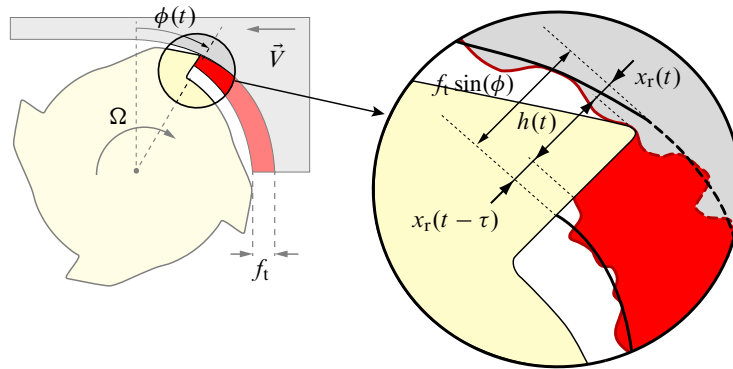


Figure 6.4: Schematic of milling with chatter

When chatter occurs, either arising from regenerative waviness or mode-coupling, the uneven surface produced during the cut results in a variation of the instantaneous chip thickness, and the corresponding variations of the cutting force give rise to self-excited vibrations [Tlu00]. The dependence of the chip thickness h on the cutter's radial position x_r —quantity directly extracted from the displacements vectors $\mathbf{x}(t)$ and $\mathbf{x}(t - \tau)$ —may be written as:

$$h(t) = f_t \sin(\phi(t)) + x_r(t - \tau) - x_r(t) \quad (6.16)$$

as illustrated in Fig. 6.4.

Accounting for the vibrations around the teeth nominal paths leads to a system of coupled DDEs, and the

typical state-space model used in milling is similar to the one defined in Eq. (6.4). It usually involves one or two degree-of-freedom models of the cutter and/or the workpiece. The stability analysis of the rest position is used to maximize material removal rates without reaching instability zones [Sté+05].

6.2.2. Abradable material removal strategy

Differing from [SBL13b], not only radial displacements of the blade boundary nodes are considered and stored in vector \mathbf{x}_b , but the tangential ones are also kept in the reduced space in order to account for frictional forces in the formulation. Depending on the number of nodes and their location, different contact configurations may be reproduced.

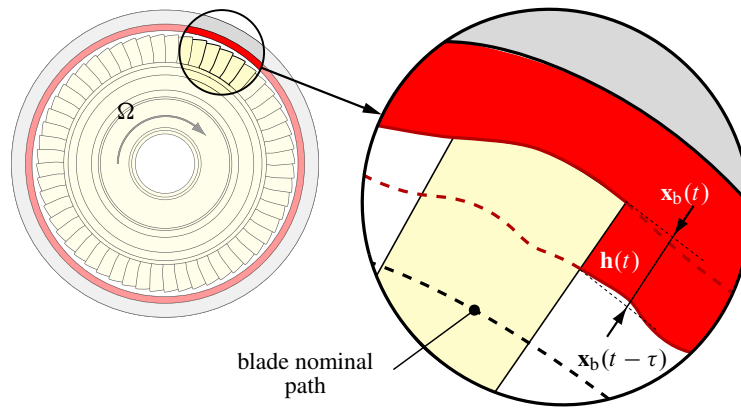


Figure 6.5: Schematic of abradable material removal

Similarly to the milling derivations, a cutting force proportional to the penetration now approximates the contact force arising from the incursion of the blade-tip in the abradable lining. This penetration is determined by the difference between the blade-tip displacement from one revolution to the succeeding one as shown in Fig. 6.5, while assuming that there is no separation between the blade and the abradable layer; the radial contact force becomes:

$$\mathbf{f}^r(\mathbf{h}(t)) = K_e \mathbf{h}(t) = K_e [\mathbf{x}_b^r(t - \tau) - \mathbf{x}_b^r(t)] \quad (6.17)$$

where the thickness of the removed abradable material is stored in vector \mathbf{h} , dependent on the radial displacement of the boundary nodes \mathbf{x}_b^r from one revolution to the next and the contact configuration modeled. The associated frictional forces are deduced by a linear Coulomb law under the assumption that permanent sliding occurs:

$$\mathbf{f}^t(t) = -\mu \mathbf{f}^r(t) = \mu K_e [\mathbf{x}_b^r(t) - \mathbf{x}_b^r(t - \tau)] \quad (6.18)$$

where μ is the friction coefficient.

Therefore, the governing equation of motion are of the form of Eqs. (6.2) and (6.3), where $\Gamma(t) = \Gamma$ becomes a constant matrix—due to the permanent contact assumption³—storing the cutting force coefficient K_e and μK_e applied on the selected boundary nodes.

As shown in [SBL13b], a convenient use of modal coordinates $\mathbf{x} = \mathbf{V}\mathbf{u}$ allows to determine the contribution of specific modes and avoid the inversion of the mass matrix. The resulting equation of motion may be written as:

$$\ddot{\mathbf{u}}(t) + 2\xi\mathbf{\Lambda}\dot{\mathbf{u}}(t) + \mathbf{\Lambda}^2\mathbf{u}(t) = \mathbf{V}^T\mathbf{\Gamma}\mathbf{V}[\mathbf{u}(t - \tau) - \mathbf{u}(t)] \quad (6.19)$$

where ξ is the modal damping coefficient, $\mathbf{\Lambda}^2$ is a diagonal matrix containing the blade eigenfrequencies and \mathbf{V} the associated eigenvectors. The system in the modal space may then be recast into its state-space form and yields a system of first order linear coupled DDE as Eq. (6.4), where:

$$\mathbf{A} = \begin{bmatrix} \mathbf{0}_n & \mathbf{I}_n \\ -\mathbf{\Lambda}^2 - \mathbf{V}^T\mathbf{\Gamma}\mathbf{V} & -2\xi\mathbf{\Lambda} \end{bmatrix} \quad \text{and} \quad \mathbf{B} = \begin{bmatrix} \mathbf{0}_n & \mathbf{0}_n \\ \mathbf{V}^T\mathbf{\Gamma}\mathbf{V} & \mathbf{0}_n \end{bmatrix} \quad (6.20)$$

the size of the matrices \mathbf{A} and \mathbf{B} depending on the number of modes n kept in the modal projection. The MATLAB code employed for the described stability analysis procedure is detailed in Appendix B.

6.3. Preliminary results

A stability analysis of the equilibrium solution with respect to combinations of the cutting force coefficient K_e , introduced in Eq. (6.17), and the rotational speed Ω . It is conducted within the interval $K_e \in [0; 2.5] \times 10^4 \text{N/m}$, so that the cutting forces are consistent with results reported in [Bat+12]. All frequencies in this section are normalized with respect to the first eigenfrequency of the blade at rest. Accordingly, the explored rotation speed range is $\Omega \in [0; 0.45]$.

6.3.1. Validation and convergence analysis

Cutting conditions are only handled at the leading edge. The respective stability diagram is shown in Fig. 6.6 where the grey lobes display unstable configurations. This diagram determines whether the rest position $\mathbf{z}(t) = \mathbf{0}$ of the blade is stable or not. These results are compared to direct time integration of the DDE (6.4) carried out with the MATLAB `dde23` function, into which a constant radial displacement of the leading edge

³In addition to this assumption, unlike machining processes, the abradable coating removal in turbomachinery does not involve a feed.

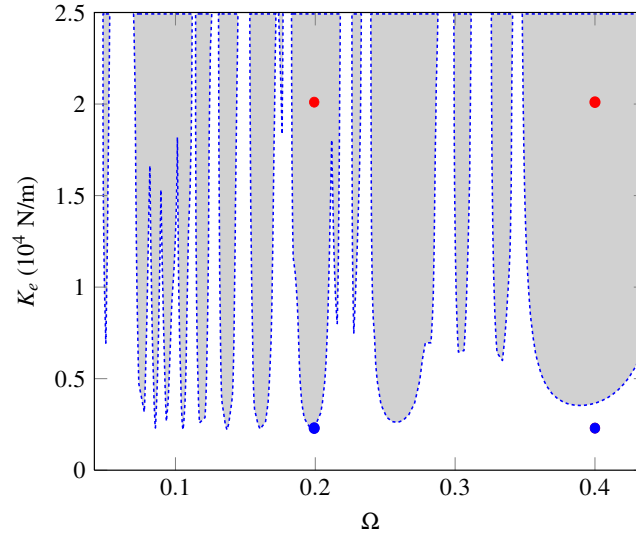


Figure 6.6: Test points: [●] stable domain ($K_e = 2 \cdot 10^3$ N/m);
[●] unstable domain ($K_e = 2 \cdot 10^4$ N/m)

over the first revolution is prescribed as an initial condition:

$$\forall t \in [-\tau; 0], \quad \mathbf{z}^T(t) = (\mathbf{x}^T(t) \quad \dot{\mathbf{x}}^T(t)) = (x_{b,LE}^0 \quad 0 \quad \dots \quad 0) \quad (6.21)$$

with $x_{b,LE}^0 = 2$ mm. Time integration is performed over 30 revolutions for four combinations of (K_e, Ω) yielding both stable and unstable configurations.

As depicted in Fig. 6.7 both stable and unstable solutions picked from diagram 6.6 are accurately reproduced with time-integration of the DDE. In Fig. 6.7a, the solution diverges faster than in Fig. 6.7b

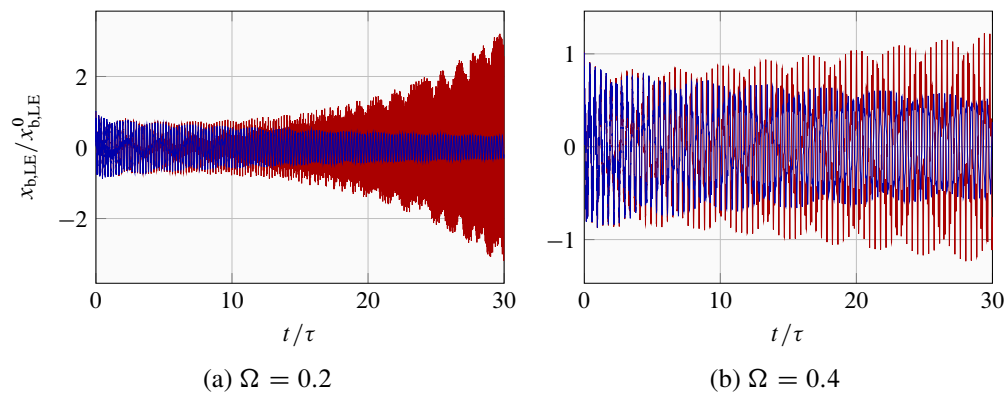


Figure 6.7: Tip radial displacement: $K_e = 2 \cdot 10^3$ N/m [—]
and $K_e = 2 \cdot 10^4$ N/m [—]

since the maximum eigenvalue modulus of the respective monodromy matrix is higher for the explored configuration.

In order to ensure accuracy, two types of convergence are pursued: time and modal convergence. The first type entails the convergence of the uniform mesh into which the time-period is discretized while the second focuses on the number of modes retained for the simulation. In these convergence studies, centrifugal stiffening effects are not accounted for and only contact at the leading edge is considered.

The number M of time steps per period depends directly on the value of the delay $\tau = M\Delta t$, since the time-step Δt must be sufficiently small for the method to converge. Therefore, it is for lower rotational speeds Ω —as $\tau = 1/\Omega$ —that a very large M may be required. Results pictured in Fig. 6.8 for increasing

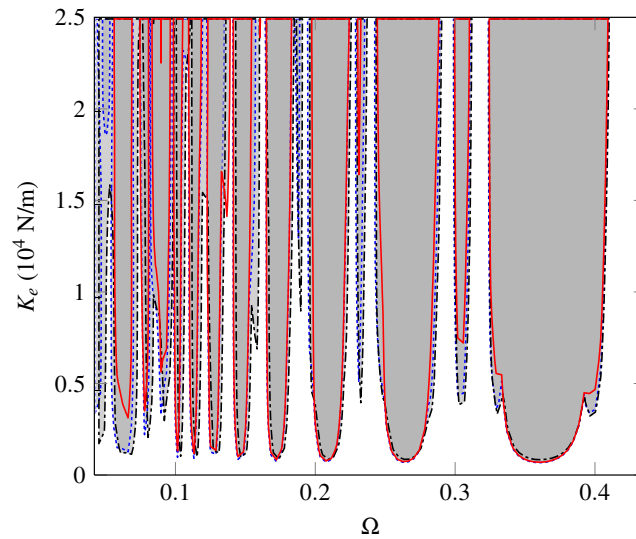


Figure 6.8: Time convergence: $M = 40$ [—]; $M = 60$ [---], and $M = 80$ [-.-.]

M highlight that for large rotational speeds ($\Omega > 0.25$), $M = 40$ is sufficient to obtain accurate results. However, for lower rotational speeds, an accurate superimposition of the stability lobes is only achieved for $M \geq 60$. Accordingly, $M = 60$ is kept for all subsequent simulations.

In addition, stability lobes are also dependent on the n modes retained in the projection of Eq. (6.19). Figure 6.9 underlines that the first eigenmode (first flexural mode or 1F) is not sufficient to suitably capture the blade dynamics within the entire targeted frequency range. Additional instability lobes appear when the second eigenmode (first torsion mode or 1T) is included. Also, considering more eigenmodes have little influence since the lobes obtained with five modes superimpose well with those obtained with two modes in Fig. 6.9. Therefore, only the first bending and torsional modes are retained for the remainder.

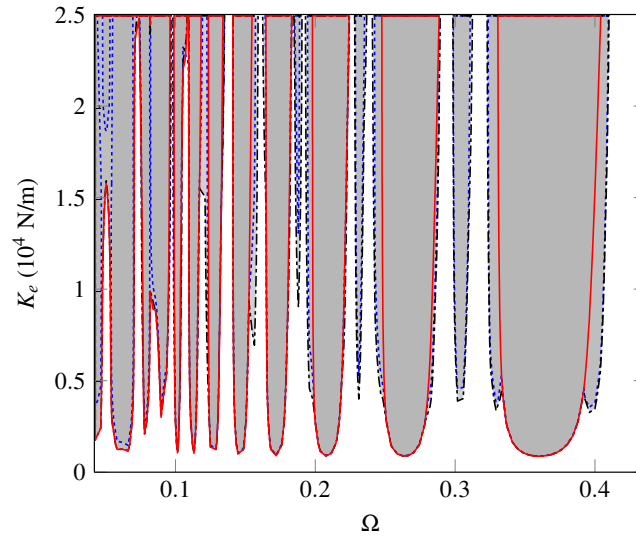


Figure 6.9: Modal convergence: mode 1 [—]; modes 1 and 2 [---]; and modes 1 to 5 [-.-]

6.3.2. Centrifugal stiffening

Similar than for the fan blade in section 5.2.1, the eigenfrequencies of the compressor blade are significantly affected by centrifugal stiffening and so are the corresponding instability lobes as depicted in Fig. 6.10. Interestingly, the stable domain gets larger at high rotational speeds. Also, as centrifugal loads mostly affect

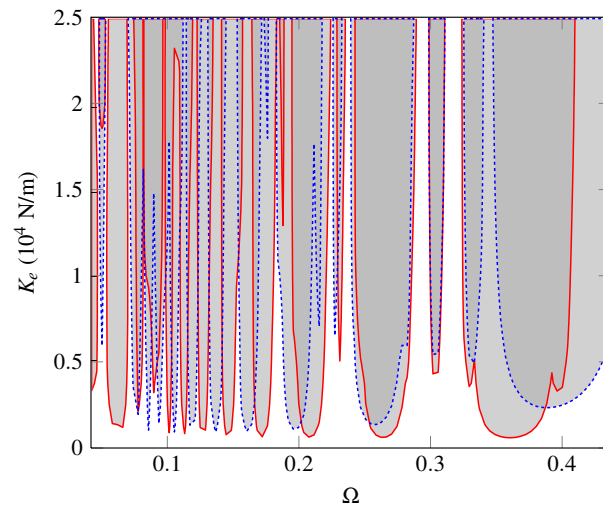


Figure 6.10: Instability lobes with [---] and without [—] centrifugal effects

the 1F mode, its influence is substantially visible on the geometry and position of larger lobes while thinner ones are essentially unmodified. Centrifugal stiffening is accounted for in all the simulations presented in the following.

6.4. Results

6.4.1. Comparison with time domain simulations

Time-domain simulation results are provided below for comparison purposes. They rely on previous developments [LBP12] which are recalled in chapter 5, where the abradable coating removal is modeled through a plastic constitutive law and contact conditions are handled on the trailing or/and leading edges to remain consistent with the DDE simulations. When blade/abradable coating contacts occur, the abradable elements—which are mono dimensional plastic bars—may undergo plastic deformations which are stored for the abradable profile update. At the end of the time simulations, the obtained abradable profile exhibits predominant contact areas.

This comparison focuses on two critical aspects of usual interaction studies:

1. the influence of the blade-tip/casing clearance distribution from leading to trailing edge to minimize the amplitude of vibration of the blade,
2. the identification of the most critical type of mode (usually bending or torsion) for a given blade design and a contact configuration.

6.4.1.1. Sensitivity to blade-tip contact location

When a worst-case interaction scenario is identified on a turbomachine stage, it is usually dealt with by opening the clearance at this specific stage which alters the overall engine efficiency. Possible finer strategies would only locally adjust the clearance distribution since contact initiation on the trailing or leading edges may have distinct consequences. As an example, two ideal fictitious configurations are considered here: (1) contact only occurs on the leading edge boundary node and the trailing edge boundary node may vibrate with no restriction, and the symmetrical configuration (2) where contact only occurs on the trailing edge and the leading edge may vibrate with no restriction. The corresponding instability lobes are depicted in Fig. 6.11. This figure indicates that the unstable domain is significantly larger when contact occurs at the leading edge. Considering that—for the design of interest—the blade stiffness on the trailing edge is much higher than on the leading edge, these results hint that the stiffer the blade, the larger the stability domain. In practice, the blade stiffness is limited by aerodynamic and weight considerations thus leading to necessary design compromises.

In order to corroborate the results obtained with the DDE, time simulations from tool derived in [LBP12] and implemented in chapter 5, are carried out over the full rotational speed range and during 50 revolutions of the blade for each idealized configuration. Attention is paid to predicted profiles of removed abradable

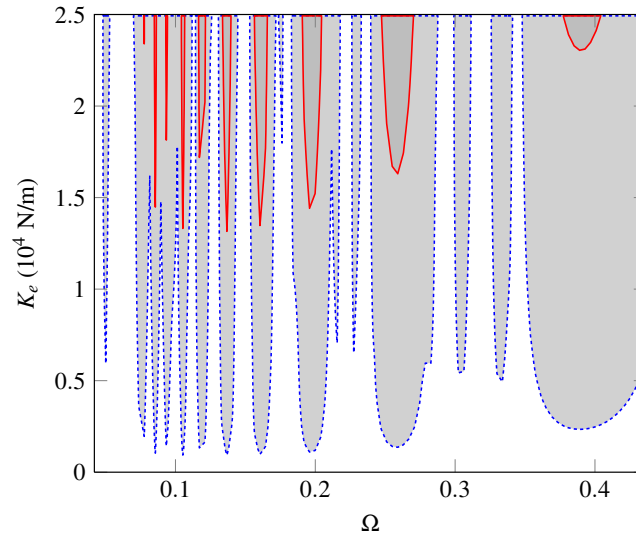


Figure 6.11: Instability lobes versus blade-tip contact location: TE [—] and LE [---]

coating at the end of each simulation. Unfolded side by side, these profiles, directly related to the blade vibratory amplitude, create a wear map where darker points indicate higher levels of removal. In order to initiate the blade/abradable coating contact the casing is ovalized, which results in two main grooves—for $\theta \in [1.4; 2]$ and $\theta \in [4.4; 5]$ —observed in the abradable profiles over the full rotational speed range in Figs. 6.12 and 6.13.

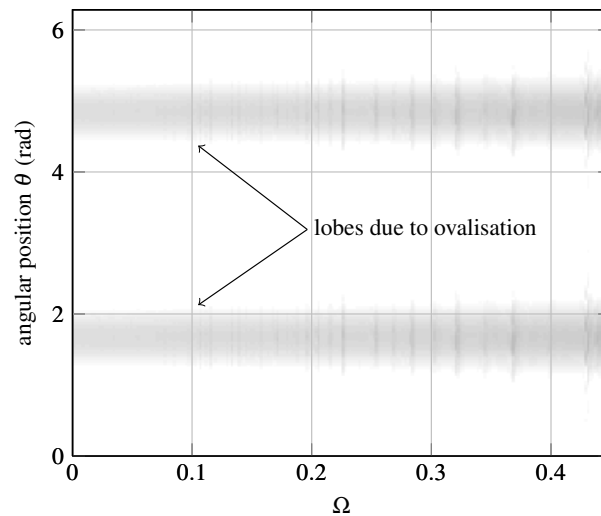


Figure 6.12: Abradable wear map: contact at blade trailing edge

Wear maps depicted in Figs. 6.12 and 6.13 are obtained when contact occurs only at the trailing edge and leading edge respectively (both figures have the same color code for comparison). On the trailing edge, the abradable profile is uniform throughout the rotational speed range: it features two main lobes as shown in

Fig. 6.12. Further, figure 6.13 highlights a much more complex blade behavior. In this case, the abradable

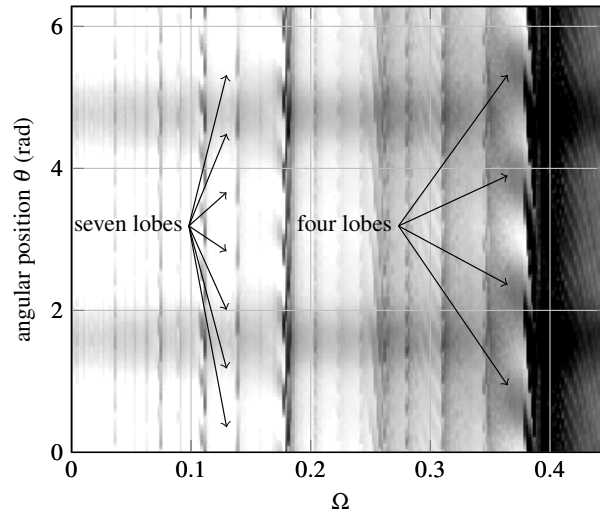


Figure 6.13: Abradable wear map: contact at blade leading edge

profile is highly dependent on the rotational speed of the blade. As an example, four main lobes are visible when $\Omega \simeq 0.37$ and seven lobes can be distinguished for $\Omega \simeq 0.14$. Dark areas in Fig. 6.13 underline that the worn lobes are deeper than in Fig. 6.12 which means that the blade amplitude of vibration is much higher in the present configuration.

Results given by the proposed DDE strategy are confirmed by time simulations since the wear maps exhibit much higher levels of penetration within the abradable coating when contact occurs on the leading edge (Fig. 6.13).

6.4.1.2. Bending/torsion instability

As mentioned above, the first two eigenmodes of the blade (1F and 1T modes) allow for accurately capturing the instability of the trivial solution. In this section, the stability analysis is carried out retaining a single modal contribution. The two sets of instability lobes are superimposed in Fig. 6.14, where the bending mode instability lobes are wider and structurally more critical than the torsional lobes since they arise for smaller K_e . Further, contrary to torsion instabilities, bending instabilities emanate at very low rotational speeds.

It is also shown in this figure how small discrepancies occur when the modal projection of Eq. (6.19) is truncated to a single mode (either 1F in blue or 1T in red) with respect to the case where both modes are retained in the change of space (in black). Indeed, even if the projected structural matrices $\mathbf{\Lambda}$ are diagonal and uncoupled in the modal space, the resulting forcing matrix $\mathbf{V}^T \mathbf{\Gamma} \mathbf{V}$ is full and the off-diagonal terms are neglected when a single mode is conserved. Furthermore, the miscalculation of the stability boundaries

perceived at low speeds is directly linked to the number of time increments utilized in the SDM [OZK14]. However, this well known limitation of the method does not impact the relevance of the obtained charts, since such a blade is generally operated in the range $\Omega \in [0.1 ; 0.4]$.

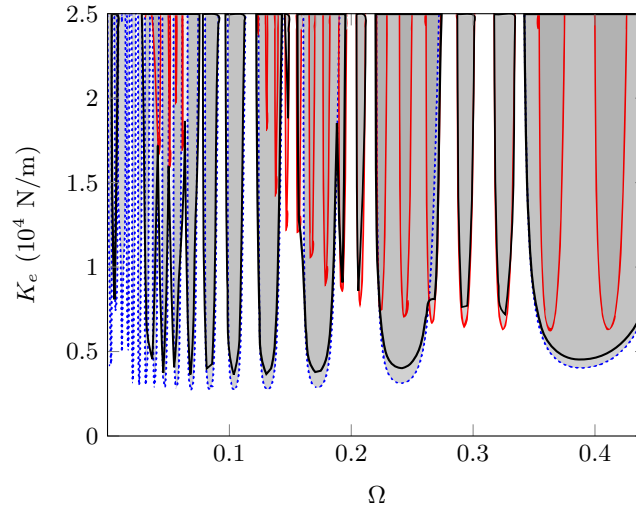


Figure 6.14: Instability lobes: bending [---], torsion [—] and bending+torsion [—] modes

Figure 6.15 shows the spectrum obtained from the time simulations results, associated with the radial displacement of the leading edge for each rotational speed. Two sets of peaks are distinguishable, around the natural frequencies of both the 1F and 1T modes. Time simulations carried out in this section account for possible intermittent contacts both on the trailing edge and the leading edge of the blade. Also in Fig. 6.15, the position of the response peaks matches very well with the predicted instability lobes associated with the first bending mode. Similar observations are made for the 1T mode, as the instability lobes predicted by the DDE approach clearly line up with the resonances of the same mode in the time integration.

Overall, results provided with DDE show that the blade is more sensitive to bending instability than to torsion instability. This is confirmed by the higher peaks detected around the 1F mode in the frequency domain analysis of the time simulations, and is consistent with previous work [Bat+12], where the dominance of the first bending mode during a blade/abradable coating interaction was both experimentally and numerically observed. Furthermore, the resonances detected in the time-domain simulations are very consistent with the instability lobes predicted by the DDE despite of the fact that the latter lies on a significantly simplified assumption of the interaction phenomenon. The fact that only two modes are sufficient for an accurate description of the stability is also confirmed with the frequency domain analysis of time simulation results, since no significant peaks of vibration amplitude are observed for high vibratory frequencies.

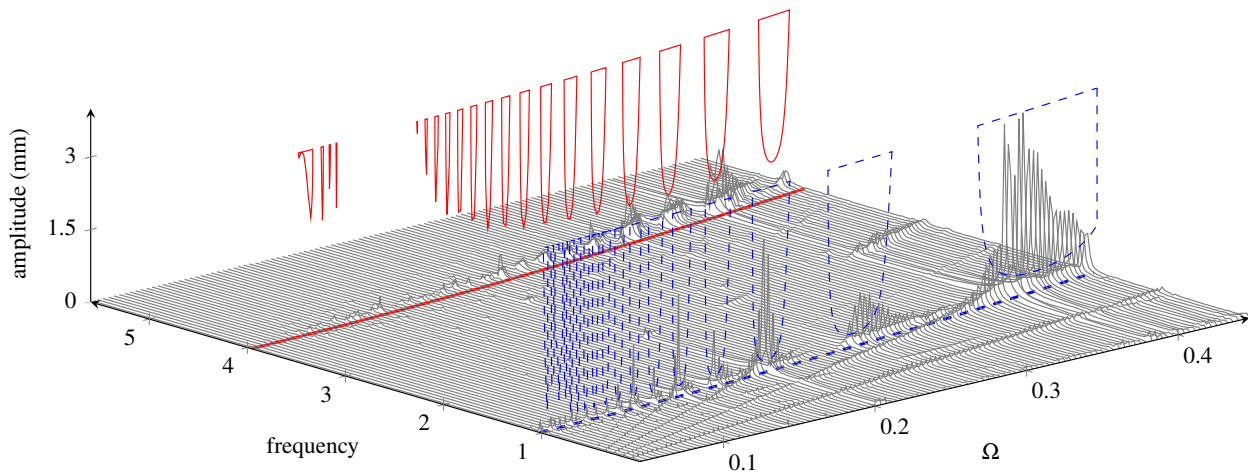


Figure 6.15: Spectrum of time-domain response: first torsion mode [—] and first bending mode [- - -]; instability lobes from Fig. 6.14 are superimposed

6.4.2. Analysis of frictional forces

Since the system of interest is a deformable body, for an accurate description of the blade penetration and subsequent contact forces, one should take into account the variations in the blade position due to the vibrations with respect to the rigid body motion induced by the rotation. In this case, the delay would no longer be constant but a function of the blade boundary nodes tangential displacements ($\tau = \tau(\mathbf{x}_b^t)$), thus yielding a system of state-dependent DDE. As frictional forces are included in the formulation and the associated tangential displacements become larger, this dependency becomes more significant. Nonetheless, due to the high operating speeds and the diameter of the disk on which the blade is mounted, the error committed in τ by neglecting the period of vibration with respect to the period of rotation is in the order of 1%, even for high vibration amplitudes. Therefore, similar to the observations made for a turning application in [IST07], the expected changes in the stability diagrams would be negligible and would not have a practical relevance and it is considered that the assumption of a constant delay still holds. Hence, the factor μK_e may easily be included in the forcing matrix $\mathbf{\Gamma}$ of the equations of motion (6.19) and the stability analysis of the equilibrium solution may be carried out in the same manner than for previous cases.

Three distinct friction coefficients, $\mu \in [0.1; 0.15; 0.2]$, are compared to the purely radial contact scenario studied above ($\mu = 0$), without accounting for centrifugal effects and assuming that contact occurs solely on the LE. The resulting stability charts are displayed in Fig. 6.16, where important variations of the unstable zones are observed. The introduction of frictional forces seems to *soften* the interaction as the clearance opening is favored when contact occurs. For the proposed contact scenario, these forces seem less

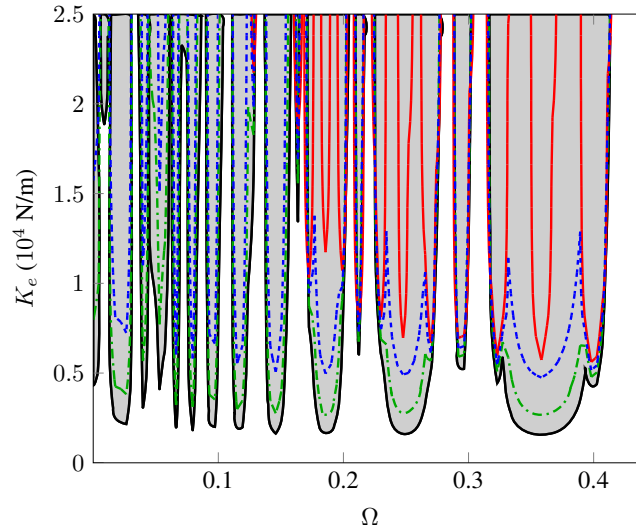


Figure 6.16: Instability lobes for friction coefficient: $\mu = 0$ [—]; $\mu = 0.1$ [- - -]; $\mu = 0.15$ [- · - ·] and $\mu = 0.2$ [—]

prone to excite bending motions and rather favor the blade torsion, thus leading to a progressive decrease of the unstable zone as μ reaches its highest value. It may be seen in Fig. 6.16 that for $\mu = 0.2$ only torsional lobes remain in the forcing coefficient K_e range of interest.

These findings are in good agreement with the numerical observations made in [LBP12], where an important decrease of vibration amplitudes results from the inclusion of tangential forces in the contact algorithm. Further, as the frictionless case ($\mu = 0$) appears to be the most critical one, it is this scenario that should be considered when assessing the performance of a given blade design.

6.4.3. Application to improved compressor blade designs

As in [Bat+12], different blade designs are studied in this section in order to assess the influence of the blade profile on the detected unstable zones: three alternative blades—BOW, IT3 and WINGLET—are investigated and compared to the reference model—REF—studied above. The associated blade geometries are illustrated in Fig. 6.17 on top of the original one, where it may be seen that these improved profiles exhibit an additional curvature that tends to open the tip-gap when contact occurs. As mentioned in [Bat+12], these designs were created from a purely structural point of view and their aerodynamic performances were ignored.

For each blade model, the relative frequency variations of the first torsional and first bending modes with respect to the reference one are presented in Tab. 6.1. It may be seen in this table how the BOW profile exhibits lower frequencies while the two others, in particular the IT3, feature a stiffer profile. These frequency variations are expected to produce a shift in the critical rotational speeds detected.

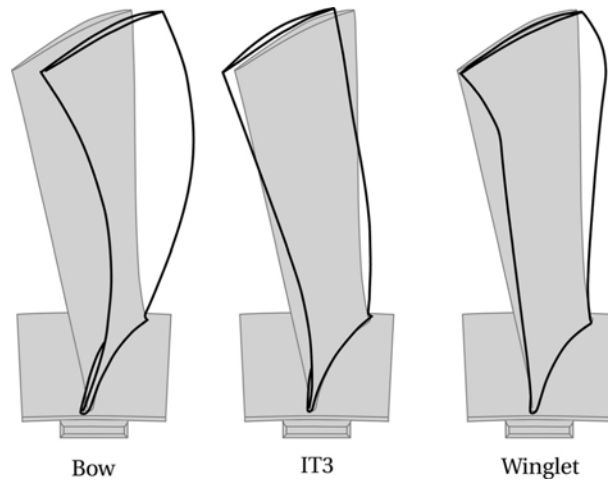


Figure 6.17: Modified blade geometries compared to reference model

		Profiles		
		BOW	IT3	WINGLET
Modes	<i>Bending</i>	-3.5	11.5	1.1
	<i>Torsion</i>	-16.6	8.6	3.93

Table 6.1: Relative frequency variations in %

The associated stability diagrams are computed considering that contact solely occurs at the leading edge, as this scenario proved to be critical for the blade of interest in section 6.4.1.1. The obtained results are superimposed to the reference ones in Fig. 6.18 without accounting for centrifugal effects nor friction ($\mu = 0$) and keeping the first two modes in the modal projection.

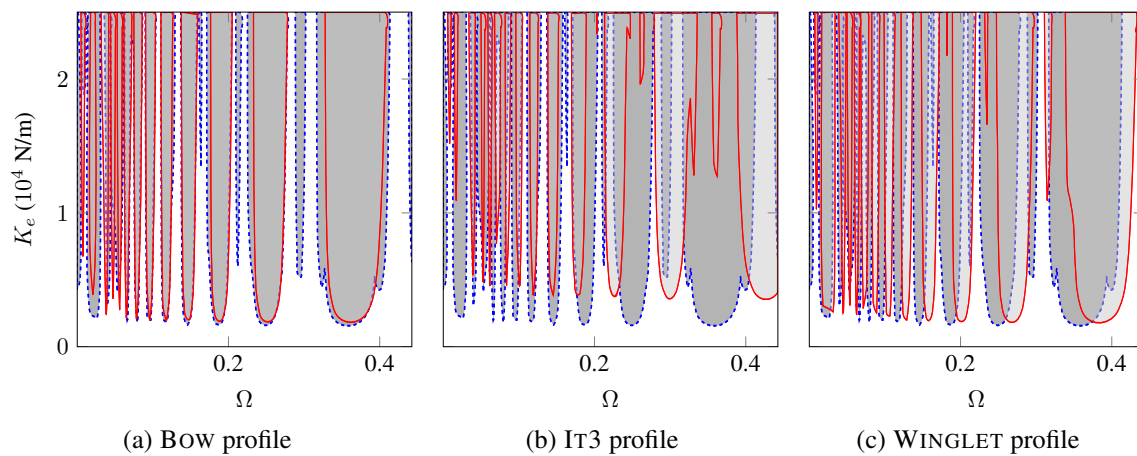


Figure 6.18: Comparison of stability maps: reference [---] and alternative [—]

Figure 6.18 shows that the IT3 profile is the one that results in a much smaller unstable zone, as all lobes

are shifted upward in the diagram. Also, the important changes in its natural frequencies alter its critical speeds significantly with respect to the reference blade. The two other profiles seem similar in terms of stability, both exhibiting a slight increase of the stable zone. Further, all the alternative blade designs seem to be less sensitive to torsion instabilities, as thinner lobes vanish from the charts, thus resulting in a smaller number of critical speeds. This finding is also in good agreement with the observations reported in [Bat+12].

These results clearly suggest that the proposed methodology could advantageously be applied in early design phases of the blades in order to discriminate blade profiles which are poorly robust to the contact events with its surrounding coating before moving to more evolved numerical strategies as in chapter 5.

6.4.4. Extension to fan blades

The mono-sector model presented in section 5.2.1 is here implemented. As mentioned earlier, similar to the compressor blade models considered above, the shaft and disk are considered as perfectly rigid thus being replaced by clamped boundary conditions.

In terms of modal convergence, the first two modes sufficed to obtain accurate results. As detailed in section 5.2.1 and illustrated in Fig. 5.4, these modes correspond to the first and second bending modes. The instabilities associated to each mode are presented in Fig. 6.19 for the same hypothetical contact configurations investigated in section 6.4.1.1. It may be seen in this figure that 2F instabilities only arise when contact occurs

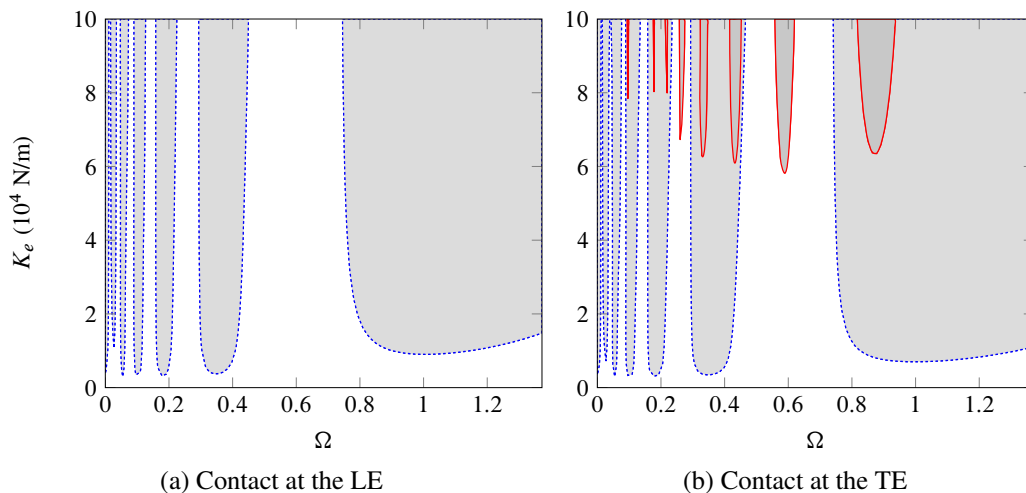


Figure 6.19: Instability lobes: first [---] and second [—] bending modes

at the TE and that the specific force coefficient K_e yielding this type of instability is about four times larger than for the compressor blades. Also, 1F instabilities are very similar in shape and position for both contact configurations, and appear at K_e values of the same order of magnitude than previous simulations.

For the targeted speed range of chapter 5, corresponding to $\Omega \in [0.95 ; 1.5]$, a single instability lobe is visible in Fig. 6.19 associated to the 1F mode. Hence, instabilities initiated by higher modes are not captured with the DDE approach, which appears to lose its predictive character for the fan blade model here considered.

6.5. Summary

This chapter introduces a qualitative analysis of abradable coating removed by incurring blades based on the theory of delay differential equations (DDE). The set of DDE is derived through an explicit expression of the contact loads resulting from the interaction and storing the wear of the abradable lining in the delayed term. Preliminary results highlight the convergence of the method and the accuracy of the instability lobes detected even when a relatively small number of blade modes is considered.

The proposed strategy accurately matches with the peaks of resonance predicted in the time-domain simulations. Furthermore, the sensitivity of stability areas to the contact locations on the tip of the blade is addressed. It is in agreement with time simulations and thus indicates that local clearance opening in a compressor stage could be a viable technological solution when facing potentially dangerous interactions. Furthermore, as suggested by the comparison of different blade geometries, engine manufacturers may benefit from the predictive features of the presented methodology as well as its low computational cost, in order to discriminate compressor blade profiles poorly robust to the interaction.

Summary and conclusions

7.1. Main findings

In modern aeronautical turbomachinery, unilateral and frictional contact events between rotating and stationary components are favored by always tighter blade-tip clearances and are expected to occur during standard operating conditions. However, it has been shown that potentially harmful interactions may arise and threaten the engine structural integrity. In particular, during test campaigns at SNECMA, important shaft vibrations—whirl motions—were witnessed at the fan stage of the engine. Hence, the need to predict whirl instabilities initiated by these contact events in early design phases of the engine is essential both for enhanced components lifespan and for safety. Accordingly, assessing the role of the shaft dynamic in this nonlinear phenomenon is the prime concern of this investigation, focusing on the dynamics of the fan stage of a commercial aircraft engine from a purely structural perspective.

A thorough analysis of the modal features of this engine module is presented, showing that the shaft participates only in 1-nodal diameter modeshapes. A methodology to build the gyroscopic matrix is developed within a cyclic-symmetric finite element framework. It is demonstrated that a non-negligible frequency split in 1-nodal diameter modes occurs when gyroscopic terms are accounted for and how these effects are accurately captured in the reduced-order Craig-Bampton space. Further, special attention is paid to the rotating shaft/bladed-disk/casing structural couplings, involving the fan frame and the bearings. A static analysis revealed how a mass imbalance load is prone to induce contact in the same direction as the shaft displacements, while the in-take flow loads during take-off induce a clearance closure in the direction opposite to the shaft deflection. A flexible bearing model through an array of linear springs is proposed, yielding a set of coupled ordinary differential equations with time-periodic coefficients when the rotation of the bladed-disk is incorporated. A change of frame allows to transform these equations into a time-invariant modal space,

in which a linear modal analysis of the three-dimensional coupled structures exposed divergent parametric instabilities emanating from the linearly predicted modal coincidence speeds. An increase in the coupling stiffness not only appeared to shift the first unstable configuration but also to widen the range of critical speeds. This novel perspective enables to treat the entire fan stage as a single structure while accounting for the rotation of the bladed-disk, thus giving access to its important modal features without the need of costly time-stepping solution methods.

As the size of the presented industrial models excludes reasonable computational times, a simplified two-dimensional model of the bladed-disk/casing system is proposed. Based on a previously established time-stepping solution strategy, the unilateral contact interactions between the two flexible structures are studied, initiated by two distinct clearance closure mechanisms: (1) initial casing distortion and (2) mass imbalance on the bladed-disk. The shaft dynamics is shown to be dominant in the divergent modal interactions detected, solely initiated in the former scenario. Further, in agreement with the modal predictions, the stiffness of the bearings/frame coupling induced a shift in the linear modal coincidence speed. In the divergent regimes detected, the whirling orbits of the shaft generally take the form of a backward traveling wave in the rotating frame that translates into a forward rotating one in the static frame. In terms of contact location versus shaft displacement, a phase comparison revealed how unilateral contact is favored as in the standard contact scenario, *i.e.* in the same direction as the shaft deflection. The targeted inverted contact scenario could not be observed with the proposed stage model.

An exploratory investigation of bladed-disk/abradable interactions is presented, considering the industrial fan bladed-disk and modeling the abradable wear through plasticity. Several interactions are predicted within the examined rotational speed range, leading to distinct worn abradable profiles and vibration levels. It is shown how the shaft dynamics play a major role in producing potentially harmful regimes as divergent backward whirling motions tend to be excited. The frequency split induced by the gyroscopic terms on 1-nodal diameter modes of the bladed-disk/shaft assembly also appeared to lead to divergent whirling motions at high rotational velocities, as the 1F ($n_d = 1$) backward mode becomes tangent to the main engine order in the Campbell diagram. These potentially critical interactions are demonstrated to necessarily involve intermittent contacts on all blades and are characterized by abradable removal throughout the entire casing circumference.

Lastly, for the modeling of blade/abradable interactions, it is proposed to replace the previously introduced elasto-plastic constitutive law by an explicit formulation of the contact forces, where the abradable wear is captured by a delay term. Under the assumption that permanent contact occurs during an entire revolution, a set of Delay Differential Equations is derived. By means of the semi-discretization method, the monodromy

matrix is built, relating current and past states of the system and for which a stability analysis of the equilibrium solution can be performed. The proposed strategy accurately predicts peaks of resonance of the studied compressor blade for both the first bending and torsion modes, when compared to previously established time-domain simulations. As suggested by the comparison of different blade geometries, aircraft engine manufacturers may benefit from the predictive side of the presented methodology as well as the low computational times involved, in order to discriminate compressor blade profiles poorly robust to the interaction.

7.2. Current limitations and perspectives for future research

The proposed analysis of bladed-disk/casing coupling through the bearings, modeled by an array of linear springs, is limited to 1-nodal diameter modes. An improved understanding on how coupled bladed-disk/casing modes may lead to the initiation of harmful interactions calls for a generalization of the coupling strategy to all possible nodal diameters. This would enhance the presented stability analysis so that additional possibly critical speeds are captured. Further, bearings inertial coupling as well as nonlinearities stemming from contact between the rolling elements and their surrounding rings could also be introduced so that the role of realistic bearing properties such as inner and outer ring diameters, rolling element geometry and material properties to name a few, may be analyzed. Also, a three-dimensional version of the model presented in [PTC14] could be developed, including the entire low pressure shaft up to the turbine stage, in order to corroborate the existence of coupled modes that may initiate the interactions in the inverted configuration. Even if more costly in terms of computational efforts, the proposed three-dimensional models have the advantage of accurately capturing the dynamics of the assembly while overcoming the modeling approximations faced in simpler energetic strategies. Additionally, complementary mechanisms of clearance closure are under investigation with the proposed two-dimensional model, particularly targeting the in-take flow load scenario that could lead to the inverted contact configuration which was not found in the current study.

In the presented industrial bladed-disk/abradable exploratory investigation, a rigid casing was assumed, thus limiting the interactions solely to pure engine-order excitations. Work is in progress to incorporate the casing flexibility and the structural coupling provided by the fan frame within this nonlinear framework [BL15]. Further, since the acceleration phases of the engine are critical, implementing a time-dependent rotational speed and the associated angular acceleration within the equations of motion stand as a major concern for the analysis of interactions, rendering the current numerical tool more predictive and versatile.

The thermal expansion of the components and the deformations of the casing induced by the highly localized thermal loads at the contact interface are yet to be incorporated.

An extensive experimental campaign will be held in the near future at the recently constructed PHARE test bench in Lyon, employing an industrial fan geometry provided by SNECMA. The experiments are supposed to target potentially dangerous interaction regimes for a proper characterization of the contact phenomena and associated bladed-disk vibratory response. In particular, a thorough comparison between experimental data and numerical results will serve as a calibration of the abradable coating mechanical properties along with other *purely* numerical parameters.

Also, future work will address the role of mistuning, which emerges from the small discrepancies between sectors that break the cyclically symmetric properties of the bladed-disk. It is known that random mistuning results in highly localized modes and amplification of vibratory amplitudes in turbomanichery, thus potentially causing premature fatigue failures [CP06]. Yet, the introduction of intensional mistuning has been demonstrated to be a promising way to avoid the large forced response amplitudes and stresses that can be caused by random mistuning [CP02]. In particular, the proposed *square-wave patterns* which only require two different blade types, could potentially suppress 1-nodal diameter bladed-disk modes that are coupled to the shaft dynamics and may thus be a viable solution to avoid high-amplitude whirling motions.

Finally, the proposed methodology of abradable removal modeling through DDE stands on three major limitations: (1) the constant delay, thus assuming that blade-tip tangential displacements are negligible, (2) the permanent contact condition, necessary for the stability analysis to be possible, and (3) a rigid casing. Accordingly, work is in progress to generalize the approach and assess the influence of blade-tip tangential displacements yielding state-dependent DDE, the effects of blade/abradable separation events in which the system oscillates between contact and free-flight phases (see appendix C), and the implementation of a flexible casing through coupled DDE. Furthermore, combining the blade/abradable separation events to the casing flexibility would serve as a comparison basis to the more evolved elasto-plastic wear law employed in [BL15].

7.3. List of publications and contributions

An article version of chapter 5 is in progress focusing on the comparison of the bladed-disk/abradable interactions accounting or not for gyroscopic terms. Another article will regard the proposed analysis of the coupled bladed-disk/casing modal features of section 3.4, focusing on how inherent instabilities emanating from the mode couplings may potentially initiate contact interactions.

Also, the two-dimensional investigation presented in chapter 4 was recently accepted as a journal paper:

- Salvat, N., Batailly, A., and Legrand, M. “Two-dimensional modeling of unilateral contact-induced shaft precessional motions in bladed-disk/casing systems.” *International Journal of Non-Linear Mechanics* 78.1 (2016), pp. 90–104. DOI: 10.1016/j.ijnonlinmec.2015.10.001. OAI: hal-01223046

Part of this work was presented at the peer-reviewed conference ASME TURBOEXPO 2014, focusing on the sensitivity of the detected high-amplitude whirling motions with respect to the shape of the casing distortion:

- Salvat, N., Batailly, A., and Legrand, M. “Two-dimensional modeling of shaft precessional motions induced by unilateral blade/casing contacts in aircraft engines.” *Proceedings of the ASME Turbo Expo*. 2014. DOI: 10.1115/GT2014-25688. OAI: hal-01090671v2

The novel methodology for the modeling of abradable removal based on delay differential equations, which is the topic of chapter 6, was presented at two conferences:

- Salvat, N., Batailly, A., and Legrand, M. “Prédiction de l’enlèvement de matériau abradable par équations différentielles à retard dans les moteurs d’avion.” *11ème Colloque National de Calcul des Structures - CSMA*. 2013. OAI: hal-01104675
- Salvat, N., Batailly, A., and Legrand, M. “Modeling of abradable coating removal in aircraft engines through delay differential equations.” *Proceedings of the ASME Turbo Expo*. 2013. DOI: 10.1115/GT2013-94400

In the latter, it was awarded the prestigious ASME BEST PAPER OF THE YEAR AWARD by the *Structures & Dynamics Committee* and was selected for publication as a journal version in:

- Salvat, N., Batailly, A., and Legrand, M. “Modeling of abradable coating removal in aircraft engines through delay differential equations.” *Journal of Engineering for Gas Turbines and Power* 135.10 (2013), p. 102102. DOI: 10.1115/1.4024959. OAI: hal-00879815



Space and time Fourier transform

The objective of this appendix is to present a small note on spatial and time Fourier transforms, utilized for the analysis the results of chapter 5.

A.1. General notations

The basic concept behind the two-dimensional Fourier transform decomposition is to exploit the cyclic properties of the studied structures in order to gain understanding on the shape of the modes that participate in the response in addition to their vibratory frequency. In this sense, as detailed in [Bla01; Ols+14], the use of cyclic coordinates is particularly adapted. The main properties of this change of space, going from physical quantities \mathbf{x} (generally displacements) to their cyclic counterpart $\tilde{\mathbf{u}}$ and achieved through the so-called Fourier matrix $\hat{\mathcal{F}}$, is summarized in Tab. A.1. It may be noted in this table that the block circulant structural matrices

	Physical or FE space	Cyclic or Fourier space
Displacements	$\mathbf{x}^T = (\mathbf{x}_1^T, \mathbf{x}_2^T, \dots, \mathbf{x}_N^T)$	$\hat{\mathbf{u}}^T = (\hat{\mathbf{u}}_0^T, \hat{\mathbf{u}}_{1,c}^T, \hat{\mathbf{u}}_{1,s}^T, \dots, \hat{\mathbf{u}}_{[N/2]}^T)$
Matrices	$\mathbf{Y} = \mathbf{Bcirc}(\mathbf{Y}_0, \mathbf{Y}_1, \mathbf{Y}_1^T)$	$\hat{\mathbf{Y}} = \mathbf{Bdiag}(\hat{\mathbf{Y}}_0, \hat{\mathbf{Y}}_1, \dots, \hat{\mathbf{Y}}_{[N/2]})$
Var. change	$\mathbf{x} = \hat{\mathcal{F}} \hat{\mathbf{u}}$	$\hat{\mathbf{u}} = \hat{\mathcal{F}}^{-1} \mathbf{x}$

Table A.1: Physical and cyclic coordinates

in the physical space yield block diagonal matrices in the cyclic space.

When a single DoF per sector is considered, the real-valued Fourier matrix is [Bla01]:

$$\hat{\mathcal{F}} = \begin{bmatrix} \hat{\mathbf{f}}_0 & \hat{\mathbf{f}}_{1,c} & \hat{\mathbf{f}}_{1,s} & \dots & \hat{\mathbf{f}}_{[N/2]} \end{bmatrix} \quad (\text{A.1})$$

which corresponds to:

$$\hat{\mathcal{F}} = \frac{1}{\sqrt{N}} \begin{bmatrix} 1 & \sqrt{2} & 0 & \dots & 1 \\ 1 & \sqrt{2} \cos \alpha & \sqrt{2} \sin \alpha & \dots & -1 \\ 1 & \sqrt{2} \cos 2\alpha & \sqrt{2} \sin 2\alpha & \dots & 1 \\ \vdots & \vdots & \vdots & \ddots & \vdots \\ 1 & \sqrt{2} \cos(N-1)\alpha & \sqrt{2} \sin(N-1)\alpha & \dots & (-1)^{N-1} \end{bmatrix} \quad (\text{A.2})$$

where $\alpha = 2\pi/N$ is the fundamental inter-blade phase shift. Equation (A.2) can then be generalized to a higher number of DoF n_s by a simple expansion as $\hat{\mathcal{F}} = \hat{\mathcal{F}} \otimes \mathbf{I}_{n_s}$, where \mathbf{I}_{n_s} is the identity matrix of the same size than the blocks composing the FE structural matrices. Once the cyclic displacements are obtained by means of the matrix (A.2), their frequency content may be analyzed using a regular FFT.

A.2. Examples

Consider a perfectly tuned cyclic structure composed of $N = 6$ identical sectors as illustrated in Fig. A.1a. Let us assume that the first bending modes (1F) appear around 10 Hz and that the 2F emerge at 30 Hz. Hence,

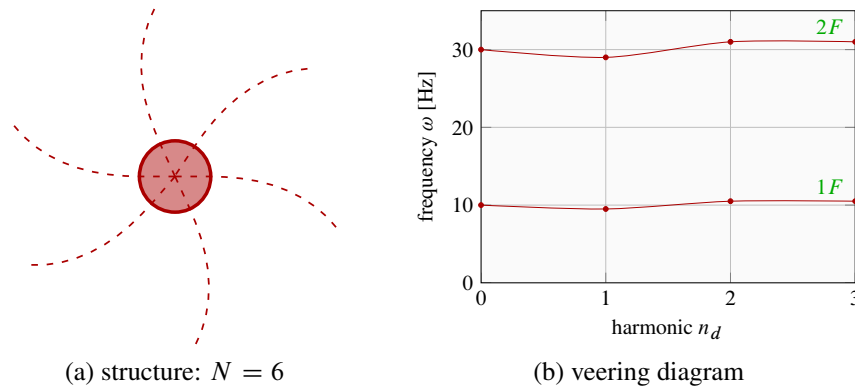


Figure A.1: Example of a cyclic structure

the associated veering diagram would typically look as Fig. A.1b, where $n_d = 0$ and $n_d = 3$ are single harmonics while $n_d = 1$ and $n_d = 2$ are double.

A.2.1. Example 1: single harmonic excitation

The first signal considered, corresponds to a simple cosine wave of frequency ω_1 , that for the j -th sector takes the general form:

$$x_j = A_1 \cos(\omega_1 t + \phi_{1j}) \quad \text{with} \quad \phi_{1j} = j2\pi n_1/N \quad \text{and} \quad j = 1, \dots, N \quad (\text{A.3})$$

where ϕ_{1j} represents the spatial phase shift between each sectors and is proportional to the wave number n_1 .

Parameter	Value
time	$T_{\text{tot}} = 0.5$ s
amplitude	$A_1 = 1$ mm
wave number	$n_1 = 1$
number of sectors	$N = 6$
frequency	$\omega_1 = 10$ Hz

Table A.2: Example 1 - signal parameters

For the parameters listed in Tab. A.2 and the signal given in Eq. (A.3), the time response of each sector is depicted in Fig. A.2. It may be seen in this figure, highlighted in blue at $t = 0$, how the response of each sector form a wave in space which is directly linked to the imposed phase shift in Eq. (A.3) ($n_1 = 1$ in this case). As each blade vibrates in time, this spatial wave will propagate giving rise to the notion of traveling wave speeds [Sch97].

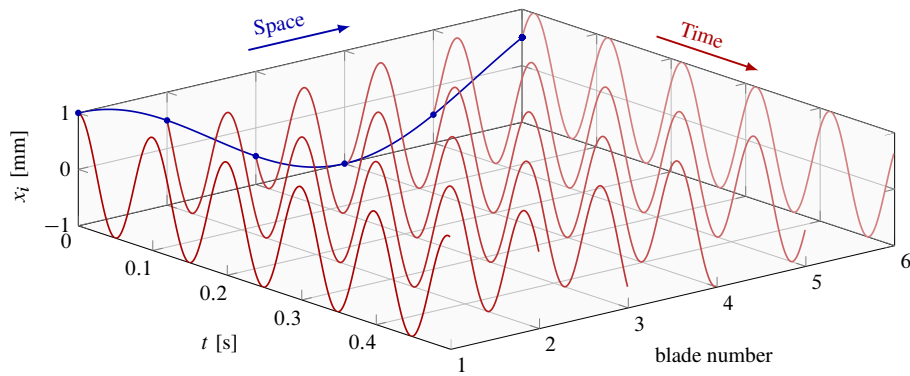


Figure A.2: Time response of all sectors

In general, the signature of the response of a single blade x_i is analyzed in the frequency domain by exploring its Fourier transform in time $\mathcal{F}(x_i)$. As shown in Fig. A.3, the frequency peak detected with this transformation corresponds to the prescribed frequency $\omega_1 = 10$ Hz. This information is useful in order to characterize the type of mode that is being excited. For instance, based on the system assumptions described above, one can state that the system is excited purely on its first bending modes. Nonetheless, this information is insufficient to determine which kind of nodal diameters or spatial harmonics participate in the response.

By employing the mathematical developments presented above, the structure response may be decomposed into its nodal diameter contributions by means of Eq. (A.2), and an FFT in time may be performed to determine the dominant frequencies for each spatial harmonic. In this manner, the diagram presented in Fig. A.4 can be obtained, where the peak at 10 Hz is solely located on the 1-nodal diameter line and all others harmonics have a negligible contribution as expected. Thus, one can clearly state that the system responds on

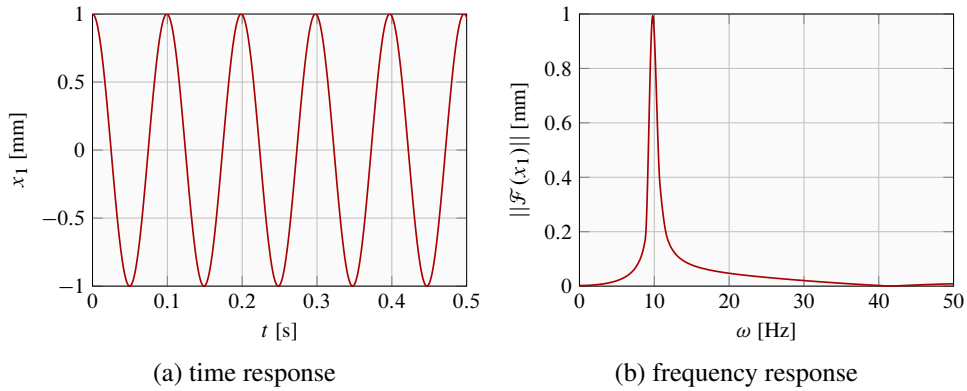


Figure A.3: Analysis of first sector response

the $n_d = 1$ harmonic of the IF mode.

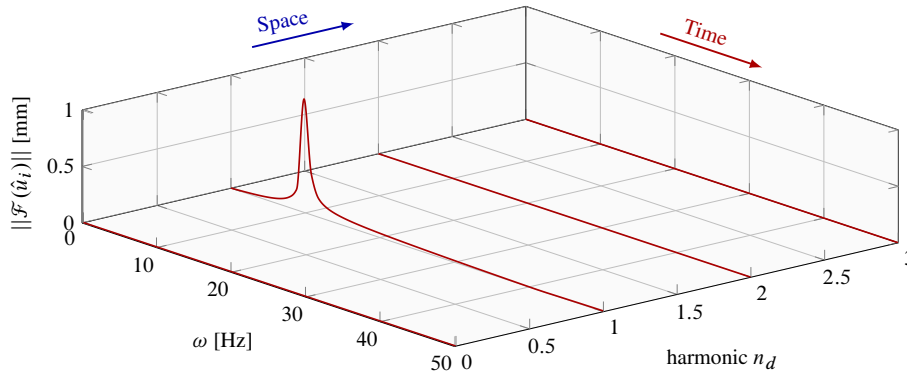


Figure A.4: 2D-FFT of time response

A.2.2. Example 2: dual harmonic excitation

These developments may seem trivial for the above example, since the response characteristics can be easily deduced just by analyzing the time signals of Fig. A.2. But when looking at more complex signals, this decomposition becomes particularly adapted. It is here proposed to add to the previously considered time signal another frequency component with a distinct frequency shift. Therefore, Eq. (A.3) becomes:

$$x_j = A_1 \cos(\omega_1 t + \phi_{1j}) + A_2 \cos(\omega_2 t + \phi_{2j}) \quad (\text{A.4})$$

with $\phi_{1j} = j2\pi n_1/N$, $\phi_{2j} = j2\pi n_2/N$ and $j = 1, \dots, N$

where the spatial phase shifts ϕ_{1j} and ϕ_{2j} may have distinct wave numbers n_1 and n_2 respectively.

For the parameters in Tab. A.3, the response associated to a single sector is depicted in Fig. A.5 along with its frequency content. The two peaks associated to the prescribed frequencies ω_1 and ω_2 are clearly

Parameter	Value
time	$T_{tot} = 0.5$ s
amplitudes	$A_1 = 0.5$ mm, $A_2 = 1$ mm
wave numbers	$n_1 = 1$, $n_2 = 2$
frequencies	$\omega_1 = 10$ Hz, $\omega_2 = 30$ Hz

Table A.3: Example 2 - signal parameters

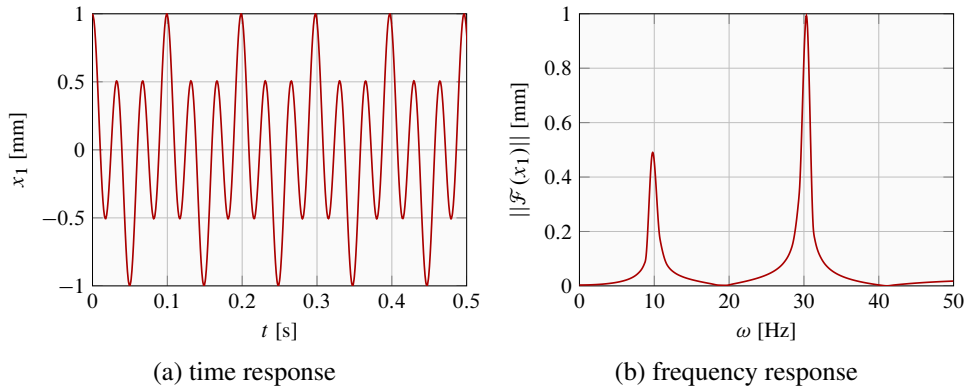


Figure A.5: Analysis of first sector response

visible, indicating that the system is subject to a combination of both bending motions (1F and 2F) with distinct amplitudes, but once again, there is no information regarding the spatial distribution of each mode.

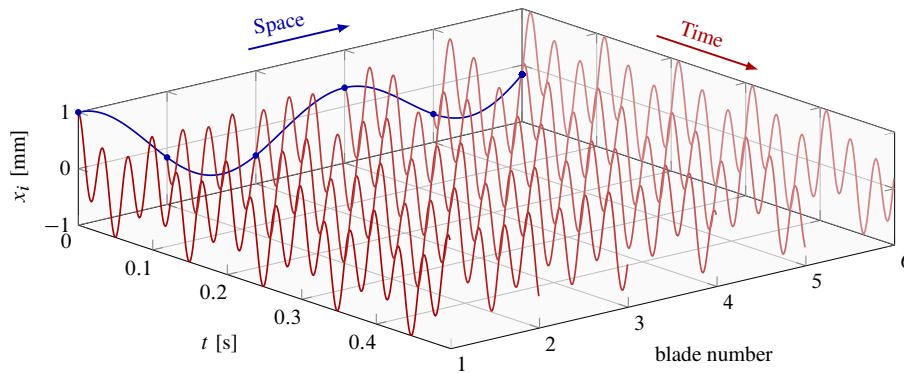


Figure A.6: Time response of all sectors

When looking at the time responses of all sectors displayed in Fig. A.6, a dominant 2-nodal diameter wave may be observed but it is no longer clear if other types of waves are also involved in the response. Therefore, the modal decomposition into spatial harmonics can improve the analysis of the response. As expected, Fig. A.7 shows how the 10 Hz peak is located on the 1-nodal diameter line while the 30 Hz appears on $n_d = 2$.

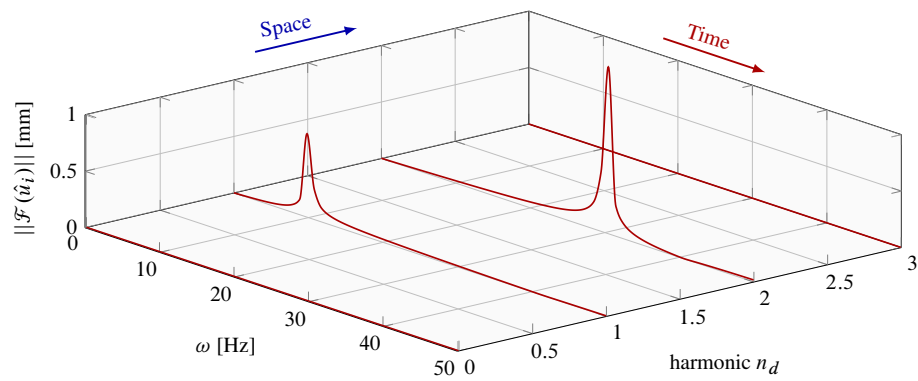


Figure A.7: 2D-FFT of time response

DDE MATLAB source code

The MATLAB source code utilized for chapter 6 is here presented, where the Semi-Discretization Method [IS04] is employed for the construction of the monodromy matrix and stability analysis of the blade equilibrium position.

```

%%%%%%%%%%%%%%%%%%%%%%%%%%%%%%%%%%%%%%%%%%%%%%%%%%%%%%%%%%%%%%%%%%%%%%%%
%%% Finite element discretization %%%
%%%%%%%%%%%%%%%%%%%%%%%%%%%%%%%%%%%%%%%%%%%%%%%%%%%%%%%%%%%%%%%%%%%%%%%%
%
% Load blade structural matrices
%
load('Blade_matrices.mat')
%
% Construction of modal damping matrix
%
[V,Lambda]=eig(Kr,Mr);           % V: eigenvectors
                                % Lambda: eigenvalues
freqs=sqrt(diag(Lambda))/2/pi;   % Eigenfrequencies
%
ksi=0.0005;                      % Damping ratio
C=2*ksi*(V')^(-1)*sqrt(Lambda)*V^(-1); % Damping matrix
%
% Modal truncation basis
N_i=1;                            % First mode kept
N_m=5;                            % Number of modes kept
Lambda=Lambda(N_i:N_m,N_i:N_m);   % Truncated set of eigenvalues
n=length(Lambda);                 % Model size
%
%%%%%%%%%%%%%%%%%%%%%%%%%%%%%%%%%%%%%%%%%%%%%%%%%%%%%%%%%%%%%%%%%%%%%%%%
%%% Computational parameters %%%
%%%%%%%%%%%%%%%%%%%%%%%%%%%%%%%%%%%%%%%%%%%%%%%%%%%%%%%%%%%%%%%%%%%%%%%%
%
Force_s=zeros(n,n);              % Force matrix
mu=0.1;                          % Friction coefficient
%
stx = 200;                       % Steps of rotational speed
o_st = 0.5;                       % Starting rotational speed (Hz)

```

```

o_fi = 2;           % Final rotational speed (Hz)
%
sty = 400;         % Steps of specific force coefficient
Ke_st = 4.5e4;     % Starting specific force coefficient (N/m2)
Ke_fi = 4.5e6;     % Final specific force coefficient (N/m2)
%
k = 60;           % discretization over one period
m = k;            % since time delay = time period
%
D = zeros(n*(m+2), n*(m+2));      % monodromy matrix D
d = ones((m+1)*n, 1);
d(1 : 2*n) = 0;
D = D + diag(d, -n);
for i=1:n
    D(2*n+i, i) = 1;
end
%
% Initialization of storage variables
%
EI=zeros(stx+1,sty+1);   % Monodromy operator eigenvalues
F_o=zeros(stx+1,sty+1); % Rotational frequency
Ke_c=zeros(stx+1,sty+1); % Critical specific force coefficient
%
%%%%%%%%%%%%%%%%%%%%%%%%%%%%%%%%%%%%%%%%%%%%%%%%%%%%%%%%%%%%%%%%%%%%%%%%
%%%%%%%% Simulation %%%%%%%%%
%%%%%%%%%%%%%%%%%%%%%%%%%%%%%%%%%%%%%%%%%%%%%%%%%%%%%%%%%%%%%%%%%%%%%%%%
%
for x = 1 : stx + 1 % loop for rotational speeds
    %
    o = o_st + (x-1)*(o_fi-o_st)/stx; % rotational speed
    tau = 1/o; % time delay
    dt = tau/m; % time step
    %
    for y = 1 : sty + 1 % loop for force
        % Force coefficient
        Ke = Ke_st + (y-1)*(Ke_fi-Ke_st)/sty;
        %
        % Construction of monodromy operator Fi
        Fi = speye(n*(m+2), n*(m+2));
        %
        % Forcing matrix
        % Contact at LE
        Force_s(1,1)=Ke*w;
        Force_s(2,1)=-mu*Ke*w;
        %
        % Contact at TE
        % Force_s(22,22)=Ke*w;
        % Force_s(23,22)=-mu*Ke*w;
        %
        % Force matrix in modal domain
        Force_s_m=V(:,N_i:N_m)'*Force_s*V(:,N_i:N_m);
        %
        % Structural matrices
        %

```

```

A = zeros(2*n, 2*n); % matrix A
A(1:n, n+1:2*n) = eye(n);
A(n+1:2*n, 1:n) = -Lambda-kappa;
A(n+1:2*n, n+1:2*n) = -2*ksi*sqrt(Lambda);
%
B = zeros(2*n, 2*n); % matrix B
B(n+1:2*n, 1:n) = kappa;
%
P = expm(A*dt); % matrix Pi
R = (expm(A*dt)-eye(2*n))*(inv(A)*B); % matrix Ri
%
% Mondromy operator
D(1:2*n, 1:2*n) = P;
D(1:2*n, n*m+1:n*(m+1)) = 0.5*R(1:2*n, 1:n);
D(1:2*n, n*(m+1)+1:n*(m+2)) = 0.5*R(1:2*n, 1:n);
D=sparse(D);
Fi = D*Fi;
ei= max(abs(eig(full(Fi))));
%
% Result storage
EI(x, y) = ei; % Largest Fi eigenvalue
F_o(x, y) = o; % Rotational frequency
Ke_c(x, y) = Ke; % Force coefficient

end
stx + 1-x
end
%
%%%%%%%%%%%%%%%%%%%%%%%%%%%%%%%%%%%%%%%%%%%%%%%%%%%%%%%%%%%%%%%%%%%%%%%%
%%%%%%%%%%%%%%%%%%%%%%%%%%%%%%%%%%%%%%%%%%%%%%%%%%%%%%%%%%%%%%%%%%%%%%%%
%%%%%%%%%%%%%%%%%%%%%%%%%%%%%%%%%%%%%%%%%%%%%%%%%%%%%%%%%%%%%%%%%%%%%%%%
%
figure(1); hold on;
contour(F_o,Ke_c,EI,[1, 1], 'r')
xlabel('Rotational frequency')
ylabel('Specific force coefficient (N/m2)')
%
%%%%%%%%%%%%%%%%%%%%%%%%%%%%%%%%%%%%%%%%%%%%%%%%%%%%%%%%%%%%%%%%%%%%%%%%
%%%%%%%%%%%%%%%%%%%%%%%%%%%%%%%%%%%%%%%%%%%%%%%%%%%%%%%%%%%%%%%%%%%%%%%%
%%%%%%%%%%%%%%%%%%%%%%%%%%%%%%%%%%%%%%%%%%%%%%%%%%%%%%%%%%%%%%%%%%%%%%%%
%
file=['results_stab_rod.mat'];
save(file, 'F_o', 'Ke_c', 'EI', 'freqs');

```


Blade/abradable separation in DDE

As detailed in chapter 6, the main assumptions on which the DDE formulation is based, is to suppose that the blade never leaves the abradable lining during the revolution considered for the stability analysis and that the engendered contact reaction is proportional to the penetration level. This is a clear simplification of the contact scenario, as the blade/abradable interactions clearly involve intermittent contacts (see chapter 5 or previous studies [Mil+09; Bat+12]).

However, this inherent limitation of the DDE approach is mandatory for the stability analyses to be performed. Indeed, if the separation between the blade and the abradable coating is accounted for, the eventual penetration of the blade-tip in the coating at a time t can no longer be deduced by the difference $\mathbf{x}_b^r(t - \tau) - \mathbf{x}_b^r(t)$ and the resulting contact force given in Eq. (6.17) does not hold. Thus, an auxiliary variable $\chi(t)$ must be introduced in order to track the abradable profile and test whether or not a penetration is detected. In this sense, the system oscillates between two possible states:

- *penetration phase*, where the contact force is now function of the abradable profile at its past state $\chi(t - \tau)$ and results in the following equations of motion:

$$\ddot{\mathbf{u}}(t) + 2\xi \mathbf{\Lambda} \dot{\mathbf{u}}(t) + \mathbf{\Lambda}^2 \mathbf{u}(t) = \mathbf{V}^T \mathbf{\Gamma} \mathbf{V} [\chi(t - \tau) - \mathbf{u}(t)] \quad (\text{C.1})$$

- *separation phase*, in which the blade is in free flight conditions:

$$\ddot{\mathbf{u}}(t) + 2\xi \mathbf{\Lambda} \dot{\mathbf{u}}(t) + \mathbf{\Lambda}^2 \mathbf{u}(t) = \mathbf{0} \quad (\text{C.2})$$

hence, the DDE (C.1) becomes a regular ODE, as the contact forcing terms vanish.

As recently reported in a turning application [LIS15], the previously established stability analysis by means of the SDM becomes obsolete and the only possible predictions may be obtained through time-

integration techniques, where an alternation between dedicated DDE and ODE solvers is required. Furthermore, the problem becomes non-linear and highly dependent on the initial conditions.

Instead of developing this time-marching strategy, which would essentially be similar to the method proposed in [LBP12] and implemented in chapter 5, it is proposed to account for the blade/abradable separation at specific locations of the casing depending on the n_d -nodal diameter distortion considered. In this sense, a penalty coefficient $k_{\text{pen}}(\theta)$ can be applied to the forcing term, whose value depends if the blade is assumed to be in contact ($k_{\text{pen}}(\theta) = 1$) or in free flight ($k_{\text{pen}}(\theta) = 0$). Accordingly, as illustrated in

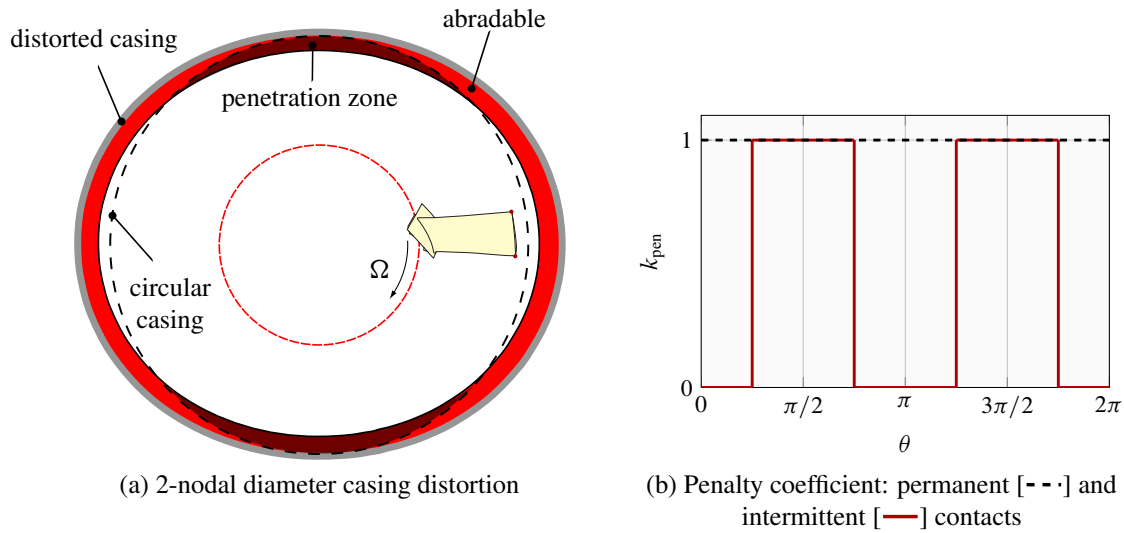


Figure C.1: Hypothetical penetration and separation phases

Fig. C.1a for a two-nodal diameter casing deformation, there are two privileged contact zones. The associated penalty coefficient is represented in Fig. C.1b. These assumptions allow to carry out the stability analysis as in previous simulations and give a preliminary insight to the effects of blade/abradable separation.

The stability chart C.2 provides a comparison of the instability lobes obtained assuming permanent contact and two distinct casing distortions ($n_d = 1$ and $n_d = 2$). It can be seen in this figure that accounting for the blade/abradable separation through the previously defined penalty coefficient appears to soften the interaction scenario and slightly increase the stable domain. It is worth noticing that it does not affect the location of the predicted critical rotational speeds. Also, results appear to be very robust to the casing configuration considered, as 1-nodal diameter and 2-nodal diameter shapes yield almost identical results.

In summary, as the most critical scenario is the one of interest from a design perspective, it can be concluded that the permanent contact assumption is to be retained in the stability analyses performed with the DDE methodology. The great gain in computational times and the predictive side of the approach are clear

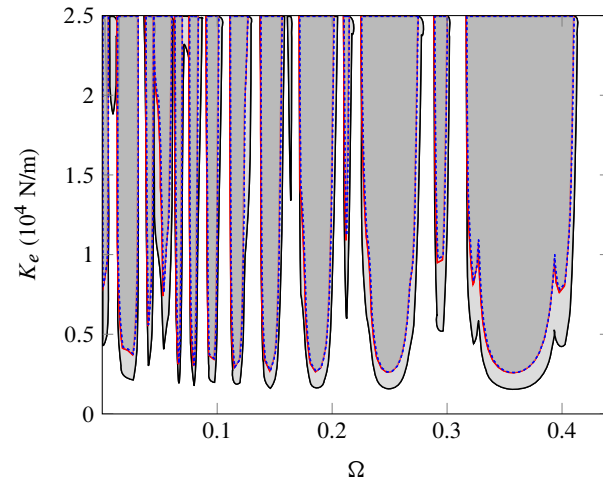


Figure C.2: Instability lobes: permanent contact [—], 2-nodal diameter [—] and 1-nodal diameter [- - -] casing distortions

assets for discriminating preliminary blade profiles poorly robust to the interactions with their surrounding abradable coatings. However, the added complexity introduced by accounting for intermittent contacts should be further investigated.

Nomenclature

Matrices

Symbol	Description	Unit
Ω	rotation matrix	rad/s
Γ	external forcing matrix	N/m
Λ	eigenvalues	(rad/s) ²
Φ	monodromy matrix	—
Ψ_c	constraint modes	—
Ψ_s	static modes	—
\mathbf{B}	contact constraints matrix	—
\mathbf{D}	damping matrix	Ns/m
\mathbf{G}	gyroscopic matrix	Ns/m
\mathbf{K}	stiffness matrix	N/m
\mathbf{K}^*	frame/bearings coupling matrix	N/m
\mathbf{K}_S	spin softening matrix	N/m
\mathbf{M}	mass matrix	kg
\mathbf{N}	FEM shape functions	—
\mathbf{P}	angular acceleration matrix	N/m
\mathbf{V}	eigenvectors	—

Vectors

Symbol	Description	Unit
$\ddot{\mathbf{x}}$	accelerations	m/s ²
$\dot{\mathbf{x}}$	velocities	m/s
$\hat{\mathbf{u}}^{n_d}$	cyclic coordinates	m
\mathbf{f}_{cn}	contact forces	N
\mathbf{f}_{ext}	external forces	N
\mathbf{f}_{ln}	linear external forces	N
\mathbf{f}_{nl}	nonlinear external forces	N
\mathbf{h}	penetration level	m
\mathbf{q}_{cb}	Craig-Bampton modal participations	m
\mathbf{u}	modal coordinates	m
\mathbf{x}	displacements	m
\mathbf{x}_{b}	boundary DoF	m
\mathbf{x}_{i}	internal DoF	m
\mathbf{z}	state-space coordinates	—

Scalars

Symbol	Description	Unit
Δt	time-step size	s
δ	initial blade-tip clearance	m
η	number of constraint modes	—
\hat{n}	number of nodes	—
κ	coupling stiffness	N/m
λ	eigenvalue	(rad/s) ²
Ω	rotational speed	rad/s
$\Omega_{n_d}^{\text{cr}}$	critical speed of n_d nodal diameters	rad/s
ω_{n_d}	eigenfrequency of n_d nodal diameters	rad/s

τ	constant delay	s
ξ	modal damping coefficient	—
f	frequency	m/s
K	strain energy	J
K_e	specific force coefficient	N/m
M	number of discretization steps in SDM	—
N	number of sectors	—
n	number of DoF	—
n_d	nodal diameter	—
SE	modal strain energy	J
T	kinetic energy	J
t	time	s
x_o, y_o	center node DoF in rotating frame	m

Subscripts and superscripts

Symbol	Description	Unit
$[\bullet]^{\text{bd}}$	elements of $[\bullet]$ of the bladed-disk	—
$[\bullet]^{\text{c}}$	elements of $[\bullet]$ of the casing	—
$[\bullet]_{\text{c}}$	cosine component of double harmonics	—
$[\bullet]_{\text{s}}$	sine component of double harmonics	—
$[\tilde{\bullet}]$	elements of $[\bullet]$ in reduced-order space	—

Bibliography

Books

- [AB08] Acary, V. and Brogliato, B. *Numerical methods for nonsmooth dynamical systems*. Springer, 2008 (p. 17, 20).
- [BKG09] Balachandran, B., Kalmar-Nagy, T., and Gilsinn, D. *Delay differential equations: recent advances and new directions*. Springer Verlag, 2009 (p. 113, 116).
- [Chi93] Childs, D. *Turbomachinery rotordynamics: phenomena, modeling, and analysis*. Wiley-Interscience, 1993 (p. 15, 16).
- [Die+95] Diekmann, O., Giles, S. van, Verduyn Lunel, S., and Walther, H. *Delay equations: functional-, complex-, and nonlinear analysis*. Springer-Verlag Berlin and Heidelberg GmbH & Co. KG, 1995 (p. 113).
- [Ern09] Erneux, T. *Applied delay differential equations*. Vol. 3. Surveys and Tutorials in the Applied Mathematical Sciences Series. Springer-Verlag New York, LLC, 2009 (p. 111).
- [Gen05] Genta, G. *Dynamics of rotating systems*. Springer Verlag, 2005 (p. 6, 15, 37).
- [Hug87] Hughes, T. *The Finite Element Method: linear static and dynamic finite element analysis*. Prentice Hall, Inc., 1987 (p. 11, 13).
- [IS11] Insperger, T. and Stépán, G. *Semi-discretization for time-delay systems : stability and engineering applications*. Springer Science+Business Media, 2011 (p. 116).

- [LF98] Lalanne, M. and Ferraris, G. *Rotordynamics prediction in engineering*. John Wiley & Sons Ltd., 1998 (p. 15).
- [Mei80] Meirovitch, L. *Computational methods in structural dynamics*. 5. Springer Science & Business Media, 1980 (p. 14, 57, 69).
- [MHP02] Mattingly, J., Heiser, W., and Pratt, D. *Aircraft engine design*. Ed. by Przemieniecki, J. 2nd Edition. AIAA Education Series, 2002 (p. 1).
- [Sto27] Stodola, A. *Steam and gas turbines. Vol. II*. McGraw-Hill Book Co., Inc, 1927 (p. 14).
- [Tlu00] Tlustý, J. *Manufacturing processes and equipment*. Prentice Hall, 2000 (p. 118).
- [WL06] Wriggers, P. and Laursen, T. A. *Computational contact mechanics*. Vol. 30167. Springer, 2006 (p. 21).

Journal papers

- [Alm+14] Almeida, P., Gibert, C., Thouverez, F., Leblanc, X., and Ousty, J.-P. “Experimental analysis of dynamic interaction between a centrifugal compressor and its casing.” *Journal of Turbomachinery* 137.3 (2014), p. 031008. DOI: 10.1115/1.4028328 (p. 27).
- [Bat+10] Batailly, A., Legrand, M., Cartraud, P., and Pierre, C. “Assessment of reduced models for the detection of modal interaction through rotor stator contacts.” *Journal of Sound and Vibration* 329.26 (2010), pp. 5546–5562. DOI: 10.1016/j.jsv.2010.07.018. OAI: hal-00524762 (p. 18, 19, 74, 80, 82, 94).
- [Bat+12] Batailly, A., Legrand, M., Millecamps, A., and Garcin, F. “Numerical-experimental comparison in the simulation of rotor/stator interaction through blade-tip/abradable coating contact.” *Journal of Engineering for Gas Turbines and Power* 134.8, 082504 (2012), p. 082504. DOI: 10.1115/1.4006446. OAI: hal-00746632 (p. 6, 23, 27, 45, 95, 96, 104, 112, 117, 120, 127, 129, 131, 149).
- [Bat+15] Batailly, A., Legrand, M., Millecamps, A., Cochon, S., and Garcin, F. “Redesign of a high-pressure compressor blade accounting for nonlinear structural Interactions.” *Journal of Engineering for Gas Turbines and Power* 137.2 (2015), p. 022502. DOI: 10.1115/1.4028263 (p. 87–90).

- [BB11] Butcher, E. and Bobrenkov, O. “On the Chebyshev spectral continuous time approximation for constant and periodic delay differential equations.” *Communications in Nonlinear Science and Numerical Simulation* 16.3 (2011), pp. 1541–1554. DOI: 10.1016/j.cnsns.2010.05.037 (p. 115).
- [BL15] Batailly, A. and Legrand, M. “Unilateral contact induced blade/casing vibratory interactions in impellers: Analysis for flexible casings with friction and abradable coating.” *Journal of Sound and Vibration* 348 (2015), pp. 344–364. DOI: 10.1016/j.jsv.2015.03.027 (p. 135, 136).
- [BML15] Batailly, A., Meingast, M., and Legrand, M. “Unilateral contact induced blade/casing vibratory interactions in impellers: Analysis for rigid casings.” *Journal of Sound and Vibration* 337 (2015), pp. 244–262. DOI: 10.1016/j.jsv.2014.10.010 (p. 27, 39, 67, 87, 90).
- [Bor+89] Borel, M., Nicoll, A., Schläpfer, H., and Schmid, R. “The wear mechanisms occurring in abradable seals of gas turbines.” *Surface and Coatings Technology* 39–40, Part 1 (1989). 16th International Conference on Metallurgical Coatings, pp. 117–126. DOI: 10.1016/0257-8972(89)90046-7 (p. 23).
- [CB07] Childs, D. and Bhattacharya, A. “Prediction of dry-friction whirl and whip between a rotor and a stator.” *Journal of Vibration and Acoustics* 129 (2007), p. 355. DOI: 10.1115/1.2731412 (p. 23, 28).
- [CB68] Craig Jr., R. and Bampton, M. “Coupling of substructures for dynamic analysis.” *AIAA journal* 6.7 (1968), pp. 1313–1319 (p. 18, 65).
- [CD81] Crandall, S. H. and Dugundji, J. “Resonant whirling of aircraft propeller-engine systems.” *Journal of Applied Mechanics* 48 (1981), pp. 929–935 (p. 28).
- [CDM86] Crawley, E., Ducharme, E., and Mokadam, D. “Analytical and experimental investigation of the coupled bladed disk/shaft whirl of a cantilevered turbofan.” *Journal of Engineering for Gas Turbines and Power* 108.4 (1986), pp. 567–575. DOI: 10.1115/1.3239948 (p. 34, 41).
- [CG89] Cameron, T. and Griffin, J. “An alternating frequency/time domain method for calculating the steady-state response of nonlinear dynamic systems.” *Journal of Applied Mechanics* 56.1 (1989), pp. 149–154. DOI: 10.1115/1.3176036 (p. 22).

- [CL07] Chu, F. and Lu, W. “Stiffening effect of the rotor during the rotor-to-stator rub in a rotating machine.” *Journal of Sound and Vibration* 308.3–5 (2007). Vibro-Impact Systems, pp. 758–766. DOI: 10.1016/j.jsv.2007.03.059 (p. 20).
- [CP02] Castanier, M. and Pierre, C. “Using intentional mistuning in the design of turbomachinery rotors.” *AIAA Journal* 40.10 (2002), pp. 2077–2086. DOI: 10.2514/2.1542 (p. 136).
- [CP06] Castanier, M. and Pierre, C. “Modeling and analysis of mistuned bladed disk vibration: status and emerging directions.” *Journal of Propulsion and Power* 22.2 (2006), pp. 384–396. DOI: 10.2514/1.16345 (p. 42, 136).
- [CP88] Cook, J. and Powell, B. “Modeling of an internal combustion engine for control analysis.” *Control Systems Magazine* 8.4 (1988), pp. 20–26. DOI: 10.1109/37.7726 (p. 112).
- [CTK91] Carpenter, N., Taylor, R., and Katona, M. “Lagrange constraints for transient finite element surface contact.” *International Journal for Numerical Methods in Engineering* 32.1 (1991), pp. 103–128. DOI: 10.1002/nme.1620320107 (p. 21, 73).
- [CYL06] Cao, J., Yuan, K., and Li, H.-X. “Global asymptotical stability of recurrent neural networks with multiple discrete delays and distributed delays.” *IEEE Transactions on Neural Networks* 17.6 (2006), pp. 1646–1651. DOI: 10.1109/TNN.2006.881488 (p. 111).
- [DEP11] Doyen, D., Ern, A., and Piperno, S. “Time-integration schemes for the finite element dynamic Signorini problem.” *SIAM Journal on Scientific Computing* 33.1 (2011), pp. 223–249 (p. 18).
- [Din+10] Ding, Y., Zhu, L., Zhang, X., and Ding, H. “A full-discretization method for prediction of milling stability.” *International Journal of Machine Tools and Manufacture* 50.5 (2010), pp. 502–509. DOI: 10.1016/j.ijmachtools.2010.01.003 (p. 115).
- [DJZ02] Dai, X., Jin, Z., and Zhang, X. “Dynamic behavior of the full rotor/stop rubbing: numerical simulation and experimental verification.” *Journal of Sound and Vibration* 251.5 (2002), pp. 807–822. DOI: 10.1006/jsvi.2001.3998 (p. 25).
- [Dom+11] Dombovari, Z., Barton, D., Wilson, R., and Stépán, G. “On the global dynamics of chatter in the orthogonal cutting model.” *International Journal of Non-Linear Mechanics* 46.1 (2011), pp. 330–338. DOI: 10.1016/j.ijnonlinmec.2010.09.016 (p. 113).

- [DZD14] Ding, Y., Zhu, L., and Ding, H. “A wavelet-based approach for stability analysis of periodic delay-differential systems with discrete delay.” *Nonlinear Dynamics* 79.2 (2014), pp. 1049–1059. DOI: 10.1007/s11071-014-1722-5 (p. 115).
- [Eme+83] Emery, A., Wolak, J., Etemad, S., and Choi, S. “An experimental investigation of temperatures due to rubbing at the blade-seal interface in an aircraft compressor.” *Wear* 91.2 (1983), pp. 117–130. DOI: 10.1016/0043-1648(83)90248-X (p. 23).
- [FBB14] Félix Patrón, R., Berrou, Y., and Botez, R. “New methods of optimization of the flight profiles for performance database-modeled aircraft.” *Part G: Journal of Aerospace Engineering* (2014), pp. 1–15. DOI: 10.1177/0954410014561772 (p. 1).
- [Föp95] Föppl, A. “Das problem der laval’shen turbinewelle.” *Civilingenieur* 1 (1895), pp. 332–342 (p. 14).
- [GE01] Groll, G. von and Ewins, D. “The harmonic balance method with arc-length continuation in rotor/stator contact problems.” *Journal of Sound and Vibration* 241.2 (2001), pp. 223–233. DOI: 10.1006/jsvi.2000.3298 (p. 22).
- [GN03] Gu, K. and Niculescu, S.-I. “Survey on recent results in the stability and control of time-delay systems.” *Journal of Dynamic Systems, Measurement, and Control* 125.2 (2003), pp. 158–165. DOI: 10.1115/1.1569950 (p. 113, 114).
- [Gre48] Green, R. “Gyroscopic effects of the critical speeds of flexible rotors.” *Journal of Applied Mechanics* 15 (1948), pp. 369–376 (p. 14).
- [Gru+11] Gruin, M., Thouverez, F., Blanc, L., and Jean, P. “Nonlinear dynamics of a bladed dual-shaft.” *European Journal of Computational Mechanics* 20.1-4 (2011), pp. 207–225. DOI: 10.3166/ejcm.20.207-225 (p. 28).
- [HL78] Hughes, T. and Liu, W. “Implicit-explicit finite elements in transient analysis: stability theory.” *Journal of Applied Mechanics* 45.2 (1978), pp. 371–374. DOI: 10.1115/1.3424304 (p. 17, 18).
- [IJR99] Irretier, H., Jacquet-Richardet, G., and Reuter, F. “Numerical and experimental investigations of coupling effects in anisotropic elastic rotors.” *International Journal of Rotating Machinery* 5.4 (1999), pp. 263–271. DOI: 10.1155/S1023621X99000238 (p. 15, 34, 37, 39, 40, 43, 44).

- [IS04] Insperger, T. and Stépan, G. “Updated semi-discretization method for periodic delay-differential equations with discrete delay.” *International Journal for Numerical Methods in Engineering* 61.1 (2004), pp. 117–141. DOI: 10.1002/nme.1061 (p. 115, 145).
- [IST07] Insperger, T., Stépan, G., and Turi, J. “State-dependent delay in regenerative turning processes.” *Nonlinear Dynamics* 47 (1 2007), pp. 275–283. DOI: 10.1007/s11071-006-9068-2 (p. 112, 128).
- [JAM01] Jean, M., Acary, V., and Monerie, Y. “Non-smooth contact dynamics approach of cohesive materials.” *Philosophical Transactions of the Royal Society of London. Series A: Mathematical, Physical and Engineering Sciences* 359.1789 (2001), pp. 2497–2518. DOI: 10.1098/rsta.2001.0906 (p. 20, 21).
- [Jef19] Jeffcott, H. “The lateral vibration of loaded shafts in the neighborhood of a whirling speed - the effect of want of balance.” *Philosophy Magazine* 37 (1919), pp. 304–314 (p. 13, 14).
- [JFR96] Jacquet-Richardet, G., Ferraris, G., and Rieutord, P. “Frequencies and modes of rotating flexible bladed disc-shaft assemblies: a global cyclic symmetry approach.” *Journal of Sound and Vibration* 191.5 (1996), pp. 901–915. DOI: 10.1006/jsvi.1996.0162 (p. 37–40).
- [JU03] Jiang, J. and Ulbrich, H. “Stability analysis of full annular rub in rotor-to-stator systems.” *PAMM* 2.1 (2003), pp. 88–89 (p. 25).
- [KB00] Kurz, R. and Brun, K. “Degradation in gas turbine systems.” *Journal of Engineering for Gas Turbines and Power* 123.1 (2000), pp. 70–77. DOI: 10.1115/1.1340629 (p. 4).
- [KCB12] Kim, C.-H., Cho, H., and Beom, H. “Exact solutions of in-plane natural vibration of a circular plate with outer edge restrained elastically.” *Journal of Sound and Vibration* 331.9 (2012), pp. 2173–2189. DOI: 10.1016/j.jsv.2011.12.027 (p. 34, 36).
- [KH10] Kyrychko, Y. and Hogan, S. “On the use of delay equations in engineering applications.” *Journal of Vibration and Control* 1.1 (2010), pp. 1–18. DOI: 10.1177/1077546309341100 (p. 114).
- [KM11] Khasawneh, F. and Mann, B. “A spectral element approach for the stability of delay systems.” *International Journal for Numerical Methods in Engineering* 87.6 (2011), pp. 566–592. DOI: 10.1002/nme.3122 (p. 115).

- [KS80] Kikuchi, N. and Song, Y. J. “Remarks on relations between penalty and mixed finite element methods for a class of variational inequalities.” *International Journal for Numerical Methods in Engineering* 15.10 (1980), pp. 1557–1561. DOI: 10.1002/nme.1620151010 (p. 20).
- [LBP12] Legrand, M., Batailly, A., and Pierre, C. “Numerical investigation of abradable coating removal in aircraft engines through plastic constitutive law.” *Journal of Computational and Nonlinear Dynamics* 7.1 (2012), p. 011010. DOI: 10.1115/1.4004951 (p. 23, 26, 87–89, 95, 109, 111, 124, 129, 150).
- [Leg+09] Legrand, M., Pierre, C., Cartraud, P., and Lombard, J. “Two-dimensional modeling of an aircraft engine structural bladed disk-casing modal interaction.” *Journal of Sound and Vibration* 319.1-2 (2009), pp. 366–391. DOI: 10.1016/j.jsv.2008.06.019. OAI: hal-00328186 (p. 5, 6, 18, 24, 25, 60, 63, 64, 72, 73, 78).
- [LK84] Loewy, R. and Khadert, N. “Structural dynamics of rotating bladed-disk assemblies coupled with flexible shaft motions.” *AIAA Journal* 22.9 (1984), pp. 1319–1327. DOI: 10.2514/3.48567 (p. 34).
- [LS04] Lattime, S. and Steinetz, B. “High-pressure-turbine clearance control systems: current practices and future directions.” *Journal of Propulsion and Power* 20.2 (2004), pp. 302–311. DOI: 10.2514/1.9255 (p. 4, 48, 72, 74, 91).
- [LST07] Lesaffre, N., Sinou, J.-J., and Thouverez, F. “Contact analysis of a flexible bladed-rotor.” *European Journal of Mechanics - A/Solids* 26.3 (2007), pp. 541–557. DOI: 10.1016/j.euromechsol.2006.11.002. OAI: hal-00322887v2 (p. 26, 28, 54, 80).
- [Lun87] Lund, J. “Stability and damped critical speeds of a flexible rotor in fluid-film bearings.” *Rotating Machinery Dynamics* 96 (1987), pp. 1–9 (p. 15).
- [Ma+15] Ma, H., Tai, X., Han, Q., Wu, Z., Wang, D., and Wen, B. “A revised model for rubbing between rotating blade and elastic casing.” *Journal of Sound and Vibration* 337 (2015), pp. 301–320. DOI: 10.1016/j.jsv.2014.10.020 (p. 28).
- [Man+15] Mandard, R., Witz, J.-F., Boidin, X., Fabis, J., Desplanques, Y., and Meriaux, J. “Interacting force estimation during blade/seal rubs.” *Tribology International* 82, Part B (2015), pp. 504–513. DOI: 10.1016/j.triboint.2014.01.026 (p. 23).

- [Mus86] Muszynska, A. “Whirl and whip–rotor/bearing stability problems.” *Journal of Sound and Vibration* 110.3 (1986), pp. 443–462. DOI: 10.1016/S0022-460X(86)80146-8 (p. 28).
- [MZ78] Michalowski, R. and Z., M. “Associated and non-associated sliding rules in contact friction problems.” *Archiwum Mechaniki Stosowanej* 30 (1978), pp. 259–276 (p. 20).
- [Nac+03] Nacivet, S., Pierre, C., Thouverez, F., and Jezequel, L. “A dynamic Lagrangian frequency-time method for the vibration of dry-friction-damped systems.” *Journal of Sound and Vibration* 265.1 (2003), pp. 201–219. DOI: 10.1016/S0022-460X(02)01447-5 (p. 22).
- [Nel07] Nelson, F. “Rotor dynamics without equations.” *International Journal of COMADEM* 10.3 (2007), p. 2 (p. 15).
- [Ols+14] Olson, B., Shaw, S., Shi, C., Pierre, C., and Parker, R. “Circulant matrices and their application to vibration analysis.” *Applied Mechanics Reviews* 66.4 (2014), p. 040803. DOI: 10.1115/1.4027722 (p. 32, 33, 139).
- [OM85] Oden, J. and Martins, J. “Models and computational methods for dynamic friction phenomena.” *Computer Methods in Applied Mechanics and Engineering* 52.1–3 (1985), pp. 527–634. DOI: 10.1016/0045-7825(85)90009-X (p. 20).
- [OS02] Olgac, N. and Sipahi, R. “An exact method for the stability analysis of time-delayed linear time-invariant (LTI) systems.” *IEEE Transactions on Automatic Control* 47.5 (2002), pp. 793–797. DOI: 10.1109/TAC.2002.1000275 (p. 115).
- [OZK14] Olgac, N., Zalluhoglu, U., and Kammer, A. “On blade/casing rub problems in turbomachinery: An efficient delayed differential equation approach.” *Journal of Sound and Vibration* 333.24 (2014), pp. 6662–6675. DOI: 10.1016/j.jsv.2014.06.038 (p. 115, 127).
- [Pad+07] Padova, C., Barton, J., Dunn, M. G., and Manwaring, S. “Experimental results from controlled blade tip/shroud rubs at engine speed.” *Journal of Turbomachinery* 129.4 (2007), pp. 713–723. DOI: 10.1115/1.2720869 (p. 27).
- [Pad+11] Padova, C., Dunn, M. G., Barton, J., Turner, K., Turner, A., and DiTommaso, D. “Casing treatment and blade-tip configuration effects on controlled gas turbine blade tip/shrouds rubs at engine conditions.” *Journal of Turbomachinery* 133.1 (2011), p. 011016. DOI: 10.1115/1.4000539 (p. 27).

- [PC87] Padovan, J. and Choy, F. K. “Nonlinear dynamics of rotor-blade-casing rub interactions.” *Journal of Turbomachinery* 109.4 (1987), pp. 527–534. DOI: 10.1115/1.3262143 (p. 25).
- [Ran69] Rankine, W. J. “Centrifugal force of rotating shafts.” *Engineer* 27 (1869), pp. 249–256 (p. 13, 14).
- [San+04] Santos, I., Saracho, C., Smith, J., and Eiland, J. “Contribution to experimental validation of linear and non-linear dynamic models for representing rotor–blade parametric coupled vibrations.” *Journal of Sound and Vibration* 271.3–5 (2004), pp. 883–904. DOI: 10.1016/S0022-460X(03)00758-2 (p. 15).
- [SBL13b] Salvat, N., Batailly, A., and Legrand, M. “Modeling of abradable coating removal in aircraft engines through delay differential equations.” *Journal of Engineering for Gas Turbines and Power* 135.10 (2013), p. 102102. DOI: 10.1115/1.4024959. OAI: hal-00879815 (p. 104, 111, 119, 120, 137).
- [SBL16] Salvat, N., Batailly, A., and Legrand, M. “Two-dimensional modeling of unilateral contact-induced shaft precessional motions in bladed-disk/casing systems.” *International Journal of Non-Linear Mechanics* 78.1 (2016), pp. 90–104. DOI: 10.1016/j.ijnonlinmec.2015.10.001. OAI: hal-01223046 (p. 63, 137).
- [SH97] Sobieszczanski-Sobieski, J. and Haftka, R. “Multidisciplinary aerospace design optimization: survey of recent developments.” *Structural optimization* 14.1 (1997), pp. 1–23. DOI: 10.1007/BF01197554 (p. 1).
- [Sha01] Shapiro, V. “Rotating class of parametric resonance processes in coupled oscillators.” *Physics Letters A* 290.5-6 (2001), pp. 288–296. DOI: 10.1016/S0375-9601(01)00693-4 (p. 56, 58, 70).
- [Sin04] Sinha, S. “Dynamic characteristics of a flexible bladed-rotor with Coulomb damping due to tip-rub.” *Journal of Sound and Vibration* 273.4-5 (2004), pp. 875–919. DOI: 10.1016/S0022-460X(03)00647-3 (p. 26, 88).
- [Sté+05] Stépán, G., Szalai, R., Mann, B., Bayly, P., Insperger, T., Gradisek, J., and Govekar, E. “Nonlinear dynamics of high-speed milling—analyses, numerics, and experiments.” *Journal of Vibration and Acoustics* 127.2 (2005), pp. 197–203. DOI: 10.1115/1.1891818 (p. 112, 119).

- [Tho79] Thomas, D. “Dynamics of rotationally periodic structures.” *International Journal for Numerical Methods in Engineering* 14.1 (1979), pp. 81–102. DOI: 10.1002/nme.1620140107 (p. 31, 32).
- [WC97] Wang, W. and Chen, L. “A predator-prey system with stage-structure for predator.” *Computers Mathematics with Applications* 33.8 (1997), pp. 83–91. DOI: 10.1016/S0898-1221(97)00056-4 (p. 111).
- [WP88] Wei, S.-T. and Pierre, C. “Localization phenomena in mistuned assemblies with cyclic symmetry part I: free vibrations.” *Journal of Vibration and Acoustics* 110.4 (1988), pp. 429–438. DOI: 10.1115/1.3269547 (p. 42).
- [WS03] Williams, J. and Starke Jr, E. “Progress in structural materials for aerospace systems.” *Acta Materialia* 51.19 (2003), pp. 5775–5799. DOI: 10.1016/j.actamat.2003.08.023 (p. 1).
- [Yi+99] Yi, M., He, J., Huang, B., and Zhou, H. “Friction and wear behaviour and abrasability of abradable seal coating.” *Wear* 231.1 (1999), pp. 47–53. DOI: 10.1016/S0043-1648(99)00093-9 (p. 5, 23).
- [Yu+02] Yu, J., Goldman, P., Bently, D., and Muszynska, A. “Rotor/seal experimental and analytical study on full annular rub.” *Journal of Engineering for Gas Turbines and Power* 124.2 (2002), pp. 340–350. DOI: 10.1115/1.1416691 (p. 25).

Conference proceedings

- [Bat+14] Batailly, A., Legrand, M., Millecamps, A., Cochon, S., and Garcin, F. “Redesign of a high-pressure compressor blade accounting for nonlinear structural Interactions.” *Proceedings of the ASME Turbo Expo*. 2014. DOI: 10.1115/GT2014-25673 (p. 27).
- [Ber+15] Berthoul, B., Batailly, A., Legrand, M., Stanier, L., and Cartraud, P. “Abradable coating removal in turbomachines: a macroscopic approach accounting for several wear mechanisms.” *Proceedings of the ASME Turbo Expo*. 2015. DOI: 10.1115/GT2015-42500 (p. 23).
- [Bla67] Black, H. “Synchronous whirling of a shaft within a radially flexible annulus having small radial clearance.” *ARCHIVE: Proceedings of the Institution of Mechanical Engineers*. Vol. 181. 31. 1967, pp. 65–73. DOI: 10.1243/PIME_CONF_1966_181_012_02 (p. 28).

- [FIO83] Funatogawa, O., Inoue, T., and Ohno, T. “Carcass deflection analysis of a turbo-fan engine.” *MSC/NASTRAN Users’ Conference Proceedings*. 1983 (p. 5, 48).
- [Her+14] Herzog, A., Krack, M., Panning-von Scheidt, L., and Wallaschek, J. “Comparison of two widely-used frequency-time domain contact models for the vibration simulation of shrouded tubine blades.” *Proceedings of the ASME Turbo Expo*. American Society of Mechanical Engineers. 2014. DOI: 10.1115/GT2014-26226 (p. 22).
- [HP14] Howard, R. and Puterbaugh, S. “Performance impact of tip clearance variation on a transonic, low aspect ratio, axial compressor stage.” *50th AIAA/ASME/SAE/ASEE Joint Propulsion Conference*. 2014. DOI: 10.2514/6.2014-3439 (p. 4).
- [KT50] Kuhn, H. and Tucker, A. “Nonlinear programming.” *Second Berkeley Symposium on Mathematical Statistics and Probability*. University of California, 1950, pp. 481–492 (p. 20).
- [LIS15] Lehotzky, D., Insperger, T., and Stépán, G. “State-dependent, non-smooth model of chatter vibrations in turning.” *Proceedings of the ASME International Design Engineering Technical Conferences & Computers and Information in Engineering Conference*. 2015 (p. 149).
- [Mei+13] Meingast, M., Batailly, A., Legrand, M., and Ousty, J.-P. “Investigation of impeller-casing interactions in the centrifugal compressor of a helicopter engine.” *Proceedings of the ASME Turbo Expo*. 2013. DOI: 10.1115/GT2013-94461 (p. 38, 53).
- [Mil+09] Millecamps, A., Brunel, J.-F., Dufrénoy, P., Garcin, F., and Nucci, M. “Influence of thermal effects during blade-casing contact experiments.” *Proceedings of the ASME International Design Engineering Technical Conferences & Computers and Information in Engineering Conference*. 2009, pp. 855–862. DOI: 10.1115/DETC2009-86842 (p. 6, 26, 117, 149).
- [Mil+15] Millecamps, A., Batailly, A., Legrand, M., and Garcin, F. “Snecma’s viewpoint on the numerical and experimental simulation of blade-tip/casing unilateral contacts.” *Proceedings of the ASME Turbo Expo*. 2015. DOI: 10.1115/GT2015-42682 (p. 87).
- [PTC14] Parent, M., Thouverez, F., and Chevillot, F. “Whole engine interaction in a bladed rotor-to-stator contact.” *Proceedings of the ASME Turbo Expo*. 2014. DOI: 10.1115/GT2014-25253 (p. 6, 29, 47, 53, 68, 80, 135).

- [Rek80] Rekasius, Z. “A stability test for systems with delays.” *Proc. Joint Automatic Control Conf., Paper No. TP9-A*. 1980 (p. 115).
- [SB06] Sternchüss, A. and Balmès, E. “On the reduction of quasi-cyclic disks with variable rotation speeds.” *Proceedings of the International Conference on Advanced Acoustics and Vibration Engineering (ISMA)*. 2006, pp. 3925–3939. OAI: HAL-00266394 (p. 18, 19, 38, 39).
- [SBL13a] Salvat, N., Batailly, A., and Legrand, M. “Modeling of abradable coating removal in aircraft engines through delay differential equations.” *Proceedings of the ASME Turbo Expo*. 2013. DOI: 10.1115/GT2013-94400 (p. 111, 137).
- [SBL13c] Salvat, N., Batailly, A., and Legrand, M. “Prédiction de l’enlèvement de matériau abradable par équations différentielles à retard dans les moteurs d’avion.” *11ème Colloque National de Calcul des Structures - CSMA*. 2013. OAI: hal-01104675 (p. 111, 137).
- [SBL14] Salvat, N., Batailly, A., and Legrand, M. “Two-dimensional modeling of shaft precessional motions induced by unilateral blade/casing contacts in aircraft engines.” *Proceedings of the ASME Turbo Expo*. 2014. DOI: 10.1115/GT2014-25688. OAI: hal-01090671v2 (p. 43, 45, 49, 63, 65, 67, 73–75, 78, 137).
- [Wil11] Williams, R. “Simulation of blade casing interaction phenomena in gas turbines resulting from heavy tip rubs using an implicit time marching method.” *Proceedings of the ASME Turbo Expo*. 2011. DOI: 10.1115/GT2011-45495 (p. 23, 112).

Other sources

- [Bar00] Bartha, A. “Dry friction backward whirl of rotors.” PhD thesis. Swiss Federal Institute of Technology, Zurich, Switzerland, 2000. DOI: 10.3929/ethz-a-004130993 (p. 28).
- [Bat08] Batailly, A. “Simulation de l’interaction rotor/stator pour des turbo-machines aéronautiques en configuration non-accidentelle.” PhD thesis. Université de Nantes, 2008. OAI: hal-00616524 (p. 25).
- [Bla01] Bladh, R. “Efficient predictions of the vibratory response of mistuned bladed disks by reduced order modeling.” PhD thesis. University of Michigan, 2001. OAI: tel-00358168 (p. 32, 34, 35, 37, 139).

- [HJW09] Hertter, M., Jakimov, A., and Werner, A. “Abradable material, useful as air seal improving covering on compressor or turbine intake, comprises cellular metal structure containing non-metallic particles.” German Patent. DE102008011244-A1. 2009 (p. 22).
- [Jar08] Jarlebring, E. “The spectrum of delay-differential equations: numerical methods, stability and perturbation.” PhD Thesis. Technische Universität Carolo-Wilhelmina zu Braunschweig, 2008 (p. 115).
- [Leg05] Legrand, M. “Modèles de prédiction de l’interaction rotor/stator dans un moteur d’avion.” PhD thesis. Université de Nantes, 2005. OAI: tel-00011631 (p. 16).
- [Lie06] Liew, K. “Aerothermodynamic cycle analysis of a dual-spool, separate-exhaust turbofan engine with an interstage turbine burner.” PhD thesis. Michigan Technological University, 2006 (p. 2).
- [Lon06] Long, X. “Loss of contact and time delay dynamics of milling processes.” PhD Thesis. University of Maryland, 2006 (p. 113).
- [Mas11] Massieux, R. “Etude de stabilité d’un moteur en contact rotor/stator.” M.Sc Thesis. Ecole Centrale de Lyon, 2011 (p. 28, 29).
- [Mei14] Meingast, M. “Investigation of rotor-casing interaction phenomena in the centrifugal compressor of a helicopter engine.” PhD thesis. McGill University, 2014 (p. 7, 27, 38, 39, 50, 97).
- [Mil10] Millecamps, A. “Interaction aube-carter: contribution de l’usure de l’abradable et de la thermo-mecanique sur la dynamique d’aube.” PhD Thesis. Univeristé de Lille, 2010 (p. 45).
- [Mus+89] Muszynska, A., Bently, D., Franklin, W., Hayashida, R., Kingsley, L., and Curry, A. *Influence of rubbing on rotor dynamics - part 1*. Tech. rep. NAS8-36179. NASA, 1989 (p. 16, 23, 25).
- [Nat73] National Airlines, I. *Aircraft accident report: DC-10-10, N60N4, near Albuquerque, New Mexico*, tech. rep. NTSB-AAR-75-2. National Transportation Safety Board, 1973 (p. 7, 8).
- [Nor12] Norris, G. *Air Canada 777 engine failure turns spotlight on GE90*. 2012. URL: <http://aviationweek.com/awin/air-canada-777-engine-failure-turns-spotlight-ge90> (p. 8).
- [Nor95] Norris, G. *GE90 power surge hits 777 ETOPS progress*. Flight International. Dec. 1995. URL: <http://www.flightglobal.com/news/articles/ge90-power-surge-hits-777-etops-progress-22992/> (p. 8).

- [OM82] Olsson, W. and Martin, R. *B747/JT9D flight loads and their effect on engine running clearances and performance deterioration*. Technical report NASA-CR-165573. NASA, 1982 (p. 5, 48).
- [Sal11] Salvat, N. "Abradable material removal in aircraft engines: a time delay approach." M.Sc Thesis. Université de Bourgogne, 2011 (p. 112, 113, 115).
- [Sch97] Schmiechen, P. "Travelling wave speed coincidence." PhD thesis. Imperial College of Science, Technology and Medicine, 1997 (p. 7, 23, 24, 58, 60, 66, 67, 72, 141).
- [Yeo11] Yeo, G.-H. *Blade failure behind Qantas 747 engine shutdown*. 2011. URL: <http://www.flightglobal.com/news/articles/blade-failure-behind-qantas-747-engine-shutdown-356849/> (p. 8).